INVESTIGATION OF ACIDIZING TECHNOLOGIES IN HIGH-TEMPERATURE APPLICATIONS FOR SANDSTONE AND LIMESTONE FORMATIONS

A Dissertation

by

AHMED MOHAMED HANAFY

Submitted to the Office of Graduate and Professional Studies of
Texas A&M University
in partial fulfillment of the requirements for the degree of

DOCTOR OF PHILIOSOPHY

Chair of Committee,	Hisham A. Nasr-El-Din
Committee Members,	Stephen A. Holditch
	Jerome Schubert
	Mahmoud El-Halwagi
Head of Department,	Jeff Spath

December 2018

Major Subject: Petroleum Engineering

ABSTRACT

Formation matrix acidizing is an essential step in the life of any oil or gas production well. The stimulation process is basically designed around the mineralogy of the formation, the goal of the treatment, the lithology, and the petrophysical properties. Due to their complicated mineralogy, sandstones are difficult formations when it comes to stimulation. Both the clay content and the clay type determines the success or the failure of any acidizing process. Calcite formations, however, are easier to acidize. The acidizing process aims to induce wormholes along the formation to enhance the overall productivity of the formation. Yet, the variation of the formation permeability, even between two adjacent low-permeability calcite veins, makes acid stimulation challenging. This work aims to investigate and refine the matrix acidizing process in high pressure high temperature environment for both sandstone and limestone formations.

The sandstone analysis was conducted through coreflood experiments on cores that were damaged by induction of fines migration using deionized water. Three formations were investigated in this study: Bandera, Grey Berea, and Kentucky sandstones. Each of the formations was stimulated in the presence of fines migration and then compared to the results of stimulating undamaged cores. All studies were conducted at 150 and 250˚F to assess the impact of the temperature. All cores were scanned using computed tomography (CT scan). A new technique was then developed to track the acidizing outcomes based on the CT scans. All cores were also scanned using nuclear magnetic resonance (NMR) to assess the variation of the petrophysical properties and to validate the data from the new CT scan analysis.

The limestone analysis in this study was based on single and dual coreflooding techniques. The experimental process was designed to investigate the viscoelastic surfactants at 150 and 250˚F in 15 wt% HCl and their compatibility with different corrosion inhibitors. The dual corefloods were assessed based on the extent of the wormhole propagation in the low-permeability cores. The rheological properties of the VES acid mixture was evaluated in the presence of acid additives such as corrosion inhibitors, emulsifiers, and iron control agents.

The acidizing of the different sandstone formations in the presence and the absence of fines migration showed a complex response with the variation of the clay mineral type and content. The new CT scan processing technique coupled with the NMR pore structure assessment succeeded in tracking the formation damage at each step of the study. In general, the formation damage from the secondary and tertiary reactions was maximized at 250˚F. Results show the mobilization of the fines to cause localized damage at the core outlets.

The examination of the VES system as a self-diverting acid system at 250˚F succeeded in increasing understanding and improving investigation of technology limitations. The cationic viscoelastic surfactant maintained a range of 200 to 800 cp at 250˚F. The apparent viscosity and the temperature range of the surfactant depended highly on the VES concentration and the chemistry and concentration of the additives. In addition, coreflood experiments showed the ability of the system to work at 150 and 250˚F.

DEDICATION

It is with love that I dedicate this dissertation and my Ph.D. to the soul of my father who died during the last year of that work. Without him I would have never been able to reach this stage. The only part missing in this work is delivering the news of finishing my Ph.D. to him. I hope that he feels what I feel.

I also lovingly dedicate this work to my wife Sara, my daughter Farida, my son Yassin, and my mother Mervat. They are the true definition of support. The process was long and painful but they made it rewarding at each stage.

ACKNOWLEDGMENTS

I acknowledge my advisor, father, friend, and mentor Dr. Hisham Nasr-El-Din. It was a pleasure to be his student. I recognized his great knowledge the first time I attended his class, the first time he showed me how to describe a graph, and the first time he showed me how to address a problem. My Ph.D. was a journey, and he was my guide. The development I witnessed in all aspects both academically and personally is attributed to his very close coaching. The time I spent with Dr. Nasr-El-Din is what molded me into what I am now. It was an honor and pleasure to spend five years with him.

I acknowledge the effort, the knowledge, and the time that my committee members, Dr. Stephen A. Holditch, Dr. Jerome Schubert, and Dr. Mahmoud El-Halwagi, dedicated to guide and support this work and my Ph.D. Their questions in the preliminary exam were the guide for most of the development of my research.

I would like to give an acknowledgment to Dr. Zoya Heidari and Abdalla Ali for their collaboration and facilitation of a part of the NMR measurements.

I would like to give a huge acknowledgement to Gia Alexander for her proofreading and technical writing support on many publications and documents I produced during my Ph.D.

I would love to show my appreciation through some words to my research group, who made me capable and successful. My first coreflood was coached by Ahmed Shehata, who is a friend and a colleague. My first SEM was coached by Wang. I had numerous interactions with each member of the group, through which my work became better and better. These people were the light in the beginning of the path, they took my hand to be able to produce every part of my dissertation.

With love I acknowledge my small family: my wife Sara, my daughter Farida, and my son Yassin for all of the fun and happiness they gave me, while I was stressed and pressured during the process of getting my Ph.D. I love you all and I remember the times we were in pressure and we took care of each other. We are done and we made it all together and it wouldn’t have been a better five years than it was.

CONTRIBUTORS AND FUNDING SOURCES

Contributors

This work was supervised by a dissertation committee consisting of Professor Hisham A. Nasr-El-Din and Professors Stephen A. Holditch and Jerome Schubert of the Department of Petroleum Engineering and Professor Mahmoud El-Halwagi of the Department of Chemical Engineering.

The apparent viscosity measurements in Chapter VI were conducted by collaborating with Dr. Ahmed Rabie and Dr. Rose Ndong of Solvay Company.

All work for the dissertation was completed by the student, under the advisement of Professor Hisham A. Nasr-El-Din of the Department of Petroleum Engineering.

Funding Sources

There are no outside funding contributions to acknowledge related to the research and compilation of this document.

NOMENCLATURE

CT-Scan	Computed Tomography Scan
EDS	Energy-Dispersive Spectroscopy
ICP	Inductively Coupled Plasma Mass Spectrometry
N_{Da}	Damkohler Number
NMR	Nuclear Magnetic Resonance
SEM	Scanning Electron Microscope
SNR	Signal to Noise Ratio
XRD	X-ray Diffraction
XRF	X-ray Fluorescence
k	Permeability
PV	Pore Volumes
S/V	Surface to Volume Ratio
T_2	Transverse Relaxation Time
T_{2bulk}	Pore Fluid Relaxation Time
$T_{2diffusion}$	Fluid Diffusion Ability Relaxation Time
$T_{2surface}$	Pore and Fluid Interaction Relaxation Time
ρ_2	Surface Relaxivity Parameter

TABLE OF CONTENTS

LIST OF FIGURES

LIST OF TABLES

CHAPTER I

INTRODUCTION[1][2][3][4]

Matrix Acidizing

The matrix acidizing treatment aims to remove the skin damage from the pay zones wellbore, which enhances the permeability and the overall well productivity. This targeted damage is mainly due to the deposition of particulate solids during drilling, work-over, or production operations. These objectives are accomplished in sandstone formations by pumping acid systems with the aim of reacting with the clays, the solid particulates, and the surrounding cementing materials, while carbonate stimulation is based on bypassing the damage zone, creating conductive channels or "wormholes."

---

[1] Part of the data reported in this chapter is reprinted with permission from "NMR Study to Assess Fines Migration Damage and Its Removal Using Regular Mud Acid in Different Sandstone Cores" by Hanafy, A. M., Nasr-El-Din, H. A. 2016. Presented at the Abu Dhabi International Petroleum Exhibition & Conference, 7-10 November, Abu Dhabi, UAE, copyright 2016 by the Society of Petroleum Engineers. Reproduced with permission of SPE. Further reproduction prohibited without permission.

[2] Part of the data reported in this chapter is reprinted with permission from "A New Method to Assess Stimulation of Sandstone Cores Damaged by Fines Migration" by Hanafy, A. M., Nasr-El-Din, H. A. 2018. Presented at the SPE Western Regional Meeting, 22-26 April, Garden Grove, California, USA, copyright 2018 by the Society of Petroleum Engineers. Reproduced with permission of SPE. Further reproduction prohibited without permission.

[3] Part of the data reported in this chapter is reprinted with permission from "New Viscoelastic Surfactant with Improved Diversion Characteristics for Carbonate Matrix Acidizing Treatments" by Hanafy, A. M., Nasr-El-Din, H. A., Rabie, A. et al. 2016. Presented at the SPE Western Regional Meeting, 23-26 May, Anchorage, Alaska, USA, copyright 2016 by the Society of Petroleum Engineers. Reproduced with permission of SPE. Further reproduction prohibited without permission.

[4] Part of the data reported in this chapter is reprinted with permission from "Evaluating the Effects of Acid Stimulation Treatment Before and After Fines Migration on Petrophysical Properties in Sandstone Reservoirs" by Hanafy, A. M., Ali, A., Nasr-El-Din, H. A. et al. 2015. Presented at the International Petroleum Technology Conference, 6-9 December, Doha, Qatar, copyright 2015 by the International Petroleum Technology Conference. Reproduced with permission of IPTC. Further reproduction prohibited without permission.

Sandstone Matrix Acidizing

Matrix acidizing of sandstone formations is one of the most challenging reservoir stimulation techniques. Sandstone mineralogy is basically a mixture of quartz, clays, calcites, and organic matter, and each component responds differently to the acids used during the stimulation process. Furthermore, the conventional technologies involve consecutive stages of different chemical formulas that would further complicate the process outcomes. Such treatments at elevated temperatures trigger secondary and tertiary reactions that have the potential to damage the formation. A key factor for successful treatment is the percentage of acid-sensitive alumino-silicate minerals and their distribution in the formation. Aluminosilicate minerals that are mobilized chemically or mechanically result in less stable clays localized at narrow wellbore pore throats, thus decreasing formation productivity.

The most common and basic acid system in sandstone is the mud acid which is a mixture of HF for its ability to dissolve the alumino silicate minerals combined with HCl for calcites dissolution. Those acids were designed for multiple formation in different ratios to accommodate the mineralogical restriction in the treated formations. Those ratios varied between 6:1.5 HCl to HF and up to 13:1.5 in some calcite reach formations. HCl was replaced by organic acids in case of HCl sensitive mineral.

After years of research the literature have concluded that matrix acidizing for sandstone is to be conducted on the light of: firstly, retardation of acid impact on different minerals present in sandstone in order to reach further in the treated formation. Secondly, suppress the secondary reactions and prevent depositions of its products.

Fines Migration

One of the biggest challenges in drilling and producing sedimentary rock reservoirs that is reach in clay minerals is fines migration damage. This damage can be triggered by the mobilization of the unconfined particulates of clay minerals during the production or stimulation phase of the well. Fines migration damage works on blocking the pore throats reducing the permeability and the overall permeability of the formation (Muecke 1979). One of the conventional clay rich reservoirs with a clear risk of fines migration damage is sandstone reservoirs. In such reservoirs minerals such as illite and kaolinite can be mobilized if the production rates exceeds a certain threshold. This mobilization leads to the travel of the detached particulates and settling in tighter pore throats, which leads to permeability restriction. Pumping incompatible fluid in such reservoir have potential to induce chemical detachment of the clay minerals. Semectite is another clay mineral on the walls of the pore throats, which have the tendency to swell upon the change of the formation fluid pH, temperature, or salinity. This changes alter the clay double layer thickness and results in more pore throat restriction and further permeability reduction (Mungan 1965).

Literature have covered fines migration in multiple aspects varying from what are fines migration and what are the triggering mechanism to clay stabilizers and how to avoid fines migration. The triggering mechanism and the sensitivity for fines migration was investigated by Khilar and Fogler (1987) who studied and reported the significant impact of brine composition on clay minerals in sandstone formation. The fines migration process is essentially a colloidal dispersion type where the clay particles detach from the pore walls. This mechanism is strictly sensitive for the salt type, concentration, and the valence of the ions.

Divalent and selective monovalent ions have a strong protecting effect that eliminate formation damage due to fines migration. The double layer analysis explained how fines migration could be triggered or suppressed based on the zeta potential studies. Musharova et al. (2012) reported the effect of the high temperature on the fines migration. The interpretation of this work explained by the double layer theory that the higher the temperature the higher the change of the matrix clay system and the more the repulsion in between clay layers. Fines migration showed to be a lethal factor that gets maximized in higher temperature wells (Schembre et al. 2006). Furthermore, the repulsion forces are maximized when the high temperature is coupled with high pH environment. Those factors in absence of strong interlayer cations to hold the clay particles together result in the detachment of the clay particle from the pore wall and its precipitation in the pore throat (Khilar and Fogler 1983).

Ji et al. (2016) studied the process of sandstone acidizing using formula that have the capability of controlling fines migration. $AlCl_3$ was introduced and proven as a retardant for the HF acid to slow down its reaction with clay minerals such as: bentonite, illite, and smectite. The work showed success of 5 wt% $AlCl_3$ addition to minimize the reaction out puts with clays and lower the formation damage based on solubility test analyses at room temperature. Furthermore, the work eliminated the theory of AlF_3 precipitation using NMR analysis and showed the presence of some reaction products such as H_2SiF_6 and $HSiF_5$, which work as a potential for tertiary damaging reactions that could lead to precipitation of Ca, Mg, and K salts of fluorides (Shuchart and Buster 1995). Those species also capable of detaching binding ions from clay structures and precipitate silica gels and AlF_x ions (Gdanski 1998). Acid stimulation for fines migration damaged formation is accompanied by many side effects such as sludging in presence of high asphaltene content (Al-Mubarak et al. 2015). Clays such as chlorite and illite are known for their sensitivity for the HCl is another problem for acid stimulation of damaged zones (Mahmoud et al. 2015).

The literature is missing a clear method to monitor the changes in the pore throat structures during fines migration stimulation. This absence make it hard to quantify and monitor the efficiency of fines migration damage treatment.

Mud Acid and the Corresponding Formation Damage

The most common acid system for use in sandstone is mud acid, which is a mixture of HF for its ability to dissolve the alumino-silicate minerals, and HCl to dissolve carbonate minerals. Different acid mixtures are designed for individual formations to accommodate specific mineralogical restrictions. Typical acid ratios vary from 6:1.5 HCl to HF to 13:1.5 in some calcite-rich formations. Furthermore, HCl is replaced by organic acids such as acetic acid and formic acid in the presence of HCl-sensitive minerals.

Clay minerals exhibited in many studies complicated set of reactions either with HCl or regular mud acid in presence of HF acid. The production of H2SiF6 proved to be of high significance in triggering secondary reactions that result in degradation of the alumino silicate structure. This type of reactions not only produce amorphous meta structure but also deposited by-products in the fine pore throats (Gdanski 1999, 2000). Chlorite minerals showed a high suitability for acid attack resulting in destroying the crystal structure. This yield to the release of structure binding ions such as Fe, Al, and Mg. This result in an amorphous body known as silica gel, which is one of the most important formation damage reasons in sandstone acidizing process. Formation damage was even witnessed in many cases in the field after application of HF acid in order to dissolve the silica gel amorphous bodies, this was attributed to the tertiary reactions with the clay minerals (Simon and Anderson 1990; Yang et al. 2012).

Secondary and tertiary reactions in sandstone acidizing have been proven in multiple studies to be detrimental to the stimulation outcomes. Treatment of K-feldspar formations with HF was reported to cause severe formation damage; stimulation at 300˚F was proven to be of a damaging nature as well. The HF primary reaction with alumino-silicates is described as shown in Eq. 1 (Gdanski 2000).

$$(5+x)HF + M - Al - Si + (3-x+1)H^+ \rightarrow HSiF_5 + AlF_x^{(3-x)+} + M^+ + H_2O \quad . \quad \ldots\ldots\ldots\ldots\ldots \qquad (1)$$

The reaction is showing that the primary reaction will consume all acid and all of the alumino-silicate will be dissolved, this will lead to improvement in the core porosity. Unfortunately, this reaction doesn't stop to this extent. Secondary reactions start from the fluosilicic acid attacking the intact alumino-silicate minerals in the pore throats producing the hydrated silica and AlF_x ions according to the reaction shown in Eq. 2 (Gdanski 1999).

$$\frac{x}{5}HSiF_5 + M - Al - Si + (3-X+1)H^+ + H_2O \rightarrow AlF_x^{(3-x)+} + M^+ + Si(OH)_4.nH_2O \quad . \quad \ldots\ldots\ldots\ldots\ldots \qquad (2)$$

But silica gel can also come from the primary reaction in a spent HF condition. Furthermore, the fluosilicic (H_2SiF_6) and fluoaluminic (H_3AlF_6) react with feldspars and precipitate silica gel, in which it reacts with sodium and potassium ions, precipitating fluoaluminates and fluosilicates. The presence of a large amount of AlF_x in the system promotes the tertiary reaction cycle, which also leads to the leaching of the Al ions from the aluminosilicate structure and precipitates more silica gel as shown in Eq. 3 (Gdanski 1998; Al-Dahlan et al. 2001).

$$AlF_x + M - Al - Si + H^+ \rightarrow AlF_y + SiO_2 . 2H_2O \quad . \quad \ldots\ldots\ldots\ldots\ldots \quad (3)$$

Sandstone Reservoirs Assessments for Matrix Acidizing Suitability

The development of clear reservoir assessment methodology to design a successful treatment have been investigated by McCune et al. (1975). They divided their criteria into four main categories: petrographic, mechanical, mineralogical, and petrophysical assessments. Petrographic assessment described the formation grain size, type, and sorting. The mechanical properties were evaluated in term of compressive strength. Mineralogy was evaluated based on XRD using an aluminum reference to enhance the semi-quantitative analysis accuracy. Petrophysics of the core was mainly the core average porosity and permeability. They stimulated 20 sandstone formations HCl at high pressure and high temperature, and the extent of the stimulation process success was compared to the formation parameters to compute a formation property factor F_v. The conclusion was the successful treatments will happen when the formation is consolidated with high quartz to clay ratio.

The complexity of the matrix acidizing of sandstone lies in the abundance of different clay types and morphologies in the same formation. The reaction between the clay minerals and the HCl results in leaching of both iron and aluminum ions precipitating silica gel (Simon and Anderson 1990; Thomas et al. 2001). Although mud acid was introduced for its ability to dissolve silica, it's secondary and tertiary reactions with clays causes more silica gel and other forms of formation damage, which is critical to the success of the stimulation operation (Smith and Hendrickson 1965; Walsh et al. 1982; Hartman et al. 2006). The nature and the abundance of the clay mineral in the core will determine the severity and the location of the damage resulting from these formation damage forms.

The ratio of the HCl to HF acids have been reported to be controlling the intensity of the resulting formation damage (Walsh et al. 1982). These ratios change according to the mineralogical and the petrophysical properties of the stimulated formation (Gatewood et al. 1970; Wehunt et al. 1993; Guichard et al. 1996). The formation damage due to CaF_2 can be reduced by proper design of a preflush stage that minimizes the HF interaction with the carbonate minerals (Smith and Hendrickson 1965). The clay content was shown to be a controlling variable to the HF percent after which the formation damage severity increases. The precipitation of fluosilicates, AlF_3, and $Al(OH)_3$ due to the secondary and tertiary reactions in addition to the silica gel precipitation signifies the permeability reduction in the damaged zones (Walsh et al. 1982; Gdanski 1994, 1998, and 1999). Silica gel damage is inevitable, but Al ions damage can be minimized by maintaining high HCl to HF ratio (Walsh et al. 1982).

The numerous studies in sandstone stimulation investigated the clay content impact on acid design. Yet, clays were examined as a bulk quantity with no other properties that would impact its interaction with acid species. Parameters such as clay morphology and its nature of presence in the pore structure were never considered. The absence of a 3D visualizing of the formation damage in the treated cores limits the ability to assess the mentioned parameters and their impact on the stimulation process. A detailed combined layout of the core original petrophysical and mineralogical properties followed by detailed tracking to the acid reaction would give an insight on how to design a successful treatment in sandstone.

Nuclear Magnetic Resonance (NMR)

The tracking of the pore structure changes after acid stimulation is an essential need for further understanding. Nuclear magnetic resonance is one of the accurate, and non-destructive, tests to determine the formation pore size distribution, porosity, wettability, and hydrocarbon saturation. The NMR science is based on the concept of exciting the hydrogen atoms that is present in either the water or the oil contained in the formation pore. The higher the concentration of the hydrogen ion the higher the NMR response. The transverse relaxation time (T_2) is the dephasing time constant of the hydrogen nuclei subjected to NMR pulse. It is variation is controlled by Eq. 4:

$$\frac{1}{T_2} = \frac{1}{T_{2\,bulk}} + \frac{1}{T_{2\,surface}} + \frac{1}{T_{2\,diffusion}} \quad . \quad \ldots\ldots\ldots\ldots\ldots\ldots\ldots\ldots\ldots\ldots\ldots \quad (4)$$

in which the $T_{2\,bulk}$ term is controlled by the pore fluid viscosity. The $T_{2\,surface}$ term is a function of the relationship between the pore and the filling fluid. Hence, it is influenced by the change in pore size. While the $T_{2\,diffusion}$ is a term that can be measured in a variable magnetic field in order to account for the effect of the fluid diffusion ability. Regular core analysis using NMR showed that both of the effects of the bulk and the diffusion terms can be eliminated in the case of water saturated cores and the absence of a gradient magnetic field. Hence, the measured relaxation time is related to the pore size using the $T_{2\,surface}$ term using Eq. 5, where ρ_2 is the surface relaxivity parameter and s/v is the surface to volume ratio (Lewis et al. 2013).

$$\frac{1}{T_{2\,surface}} = \rho_2 \frac{s}{v} \quad . \quad \ldots\ldots\ldots\ldots\ldots\ldots\ldots\ldots\ldots\ldots \quad (5)$$

Limestone Matrix Acidizing

Matrix acidizing is the process to stimulate the near wellbore zones. In lime stone formations this process is conducted by opening artificial channels to bypass the damaged area. Those channels are commonly known as wormholes. Matrix acidizing is employed when acid fracturing is not favored. It is favored whenever a natural boundary is to be preserved to avoid mixed phases production. Chalky limestone formation is another case were matrix acidizing is favored on the acid fracturing due to the softness of the formation. In order to ensure a matrix stimulation rather than acid fracturing the injection flow rate is highly reduced. This low rate treatment suffers the early spending of the acid resulting in shallow acid penetration. Furthermore, it leads to face dissolution or even total matrix dissolution which can lead to a weak near wellbore structure.

The problem of the fast spending of the acid was tackled using multiple techniques. Acid retardation started by substituting the strong HCl by weaker acid such as organic acids. Other techniques to retard the acid was employed by emulsifying the acid in oil droplets. This technique retarded the acid through a controlled diffusion in the oil droplet before reaching the rock surface. This approach made it possible to reach deeper zones by the same acid volume. Furthermore, acid was assisted by nitrogen and surfactant foaming foam helped lowering the acid leaks out of the wormhole resulting in longer more efficient channel (Fredd and Fogler 1998a).

Wormhole Propagation in Limestone

The wormhole channels are a result of the heterogeneous pore size distribution. The acid tends to flow in the wider high permeability pores on the formation face. Upon the exposure of those large pores to acid the dissolution reaction progress fast that the acid progress deep from this initial pore forming a wormhole like structure. This whole tends to draw all the acid flow since it is the channel with the least resistance to flow.

The wormhole propagation is mainly depends on the ratio between the acid/mineral rate of dissolution to the mass transfer of the H^+ ion by convection. This phenomena is known as the Damkohler number N_{Da}. In the case of the rate of reaction is fast compared to the mass transfer, the rate of dissolution is described by the mass transfer efficiency. At this stage the Damkohler number is described by Eq. 6.

$$N_{Da} = aD_e^{2/3}\frac{L}{q} \quad . \quad \ldots\ldots\ldots\ldots\ldots\ldots\ldots\ldots \quad (6)$$

Knowing that the q is the flow rate, D_e is the diffusion coefficient, a is the minerology constant, and L is the pore length. According to this equation the dissolution structure is influenced by the flow rate of the acid assuming the rest of the parameters are fixed (Fredd and Fogler 1998a). And from this study it is clear that is there is an optimum flow rate at which the thin non branched wormhole is constructed. The deviation from this flow rate results in face dissolution or ramified wormhole structure at high and low flow rate consecutively.

Acid Diversion

However, in heterogeneous carbonate reservoirs, another challenge arises when a large contrast in permeability exists between different producing zones. **Fig. 1** shows the extent of wormhole propagation with acid diversion in the low permeability zones with the change in the permeability contrast between the high permeability and the low permeability sections. In order to get over such a limitation acid diversion was investigated as an important technology that ensure the placement of the acid in both the low and high permeability zones (Woo et al. 1999; Chang et al. 2001; Kalfayan and Martin 2009).

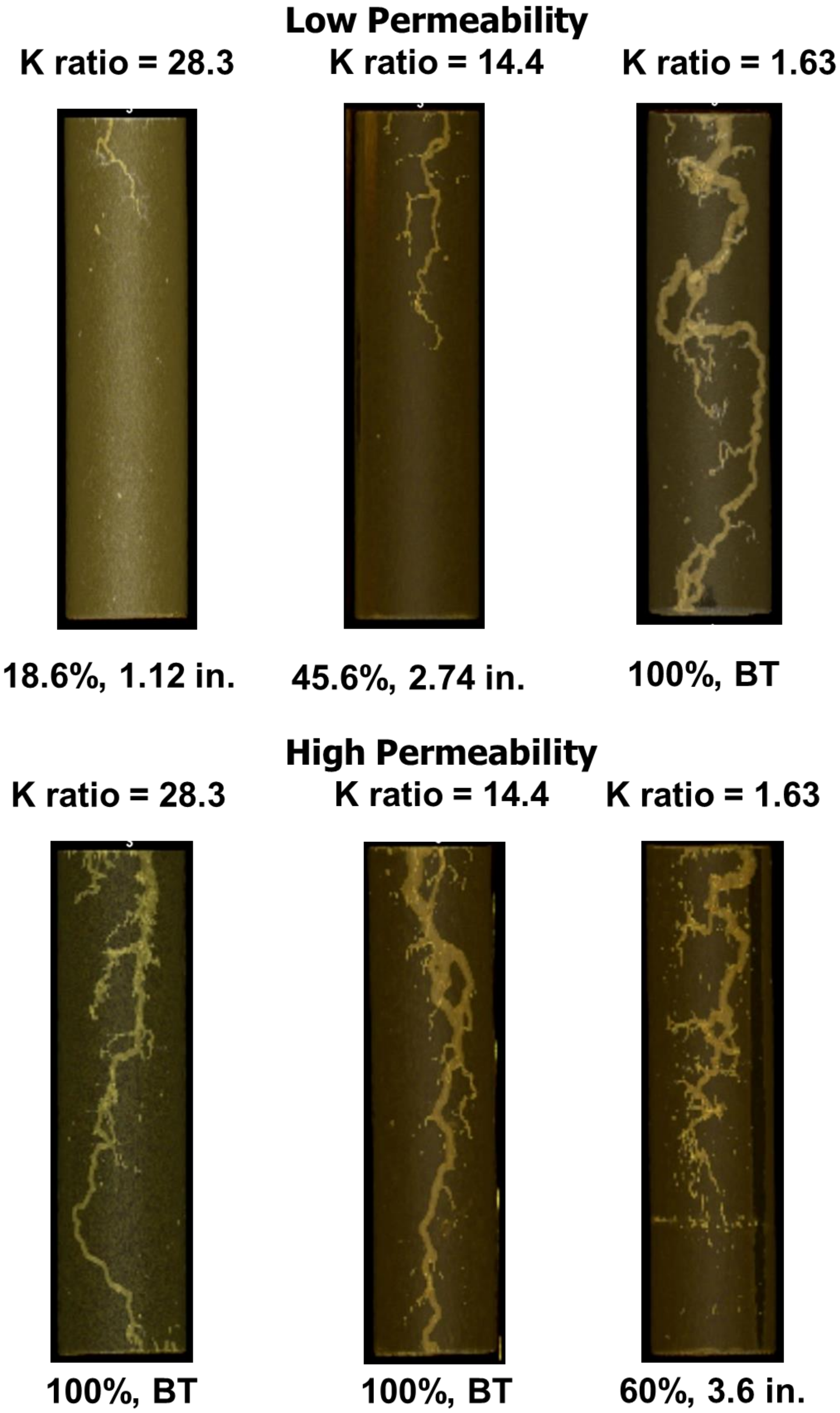

Fig. 1— Wormhole structure variation with the flow fractionation due to different permeability contrast.

Several chemical formulations were developed in the laboratory then applied in the field to achieve acid diversion such as foam-based acids, in-situ gelled acids, and surfactant-based acids (Smith et al. 1969; Dill and Keeney 1978; Nasr-El-Din et al. 2005, 2006; Yeager and Shuchart 1997). In-situ gelled acids are polymer-based acids that consist of mainly of polymer, crosslinker, pH buffer, and corrosion inhibitor mixed in an acid solution. The acid-rock reaction increases the pH, which deprotonates the polymer and leads to a polymer-crosslinker reaction, resulting in a strongly connected polymer network that have high viscosity and described as gel. This gel fills and close the high-permeability zones forcing any subsequent injected acid toward the low-permeability zones. Several concerns have been noted from the use of such a system, including the extensive number of chemicals needed to make the fluid work, formation damage caused by the filtration of the polymer onto the surface of the formation matrix or onto the inner surfaces wormhole, and the in efficiency of breaking the gel, especially in tight formations (Yeager and Shuchart 1997; MaGee et al. 1997; Taylor and Nasr-El-Din 2002; Hill 2005).

Viscoelastic Surfactants

To overcome these problems associated with using the in-situ gelled acids, viscoelastic surfactant-based acids were introduced, tested in the laboratory, and applied in the field with a very acceptable rate of success over the last twenty years (Chang et al. 2001, 2002; Qu et al. 2002; Nasr-El-Din et al. 2003,2006; Fu and Chang 2005). The main advantages of the VES-based acids include that they are easy to clean, easy to mix in the field, and require fewer additives compared to the in-situ gelled acids (Taylor and Nasr-El-Din. 2003; Al-Mutawa et al. 2005; Nasr-El-Din et. al 2005; Lungwitz et al. 2007). Results from the field were very positive, such as those reported by Samuel et al. (2003) and Nasr-El-Din and Samuel (2007).

VES-based acids for diversion purposes work through a very special mechanism that depends on the reaction of the acid with the formation matrix. The mechanism depends on the spending of the acid via the reaction with calcite or dolomite, which leads to two main results: increasing the pH and the calcium ions in the bulk solution. Both effects result in changing the VES structure from spherical micelles to rod-like structures which undergo significant entanglement and create a 3D structure with higher viscosity. Therefore, the acid type and concentration should be carefully selected to be compatible with the VES used, to be sufficiently reactive to result in increasing the pH, and to produce enough Ca and Mg ions to help the VES build up the rod-like structures (Nasr-El-Din et al. 2008).

Breaking the VES-gel structure at the end of the treatment is a determining factor of success, since the residual gel presence can block the matrix and cause further formation damage. Converting the micelles again to a low-viscosity spherical structure can be achieved by several methods such as: contracting with hydrocarbon phase (oil or condensate), using a mutual solvent such as ethylene glycol mono-butyl ether (EGMBE), or using an internal breaker (Nelson et al. 2005; Crews and Huang 2007).

Breaking the VES-gel structure at the end of the treatment is a determining factor of success, since the residual gel presence can block the matrix and cause further formation damage. Converting the micelles again to a low-viscosity spherical structure can be achieved by several methods such as: contracting with hydrocarbon phase (oil or

condensate), using a mutual solvent such as ethylene glycol mono-butyl ether (EGMBE), or using an internal breaker (Nelson et al. 2005; Crews and Huang 2007).

Field experience has shown that testing the VES-based acids for diversion in coreflood experiments is very important before applying in real treatments. Single and dual coreflood experiments at reservoir conditions can be used to evaluate the efficiency of a certain VES-based fluid for diversion. Al-Ghamdi et al. (2014) examined the constraints that limit the success of using VES-based fluids in terms of the initial contrast in permeability of the two zones for which the diversion is intended. The study concluded that the maximum performance of VES acid systems is achieved when the ratio of permeability is initially lower than 10. However, this study did not consider the effect of containing Fe (III) or other additives that are practically mixed with VES on this criterion.

Acid Additives

Several additives such as corrosion inhibitors, non-emulsifiers, mutual solvents, and iron-controlling agents, or the presence of contaminating ions such as Fe (III), can have a dramatic impact on the performance of VES. All of these additives have been reported to lower the VES-acid viscosity in both live and spent conditions (Shu et al. 2015; Nasr-El-Din et al. 2008; Li et al. 2010; Rabie and Nasr-El-Din 2015). Hence, the development of a compatible package of additives for the VES-acids is a challenging task that involves proper chemical selection, concentration limitation, and cost evaluation to maintain the VES functionality intact.

The usage of a strong acid such as HCl in the presence of crude oil results in asphalten deposition problems. This problem even gets worse in the presence of iron ions in the acid solution. This iron ions are the outcomes of the production tubing corrosion. In order to control the iron concentration in acid and to preserve the integrity of the tubing multiple acid additives are used. Corrosion inhibitors, anti-sludge, and iron control agents are examples of chemicals to avoid asphalten sludge. Although, those additives are essential to minimize the formation damage, their complex chemistry makes it difficult to predict their compatibility to the acid mixture (Fredd and Fogler 1998a).

Corrosion Inhibitor Viscoelastic Surfactant Interactions

There are two main corrosion inhibition families in the oil industry the thiourea based inhibitors, and the quaternary ammonium compounds. The effective material in each of them works on forming a thin layer on the surface of the metal to prevent the fluid from interacting physically, chemically, or electrochemically with the surface causing corrosion. This layer gets attached to the surface mainly by adsorption. The adsorption responsible polarity charges come from the sulfur, nitrogen, and oxygen groups in the monomer structure. Those polar groups work on forming Vander Waals forces with metal oxides or halides. This layer gets strengthened by donor bond causing a chemisorption attachment to the metal surface. Additives such as fatty acids, alcohols, solvent, and alkenes are added to the inhibitor in order to let the active element does its function (Rostami et al. 2009).

Thiourea is classified as an organic corrosion inhibitor that stick to the metal by adsorption followed by the complexation of metal in chelating compound form. Thiourea formulated inhibition systems are usually combined with different fatty acids. Those acids are selected to be between 1 to 20 carbon atoms with one or two un-saturated position on the string. They work on depositing on the metal surface using the week Van der Waals effect and help connecting the thiourea strings for better coverage. Then the unsaturation helps the fatty acid to get additional attachment mechanism to the metal surface using the covalent bond in the unsaturated location. Those fatty acids were proven in multiple publications to be of effective protection ability against acid attacks. Acids such as octanoic, acetic, tall oil, and formic showed capability of aiding the thiourea for better corrosion inhibition. The percentage of the fatty acid to the thiourea is proven to be of detrimental impact on the overall corrosion inhibition performance.

One of the electron donor structures that is used in the corrosion inhibition industry is the quaternized ammonium surfactants. In the early stages of this family the alkyl quaternary ammonium compounds were studied and reported as a successful inhibitor. Yet, the topography of the formed layer was exhibiting poor packing and less protection efficiency. Aromatic quaternized ammonium compounds were introduced to enrich the anisotropy of the molecules and strengthen the intermolecular attraction forces on the metal surface. This resulted in tighter packing that produced a polymer similar films on the metal surface. In this family fatty acid was still used since it is involved in the quaternization process and to function as an additional source of protection on the metal surface for better film packing.

Visco elastic surfactants (VES) are relatively short molecules that were introduced around (1977) as an additive to HCl acid system for self-diversion and as a standalone fracturing fluid. They were proven to be a successful additive in limestone diversion technology. Its ability of fast and effective apparent viscosity built only driven by the change of the pH which eliminated the necessity for crosslinker promoted the VES as a technology to replace the polymer diversion. The VES technology was promoted in the field due to its transient nature of continuous forming and deforming giving it a viscoelastic nature. Compared to polymers the VES showed the capability to divert in high contrast sections of lime stone with minimal formation damage. Their solubility in hydrocarbon phase and the ease of its removal using mutual solvent promoted it as a clean diverting technology (Yu et al. 2012). On the other hand, the VES technology was reported as expensive technology compared to polymers. Furthermore, its temperature sensitivity limited its application in temperatures higher than 200˚F. Also, it was reported to be sensitive to acid additives such as corrosion inhibitor, emulsifier, and iron control agents. Those additives contributed more to the breakdown of the VES at elevated temperature.

The viscosity built up of such chemicals is driven from the aggregation of the hydrophobic functional groups on the surfactant that forms different geometry micelle. In which their geometry and dimensions change according to the surfactant charge and its concentration. Also, parameters such as temperature, pH, ionic strength, and cations concentration were shown to be of valuable input to the micelle formation and its corresponding apparent viscosity. The micelle shape and size was studied and a model was developed to predict its behavior. It was based on a geometrical quantity named as the spontaneous curvature (CP) which is a function of the maximum length of the surfactant, the area at the interface between the molecule and water, and the volume of the surfactant. According to the CP value, the micelle shape is predicted. A CP value less than 0.33 is an indication for a spherical aggregate, while a CP value between 0.33 and 0.5 predicts a rod-like micelle, and a value more than 0.5 predicts a lamellar structure. Finally, at a certain combination of conditions and above a certain critical concentration the micelle can form a worm-like that behaves in a polymer like growth. This entanglement in a transient soft polymer manner network gives it the viscoelastic nature. (Dreiss 2007).

Chemically all surfactants are basically a hydrocarbon hydrophobic tail connected to a polar hydrophilic head. According to the head charge, the surfactants are divided into four main families: non-ionic long alcohols, cationic quaternary ammonium, anionic sulfates, and amphoteric betaines (Hull et al. 2016). Most of the anionic and cationic surfactants have a peptide bond (-CO-NH-). This bond is in the middle of the surfactant structure separating the hydrophobic and the hydrophilic groups. In an acidic medium, it is easily broken and the corresponding fatty acid produced. This type of bond breaking explained the hydrolysis process of different VES systems. (Yu et al. 2012) reported that the VES undergoes hydrolysis, this was based on rheological measurement followed by mass spectroscopy analysis for the organic phase that separates from the acid after hydrolysis. This data showed that the anionic carboxylate VES system breaks into oleic acid. The extent of the hydrolysis was reported to be of direct relationship to the rheological response of the VES. Most of the VES systems shows an enhancement in the rheology as the temperature increase and then it deteriorates. This is attributed to the extent of hydrolysis which corresponds to the ratio of the fatty acid to the unaltered VES which is essential for the micelle formation. And explains the enhancement of rheology at the ultimate ratio and the deterioration upon the increase of the fatty acid and the disappearance of the VES strings.

Due to the polarity of the hydrophilic functional group of the VES systems, its compatibility with additives was always a concern. The charge type based on being anionic, cationic, nonionic or amphoteric determines the interaction nature of the VES strings with other additives such as: corrosion inhibitor, emulsifiers, and iron control agents. The complexity of this type of interaction is in the positive synergetic impact at certain concentration beyond which the performance deteriorates. This synergies and impairments are function of the additives polarity charge and type, and their concentrations.

One of the challenges in the industry now a days is to find a self-diverting acid system to perform at temperatures higher than 250˚F with acceptable rheological performance and enough corrosion inhibition. All reported work showed that addition of corrosion inhibitor work on breaking the VES performance either instantaneously or in couple of hours. Furthermore, although the VES presence results in a higher viscosity acid mixture, those systems failed to protect the metal surface using corrosion inhibitors that was successful to protect using straight 15wt% low viscosity HCl acid.

CHAPTER II

BANDERA SANDSTONE MINERALOGICAL ASSESSMENT

Summary

This study is conducted in order to fully apprehend the mineralogical properties of the Bandera sandstone. This formation is considered the most complicated type of sandstone due to the presence of high percentage of dolomite, illite, chlorite, and quartz. This work will be conducted through primary destructive method to separate each of the stone constituent and study it separately. This study will be conducted through X-ray diffraction (XRD), X-ray fluorescence (XRF), Fourier transform infrared (FTIR), scan electron microscope (SEM), and chemical methods aided with atomic adsorption.

Materials

This phase of the work is a heavy labor work with usage of advanced and sophisticated analytical equipment's (Deng et al. 2009). Chemicals like: hydrochloric acid, hydrogen peroxides, acetone, sodium bicarbonate, sodium citrate, sodium dithionite, saturated NaCl, magnesium chloride hex hydrate, glycerol, potassium chloride were used during the study. All chemicals are reagent grade supplied by local supplier. Bandera sandstone cores were purchased and supplied from an outcrop; it was supplied in an eight-inch cube.

Procedures

Preparation of the Sample

The sample was air dried at 105°C overnight with regular check on weight every two hours. This procedure was stopped when the core weight reached constant value. Core was crushed and grinder using a chatterbox at petroleum engineering department. The sample was passed through a 2mm sieve and larger aggregates were grinded in a mortar and passed again in the sieve.

Sample Evaluation

Moisture content. For the moisture content an aluminum weight dish was labeled and weighted empty and 2 grams of the sample were added and the weight was recorded at each step. The dish with the sample was dried in air drying oven over night at 105°C and the weight was taken once again. This procedure was repeated one more time to assure consistency of results and moisture percent was calculated.

Check for carbonate minerals. Through this step carbonate minerals such as calcite and dolomite presence was investigated. Those minerals are reactive with HCl and they produce CO_2 which reflect as effervescence in high reaction rate. Also dolomite is carbonate its structure with Mg and Ca carbonates make it more difficult to react with HCl and effervescence is hard to detect due to slow rate of reaction. Through this experiment 0.5 gm of the sample was placed in a plastic dish and two to three drops of HCl on the sample.

Check for oxidizing reducing components. This step of the analysis is targeting the detection of compound such as the manganese oxides, sulfides, and organic matter. This test simply was conducted by addition of 30% hydrogen peroxide solution droplets on a 0.5 grams of the sample.

Check for magnetic minerals. This section of the analysis was mainly for magnetic minerals. Minerals can be divided to magnetic, paramagnetic, and anti-magnetic. Through this test 0.5 grams of the sample was weighted in aluminum dish and subjected to a magnet.

Check for evaporate minerals. This part was to investigate the presence of evaporates minerals such as gypsum and water soluble salts. Through this section of the work the sample 25 grams of the sample was weighted and added to a centrifugation bottle. This was followed by addition of de ionized water of ratio 5 ml to each gram of sample, 125 ml of deionized water was added in total. The bottle was securely closed and shake on mechanical reciprocating shaker for 30 minutes. Upon completion of shaking sample was installed with equal counter weight in centrifugation setup for 10 minutes at 2000 rpm. The supernatant was examined for the electric conductivity (EC) and pH using a conductivity prop and pH meter. After conducting the last procedure, the results came out as a cloudy supernatant. This was indication of clay presence. Upon this results the analysis for gypsum and anhydrite was stopped.

XRD preparation and analysis. X-ray diffraction is one of the most reliable tests to understand the mineralogical structure of the sample. In order to have a representative reliable results samples have to be prepared in the following procedure:

1- Dry samples in temperature below 105°C to avoid clay alteration.

2- Particle size distribution that pass through 140-180 mesh sieves.

3- Smooth surface of sample ash shown in **Fig. 2** leveled by glass slit.

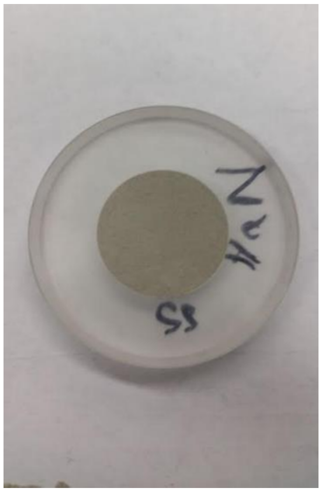

Fig. 2— Bulk XRD sample for Bandera sandstone.

Pre-Treatment Removal of Flocculating and Cementing Material

This section of the work is a preparation step for the size fractionation and further analysis step. The removal of cementing materials such as carbonates and organic matter enhance the dispersion of clay and silt phases and ease the sand separation. To ensure fully dispersed sample we have to ensure removal of flocculating materials like soluble salts and poly valence cations. Furthermore, cementing material such as Ca, Mg, organic, and oxides should also be removed. This section mainly will use chemical methods to disperse the sample using combination of high pH and low pH cycles of treatment.

Removal of carbonate. This step was conducted on the residual sample from sample evaluation step after centrifugation and supernatant storage due to clay suspension presence. 50 ml of pH 5 sodium acetate buffer was added as a low pH solution to react with carbonates and dissolve it in the solution. This was followed by shaking and heating up to 90 °C and shake every ten minutes three times each for total of 30 minutes. During the reaction a close eye was maintained on the sample to detect effervescence.

Centrifugation at 2000 rpm for 5 minutes was conducted after effervescence detection at the end of the treatment the supernatant was discarded and the procedure was repeated until no effervescence is witnessed. In this experiment, the effervescence was slow and happened at very low rate and this could be an indication of the type of the carbonate mineral in this sample to be dolomite rather than calcite.

Removal of Organic matter. 20 ml of sodium acetate was added to the residual sample from carbonate treatment and shacked by hand to ensure suspension of sample in the solution. This step was followed by addition of 10 ml hydrogen peroxide. The centrifuge bottle was placed in large beaker and covered by a glass watch for 24 hours. If there is bubbles in the first 30 minutes further steps should have been taken. This sample didn't exhibit any response to the peroxide which relates to the initial peroxide test in the evaluation step.

Sample Dispersion and Size Fractionation

After removal of cementing materials and flocculating materials it’s easier to disperse the clays and the silt and separate it from the sandstone particles. This operation will be conducted in multiple step using variation of pH through the process to change the charge on the minerals in away serve the purpose of the step, the work was conducted as follow:

Sample dispersion. In this step an increase in pH will change the charge on the clay minerals to negative charge which will enhance the segregation of the layers. This been done in collaboration of high dilution of the electrolyte results in an increase in the double layer thickness enhancing the dispersion of the clay minerals. This process was conducted using mono valence cation that enhance the dispersion, in this work sodium carbonate will be used during the dispersion step.

50 ml of pH 10 sodium carbonate solution have been added to the residual paste from the cementing removal step and shake by hand to disperse the particles in the solution. The bottle was centrifuged for 10 min at 2000 rpm and supernatant was examined for clay dispersion and clear superannuate was discarded. This was repeated 5 times and at the 6-time ultrasonic shifter was used to help the dispersion procedure. At the 6 time the supernatant was turbid with clays. The cloudy supernatant was kept and the mixture was proceeded for the sand separation.

Separation of sand fraction with particle size more than 53 µm. In this step ASTM number 270 (53µm) sieve was used on a funnel fixed in a holder. The sand with the turbid fluid was poured in the sieve using sodium carbonate to make sure that all particles are out of the solution. The sand that stayed on the sieve was washed multiple time with pH 10 sodium carbonate solution to make sure that all clays are washed from the sand and went in the solution below the funnel. The sand on the sieve was rinsed with de ionized water.

The total sand collected on the sieve was placed in a weighted aluminum dish and weighted. The dish was placed in the oven at 105°C over night to remove wet phase and the dry sample was weighted again to find the sand fraction.

Separation of Silt. Silt is basically a particle size ranging between sand and clay in size range between 53 to 2 micro meters. The supernatant from sand separation phase was treated to separate the clays from the silt. Centrifugation method was selected for this step. This method basically is a modified manual segregation method that proceed as follow:

The centrifugation bottle was marked two marks, one at the top 9 cm above the aggregate and 0.5 cm the aggregate was left to settle after the sand separation the supernatant was cloudy with clays and was separated to be added to clay separation step. The aggregate was added to 250 ml of pH 10 sodium carbonate solution and shake before centrifugation for 3.2 minutes at 750 rpm to make sure that the clay will be kept in the suspension according to stocks law. The supernatant was preserved as long as it’s cloudy. This step was repeated until the supernatant comes out clear which is indication that the clays are all out of the aggregate. The left aggregates were placed in a weighted aluminum dish and weighted before and after oven dry to quantify the silt fraction.

Clay separation. All the cloudy supernatant collected from each experiments was kept for clay quantification. Both course and fines clay will be harvested together. Since the clays particles are extremely dispersed due to high pH and high dilution of the electrolyte sodium chloride powder will be added to the mixture to decrease the double layer thickness and flocculate the clays and force them to aggregate. The supernatant of the clay suspension will be moved to a 750 ml-1,000 ml beaker to conduct the procedure as follow:

Left the clays to settle after addition of 50 grams of sodium chloride. Since the supernatant was still turbid after couple of hours we added more sodium chloride until the solution was clear. Once clear solution is achieved, we syphoned it and took the clay wet paste in the 250 ml centrifugation bottles and centrifuge it at 1,000 rpm for 5 minutes.

The collected clay paste should be separated from the huge amount of salts added to it during the procedure. This is to be conducted using the dialysis tube as shown in **Fig. 3** The clay aggregate was added to a tied from both side dialysis 10 cm long tube and emerged in de ionized water bath of 3000 ml capacity and the electric conductivity was measured every couple of hours to make sure that the water is not saturated. In case water has high EC fresh water was added until the EC is constant below 2 micro Siemens. Clay aggregate was collected and 1ml of the paste in a weighted aluminum dish and weighted before and after oven drying to qualify the clay fraction content, then the total clay weight is calculated for the weighted total sample.

Fig. 3— Dialysis tube with clay slurry for salts wash.

Free Iron Oxides Quantification

This procedure is based on comparative analysis against iron standard source. The basic concept is dissolving the iron from subject sample in sodium citrate, at the same time dissolve a known amount from standard sample in the same reagent and study it under the atomic absorption spectroscopy. This basic concept is conducted through consecutive steps of reacting and washing that proceeded as follow:

Maximum of 2.5 gm of the bulk soil was added to 50 ml centrifugation tube. Four tubes are handled in this test; two sample tubes were for the soil bulk and two others for the standard iron source. For each tube and simultaneously 20 ml 0˚F 0.3 M sodium citrate was added to the samples. Furthermore, 2.5 ml of 1 M sodium bicarbonate were added and the samples were warmed in a water bath adjusted for 75°C. upon the temperature increase sodium dithionite is added as 0.5 gm powder addition. The sample was mixed on a vortex mixer every three minutes and dipped back in the water bath along a 15 minutes total heating time. Addition of 2 mL of saturated sodium chloride solution in order to flocculate the sample is followed by centrifugation for 15 minutes at 2000 rpm to separate the supernatant from the soil. The supernatant was transferred to a 100ml volumetric flask. This procedure is repeated two more times in the same sequence.

The second part of this test was mainly dilution of the collected supernatant to the equipment detection level. Each volumetric flask was filled up with deionized water tell the 100 ml mark. The flasks were covered in paraffin film and shacked thoroughly. Since the detection ability of the machine is limited, 1 mL of the supernatant was transferred to another volumetric flask and then it was filled up to the 100 mL mark with deionized water in order to achieve a 1 to 1000 dilution factor. After mixing the new dilution flasks, 20 ml bottles were filled from the diluted solution and marked as standard 1, standard 2, sample 1, and sample 2. Those 4 bottles were analyzed using atomic absorption spectroscopy to determine the iron oxide content in the subject sample.

X-Ray Diffraction (XRD)

The X-ray diffraction was conducted on the sand fraction, silt fraction, and clay fraction; clays were conducted multiple times after saturation with different Mg or K as elaborated latter. In order to have a representative reliable results sand and silt samples have to be prepared in the following procedure:

1- Dry samples in temperature below 105°C to avoid clay alteration.

2- Particle size distribution that pass through 140-180 mesh sieves.

3- Smooth surface of sample leveled by glass slit.

In ordered to conduct a reliable XRD analysis for clay fraction a consecutive XRD tests should be conducted on the subject sample at different temperatures, cations saturation, and solvents. One clay sample was prepared with magnesium saturation; the other sample was saturated with potassium. The procedure through which the XRD clay samples were prepared proceeded as follow:

Both magnesium saturation and potassium saturation were conducted simultaneously. The magnesium saturation was conducted by addition 50 mg of clays in a 50 ml centrifugation tube, this was conducted by addition of 2.314 ml of clay suspension after determining its clay content to be 21.6 mg per mL of clays suspension from clay fractionation procedure. To this solution 0.5 M $MgCl_2$ solution was added tell the 15 ml mark, the tube was placed on the vortex mixer to suspend the mixture for 5 minutes. This was followed by placing the tube in the orbital shaker for 20 minutes. Centrifugation tubes were later placed with balanced counter weights in centrifugation unit for 10 minutes at 2000 rpm. The resultant supernatant was pipetted out and the procedure was repeated 2 times. The residual clays from the magnesium saturation procedure was washed using deionized water in three step washing procedure. Every wash was conducted using less water than the preceding step: to 15 mL, 10 mL, and 5 mL marks consecutively the water was added to the sample. Each run was conducted through 5 minutes' vortex mixing for suspension of the clay, this was followed by 10 minutes of centrifugation at 2000 rpm. The resulting supernatant was discarded. And the residual clay was suspended in a 1 mL deionized water and pipetted. These pipetted mixtures were added one droplet at a time on a glass surface mounted on an XRD holder and samples were left to dry out for XRD analysis.

After the Mg saturated sample run on XRD, the disk was sprayed by glycerol in order to replace the water in the samples. After drying and enough time to ensure the replacement another XRD run was conducted.

The same procedure was repeated for potassium saturation using 1 M KCl instead of $MgCl_2$. This time two glass disks of potassium saturated sample should have been prepared for the high temperature XRD runs as a backup if the clay film pealed during heating phase. For potassium saturated samples three XRD runs were conducted. The first run was conducted at room temperature. The second run was conducted after placing the disk in oven at 330°C. the third run was conducted at 550°C after cautious retrieval of the clay film disk in order to prevent the film from peeling off.

Fourier Transform Infrared (FTIR) Analysis

This type of analysis gives a deeper insight on the mineral since it shows the fine structure. Resulting absorption band from any sample will give enough information about the polyhedrons inside the minerals but will not reflect much on which mineral we are studying. FTIR is more important for the identification of the adsorbed species on the mineral, and helps in the interpretation of the XRD, but can’t be run independently for mineralogical identification.

Through this study FTIR was used twice: firstly, bulk dry sample was analyzed using the diffuse reflectance infrared Fourier transform (DRIFT) method. Secondly, clay fraction was analyzed using the pressed pellets technique.

The pressed pellet technique was applied to the clay fraction through two steps: sample preparation and sample testing. Both of them was conducted as follow:

Sample preparation was a consecutive of mixing with KBr, vacuum pumping, and pellets pressing using hydraulic press. The first step was mixing 0.001 gm of clay with 300 mg of KBr using the Wig-L-Bug cell for 30 seconds. The mixture was transferred to the pellet dying chamber and the chamber was fitted with lower and upper piston setups. The die was placed under the hydraulic press and pressure was applied tell the sample is hold between the press sides. Vacuum pump was connected to the airline coming out from the die and pumping started and kept running throughout the pressing procedure. After vacuum pumping for 5 minutes more pressure was applied by the press tell 20,000 psi. Vacuum pump kept running for 5 minutes more to ensure all air bubbles is out. The hydraulic press was loosened and the die was retrieved after the vacuum pump was stopped. The lower support plate was removed and the press was used once more to force the die chamber disks out of the die body and the pellet was retrieved and stored in glass container.

The pressed pellet was examined using the spectrum 100 machine. The pellet was placed in the pressed pellet accessory and the spectrum was generated.

Scan Electron Microscopy (SEM)

In the SEM analysis, a field emission scan electron microscope was used in the imaging center at Texas A&M University. This facility gives the ability of imaging the surface of the particles using a highly focused electron beam (2-3 nm spot size). This beam reflection can be detected using different sets of detectors among them: secondary electrons detector which is responsible for tomography and morphology-, backscattered electrons detector which is responsible for contrast in densities of the detected particles-, and auger electron. In addition to that, this machine can provide chemical composition of the surface under study using energy dispersive x-ray or spectrophotometry (EDX or EDS) which gives atomic and weight percent of the elements present in the sample.

The SEM sample was prepared after dispersion of silt size fraction of the Bandera sandstone in liquid phase and spread on a carbon conductive tap fixed to a circular holder. This sample was fixed under high temperature light to evaporate the liquid phase. This was conducted to ensure a high dispersion of the sample to prevent agglomerations. Furthermore, the sample was coated by Pt in order to increase its conductivity for a higher resolution images.

Cation Exchange Capacity (CEC)

Cation exchange capacity is one of the most important properties for any soil due to its significance to the plant growth and the control of the nutrients. Furthermore, in the oil field industry in formations such as the shale, one of its characteristics is presence of clays in high concentration that may exceed the 50%. The clay CEC is essential to design a stabilization process specific for those formations and prevent their swelling and further damages in the wells. Basically its measurement of the quantity of readily exchangeable cations neutralizing negative charge in the soil reported as cmol/Kg of soil. To assess the CEC there is multiple procedures and every one of them report a different reading according to special consideration, but the magnitude can be compared for the same method applied to two different samples. The procedure used for Bandera sandstone was carried out against a standard montmorillonite sample with known characteristic and the procedure for both of them was as follow:

1- 100 mg of clay was added to two 50ml centrifuge tubes each.

2- Two other 50ml tubes were filled with 100 mg of standard each.

3- Sample was washed with 0.5 M $CaCl_2$ through its addition to the 20ml mark and shaking for 15 minutes, followed by centrifugation for 10 minutes at 1500 rpm, this procedure was repeated 3 times.

4- Then another wash was conducted using 0.005 M $CaCl_2$ using the same procedure at point 3.

5- Sample was weighted after all the wash steps and after discarding the supernatant.

6- Sample was washed with 0.5 M $MgCl_2$ added to 15 ml mark, samples were shacked for 15 minutes and this was followed by centrifugation at 1500 rpm for 10 minutes.

7- This wash was conducted 4 times in total

8- Supernatant from each wash was transferred to a 100ml volumetric flask.

9- The supernatant was diluted 1 to 1000 and 20ml was separated to conduct the CEC using the atomic adsorption for Ca.

Transmission Electron Microscope (TEM)

Transmission electron microscope is a high energy microscope that can investigate in sublayers to the surface, with higher magnification and resolution than the SEM. The TEM facility used was also in the imaging center at Texas A&M University. In this study the clay fraction was used in order to make sure they are thing enough for TEM and with sufficient crystallinity. The sample was prepared in the same manner of the SEM sample after dispersing the dry clay fraction sample in distilled water in a very low concentration.

Total Potassium Content

The measurement of K content was intended to quantify the mica percentage in the sample assuming that the only source of K is the mica and there is no presence of the k-feldspars or any other K sources in the sample. This an extremely dangerous taste that a lot of safety procedure should be taken strictly. The K ion was dissolved in the solution through the reaction of the sample (clay fraction) with hydrofluoric acid and aqua regia which is a mixture of HCl and HNO_3. Two 100mg of clay were added to wo 50ml plastic volumetric flask; to this flask 2ml of aqua regia was added in addition to 3ml of HF each. This study was conducted versus a standard source of K (illite) by weighting the same amount of clay and its addition to two other flasks with the same added reagents. The four flasks were covered using para-film and placed in an elliptical shaker on moderate speed for 24 hours. This procedure was followed by recovery of the flasks and quenching of the reaction by addition of sodium chloride. All samples were brought to the 50ml mark and a dilution 1 to 10 was carried out using deionized water. A 20ml samples were taken and tested using the atomic adsorption machine.

Results and discussion

Moisture Content

This test reflected a low moisture content, this could be attributed to the successful air drying and the fine grinding. The moisture content was determined according to the following Eq. 7 and results are shown in **Table 1**.

$$Moisture\% = \frac{Air\ Dry\ Weight(W_2) - Oven\ Dry\ Weight(W_3)}{Oven\ Dry\ Weight(W_3 - W_1)} * 100\% \quad . \qquad (7)$$

Replication	Dish weight, gm, W1	Dish+ Air Dry Solid, gm, W2	Dish+ Oven Dry Solid, gm, W3	Moisture%
1	1.3155	1.851	1.846	0.94
2	1.3202	2.157	2.151	0.72

Table 1— Moisture content for Bandera Sandstone.

Carbonate Detection

The observation was a slight reaction with very slow effervescence rated on a scale from 0 as no reaction to 5 as vigorous to be 1 as shown in **Fig. 4**. This could be attributed to the presence of dolomite rather than calcite, which later proved by XRD analysis.

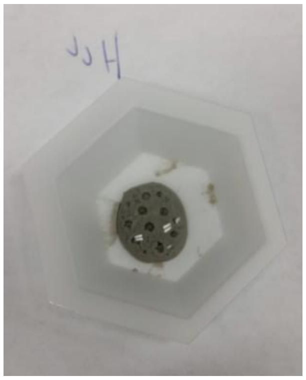

Fig. 4— HCl reaction with Bandera sandstone.

Sulfide and Oxides Detection

Through this test effervescence was again so little to be detected. This indicated the low presence of the sulfides and oxides as shown in **Fig. 5**.

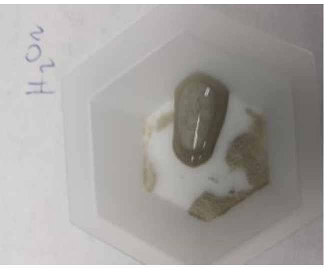

Fig. 5— Sandstone response with hydrogen peroxide.

Check for Evaporates

The results came as follow:

EC= 467 μS/cm and pH= 8.38

This pH result was interpreted as carbonates presence. The high EC indicate the presence of soluble salts in the solution that can't be detected by acetone addition due to the cloudy nature of the sample.

Check for Magnetic Minerals

Upon exposing the sample to magnetic field it didn't show any attraction to the magnet. This result means that the Bandera sandstone doesn't contain any of the magnetic minerals. This result also matches the XRD analysis shown later which confirm absence of the magnetic minerals.

XRD Analysis

The XRD analysis turned out with a complex mineralogical analysis for Bandera sandstone which is predicted from literature. The pattern shown in **Fig. 6**. reflects the presence of major elements such as the Quartz, Dolomite, and Clay minerals.

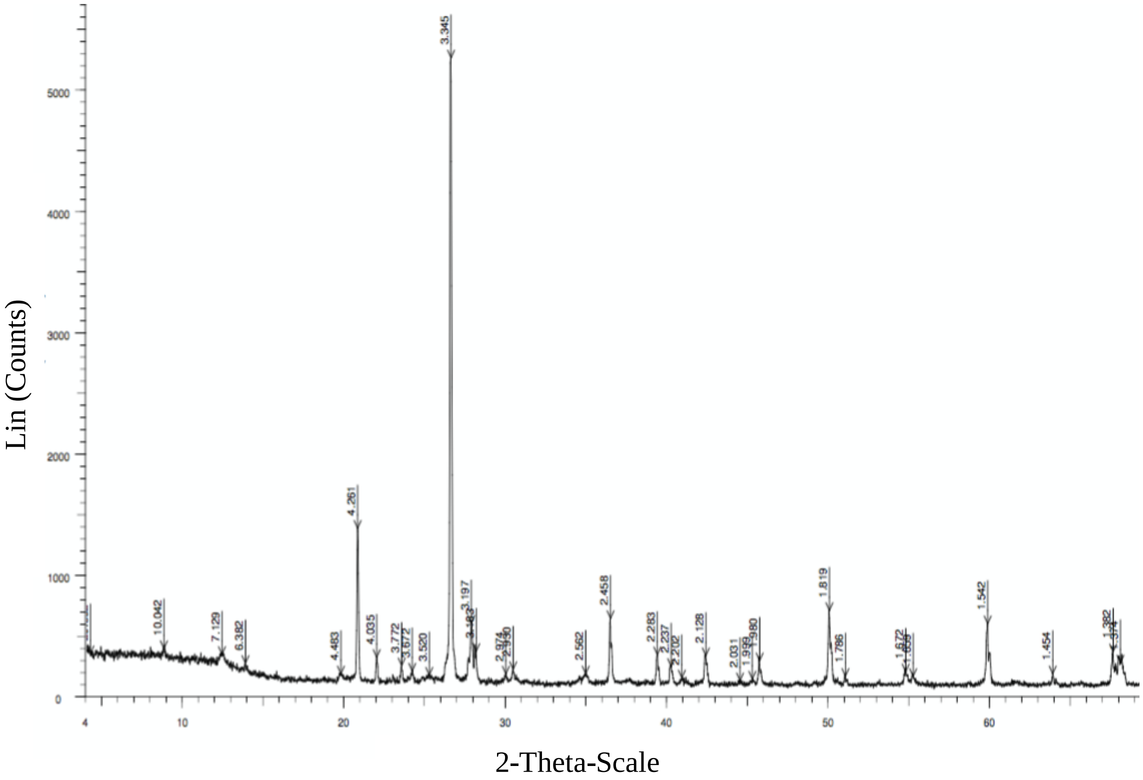

Fig. 6— XRD pattern for Bandera sandstone.

The interpretation of the XRD was conducted by matching some of the expected minerals with their pure XRD patterns. Each peak is assigned to its mineral as shown in Fig. 6. At 2 theta 8.8 and d-spacing 10.42 it is illite indication, at 2 theta 12.5 and d-spacing 7.129 its kaolinite, at 2 theta 14 and d-spacing 6.382 its albite, at 2 theta 22 and d-spacing 4.261 its quartz, at 2 theta 22 and d-spacing 4.035 its dolomite.

Sand Content

After aluminum dish was placed in the oven over night it was weighted again to know the amount of sand in the experiments and the results came as shown in **Table 2** the total sand content of the sample is 65%.

Sample	Dish weight W1, gm	Dish+ Sand Oven Dry, gm, W2	Weight of Sand, gm
1	1.3199	17.59	16.27

Table 2— Sand content calculations.

Silt Content

After the aluminum weighted with silt slurry it was placed in the oven in order to get the dry weight of the silt in the studied sample, the results of this analysis is shown in **Table 3**. This results shows a high silt content equal to 17.45%.

Sample	Dish weight W1, gm	Dish+ silt oven dry W2	weight of silt, gm
1	1.3329	5.696	4.3631

Table 3— Silt content calculation

Clay Content

One way to report the clay content is the total weight minus the silt and the sand which makes the clay content approximately equal to 4.36 grams which correspond to 17.46 %. This on an assumption that the sample didn't lose any minerals during the cementing material decomposition process. The other method is the one we reported in the experimental part with results shown in **Table 4**. The clay content percent in the 1 ml sample is 1.8%. By multiplying this percentage by the weight of clay solution (W2-W1) the clay fraction weight turned out to be 2.29 grams. This result shows that approximately 2 grams of the sample was lost during cementing and flocculation consumption to disperse the rest of the sample.

Sample	Dish weight, W1, gm	Dish+ clay 1ml, wet, W2	weight of clay+ dish, Oven dry, gm
1ml clay sample	1.3064	2.5166	1.3280
Total clay sample	47.9	175.24	Total Clay Content=2.29 grams

Table 4— Clay content calculation

XRD Results

Sand fraction sample. The sand sample analysis shown in **Fig. 7** reflect absence of clay minerals. The main peaks at d-spacing 4.261 and 3.345 shows the presence of quartz which is the main body of the sample. The other important peak at d-spacing 4.037 shows the presence of dolomite. And feldspar was present at two theta of 27.7 with d-spacing around 3.

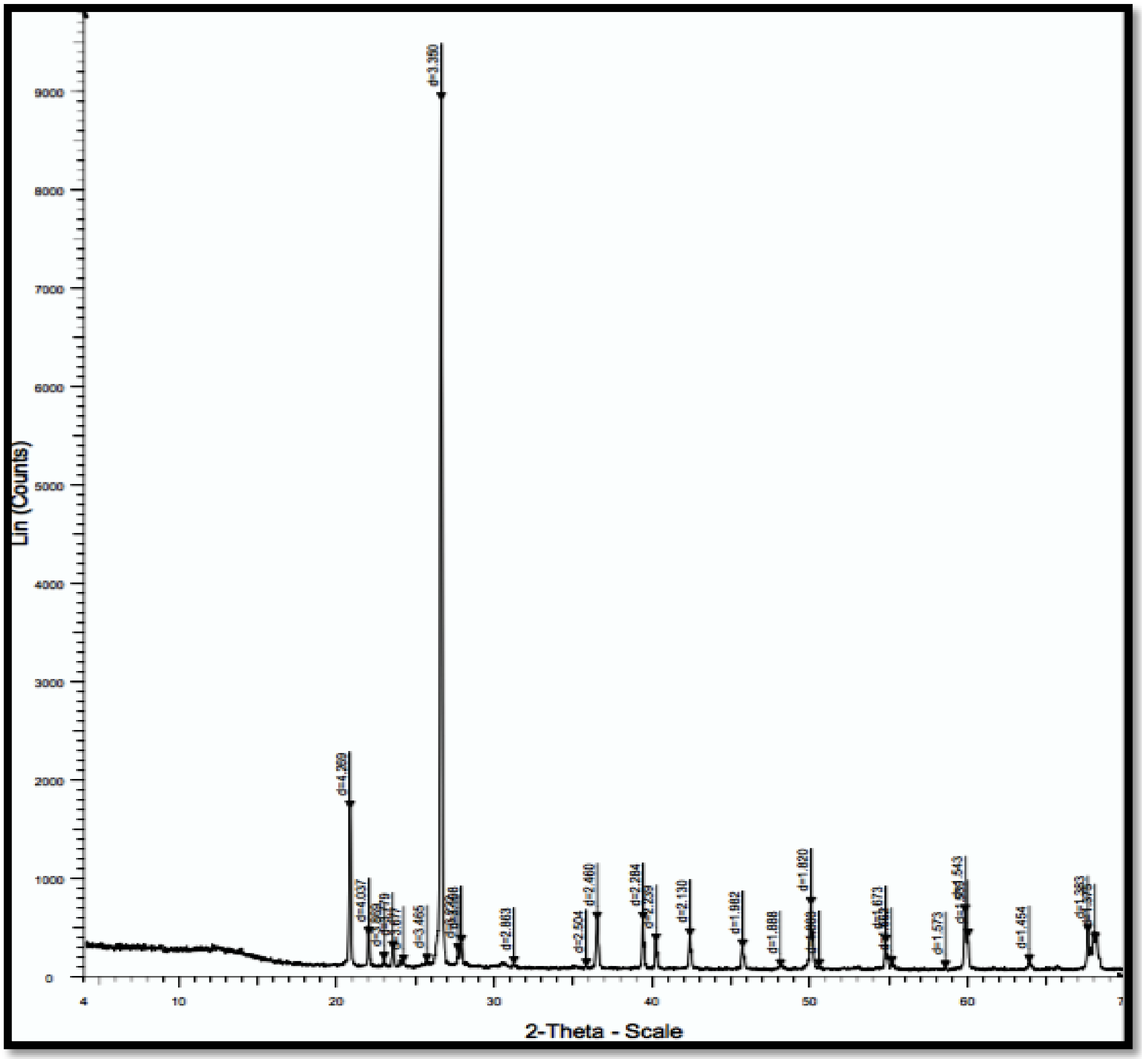

Fig. 7— XRD result for sand fraction of Bandera sandstone sample.

Silt fraction sample. The XRD analysis turned out with a complex mineralogical analysis for Bandera sandstone which is predicted from literature. The pattern shown in **Fig. 8** reflects the presence of major elements such as the Quartz, Dolomite, and Clay minerals.

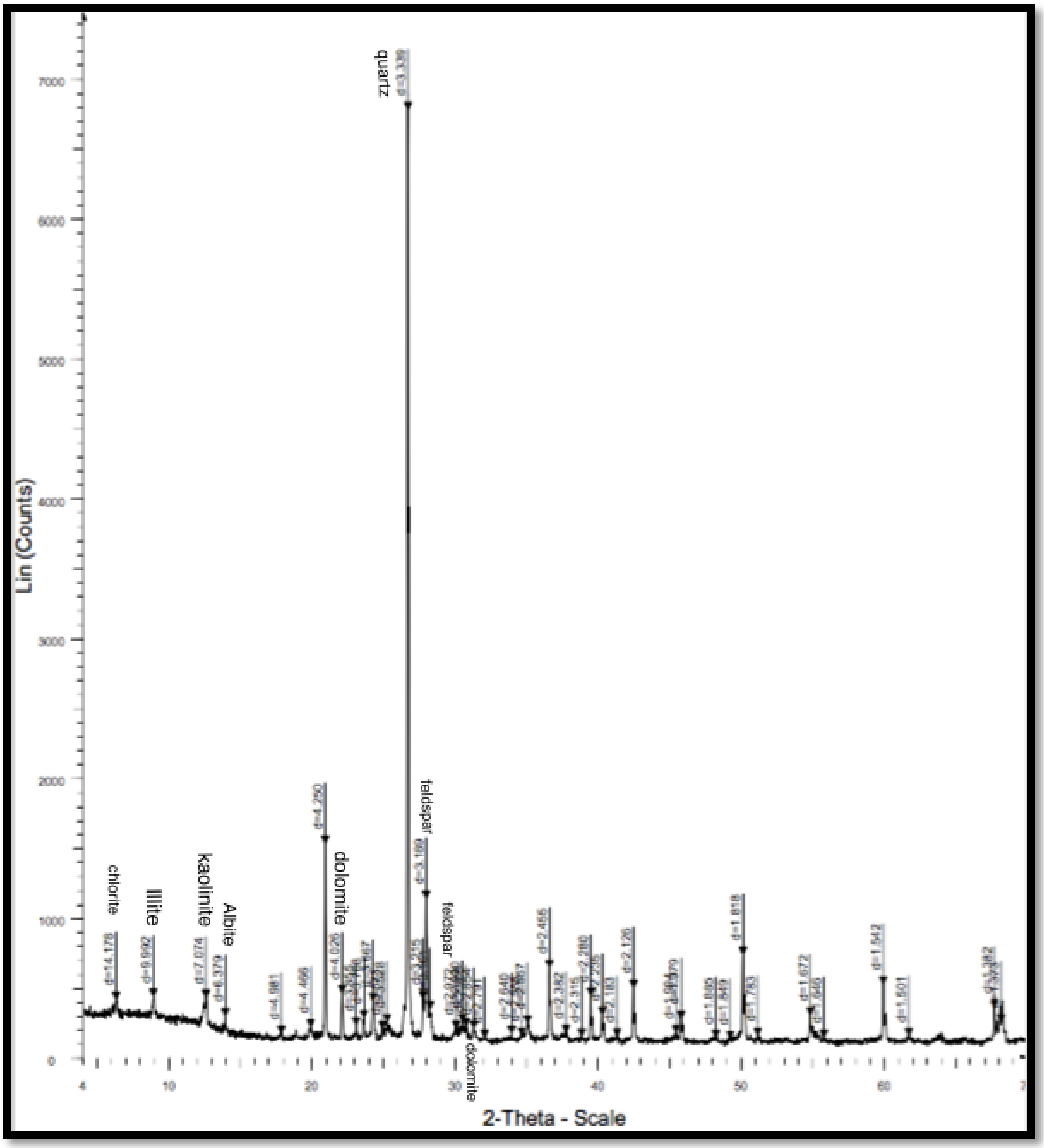

Fig. 8— XRD pattern for silt fraction, Bandera sandstone.

The interpretation of the XRD was conducted by matching some of the expected minerals with their pure XRD patterns. Each peak is assigned to its mineral as shown in Fig. 8. At two thetas equal to 6 and at d-spacing equal to 14.17 this is indication of chlorite. At 2 theta 8.8 and d-spacing 10.42 it is illite indication, at 2 theta 12.5 and d-spacing 7.129 its kaolinite, at 2 theta 14 and d-spacing 6.382 its albite, at 2 theta 22 and d-spacing 4.261 its quartz, at 2 theta 22 and d-spacing 4.035 its dolomite. At d-spacing 3.18 at two theta equal to 27.7 indication of feldspar which also proved by the 2.97 d-spacing at 2 theta 30.6.

Clay fraction samples. The XRD pattern generated for the clay fraction showed a differences in the detected peaks. The sample showed additional peaks to what was present in the bulk sample results. Shown in **Fig. 9** five XRD graphs representing Mg-saturated, Mg-Glycerol, and K-saturated at room temperature, 330, and 550 °K. Upon the comparison of each graph new minerals were identified. Graph (a) (Fig. 9) showed chlorite at two θ equals to six with d-spacing equals to 13.894; this peak was followed at two θ equal to nine indicating illite with d-spacing 9.862. The third peak in graph (a) shown at two θ equal to 12 can be connected to the chlorite, yet it can be indication for kaolinite presence. Two small peaks at two θ 17.7 and 18.8 with d spacing 4.938 and 4.687 was interpreted to belong to the illite and chlorite minerals respectively. Around two θ equal to 25 again chlorite mixed with kaolinite was suspected in the sample with d-spacing equal to 3.550 and 3.511 respectively. The last peak at two θ equal to 27 showed the quartz presence with d-spacing equal to 3.311.

The second graph (b) showed the XRD pattern for the sample after spraying with glycerol, this step was made to show minerals that have differential swelling properties in presence of differ solvents such as low-charge smectite and high-charge vermiculite. The sample didn’t show any difference in this step which indicates the validity of the minerals identification from graph (a).

The treatment with potassium was conducted in the first place in order to check for minerals that would collapse upon K ion introduction into the double layer such as smectite and vermiculite. Results at graphs (c, d, and e) showed identical patterns with slight changes of the d spacing resulting from thickness of the analyzed film. Graph (e) showed a drastic change in the peaks; peak attributed for chlorite kaolinite at d-spacing 7.1 totally disappeared and other chlorite/ kaolinite peaks as well. This result confirms the kaolinite presence, since literature reports its decomposition above 550°C.

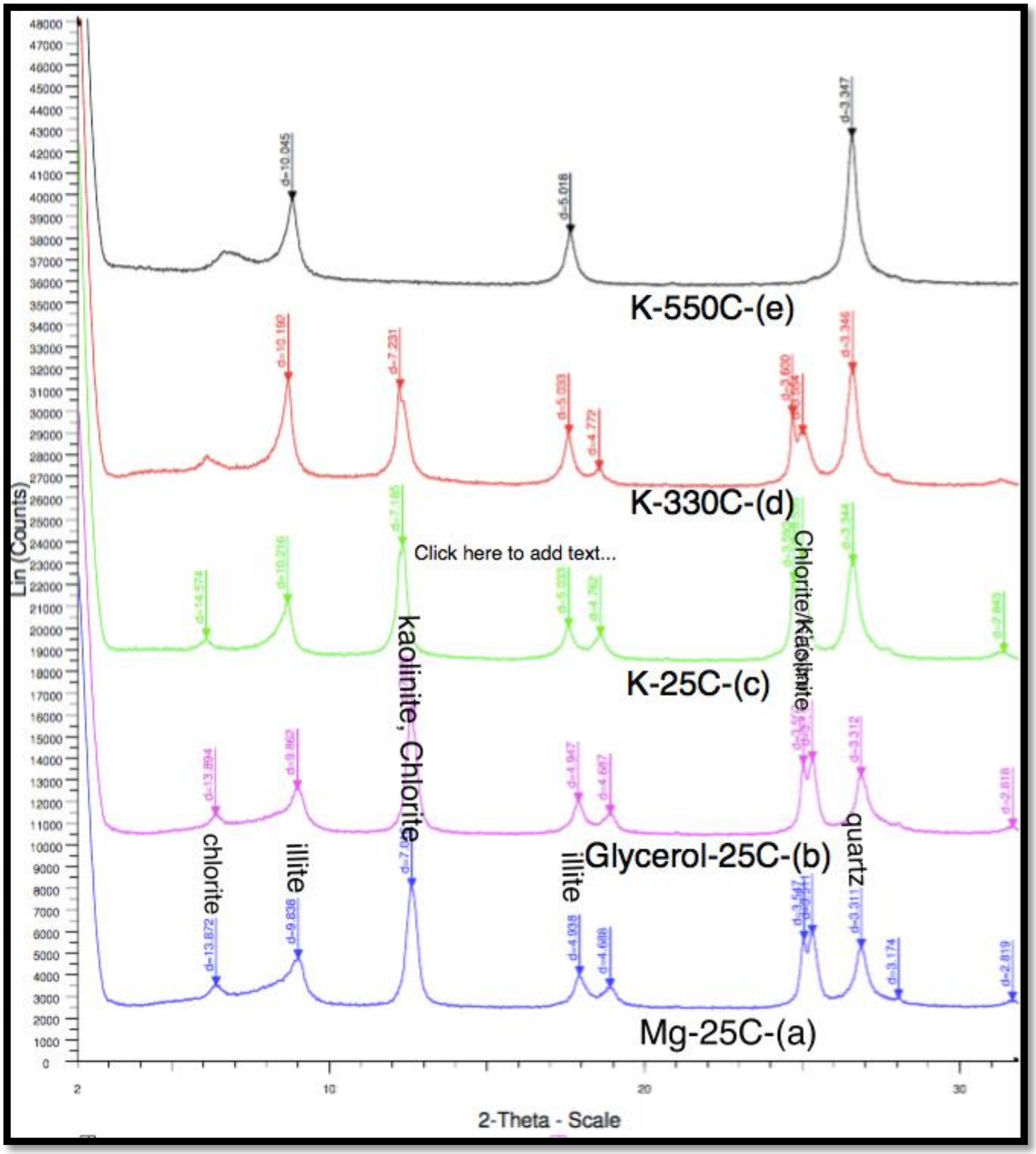

Fig. 9— XRD analysis for clay fraction with Mg, glycerol, and K saturation at 25, 330, and 550°C.

FTIR Results

The FTIR results came as shown in **Fig. 10** for bulk sample and in **Fig. 11** for clay fraction. The bulk sample lacked peaks present and wasn't helpful to identify with high certainty any of the minerals. The key findings from the bulk sample was identification of one peak of illite mica at 3625, another peak at 781 was attributed to quartz, and a peak at 693 showed Al rich chlorite minerals. At 910 a peak was identified to be indication for two Al ions occupying the octahedron structure. On the other hand, the clay fraction sample showed multiples peaks showing different minerals. Furthermore, some peaks showed the type of the cations occupying the interlayer spaces.

The key results from the graph in Fig. 11 shows clay fraction FTIR reflects mainly kaolinite minerals at 3694, 3620, and 914. At 3434 water adsorption band was clear; in addition to that at 1634 OH of adsorbed water was clearly identified. Quartz was identified at 779 and 798. Moreover, chlorite was identified at 475 and was doubting to overlap with muscovite at 827. The chlorite was detected at different peaks at 827 and 751, and muscovite at 535. Finally, hallyosite was detected at 695. Also, worth to be mentioned that peaks between 2000 and 2500 can be attributed to organic matter residues in the sample.

This results came confirming some of the minerals in the XRD but showed some other minerals that didn't show up at the bulk or the clay fraction sample. This could be attributed for their low concentration and the limitation of the machine in terms of detection level.

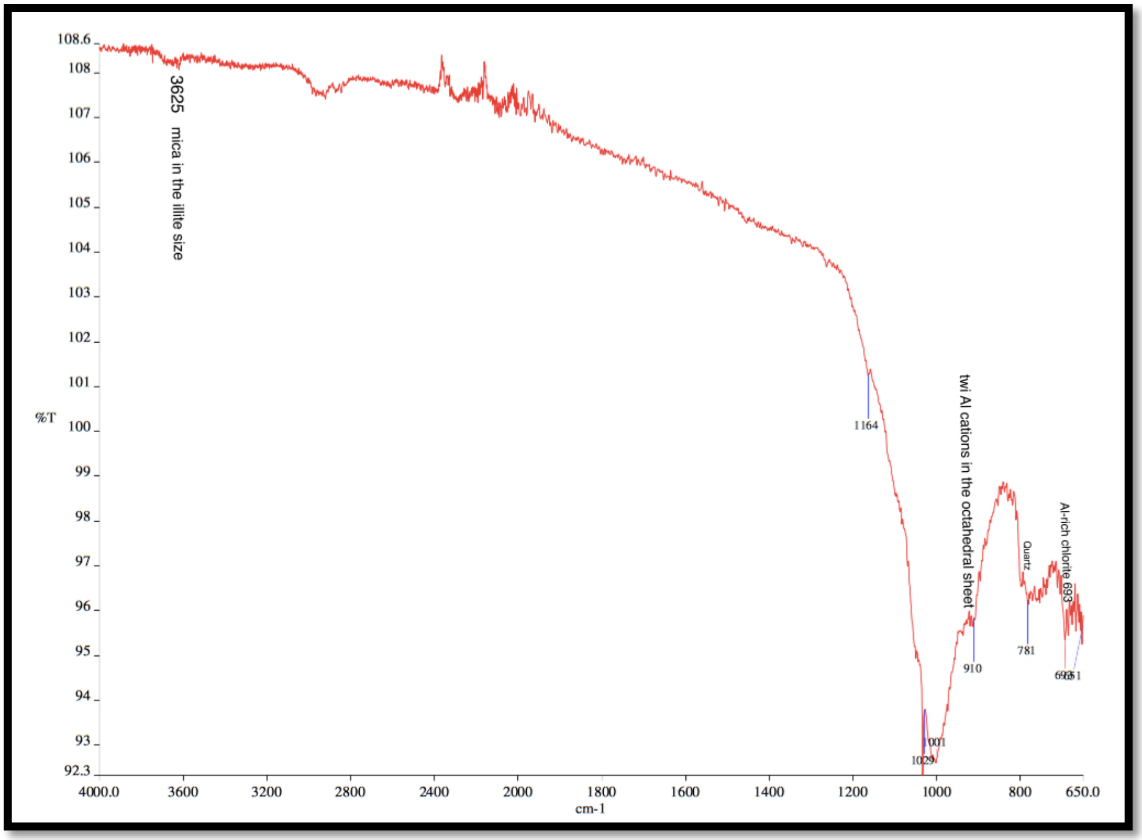

Fig. 10— FTIR analysis for the Bandera sandstone.

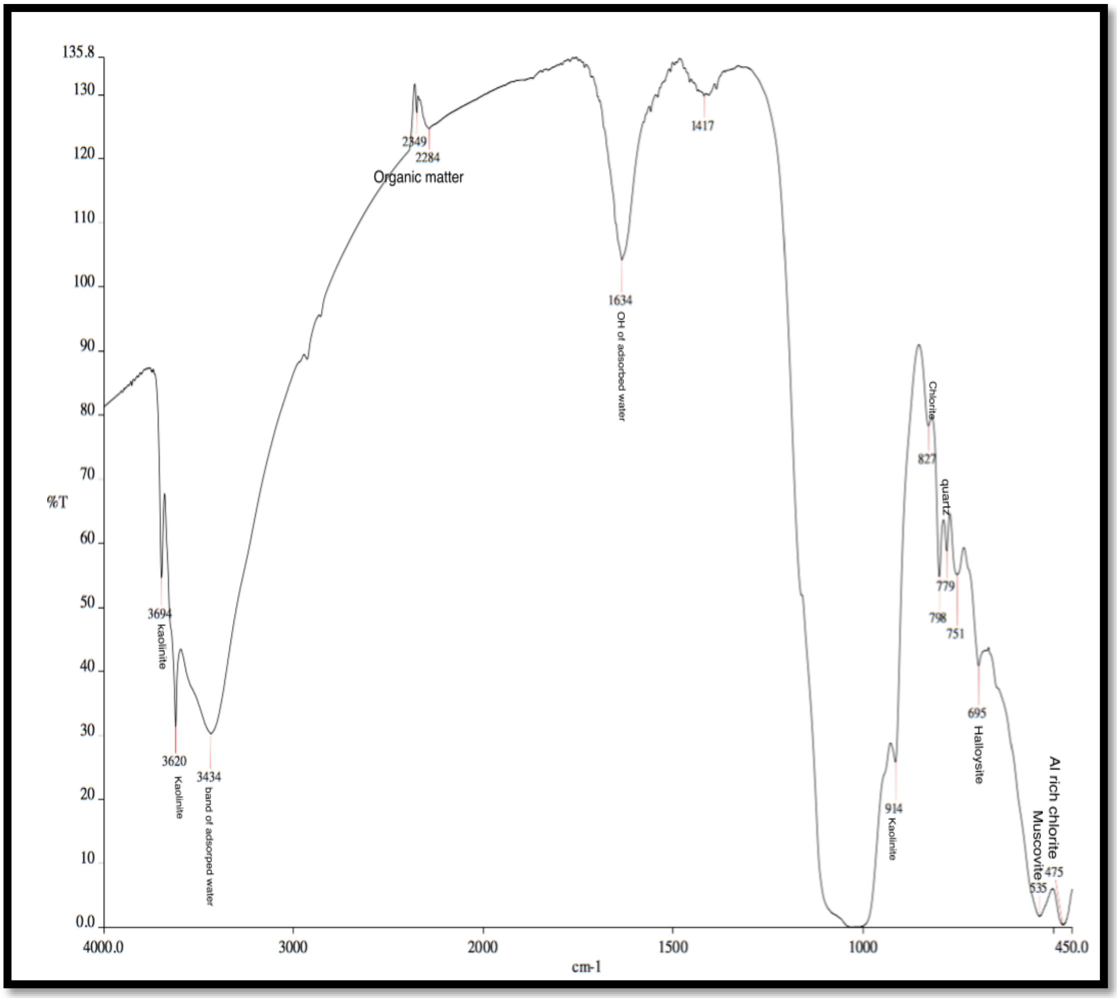

Fig. 11— FTIR analysis for the clay fraction of the Bandera Sandstone.

Scan Electron Microscope Morphology and Chemistry Analysis and Mineral Identification

The SEM results came out with confirmation to most of the minerals identified in report 2 such as kaolinite, chlorite, illite (mica), and quartz that was already identified during the XRD analysis. Furthermore, it showed the presence of some iron manganese oxides and titanium oxides bodies in very low concentration.

The first point that was investigated under the SEM was mainly kaolinite, mica, chlorite, and quartz as shown in **Fig. 12**. Worth to be mentioned that kaolinite exhibited pseudo hexagonal morphology and platy foundation. Chlorite was detected in spectrums 2, 4, 5, and 7; it is irregular shaped particles with higher brightness than the rest of the sample in the backscattered electro processed images. On the other hand, the mica was present as platy morphology, sometimes it was underlying the kaolinite and this was clear in spectrum 9. This spectrum chemistry only explanation is a mixture between 1:1 kaolinite and 2:1 mica in presence of the K^+.

Minerals such as albite was witnessed and their morphology and particle size was detected, bulky samples of 30 micro m length and width were witnessed as in **Fig. 13**. Worth to be mentioned that at spectrum number 6 at this point there was a sharp cornered particle with 1:1 ratio of Al to Si, this particular particle couldn’t be identified. At spectrum 3-point zirconium silicate was present and identified as a tiny standalone irregular shaped particles.

At the third point (**Fig. 14**) multiple particles were identified as titanium oxide particles in addition to some particles of mica, quartz, and chlorite. Most of the morphologies was irregular and can’t be described.

The fourth point (**Fig. 15**) similar to point two a bulky albite particle was present as shown in spectrum one. At spectrum 5 muscovite (or Mica covered in clays) was present for the first time as a bulky particle with a fracture perpendicular to the log side. Spectrum 2 was a muscovite guess since it’s over lying on a big mica layer that interferes with the chemistry response in the EDS and the presence of iron wasn’t explained unless it’s chlorite.

The investigation of the fifth point (**Fig. 16**) showed three distinctive particle densities. Again at spectrum one the sample showed titanium oxide at a higher particle size this time. Next to it quartz was present showing fracture lamination. Spectrum three showed some amphiboles. The rest of the sample was mica platelets, and chlorite pseudo cubic block.

Heterogeneous complexed bodies were detected such as: iron oxide, and manganese oxides scattered on quartz body as shown in **Fig. 17** at point 6.

The seventh point (**Fig. 18**) was distinctive from particle size and shape normality point of view relative to the rest of the points. Bulky samples were present at points 5 and 6 was interpreted as quartz after comparing its EDS data. A uniform rhombic body at spectrum 1 was identified again as titanium oxide. At spectrum 6 calcium phosphate apatite is present according to its unique chemistry. Finally, spectrum 3 and 4 showed muscovite particles or mica covered in clays. The last point shown in **Fig. 19** shows a big quartz particles included inside smectite aggregates.

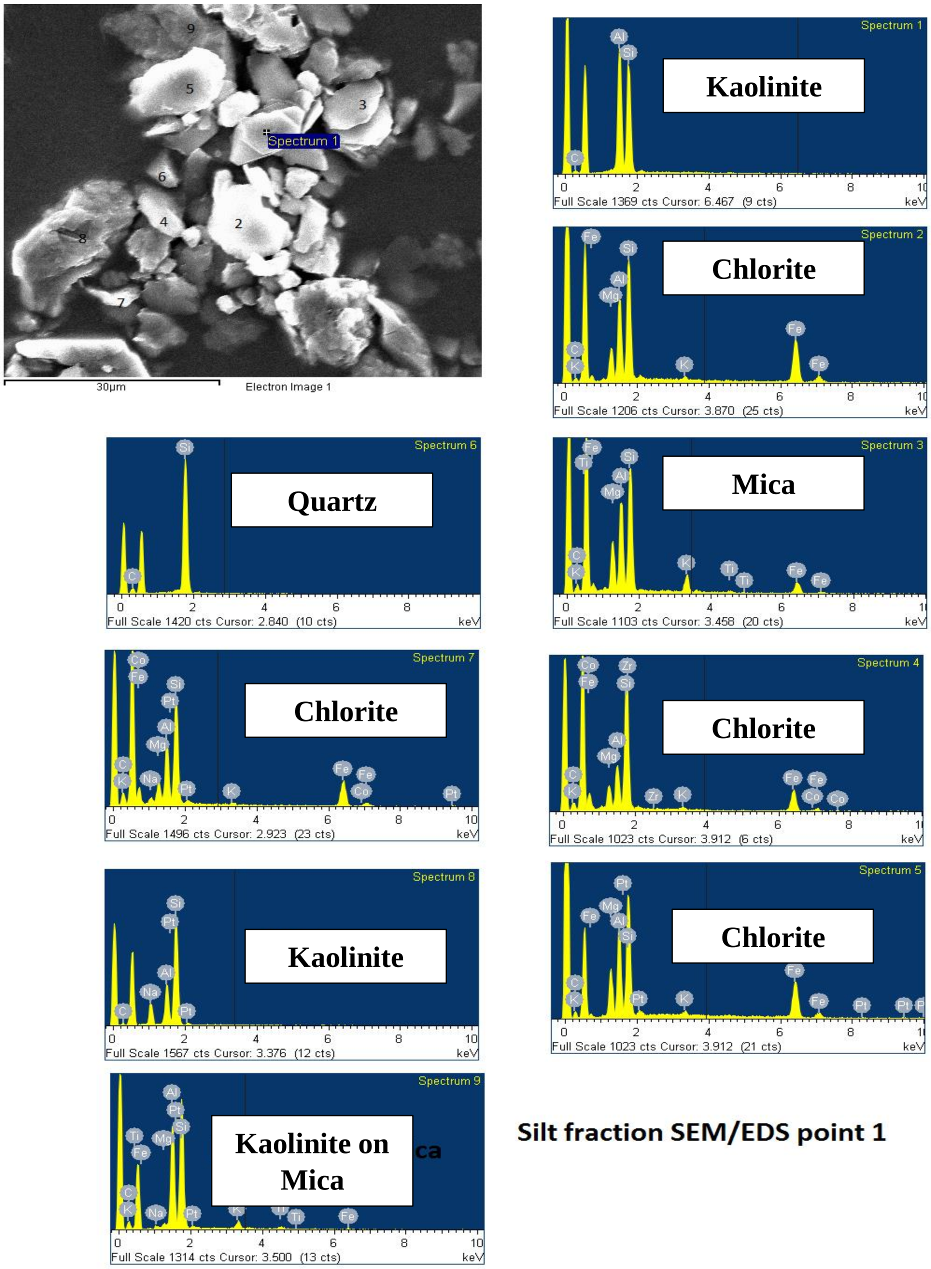

Fig. 12— Silt fraction SEM/EDS point 1.

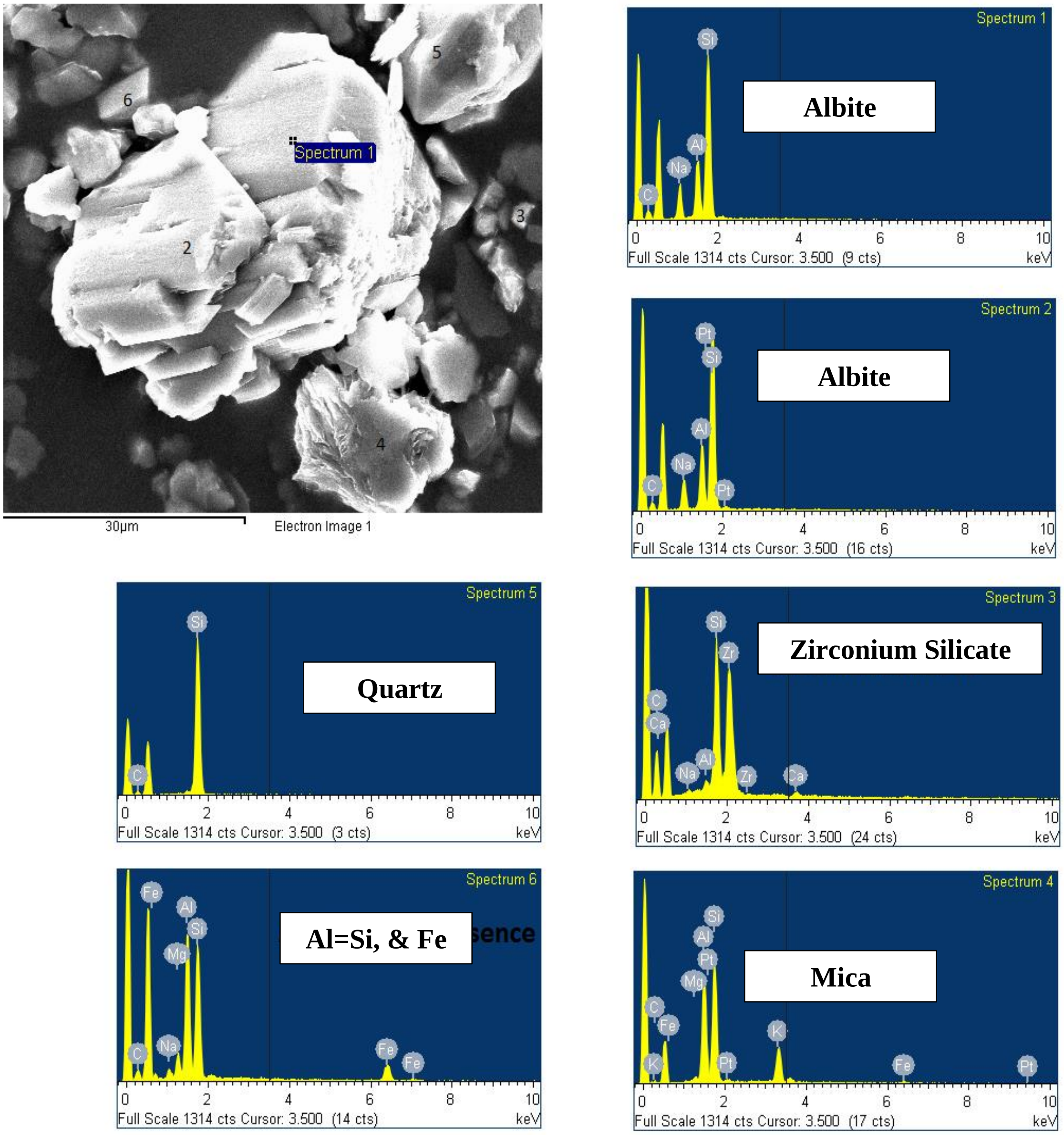

Fig. 13— Silt fraction SEM/EDS point 2.

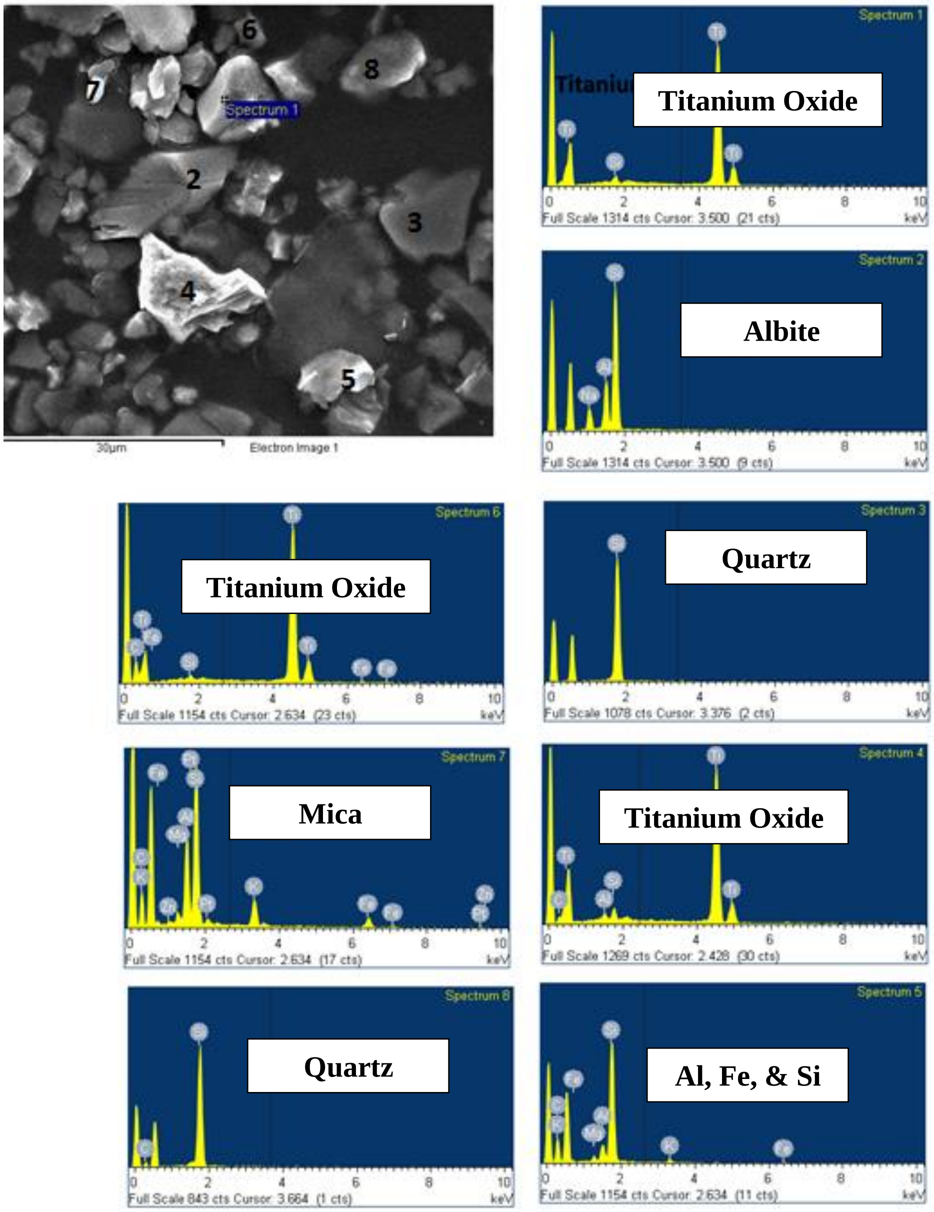

Fig. 14— Silt fraction SEM/EDS point 3.

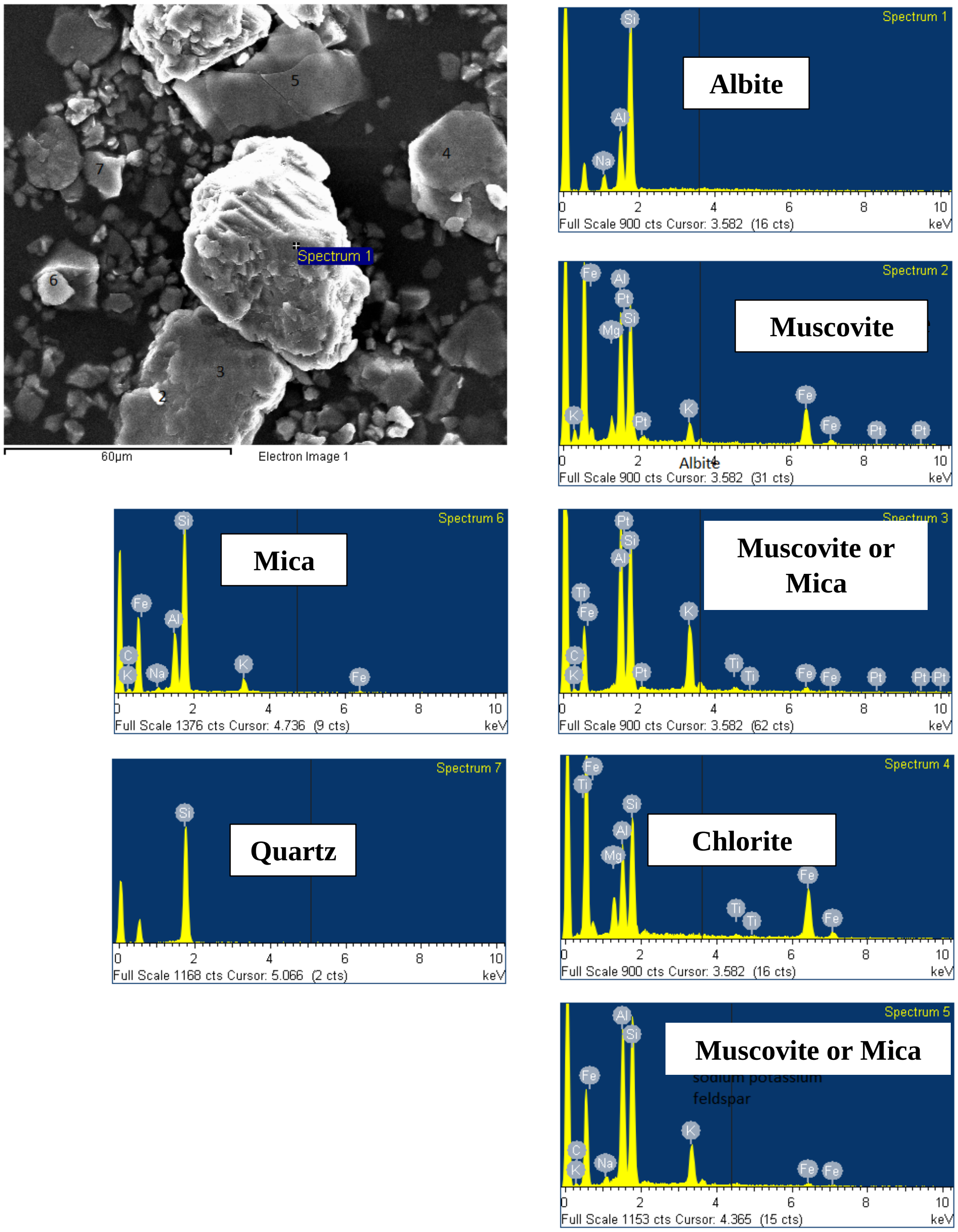

Fig. 15— Silt fraction SEM/EDS point 4.

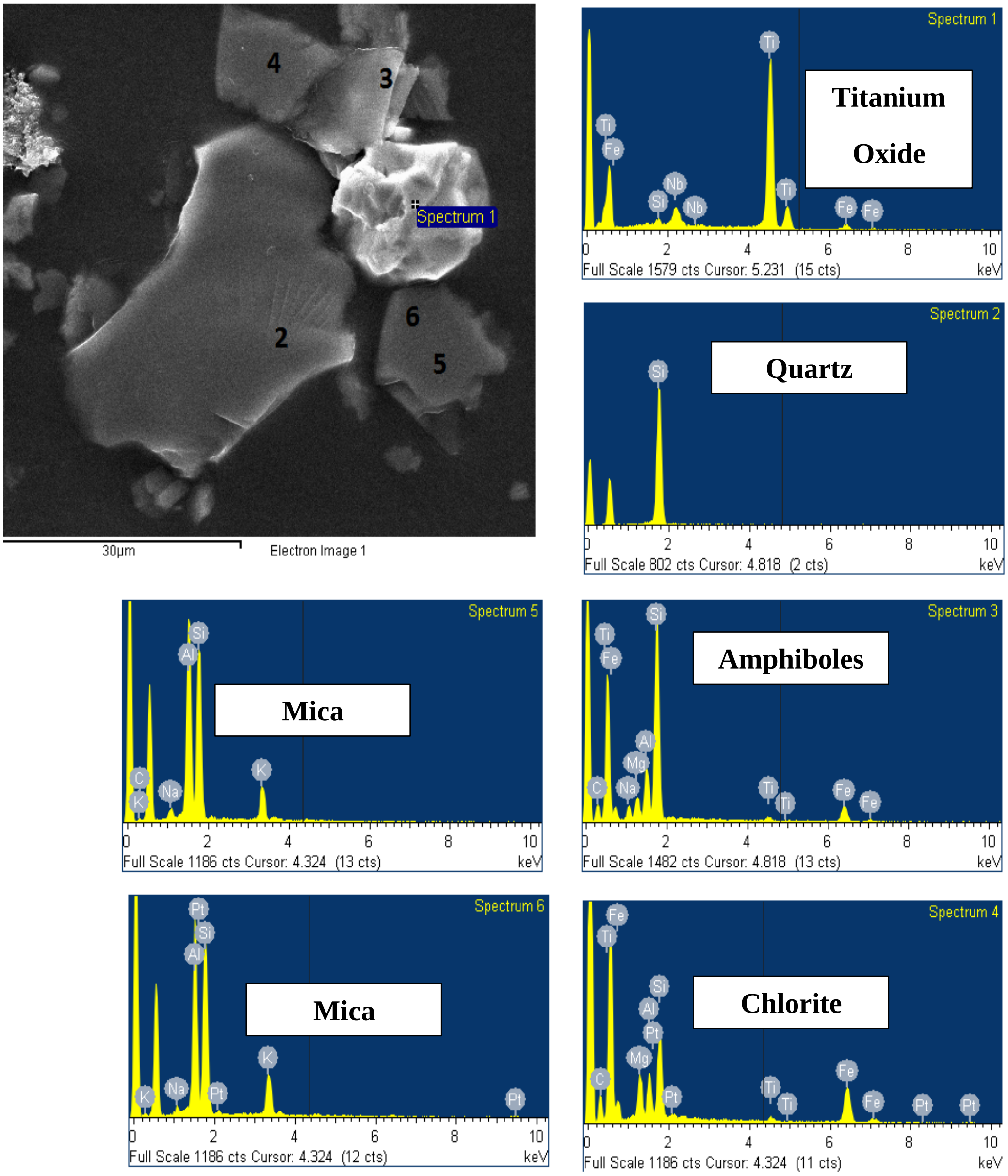

Fig. 16— Silt fraction SEM/EDS point 5.

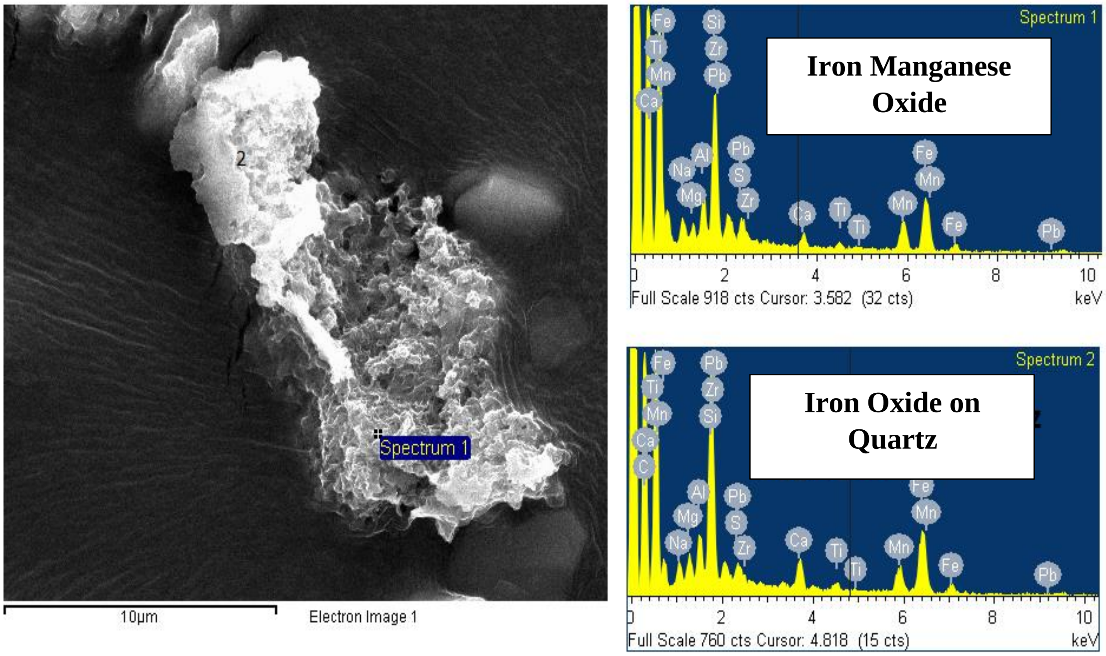

Fig. 17— Silt fraction SEM/EDS point 6.

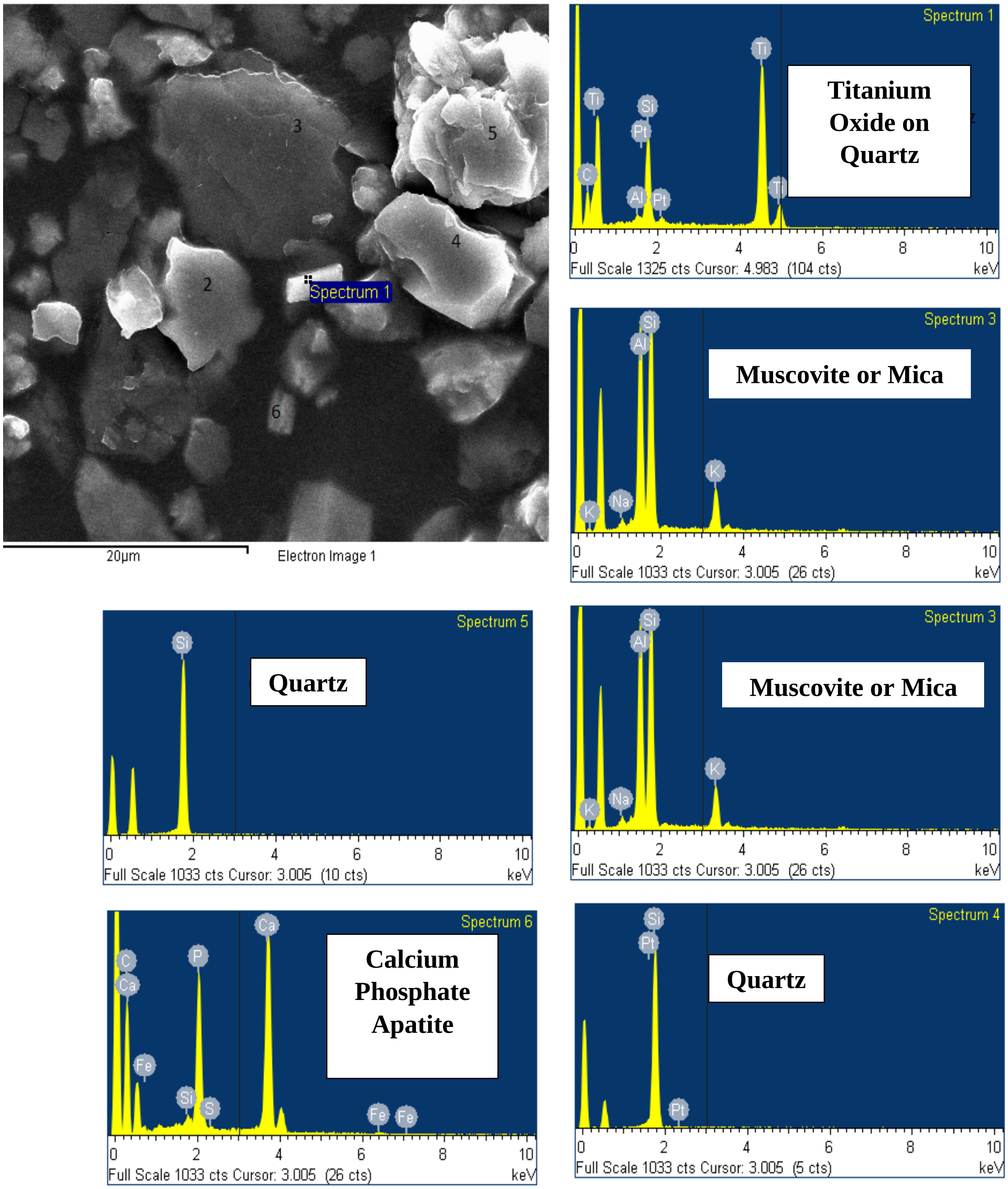

Fig. 18— Silt fraction SEM/EDS point 7.

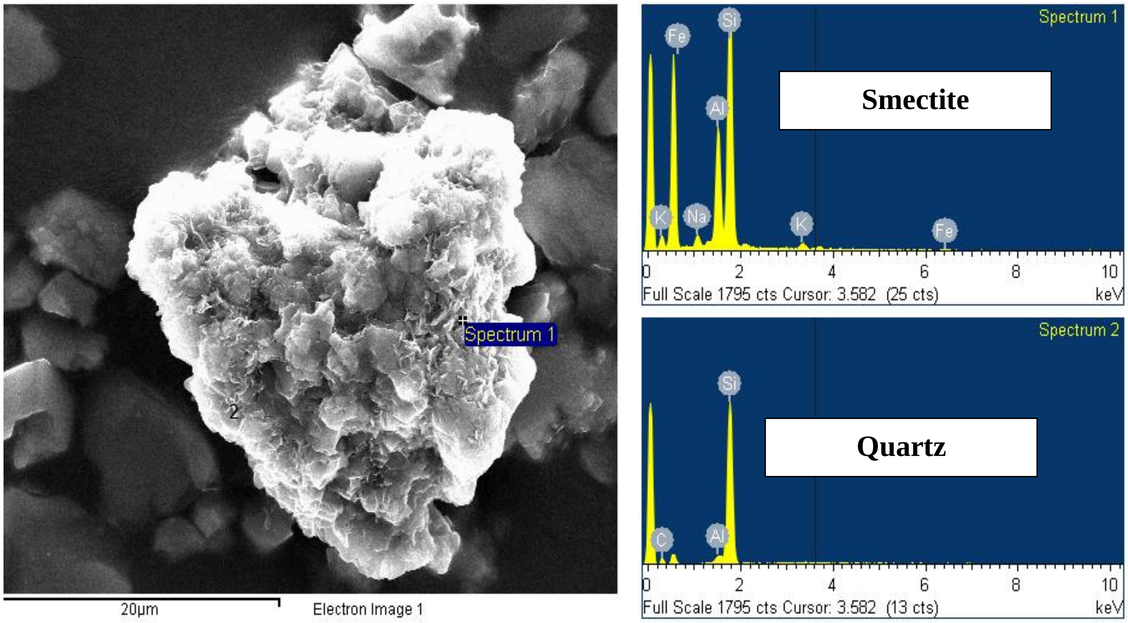

Fig. 19— Silt fraction SEM/EDS point 8.

Cation Exchange Capacity Analysis

The CEC results came as follow in **Table 5**, showing a low CEC for the sample at an average of 5.2 cmol/kg in comparison to the standard samples at average of 83.5 cmol/kg. Also worth to be mentioned that the sample suffered significant amount of losses (>10%). This low CEC is attributed for the presence of minerals such as kaolinite and chlorite which are low CEC minerals. On the other hand, Mica and smectite presence didn’t contribute to the CEC which is an indication of low smectite concentration when compared to kaolinite and chlorite.

	sample 1	sample 2	standard 1	standard 2
W1, g	12.593	12.567	12.847	12.867
W2, g	12.703	12.678	12.948	12.97
W3, g	13.449	13.4399	13.431	13.41
W4, g	12.95	12.922	12.948	12.973
CaS, ppm	1.104	1.041	3.631	3.694
CaI, ppm	5.463	5.463	5.463	5.463
A	0.552	0.5205	1.8155	1.847
B	0.163016	0.16649	0.105545	0.096149
CEC	5.437082	4.976099	84.48227	82.42248
Average CEC	Samples	5.20659	Standard	83.45237

Table 5— CEC calculations for Bandera sandstone.

Transmission Electron Microscopy (TEM)

In **Table 6** the d-spacing of the different electron diffraction was measured and calculate after scale definition using the Image-J software. According to the d-spacing of each particle the mineral causing this pattern could be identified.

Through examining multiple points during the TEM analysis it was clear that we over diluted the clays; this resulted in low to no response on the EDS. Particle number four (**Fig. 20**) shown in two magnifications is showing goethite threads and the electron diffraction (**Fig. 21**) is showing low crystallinity and multiple crystals. Particle number five (**Fig. 22**) was examined in three locations showing free edges of mica in part 5a; the electron diffraction pattern (Fig. 21) of this sample is showing multiple crystals overlying in a circular pattern, this reflect the possibility of combined crystals of smectite with mica. Particle number 11 (**Fig. 23**) showed a platy shape with cavities on the surface, it worth to be mentioned that those cavities wasn't original in the sample and they were induced by the beam damaging. Through the shape and the cavity presence kaolinite was suspected to be the mineral in this sample. On the other hand, the particle number 13 (**Fig. 24**) showed a clear result on the EDS response and showed a singular crystal structure (**Fig. 25**) of high crystallinity. Also the shape of the particle was the same like particle three, the EDS showed an almost one to one Al to Si ratio. This ratio with the shape in presence of the K and Mg could reflect a biotite or mica covered with kaolinite; this combination is common and have been witnessed in the SEM data. Furthermore, this sample didn't show the fringes. In this same sample there was iron that couldn't be attributed to the mica or the kaolinite, but it may be the iron oxides coating the sample or original in the structure of the biotite. Particle 14 (**Fig. 26**) also showed a good response on the EDS showing a 2:1 ration of Si to Al and a high crystallinity of single crystal structure. This result combined with the sharp cornered plates of the particle with presence of the K and Mg could have been described early as more biotite particle which also comply with the SEM results. The ratio of Al, Si, K, and Mg doesn't comply with the ideal structure of biotite.

At point eight (**Fig. 27**) there was some fringes observed upon processing the image by Image-J the fringes were more clear. Through this program the scale was digitized and an electronic scale was constructed to measure a band of fringes and calculate the d-spacing. Through this step nine band were measured together to be 3.07 nm; this resulted in d-spacing equal to 0.34 nm.

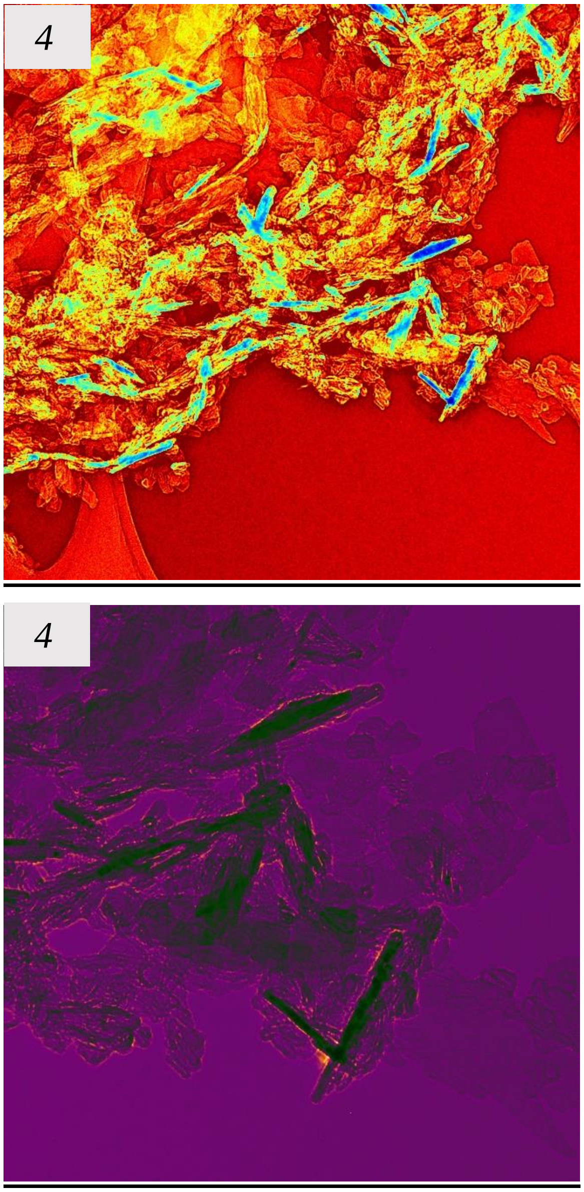

Fig. 20— TEM image at point 4.

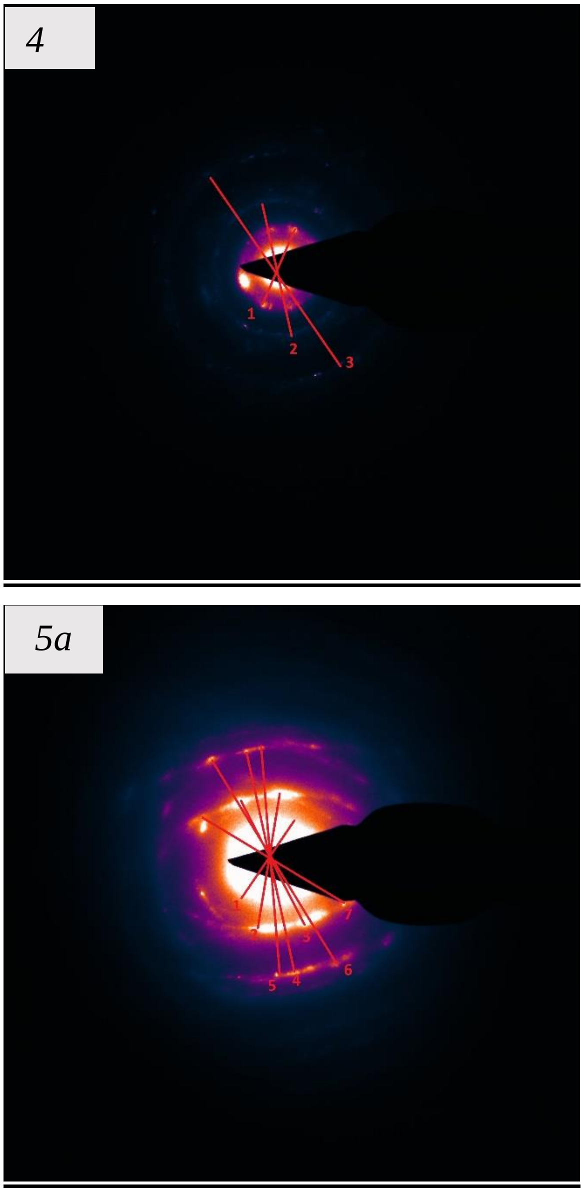

Fig. 21— Electron diffraction pattern points 4 and 5a.

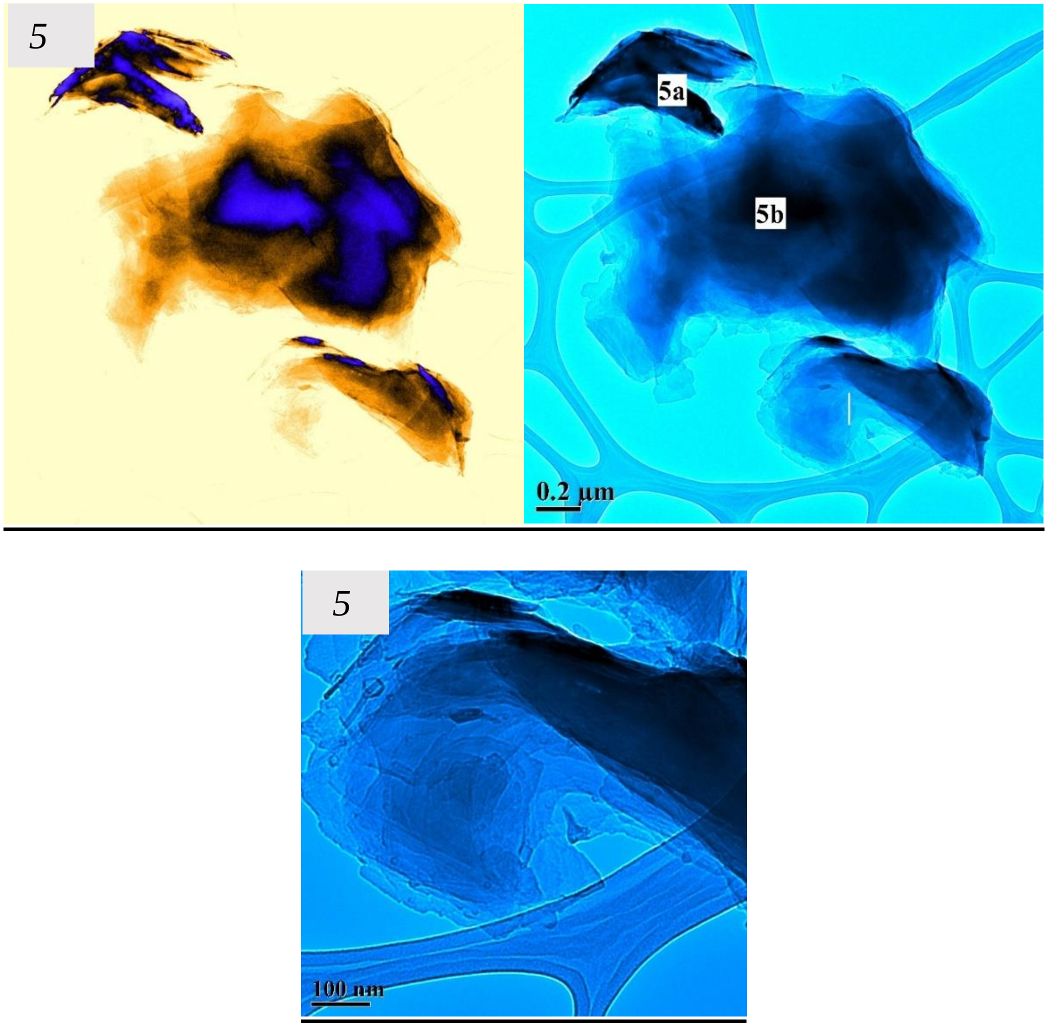

Fig. 22— TEM image at point 5.

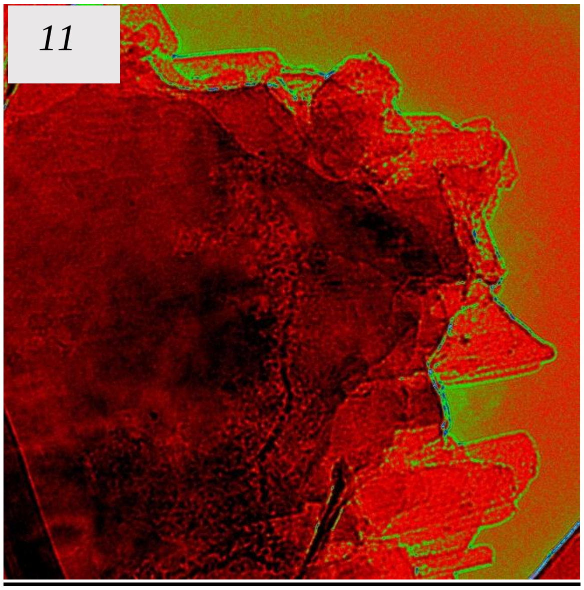

Fig. 23— TEM image at point 11.

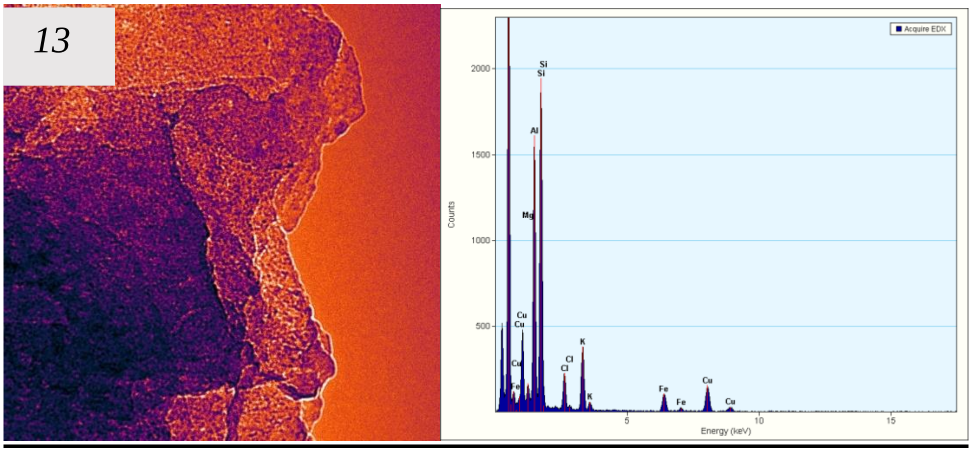

Fig. 24— TEM image and EDS at point 13.

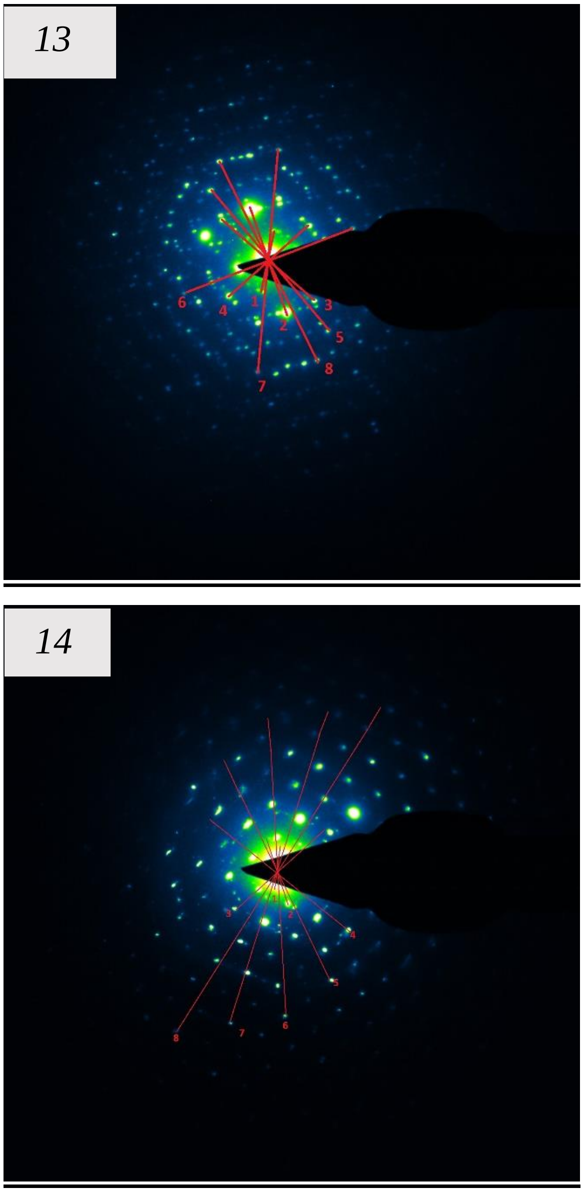

Fig. 25— Electron diffraction pattern points 13 and 14.

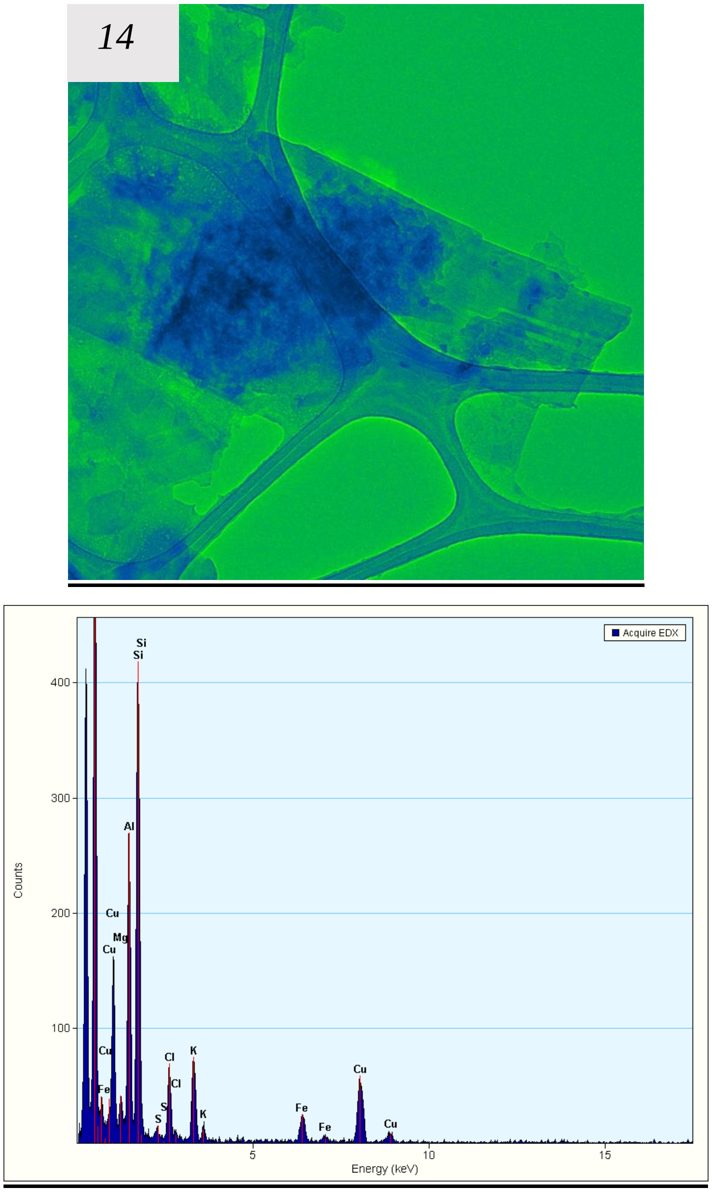

Fig. 26— TEM image and EDS at point 14.

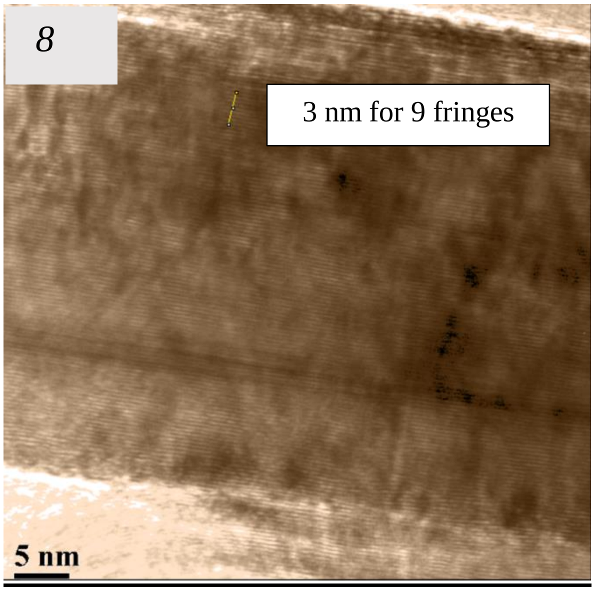

Fig. 27— TEM image showing fringes.

Picture	Point	2d	d	Picture	Point	2d	d
pic1	1	0.253	0.1265	pic5b	6	0.87	0.435
pic1	2	0.374	0.187	pic5c	1	0.288	0.144
pic1	3	0.709	0.3545	pic5c	2	0.409	0.2045
pic2	1	0.239	0.1195	pic5c	3	0.561	0.2805
pic2	2	0.4	0.2	pic5c	4	0.705	0.3525
pic2	3	0.536	0.268	pic5c	5	0.849	0.4245
pic2	4	0.713	0.3565	pic5c	6	1.17	0.585
pic4	1	0.25	0.125	pic13	1	0.181	0.0905
pic4	2	0.397	0.1985	pic13	2	0.336	0.168
pic4	3	0.695	0.3475	pic13	3	0.358	0.179
pic5a	1	0.13	0.065	pic13	4	0.317	0.1585
pic5a	2	0.255	0.1275	pic13	5	0.545	0.2725
pic5a	3	0.245	0.1225	pic13	6	0.663	0.3315
pic5a	4	0.685	0.3425	pic13	7	0.658	0.329
pic5a	5	0.689	0.3445	pic14	1	0.125	0.0625
pic5a	6	0.684	0.342	pic14	2	0.206	0.103
pic5a	7	0.462	0.231	pic14	3	0.356	0.178
pic5b	1	0.256	0.128	pic14	4	0.52	0.26
pic5b	2	0.434	0.217	pic14	5	0.717	0.3585
pic5b	3	0.431	0.2155	pic14	6	0.888	0.444
pic5b	4	0.679	0.3395	pic14	7	0.967	0.4835
pic5b	5	0.78	0.39	pic14	8	1.144	0.572

Table 6— d-spacing for electron diffraction patterns.

Total Mica Percentage by Potassium Quantification

According to the XRD analysis it was clear that chlorite is present in the sample. Although feldspars were available in the silt fraction XRD it was absent in the clay fraction.

According to this all the detected K can be attributed to mica mineral. According to the calculations applied on the atomic adsorption data mica was quantified to be 40% of the clay fraction as shown in **Table 7**. This result was also supported by the XRD, SEM, and TEM analysis.

	Sample 1	Sample 2	Standard 1
Sample Weight, mg	103.2	100.6	101.2
K (ppm) in solution	6.281	7.45	9.384
Total K (mg) in digestion solution	3.1405	3.725	4.692
%K in sample	3.04	3.7	4.636
%Mica in sample	36.6	44.57	55.8
Average %Mica	40.58	40.58	55.8

Table 7— Mica% calculations for Bandera sandstone.

Newmood Analysis

This software enables the creation of hypothetical minerals and combine them together in order to simulate your soil sample. Through this process you can learn more about the mineral such as: the interlayer cations, their concentration, particle size, number of sheets, and finally can conduct semi qualitative date. The only limitation of this software is that it can imitate the quartz peaks. This limitation is significant for sandstone sample, since after separating the clay fraction there is residual quartz particles in the clay that shows up in the XRD pattern. This result in error in the percentage of each mineral calculation due to the absence of correction for the quartz peak. In order to simulate the Bandera sandstone three main minerals were created Chlorite, Kaolinite, and Mica. Shown in **Fig. 28**, **Fig.**

29, and **Fig. 30** the XRD patterns of pure elements and their parameters as discussed later. In **Fig. 31** a combined pattern was generated to match the XRD pattern of the clay fraction when it was saturated with Mg, K, and glycerol. Since the three experimental peaks match the comparison was conducted with the Mg saturated pattern. This analysis showed that the chlorite is present in the clay fraction with a percentage of 55 % which comply with the K Mica quantification at 40%. The kaolinite is 22% and the mica is 15%. The percentage error can be attributed to the presence of quartz.

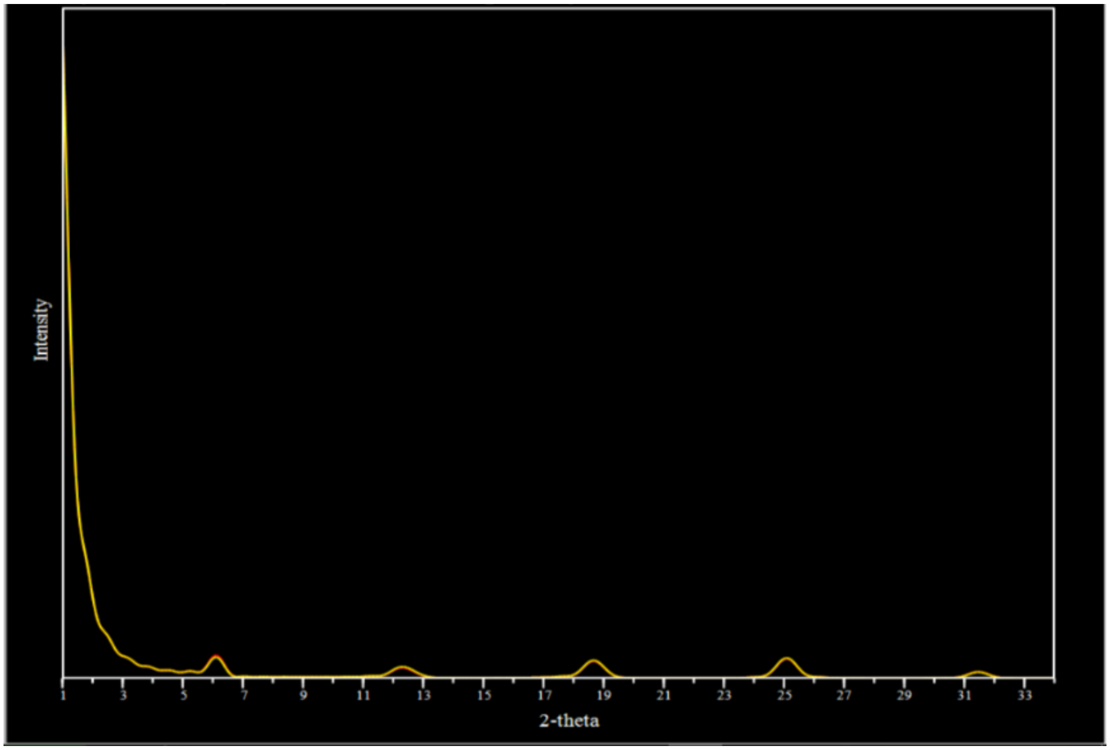

Fig. 28— Theoretical chlorite XRD.

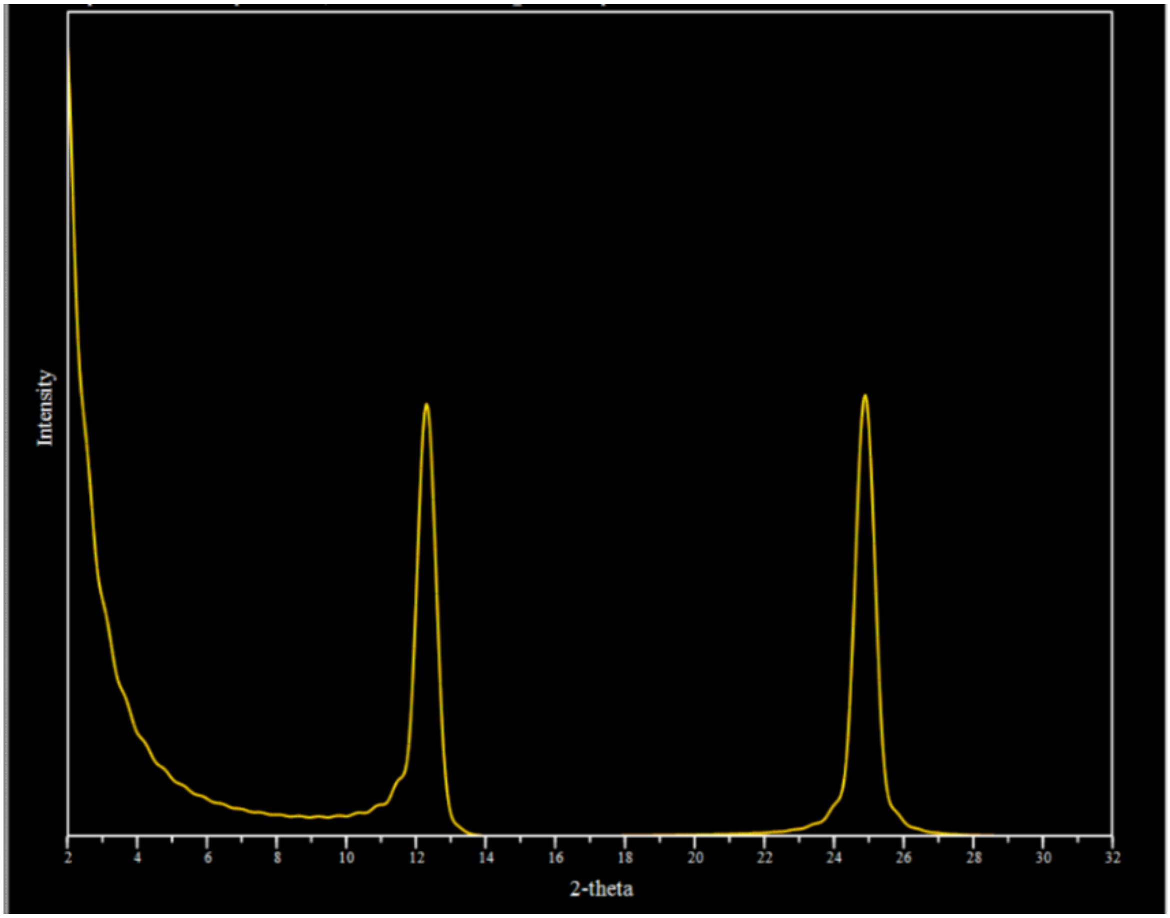

Fig. 29— Theoretical kaolinite XRD.

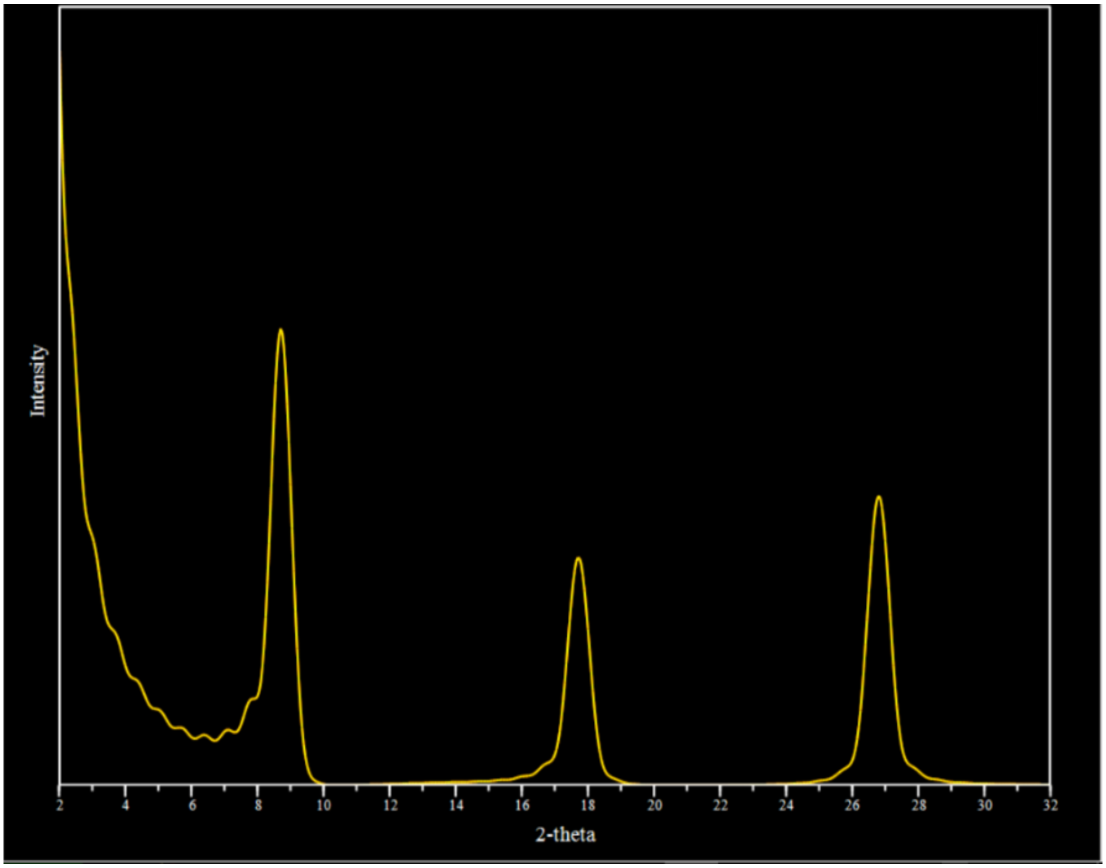

Fig. 30— Theoretical mica XRD.

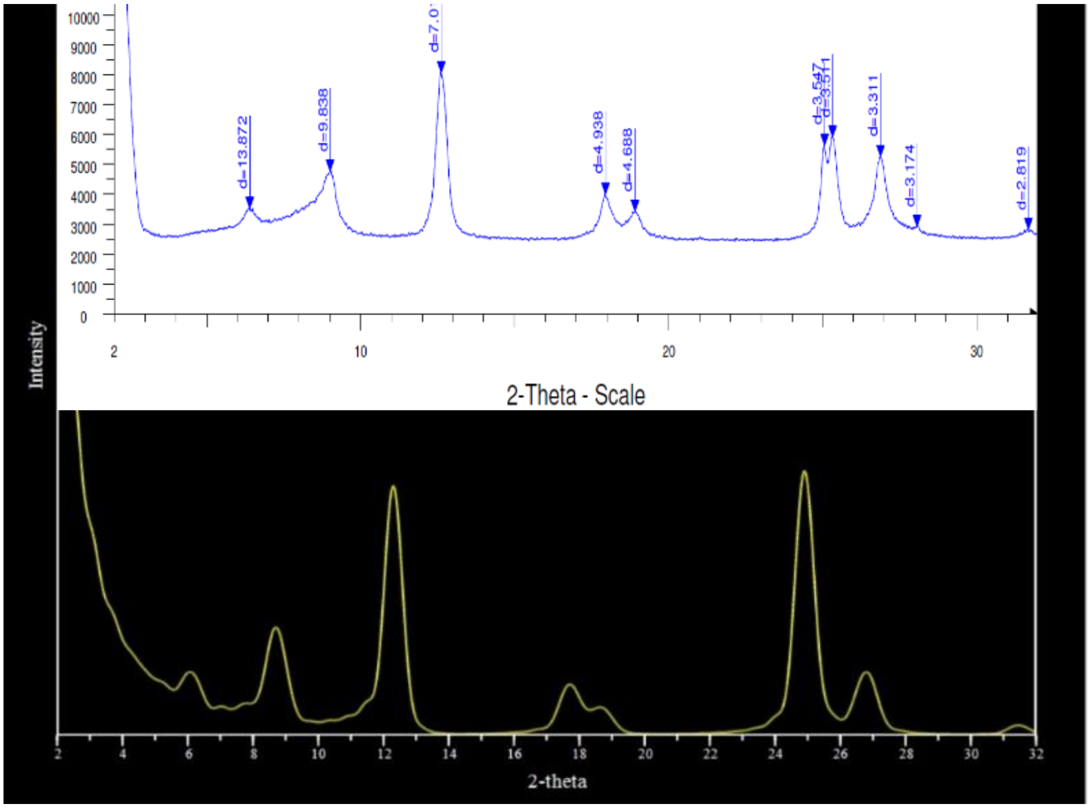

Fig. 31—Theoretical combined XRD versus experimental XRD.

Conclusions

Key findings from this study leads to the following conclusions:

The Bandera sandstone is very complicated formation with complex minerology. The sample moisture content was low to non. The sample contains carbonate mineral but not calcite since the HCl response was so weak and slow. The sample contains vvery little reducing materials as the peroxide test and treatment came out almost negative. The sample doesn’t contain magnetic matter, and has a high 8.3 pH due to carbonates presence and had high EC=467 μS/cm. Also we have high EC we couldn’t determine the evaporates types since the sample was extremely cloudy with clays. The XRD pattern showed the presence of the Quartz, Dolomite, Kaolinite, Illite, and Albite. The sample contains 65%

sand, 17.45% silt, and 9.17% clays. Also we lost around 10 % of the sample as cementing and flocculant materials.

This study showed that, it’s clear that mineral identification through bulk sample is not cloth to the truth about Bandera sandstone. Sample fractionation to sand, silt, and clay sizes helped to understand and analyze for further depth the nature of minerals in this formation. This work has shown from XRD analysis of sand fraction presence of quartz, dolomite, and feldspar. Moreover, the silt fraction showed chlorite, illite, kaolinite, albite, quartz, dolomite, and feldspar. And at the end of XRD analysis the clay fraction results proved most of the minerals in the silt fraction. Again chlorite, illite, Kaolinite, and quartz was detectable by XRD techniques; minerals such as smectite and vermiculite were not in any step of the analysis and didn’t show up in the glycerol and K saturation steps. Kaolinite and chlorite totally decomposed from the sample upon exposure to 550°C.

The FTIR analysis proved presence of the minerals we discussed in the XRD. The data from bulk sample was so few showing mica and chlorite; it also shown the presence of two Al ions in the octahedrons found in the sample. Overall the bulk sample didn’t give enough data to be analyzed versus the XRD patterns. On the other hand, pressed pellet technique showed the presence of kaolinite, chlorite, quartz, and proved water adsorption peaks. The other part of the work concerning the CEC analysis showed a low CEC at 5 cmol/Kg. This level of CEC corresponds to kaolinite and chlorite minerals. This been told its clear that from quantitative point of view the chlorite and kaolinite minerals are present in higher concentrations in comparison to mica, and smectite.

This work further understand the Bandera sandstone formation. It is clear that some minerals are beyond detection abilities of machines such as: XRD, and FTIR at their present concentration. Particles such as titanium oxide, zirconium silicate, muscovite, phosphate calcium apatite, and amphiboles is detected in the investigated samples using the SEM/EDS analysis. Some of those particles are in high concentration such as titanium oxide and some others showed up one time. Also from this study particle size and morphology of already identified minerals such as: Kaolinite, mica, chlorite, and quartz are identified; this information can be used to understand the average surface area and the morphology which can help predict their behavior during acidizing.

CHAPTER III

NEW NMR/CT-SCAN ANALYSIS TO INVESTIGATE THE ACID STIMULATION IMPACT ON THE PETROPHYSICAL PROPERTIES OF SANDSTONE CORES IN THE PRESENCE OF FINES MIGRATION[5]

Summary

Fines migration is one of the toughest challenges in the sandstone stimulation process. Clay mineral mobilization happens either chemically or mechanically. This phenomenon results in plugging the dominant pore throats and creates tighter pore structure in the formation, thus reducing productivity. Furthermore, the stimulation of clay-rich formations using either the HCl-based pre-flush or mud acid triggers secondary and tertiary reactions that result in severe formation damage. This work aims to assess the mechanism, extent, and depth of formation damage that occurs during acid stimulation of Bandera sandstone. This work included testing untreated cores and cores damaged by fines migration. This work further aims to introduce a new processing technique for CT scan data to track the mentioned formation damage with a high level of resolution.

In the experimental procedure, half of the cores were damaged by the injection of deionized water; afterward all cores were stimulated by different acid systems. During the damage process, the impact of the brine composition on the severity of the fines migration

---

[5] Part of the data reported in this chapter is reprinted with permission from “Evaluating the Effects of Acid Stimulation Treatment Before and After Fines Migration on Petrophysical Properties in Sandstone Reservoirs” by Hanafy, A. M., Ali, A., Nasr-El-Din, H. A. et al. 2015. Presented at the International Petroleum Technology Conference, 6-9 December, Doha, Qatar, copyright 2015 by the International Petroleum Technology Conference. Reproduced with permission of IPTC. Further reproduction prohibited without permission.

was investigated. A total of eight coreflood experiments were conducted at temperatures of 150 and 250°F. A pre-flush stage of 15 wt% HCl was injected to 6 in. long by 1.5 in. diameter core samples at a flow rate of 3 cm^3/min; some of the cores were stimulated after the pre-flush stage using a mud acid stage of 12 wt% HCl + 3 wt% HF. The cores were selected to be consistent in terms of clay content, mineral composition, pore-size distribution, porosity, and permeability. A combination of characterizing measurements were conducted before and after acid treatments. This tests included conducting X-ray diffraction (XRD) and X-ray fluorescence (XRF) measurements to assess the mineralogical and elemental composition of the rock. Different stimulation stages were injected using a coreflood setup. Cores were scanned using computed tomography (CT) to evaluate pore-scale heterogeneity. The changes in pore-size distribution and the pore structure were investigated using nuclear magnetic resonance (NMR) coupled with CT scan histograms.

The alteration of the salt composition exhibited a significant impact on the fines migration magnitude. The injection of deionized water in the core inhibited using sodium chloride exhibited severe fines migration damage, while minimal formation damage was noticed upon the injection in the core inhibited using ammonium chloride. This work showed that although HCl succeeded in dissolving dolomite, the precipitated products from the secondary and tertiary reactions with HCl and HF lowered the total porosity gain. The presence of fines migration toward the outlet triggered localized damage at the same section, while undamaged cores showed a uniform porosity gain along the core. The stimulation of the undamaged core at 250°F triggered fines migration damage that was spread along the entire core. The treatment with mud acid resulted in more damage compared to the pre-flushed stage. Combining CT-scan and inductively coupled plasma (ICP) measurement results revealed a high sensitivity of both damaged and undamaged cores to mud acid at temperatures of 150 and 250°F. The coupling of the new CT scan histogram with the NMR analysis succeeded in detecting and discretizing the process of fines migration and its stimulation outcomes.

The literature is rich with reports on the interactions of sandstone formations and acid systems. However, this comparative study provides a broader overview of how stimulation treatments influence the petrophysical properties in porous sandstone. This work introduces a deep look at dissolution/precipitation through the newly introduced approach to process the CT scan data and integrate it with the NMR data. Finally, this work contributes a new reliable design technique for sandstone matrix acidizing to enhance the chances of a successful acid stimulation treatment.

Introduction

This work aims to describe, measure, and locate the extent of fines migration damage upon stimulating Bandera sandstone. It aims to track down the acidizing process of both fines migration damaged and undamaged sandstone cores. This is aiming at measuring the fines migration damage magnitude and how it impacts the stimulation process. That will be monitored in terms of change in the pore structure geometry and the corresponding permeability. In this work a new method is introduced, which is based on combining the computer tomography analysis with the NMR analysis to track down the pore structure changes. The Bandera sandstone cores were evaluated using CT-scan, NMR, XRF, XRD, SEM, and EDS at each step between fines migration induction to acid injection to monitor the changes in the pore structure.

Experimental Equipment and Materials

Materials

The work was conducted using Bandera sandstone outcrop cores. A detailed analysis was obtained using XRD, XRF, and SEM/EDS to evaluate the formation mineralogy. The Bandera sandstone is composed of 15 wt% dolomite and 14 wt% combined clays; the rest of the core contains albite and quartz minerals (**Table 8**). The used core plugs are 6 in. long and 1.5 in. diameter.

Two acid systems were used in this study; the first acid was a pre-flush composed of 15 wt% HCl solution that was prepared from a 36 wt% HCl acid solution, while the second acid was a mud acid of 12 wt% HCl coupled with 3 wt% HF that was prepared from ammonium bi-fluoride. Sodium chloride and ammonium chloride were purchased from a chemical company and were used in pre-and post-flush brines at 5 wt% concentration. A 17.8 mΩ.cm deionized water was the based solvent for the brine and the acid fluids. Industrial corrosion inhibitors and formic acid corrosion inhibitor intensifiers were used to maintain the integrity of the system and minimize corrosion during acid stages.

Mineral	Concentration, wt%
Quartz	59
Kaolinite	3
Albite	12
Chlorite	1
Illite	10
Dolomite	15

Table 8— Mineralogy of Bandera sandstone, by XRD measurements.

Coreflood Tests

The coreflood setup was built around a 6 in. long stainless-steel core holder installed inside an oven. This was connected to a pumping system that was built around three piston-cylinder accumulators connected to a digitally controlled syringe pump. The overburden pressure was applied using a hand hydraulic pump. In addition, a pressure transducer was used to monitor the pressure drop across the core with time. Finally, the pressure drop, the oven temperature, the pump flow rate, and the pump pressure were all connected to a data acquisition system based on a custom built LabVIEW™ software. **Fig. 32** shows a schematic of the coreflood setup.

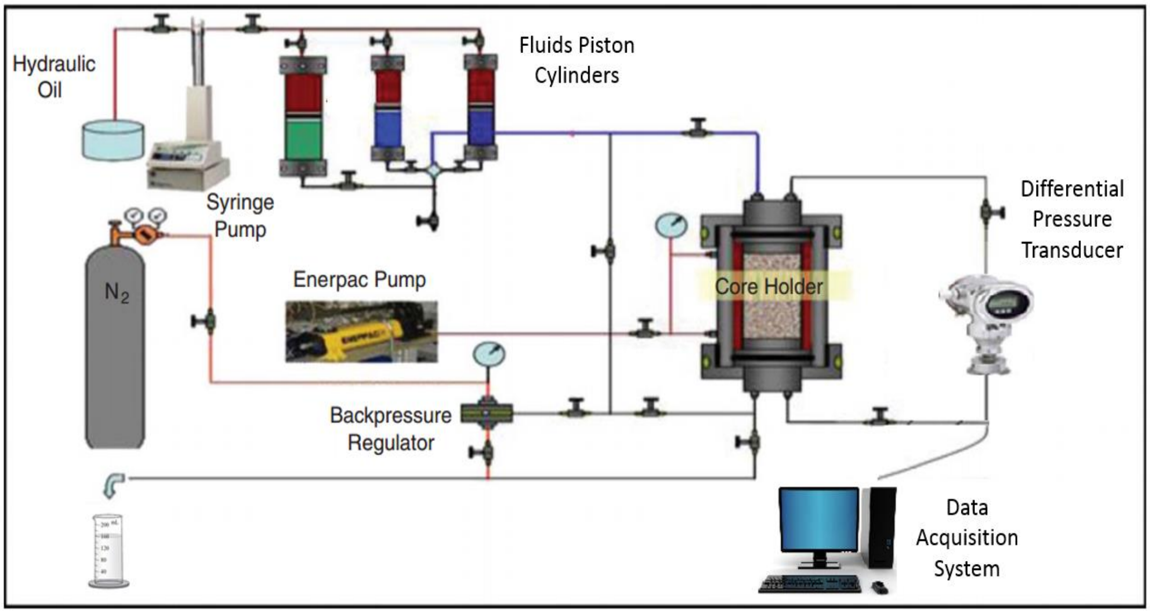

Fig. 32— Coreflood setup schematic.

NMR Laboratory Measurements

NMR measurements were used to study the impact of fines migration induction and acid stimulation on the pore-size distribution of the Bandera sandstone. The measurements were conducted using a 2 MHz NMR bench-top spectrometer, GeoSpec2 Core Analyzer (Mark of Oxford Instruments). Samples were immersed in brine in a saturation cell kept under vacuum for four hours. This was followed by a coreflood saturation using an overburden pressure of 1,000 psi to ensure a 100% saturation at all times. T_2 relaxation measurements were carried out using a Car-Purcell-Meiboom-Gill (CPMG) pulse sequence. The Echo Spacing Time (TE) was kept at 200 µs, the target signal-to-noise ratio (SNR) was adjusted to 200, and the number of scans to 48. The SNR of the measurement was more than 300 after 48 scans of these samples.

Experimental Method

Initial Tests

All of the cores were assessed for their porosity based on the difference between the saturated weight and the dry weight. They were dried at 150°F overnight, and then saturated under vacuum in a saturation cell. Each core was initially CT-scanned under saturated and dry conditions for porosity calculation. A selected number of saturated cores were cut down to three sections, each 2 in. long; then, each section was scanned using NMR to describe its initial pore size distribution. The cores were cut down into three sections to satisfy the equipment sample size requirement and to investigate any change in the pore size distribution along the core.

The permeability of each core was measured using a coreflood setup at pumping flow rates of 1, 2, and 3 cm^3/min. Those flow rates were selected to avoid mechanical detachment of clay particles and the unintended induction of fines migration. The measurements were conducted at room temperature with a back pressure of 500 psi and an overburden pressure of 1,000 psi.

Damaging the Cores and Fines Migration Impact Assessment

A selected number of cores were saturated using a 5 wt% ammonium chloride brine, while the rest were saturated using a 5 wt% sodium chloride brine. This design aimed to investigate the impact of the initial inhibition cations and their ability to inhibit fines migration damage upon exposure to incompatible fluid. After the cores were saturated, they were subjected to 1/3, 1, and 3 PV of deionized water at a flow rate of 3 cm^3/min.

During the deionized water injection, the damage was tracked based on the variation of the pressure drop across the core.

After the cores were damaged using deionized water, they were once again scanned using a CT-scanner while they were saturated with ammonium or sodium chloride brine. Then, those cores were cut down into three sections as previously mentioned and examined for their pore-size distribution using NMR. Finally, the CT and NMR data sets were combined to track down the formation damage induced by fines migration and to describe the mechanism of such phenomena.

Pre-Flush and Fines Migration Impact on the Stimulation Process

Both the undamaged and the damaged cores were subjected to a pre-flush stage of 15 wt% HCl to compare their response. The stimulation was conducted using the coreflood at 150 and 250˚F using a flow rate of 3 cm^3/min. This time the back pressure was raised to 1,000 psi to keep the CO_2 resulting from the dolomite dissolution in solution. This required raising the overburden pressure to 1,500 psi to maintain the flow in the axial direction and to suppress the radial flow across the core. During the stimulation, the pressure drop across the core was measured to track the damaging and dissolution cycles. The four cores were scanned before and after the stimulation procedure using CT and NMR scanners. The effluent from the stimulation process was analyzed using ICP. This process included measuring the concentration of key cations such as Ca, Mg, Si, Fe, Al, and K.

Mud Acid Impact on Pre-Flushed Cores with Damage

This stage was designed to investigate the impact of the regular mud acid of composition 12 wt% HCl and 3 wt% HF on the cores that were pre-flushed in the later stage. Those cores were subjected to 3 PV of regular mud acid using the same coreflood setup at the same conditions of the pre-flush stage. The cores were scanned using CT and NMR scanners, and the effluents were analyzed using ICP.

New Formation Damage Tracking Technique

The CT scans traditionally were plotted as a porosity profile along the depth of the core. These porosity values were based on the variation of the average CT number. The new approach intended to dissect the whole core CT scan data into five small data sets, each representing 1.1 in. of the core. Each section was divided into 100 slices in which the CT number of each 0.3 µm by 0.3 µm pixel was recorded. Each individual CT-number in each of the cores was represented against the frequency of its presence across the section. Those CT numbers were plotted against their frequency across each 1.1 in. of the core. The change in CT number represents a change of the attenuation number, which is inversely proportional to the porosity. The CT number histograms from core scans before and after each stimulation stage were compared to track down the dissolution of the dolomite mineral and investigate the re-filling of those pore spaces by the secondary and tertiary reactions by-products. Finally, The CT scan analysis was compared to the pore-size distribution using NMR scans.

Workflow Schematic

The workflow schematic (**Fig. 33)** was followed to obtain results that would quantify the damage caused by fines migration and its effect on acidizing performance at temperatures of 150 and 250°F. For all cases Bandera sandstone homogeneity was examined via XRD and CT-scan measurements. All cores were homogenous without biding. The following section presents and discusses the results of this work.

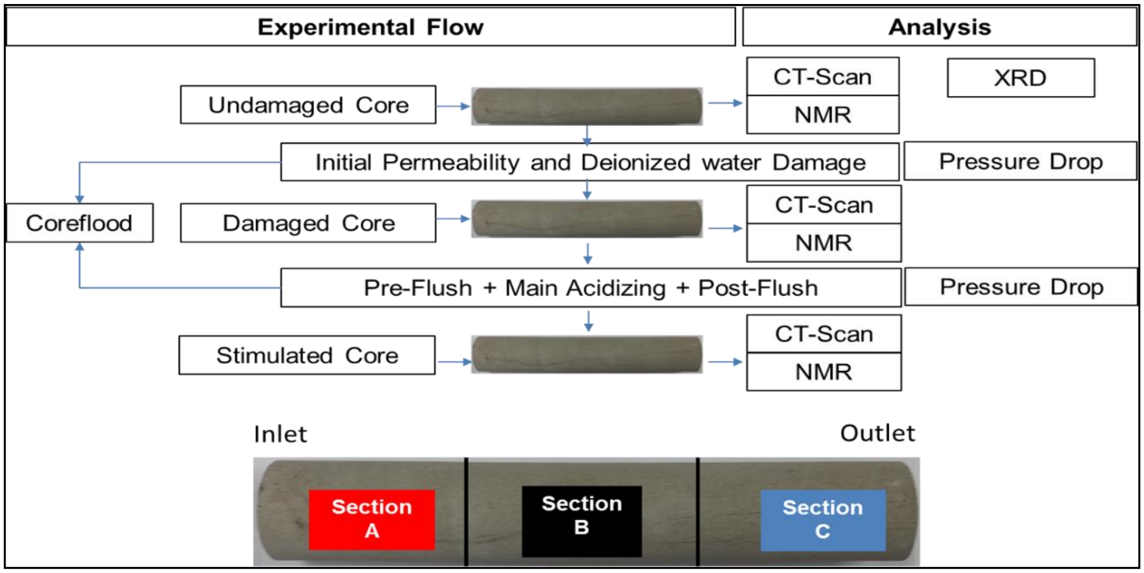

Fig. 33— Schematic diagram describing the work flow.

Results and Discussion

Salt Type Inhibition Ability

This part of the work investigates the effect of changing the brine composition on the magnitude of fines migration damage after the exposure to deionized water. The core inhibited by ammonium chloride exhibited a pressure drop increase from 36 to 77 psi upon exposure to six pore volumes of deionized water **(Fig. 34)**. This type of response shows a slow and controlled fines migration impact compared to the deionized water damage impact reported in the literature (Khilar and Fogler 1983). This result can be attributed to the ammonium ion stabilizing effect on the clay particles in the pore throats. The small size of the ammonium ion works on minimizing the aluminosilicates double-layer thickness. This condition results in a more torturous pass for deionized water to get in between the clay sheets. Hence, the clay becomes more stable against deionized water. The core inhibited using 5 wt% NaCl exhibited a severe pressure drop increase from 78 to 1,000 psi upon exposure to one pore volume of deionized water (Fig. 34). This severe increase in the pressure drop can be attributed to the swelling of the clay particles that yielded to its cracking and migration across the core, blocking some of the pore throats. Such magnitude of damage can be explained by the double-layer theory, since the large size of sodium ion makes it a less efficient clay inhibitor. This size results in a wider double layer that makes the pathways for deionized water wider and facilitates the sodium ion detachment from the clay interlayer. This mechanism results in detaching the clay particles and makes it easier to migrate them across the core.

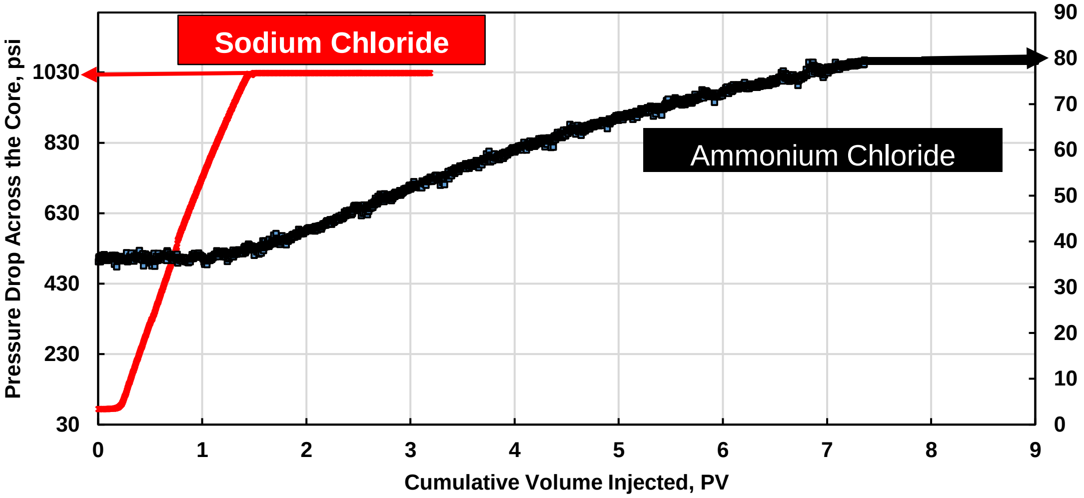

Fig. 34— Pressure drop across the core during initial permeability measurements and deionized water injection after ammonium chloride and sodium chloride inhibition.

Both of the cores were scanned using a CT scanner before and after the induction of fines migration damage. The generated data was processed using 150 slices representing the 6 in. core length. Each slice's average CT number was plotted as an inverse proportional indication of the porosity variation across the core. The data in **Fig. 35** shows a comparison between the average CT number along the core before and after the fines migration in the cores inhibited by the sodium chloride brine. The first two inches of the core shows a decrease in the CT number after the induction of fines migration. This could be attributed to the mobilization of the clay particles such as illite and kaolinite from the core inlet. The last four inches of the core show an increase in the average CT number along the section. This increase results in more dense pixels in the CT scan images. Higher pixel density was related in the literature to a less porous medium. Hence, the clay particles that moved from the core inlet were blocking the pore throats in the rest of the core. The last two inches of the core exhibited a higher increase in the average CT number compared to the two inches in the middle of the core. The sodium ion inhibited core exhibited severe formation damage localized at the core outlet.

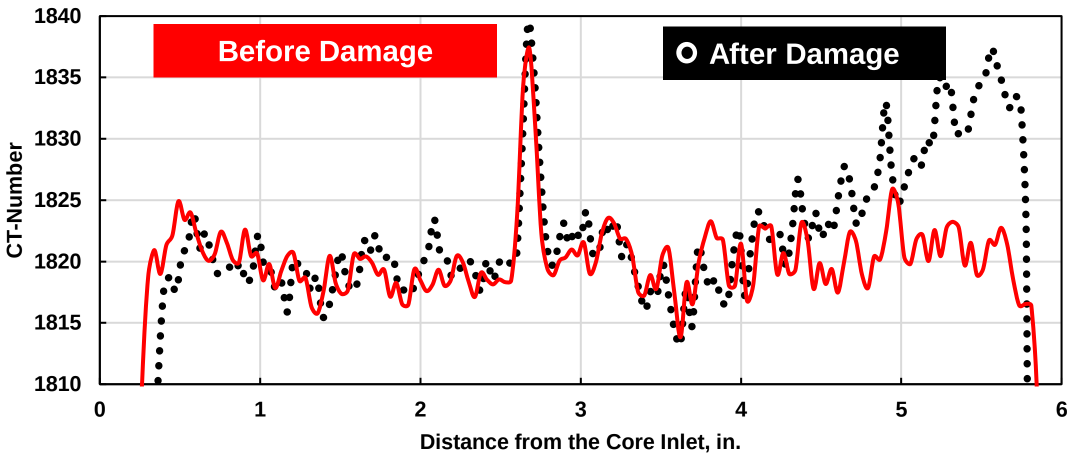

Fig. 35— CT number comparison before and after fines migration mobilization for sodium chloride inhibited core.

The final part of this analysis was conducted using NMR scans for multiple cores at different steps of the study. The data in **Fig. 36** shows the pore-size distribution of the untreated Bandera sandstone; the core is proven to be homogenous with a dominant pore size of 3.5 µm.

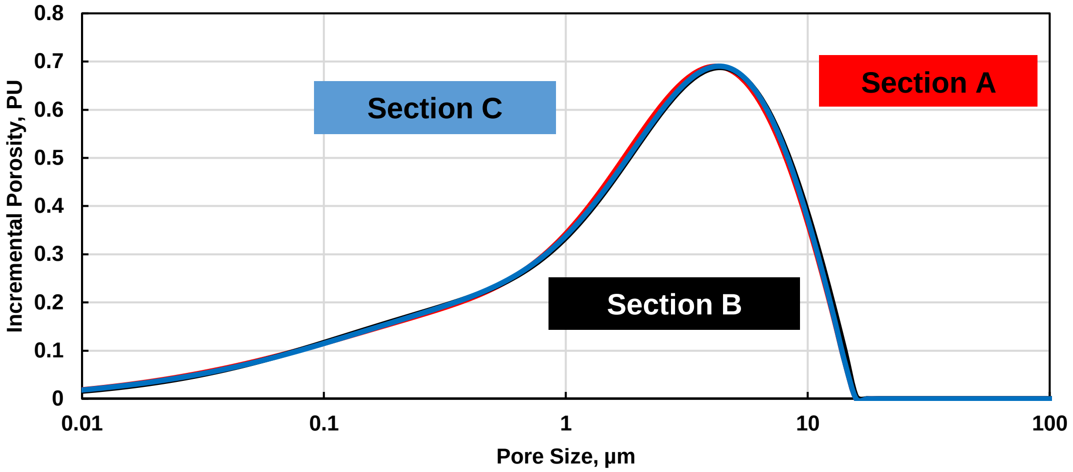

Fig. 36— NMR pore-size distribution of untreated Bandera sandstone saturated with brine.

The NMR pore-size distribution for the ammonium chloride inhibited core after damage shown in **Fig. 37** exhibited a decrease in the dominant pore size of the core inlet from 3.5 to 3 µm that is represented as a 0.7 porosity unit (PU).

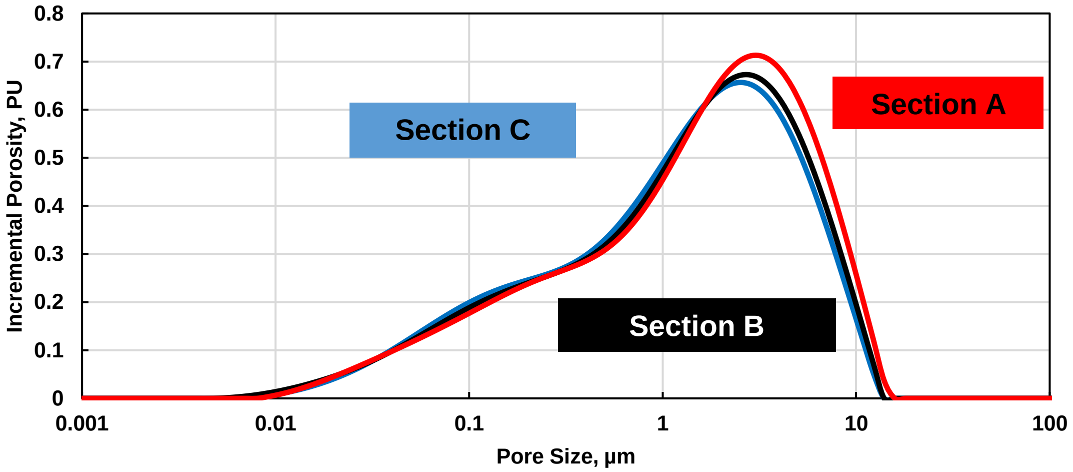

Fig. 37— NMR pore-size distribution of Bandera sandstone after injection of deionized water to ammonium chloride inhibited core.

Furthermore, the incremental porosity of the middle and the outlet sections at the same dominant pore size went down to 0.65 PU, and a new pore size of 0.3 µm exhibited an incremental porosity of 0.3 PU. At this new size, the incremental porosity of the middle and outlet sections shows a slight increase compared to the core inlet. This data set shows the mild blockage of the middle and outlet sections of the core by the fines coming from wider pore throats at the inlet, yet the magnitude of the change was minimal due to the ammonium ion stabilizing effect. The second core inhibited using sodium chloride exhibited a more severe alteration of the pore-size distribution (**Fig. 38**). The inlet and mid sections witnessed a clear widening of the dominant pore size from 3.4 to 4 µm at an incremental porosity of 0.68 PU. On the other hand, the core outlet showed a decrease in the incremental porosity of the dominant pore size at 4 µm from 0.7 to 0.6 PU. Furthermore, the incremental porosity of the pores of sizes between 0.1 to 1 µm increased by a difference of 0.1 PU compared to the core inlet and middle sections. The magnitude of pore size distribution change across the core came matching the CT number profile. The result shows that the fines migration tends to be localized at the last inch of the core, and such damage is capable of decreasing the permeability from 13 to 0.1 md after injection of one pore volume of incompatible deionized water. On the other hand, the cores treated with ammonium chloride suffered only a 50% reduction in permeability after injection of six pore volumes of deionized water.

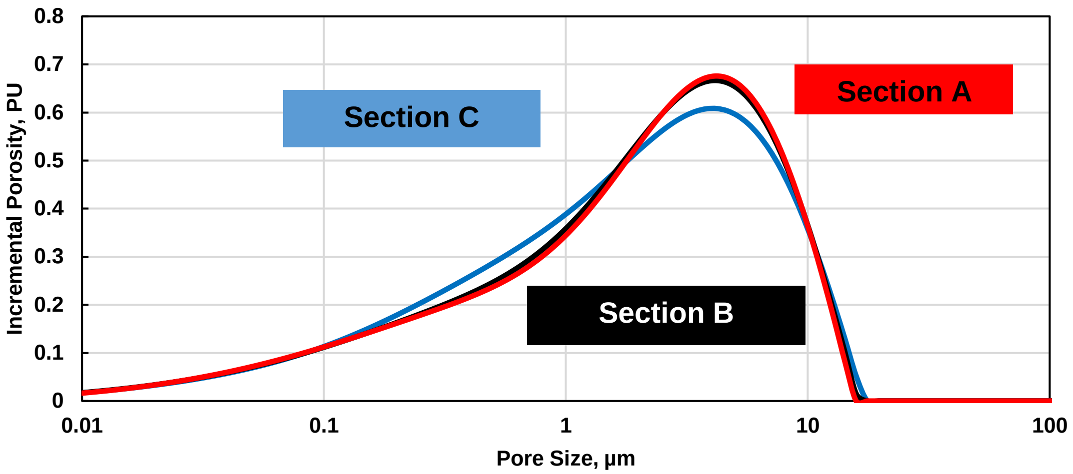

Fig. 38— NMR pore-size distribution of Bandera sandstone after injection of deionized water to sodium chloride inhibited core.

Pre-Flush Outcomes in Presence and Absence of Fines Migration

The second part of this work was designed to investigate the impact of the fines migration damage on the pre-flush stage stimulation outcomes. Four cores were used; the first set included two cores that sustained mild fines migration damage after they were inhibited by ammonium chloride brine, while the second set included two undamaged cores. Each core set was stimulated using three pore volumes of 15 wt% HCl at 150 and 250˚F using a flow rate of 3 cm^3/min. All cores were scanned before and after the stimulation using both CT-scanner and NMR. Data was processed in the same manner mentioned earlier.

The change in the core porosity after the stimulation at 150˚F was plotted along the distance from the core inlet as represented in **Fig. 39** to describe both the dissolution and precipitation patterns. The core with fines migration exhibited a consistent positive porosity gain rising from 18 to 25 vol% along the first four inches from the core inlet. The last two inches toward the outlet of the core exhibited a decline in the porosity down to 22 vol%. On the other hand, the treatment of the undamaged core at the same condition exhibited consistent positive porosity gain rising from 17 to 21 vol% along the core. Such results show a moderate dissolution rate of dolomite at 150˚F in both cores. The core with a fines migration porosity profile suggests a localized precipitation of the alumino-silicate deformed structures coming from the attack of HCl on the mobilized illite, kaolinite, and chlorite minerals. The cores with no damage showed a consistent response of dissolution along the core, and the HCl damaging effect was consistent along the core as well.

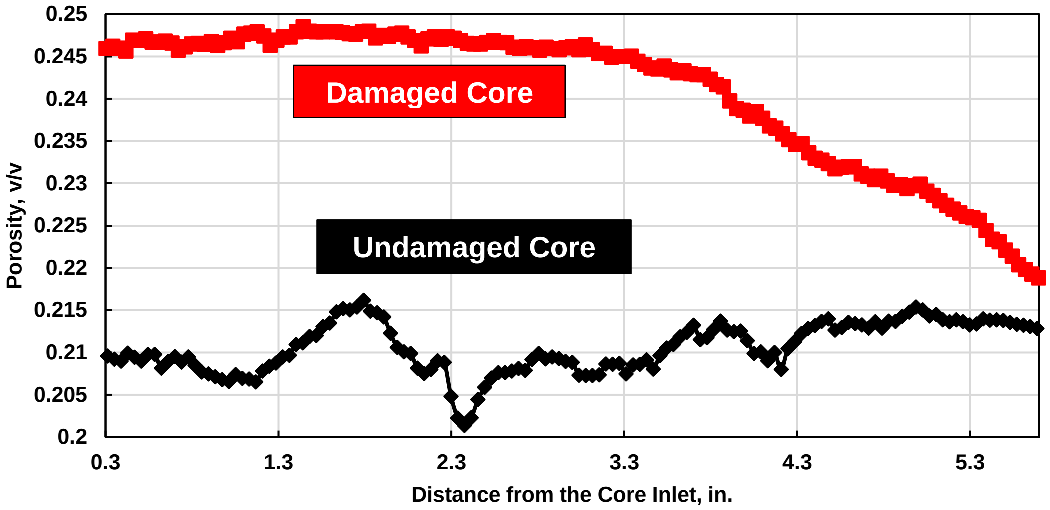

Fig. 39— Change in porosity along the stimulated core at 150˚F in undamaged and fines migration damaged cores.

The same work was repeated at 250˚F to examine the sensitivity of the system to the variation in temperature. The porosity gain of both damaged and undamaged cores declined with the distance from the core inlet, as represented in **Fig. 40**. The decline went from 25 vol% at the core inlet down to 20 vol% at the core outlet. Both dissolution and precipitation were accelerated due to the higher temperature. The porosity profile for the undamaged core can be attributed to the dissolution of dolomite minerals that was followed by deformation of alumino-silicate sheets due to the leaching of iron and aluminum ions by the HCl along the core. This attack on clay minerals mobilized fines migration during acidizing. On the other hand, the steep drop in the porosity gain at the last two inches of the core with fines migration can be described as a localized damage after the HCl attacked the localized fines migration.

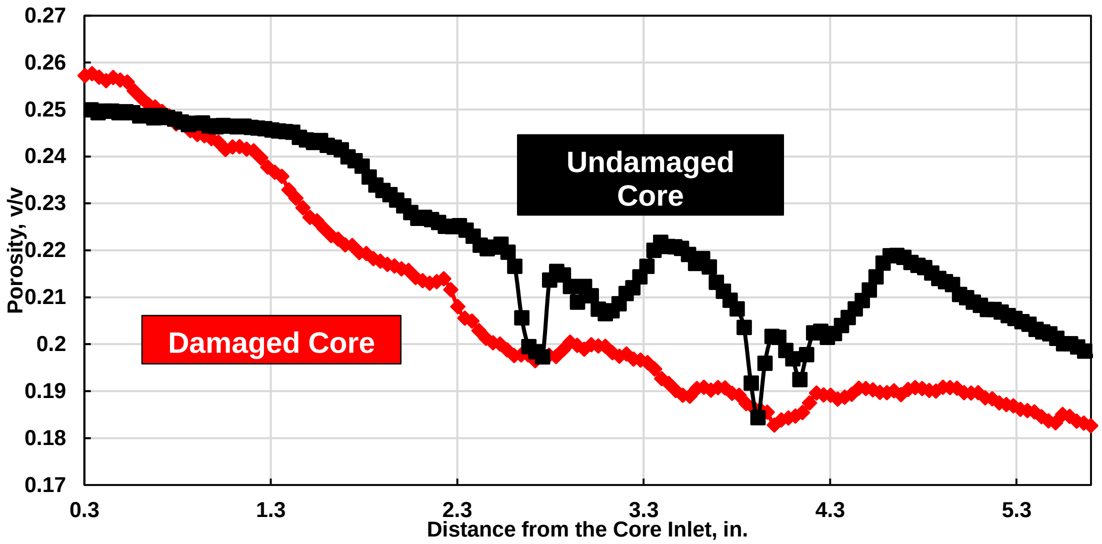

Fig. 40— Change in porosity along the stimulated core at 250˚F in undamaged and fines migration damaged cores.

ICP analysis of the stimulation fluid at 150˚F for the untreated and the damaged cores (**Fig. 41**) showed similar concentrations profiles. The damaged core showed overall lower concentrations for all species of about 15,000 mg/L compared to the undamaged core. Both Ca and Mg relative concentrations were similar to the general trends reported in the literature for dolomite dissolution concentrations. The undamaged core exhibited a higher iron concentration of 30,000 mg/L compared to 25,000 mg/L in the damaged cores. This high iron and aluminum concentrations and the absence of the silicon ion explain the low gain of porosity along the core by the precipitation of silica gel. Although the dolomite dissolution was high, the extent of alumino-silicate deformation due to the HCl attacking the chlorite and illite minerals was strong at each point of the core. On the other hand, the damaged core wider pore size at the inlet lowered the dissolution rate of the dolomite mineral at such moderate temperature. The core inlet gained higher porosity in the first four inches of the core; this could be attributed to the absence of alumino-silicate debris at the inlet section. The localization of the fines toward the core outlet forced the precipitation reaction to be localized toward the outlet. This could be explained by the low iron and aluminum concentrations, which directly correspond to the extent of HCl destruction of the alumino-silicate sheets.

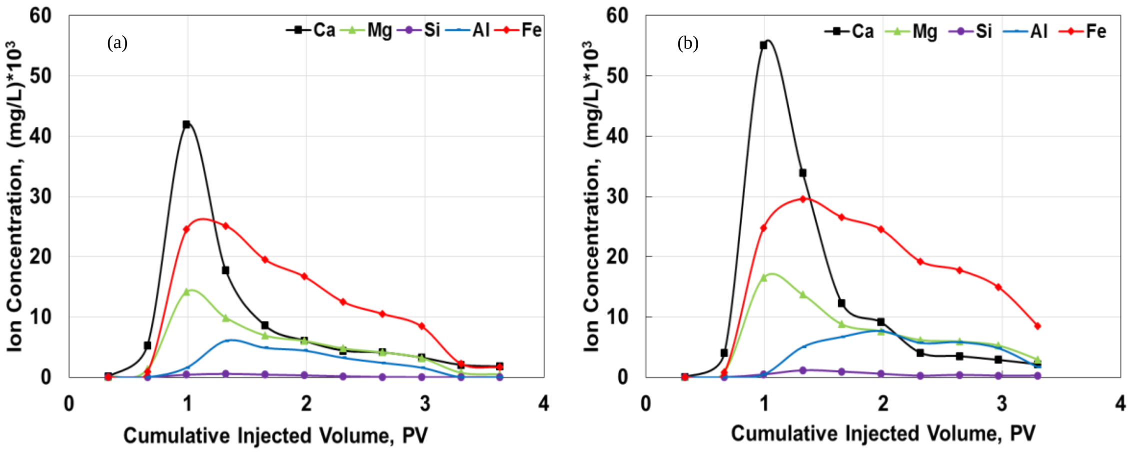

Fig. 41— ICP analysis for stimulation effluent of (a) undamaged core, and (b) damaged core at 150˚F.

The work at 250˚F yielded opposite results to the data reported at 150˚F. The high temperature raised the rate and the extent of both the dissolution and the precipitation reactions (**Fig. 42**). The undamaged core exhibited lower concentrations of all cations of about 20,000 mg/L. Both Ca and Fe exhibited similar concentration profiles. This result shows that the dissolution was of the same magnitude as the precipitation. The porosity gain profile suggested that fines migration was induced after the stimulation began. This assumption can be supported by the matching patterns of Ca and Mg concentrations to the Fe and Al which shows that the HCl was attacking the alumino-silicates at the same time it was dissolving the dolomite. On the other hand, the first four inches of the damaged core were open for dissolution and the extent of precipitations was minimal due to the early clay migration toward the core outlet. Furthermore, both Fe and Al concentration came as a high peak followed by a sharp decay, indicating that the precipitation happened at the damaged section in the last two inches of the core only.

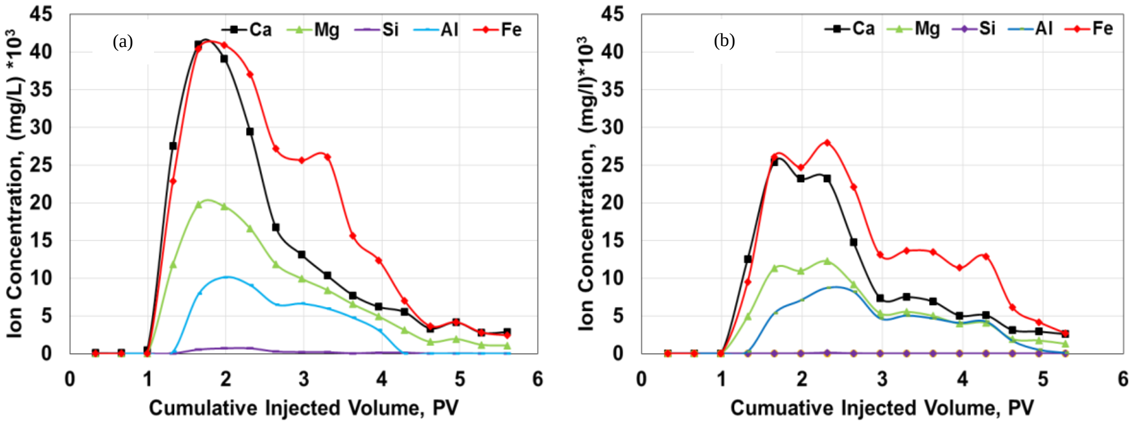

Fig. 42— ICP analysis for stimulation of (a) undamaged core, and (b) damaged core at 250˚F.

Pre-Flush and Mud Acid Impact on Formation Damage

This section was designed around four core floods at 150 and 250˚F. Each temperature was assessed for both the pre-flush stage and the mud acid stage impact on the Bandera sandstone after the induction of fines migration damage. The first two cores were flooded at 3 cm^3/min using 3 PV of a 15 wt% HCl. The second set was pre-flushed as well, then stimulated using a 3 PV of a 12 wt% HCl and 3 wt% HF mud acid at the same temperatures. **Table 9** shows all of the mentioned treatments succeeded to gain back the permeability.

Property	**Pre-flush@150˚F**	**Pre+Mud@150˚F**	**Pre-flush@250˚F**	**Pre+Mud@250˚F**
k_I, md	13.37	13.37	13.28	13.34
Porosity, vol%	19.6	19.42	19.48	19.43
Deionized water injected volume, cm^3	11	11	11	11
Pore Volume, cm^3	34.3	34.1	34.1	34.01
$k_{damaged}$, md	3	2	2	2
$k_{stimulated}$, md	12	7.9	11.3	14.01

Table 9— Petrophysical properties summary.

The pressure drop across each of the cores was recorded and plotted versus the injected pore volumes. The pressure drop trend in the pre-flush stage at 150˚F was similar to the 250˚F. The switch from brine to the pre-flush stage took the pressure drop from 60 psi to 225 psi (**Fig. 43**). This sudden increase is explained by the aggressive reaction at the core inlet. This sudden peak is followed by a drop down to 200 psi. Then, the pressure kept rising to 250 psi during the injection of the first pore volume. During the injection of the rest of the pore volumes, the pressure drop exhibited cycles of pressure drop decrease, indicating dissolution, followed by a sudden sharp increase, indicating precipitation. Such high-pressure drop peaks indicates the severity of precipitation.

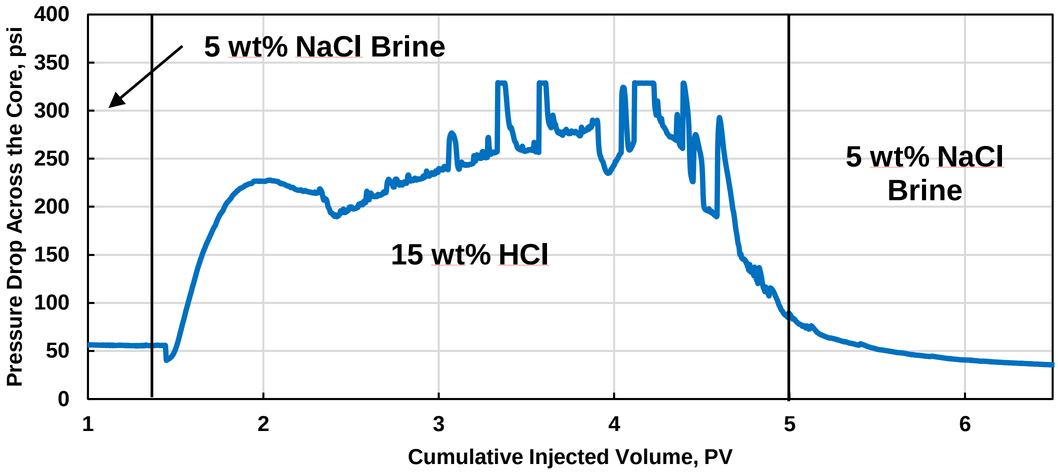

Fig. 43— Pressure drop across the core during pre-flush stage at 250°F after fines migration induction.

Overall, the pre-flush stage showed an enhancement of permeability, increasing from 2 md to 11.3 md. The main mud acid stimulation stage came out with an increase in the pressure drop across the core that reflects the precipitating nature of the alumino-silicate secondary and tertiary reactions in presence of HF (**Fig. 44**). The pressure once again increased from 20 to 40 psi upon the injection of the mud acid. This was followed by a continuous increase up to 70 psi along the injection of the first two pore volumes. The last pore volume showed again a cycle of pressure drop increase and decrease with sharp peaks of 100 and 180 psi. Such pressure drop response reflects a damaging nature for the mud acid stage.

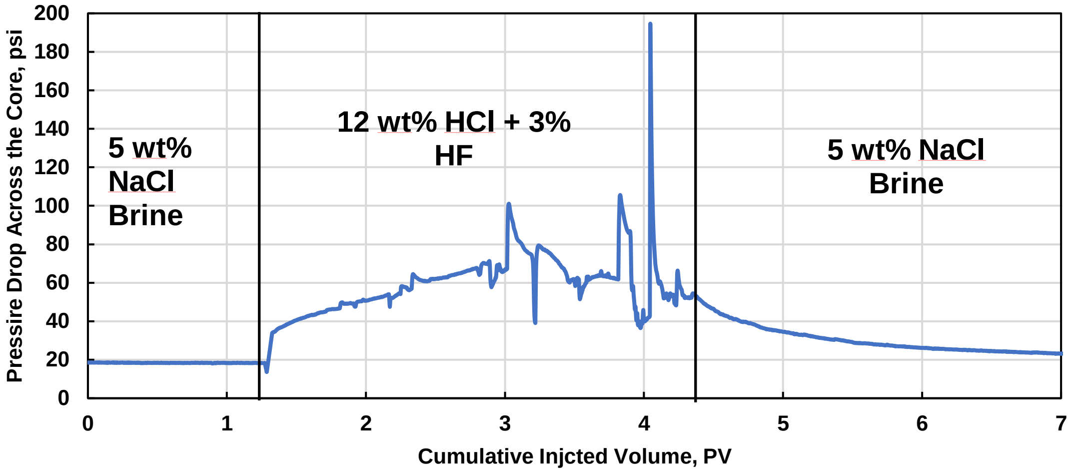

Fig. 44— Pressure drop across the core during mud acid stage at 250°F after fines migration induction.

The effluent of all of four corefloods were analyzed using ICP (**Fig. 45, and Fig. 46**). The pre-flush stage at 150 and 250˚F revealed a similar trend of cations concentrations. Both Ca and Fe ions went up to 22,000 mg/L at 150˚F and raised up to 35,000 mg/L at 250˚F. This similar trend of iron and calcium shows a dissolution of the dolomite followed by precipitation of chlorite deformed structure after leaching the iron. Both Mg and Al ions concentrations came as reported in the literature for typical dolomite dissolution, and the clays reactions with HCl. On the other hand, the mud acid stage results at 250˚F came on the contrary to the 150˚F treatment. While the iron concentration was the highest at 150˚F, the aluminum ion concentration came higher than iron at 20,000 mg/L at 250˚F. The aluminum ion concentration increase can be attributed to the acceleration of the secondary and tertiary reactions of the HF with the illite, kaolinite, and chlorite minerals. Potassium ion was detected in both the 150 and 250˚F effluents. The concentration of potassium ion was higher at 150˚F compared to 250˚F. The appearance of potassium ion indicates that the HF have a more damaging effect to the illite/mica minerals. Leaching of the potassium ion results in deforming the mineral structure and transforming it to a metamorphic structure with reduced order. The silicon ion kept at 0 mg/L along the mud acid stage; this indicates the precipitation of most of the silica in form of silica gel. The ICP data showed that the HF is of detrimental effect in high temperature and the amount of dolomite dissolution is not sufficient to accommodate the silica gel and alumino-silicate deformed structures produced from secondary and tertiary reactions.

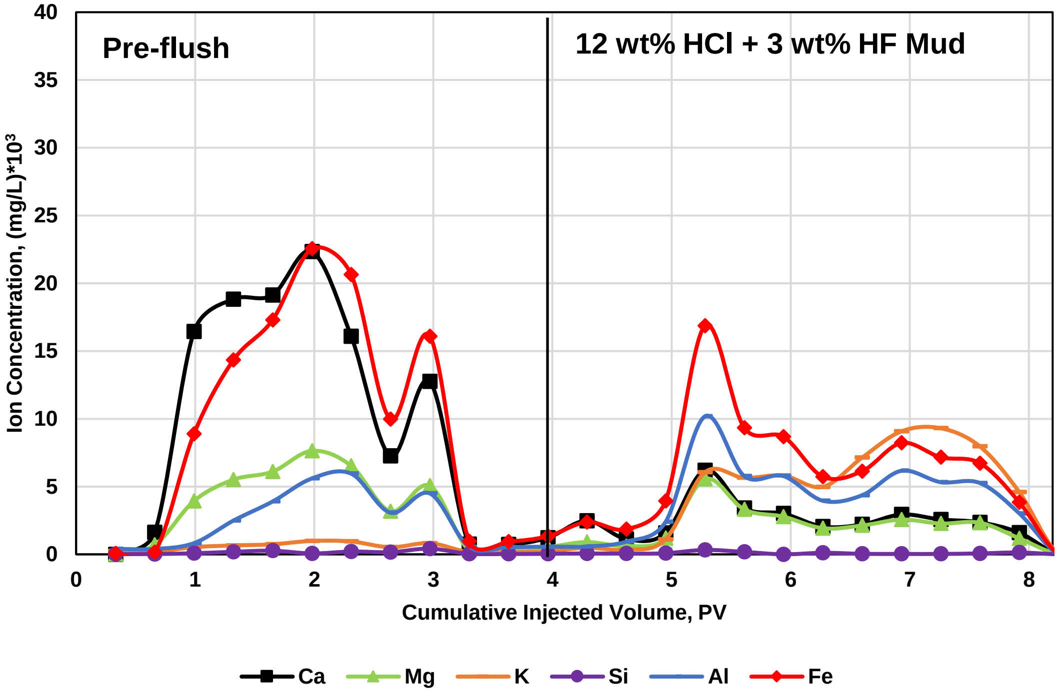

Fig. 45— ICP analysis for the resulting effluent at pre-flush and mud acid stages at 150˚F.

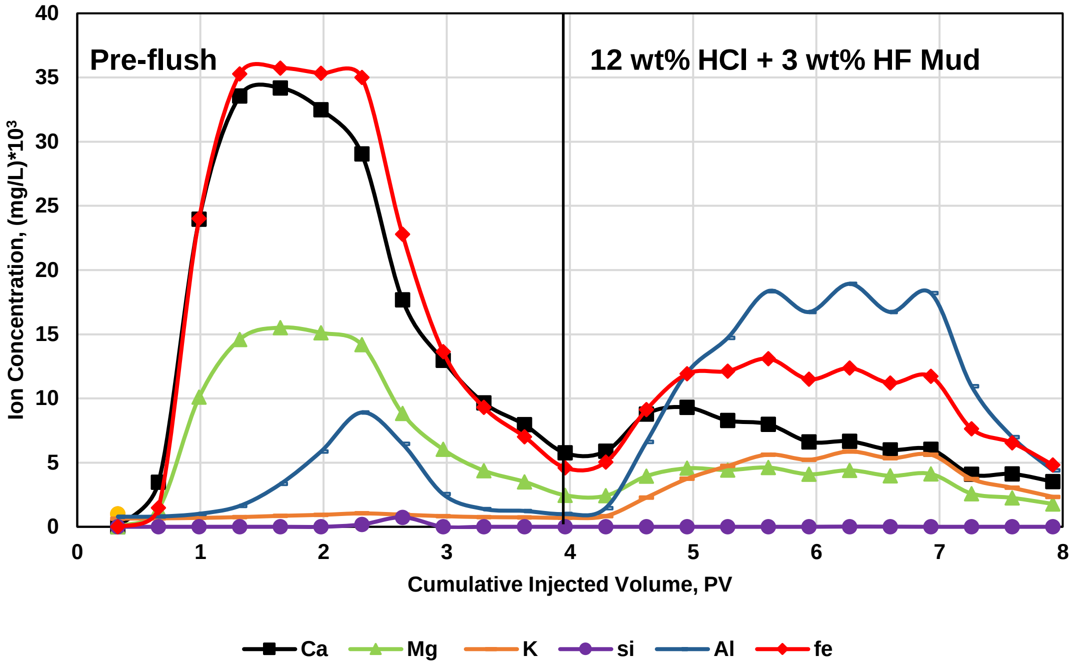

Fig. 46— ICP analysis for the resulting effluent at pre-flush and mud acid stages at 250˚F.

New Technique for Formation Damage Tracking

The combination of the pressure drop and the ICP data highlighted the magnitude of formation damage in the Bandera sandstone, this dictated a need for a full description of the mechanism and an efficient tracking. A CT number histogram for each coreflood was created to show the changes that happen on the level of each pixel. CT scan histogram was coupled with the NMR pore size distribution in order to examine the changes that happen to the pore structure.

The first core treated by the pre-flush at 150˚F showed an enhancement in the permeability after stimulation. Upon examining it using the new processing technique the reaction was shown to be of devastating impact on the core outlet. The data shown in **Fig. 47** suggest an efficient dissolution increasing the porosity from 19 to 35% in the inlet section. This was interpreted from the first slice CT number frequency drop from $2*10^6$

down to 1.2*10^6. The profile of CT number distribution shows that the pore structure is uniform with high porosity. The slices 2, 3, and 4 representing three inches in the middle of the core showed a deterioration in the porosity.

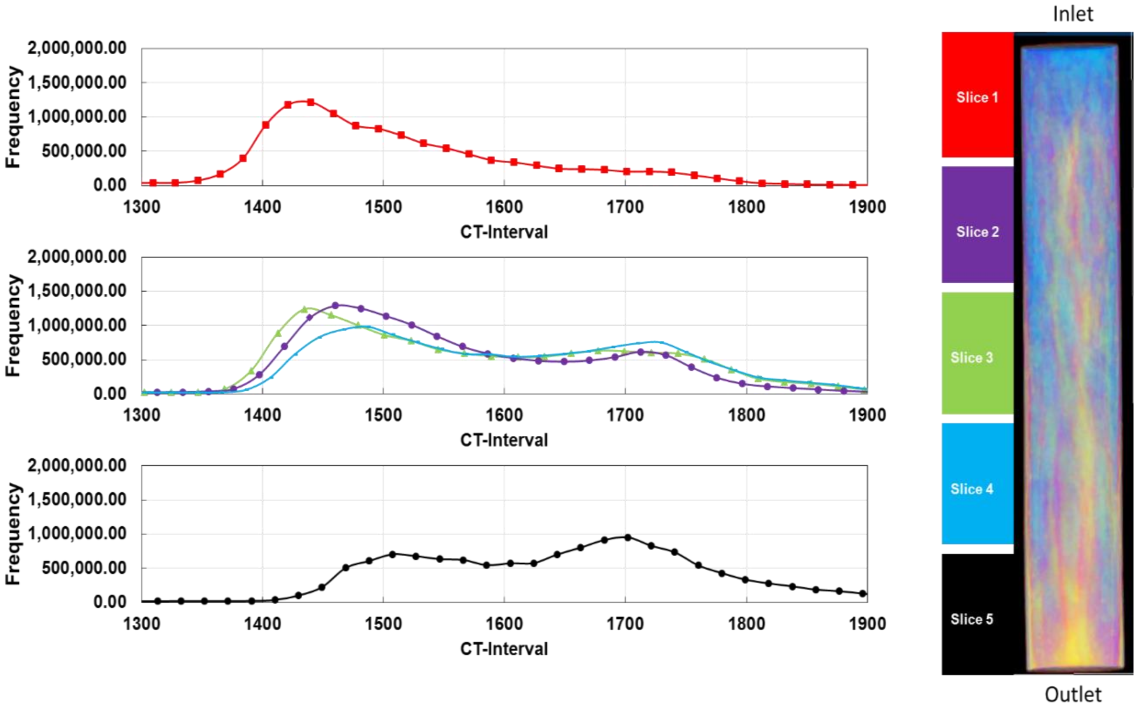

Fig. 47— CT-number histogram for each inch along the core for pre-flush stage at 150˚F.

The presence of two peaks one between CT numbers 1400 and 1500 and the other between CT numbers 1650 and 1750, suggest a change in the pore structure. The total porosity change from 19 to 28% is a resultant of the combination of two porosity ranges in the same slice. These two zones are reflected in the CT number 3D graphical representation showing a wide porosity channel on the sides of the cores with a blocked section in the middle of the core. The last slice of the core showed a relatively lower increase in porosity from 19 to 26 %. This can be interpreted from the presence of a dual CT number peaks. This time the 1750 CT number which reflects lower porosity is the one with higher frequency of 1.1*10^6. The 1500 CT number frequency decreased from 1.2*10^6

to 0.65*10^6. Furthermore, the graphical representation showed a severe damage in the last slice. Although the porosity change along the core was positive explaining the permeability gain, the damage was increasing along the pass of the induced fines migration. The pore size distribution (**Fig. 48**) came out showing the same results reported form the CT data. The uniform pore structure at 3 µm was slightly shifted at each section. The core inlet showed a wider dominant pore-size frequency. The core outlet witnessed a reduction in the dominant pore size. The mid-section was kept balanced between the inlet and the outlet.

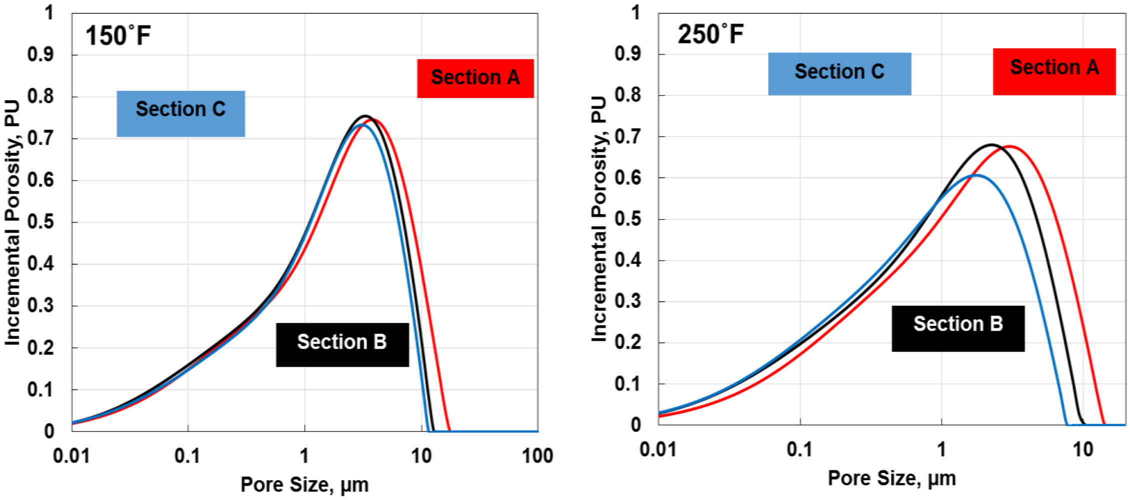

Fig. 48— NMR pore-size distribution comparison for pre-flush stage at 150 versus 250˚F.

The second core at 150˚F was subjected to the same pre-flush condition, then followed by three pore volumes of mud acid. The data shown in **Fig. 49** highlighted a damaging effect for the mud acid stage. The core inlet kept its high porosity gain with CT number of 1450 as a single peak. The mid-section sustained higher magnitude of damage. The second peak, representing the lower porosity section, became clearer and its frequency went up to the 1*10^6. Moreover, the slice number four peak at CT 1450 went down to

$1*10^6$ compared to both slice 2 and 3 at $1.5*10^6$. Finally, the outlet slice showed a complete domination of the CT number of 1750 and the decay of the 1450 CT number to a flat trend at frequency $0.4*10^6$. This data was reflected in the graphical representation, showing a deeper and more intense damage. The porosity gain from dolomite dissolution along the core was suppressed by the secondary and tertiary reaction products.

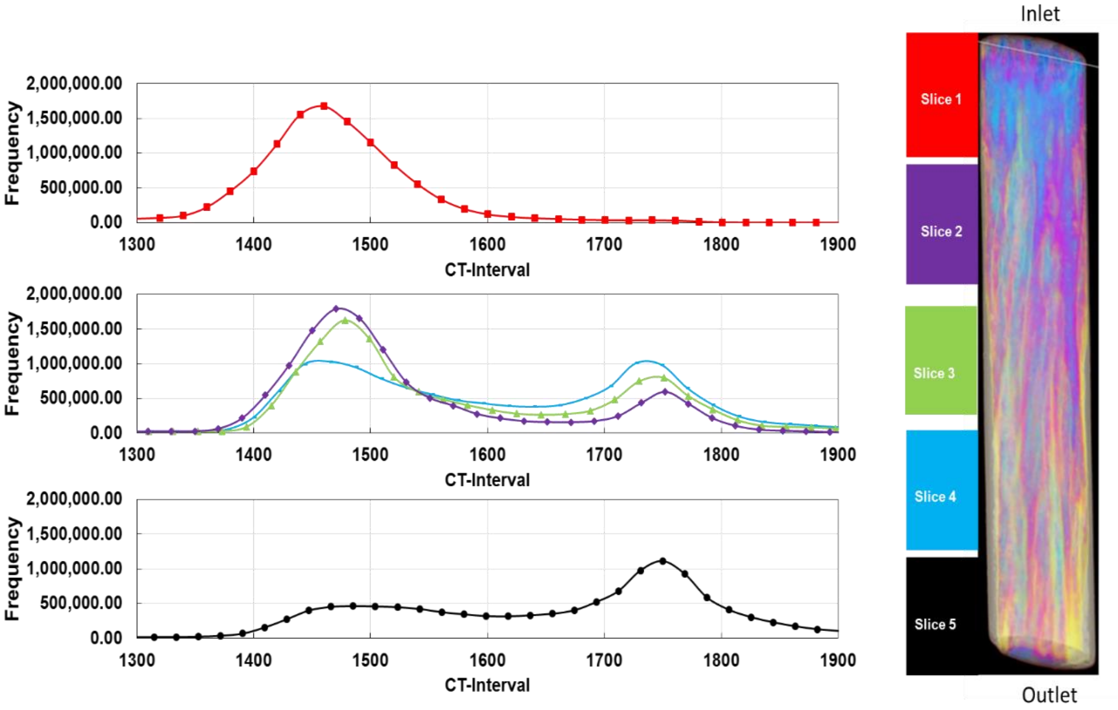

Fig. 49— CT-number histogram for each inch along the core for mud acid stage at 150˚F.

Again the NMR pore size distribution (**Fig. 50**) came out proving and supporting the new CT scan data. The inlet section dominant pore size went up to 5 µm with incremental porosity 0.91%. On the other hand, the middle section went down to 3.5 µm with an incremental porosity 0.79%; which shows an increase in the frequency of the smaller pore sizes predicted from the CT histogram data. Finally, the outlet pore size and its frequency went down to 3 µm and incremental porosity 0.74%. Both mid and outlet sections showed an increase of the incremental porosity coming from the pore-size range between 0.01 to 2 µm. This data could be used to support the idea of restructuring the pore throat. The dissolution followed by the precipitation creates a genuine pore-size distribution.

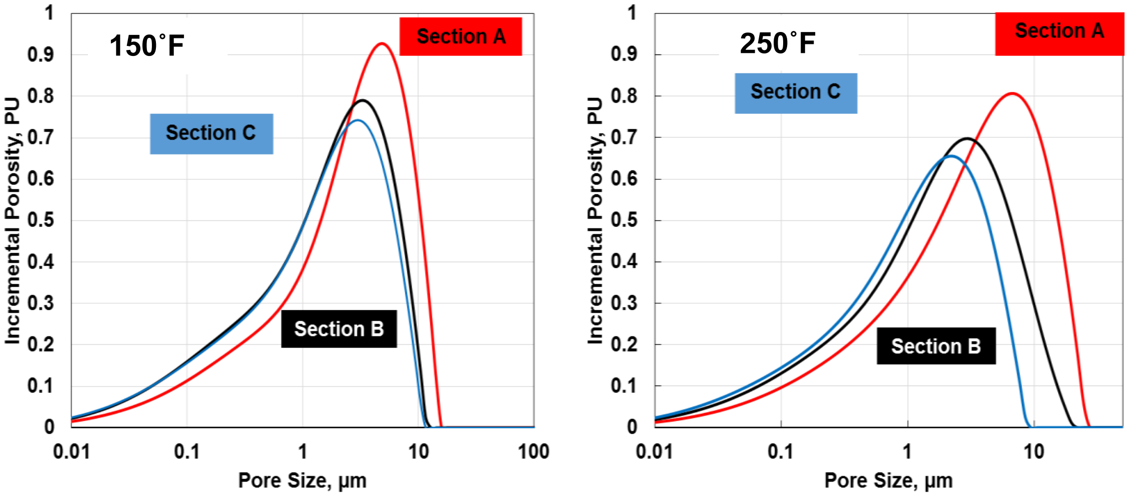

Fig. 50— NMR pore-size distribution comparison for mud acid stage at 150 versus 250˚F.

The data, from both the pre-flush and the mud acid stages at 250˚F, proved that temperature increase magnified the impact of secondary and tertiary reactions. The CT histogram of the pre-flush shown in **Fig. 51** suggests that the higher temperature dissolved more dolomite as the dominant CT number went down from 1450 to 1280. Yet, the precipitation resulting from clays interaction with HCl was prevailing in the core inlet by the lower frequency of the dominant peak. The presence of another peak at CT number 1700 also shows the impact of precipitation in the inlet. The mid-section sustained more damage, the peak between CT number 1600 and 1700 was dominating the histogram at a frequency of $0.65*10^6$. Also, the dissolution efficiency went down as shown in the peak shift from 1200 in the inlet to 1400 at the middle sections. The outlet came out clearly damaged with a singular peak at CT number 1650 of frequency $0.7*10^6$. The pore-size distribution (Fig. 48) came out similar again with the same response from the CT histogram analysis. Upon the comparison between the pre-flush stages at 150 and 250˚F, the pore size distribution variation is severe in the higher temperatures.

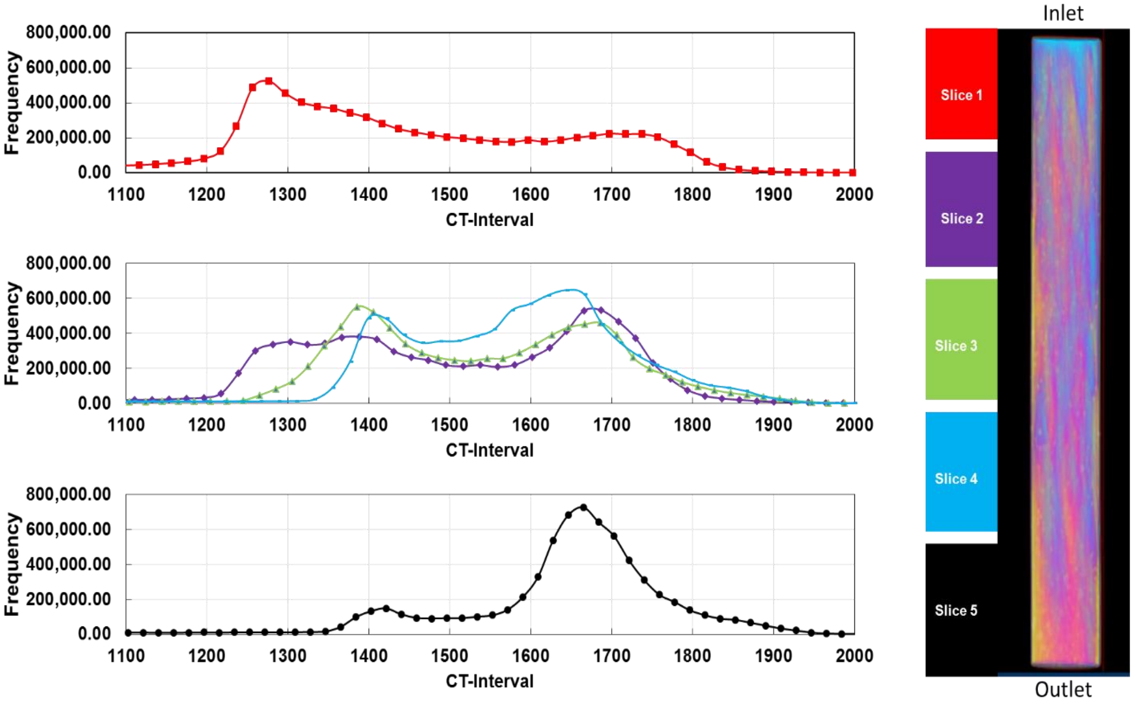

Fig. 51— CT-number histogram for each inch along the core for pre-flush stage at 250˚F.

The final coreflood was a pre-flush followed by mud acid at 250˚F. The data in **Fig. 52** shows that HF presence in higher temperature caused more damage. The inlet showed a clear damage peak at CT number 1700. The mid-section showed a decrease of the CT number 1400 frequency from $0.5*10^6$ to $0.4*10^6$ which shows less dissolution and more precipitation. The outlet again came out completely damaged with a single peak at CT number 1700. The NMR data (Fig. 50) showed how severe the pore size distribution at the outlet is impacted by the precipitation. Also, it shows that the inlet is less impacted and more open pores are still viable but the mid-section is as damaged as the outlet.

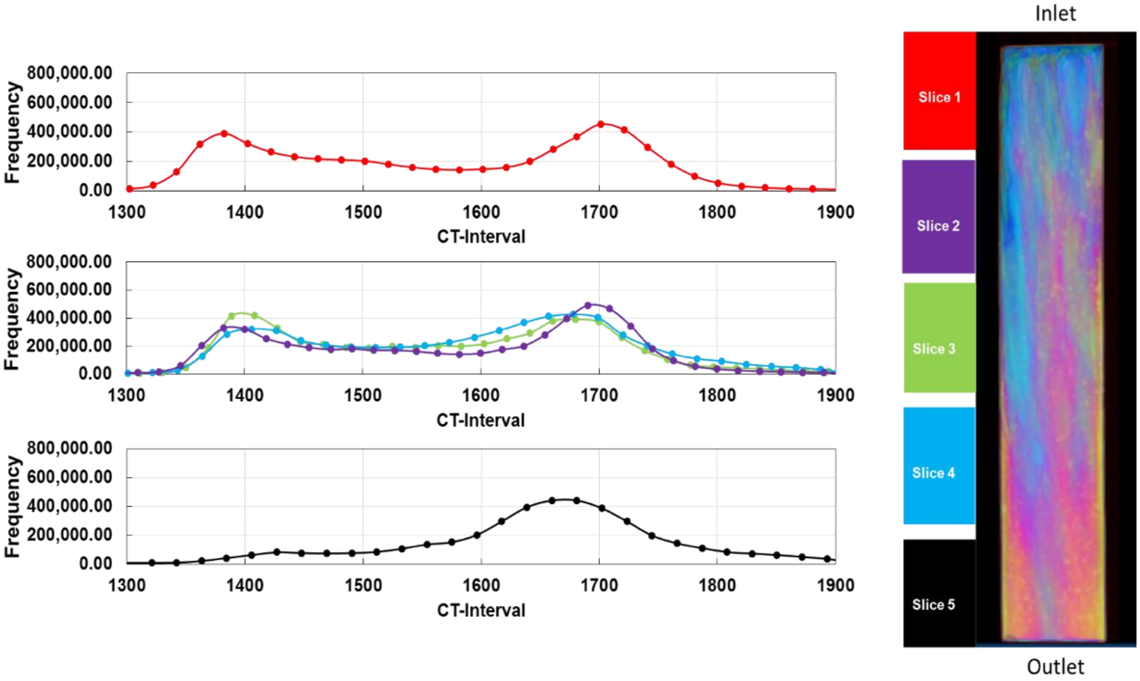

Fig. 52— CT-number histogram for each inch along the core for mud acid stage at 250˚F.

XRF Analysis

The mud acid stimulated cores were sliced into 1.1 in. long sections. Each was scanned using XRF, where the elemental analysis distribution was plotted along the core depth. The first data set shown in **Fig. 53** compared the concentrations of Na ions in the cores stimulated after different brines injection. Both cores showed a 5 wt% Na ion concentration after the mud acid injection, which comes from the albite mineral in the core. This result suggests that although mud acid was injected in presence of NaCl brine, its interaction with the mud acid by products such as fluosilicic acid was not sufficient to precipitate sodium hexafluorosilicates.

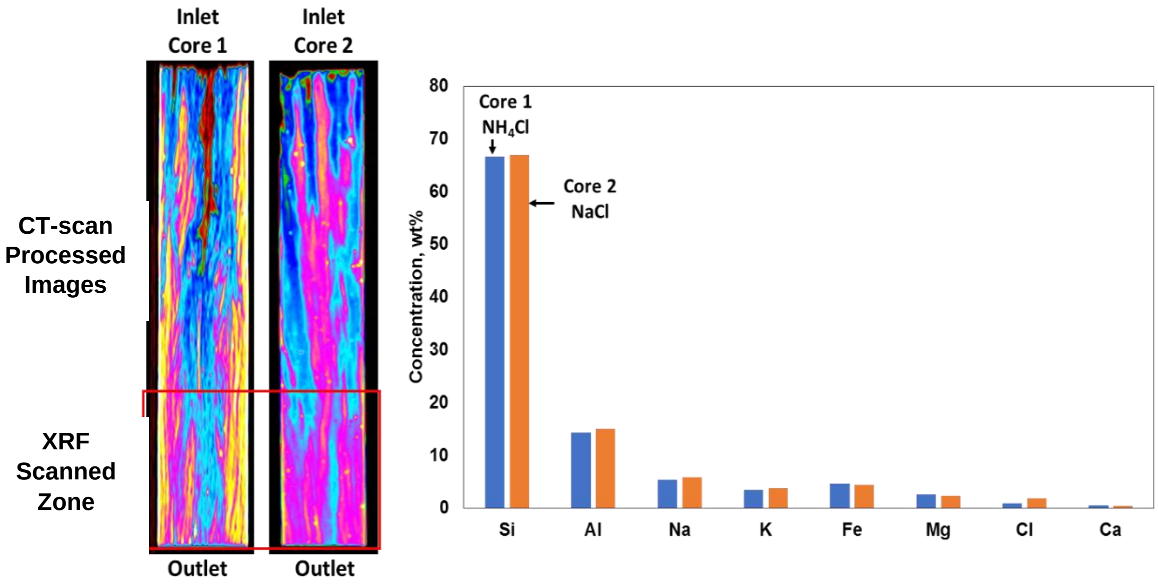

Fig. 53— XRF analysis for the outlet sections in 2 cores treated as follows: (1) flooded with 5 wt% NaCl, followed by deionized water, 5 wt% NaCl brine, 15 wt% HCl, 5 wt% NH_4Cl brine, and mud acid at 250˚F. (2) Flooded with 5 wt% NaCl, followed by deionized water, 5 wt% NaCl brine, 15 wt% HCl, 5 wt% NaCl brine, and mud acid at 250˚F.

The second part of this analysis tracked the elemental analysis along the core flushed with NH_4Cl before the mud acid stage to describe the nature of the detected formation damage in the CT scans. The data shown in **Fig. 54** shows that the concentration of Si have raised from 59 wt% to 80 wt% at the core inlet, then decreased along the core depth until it reached 65 wt% at the core outlet. This increase is attributed to the dissolution of Ca, Mg, Al, Fe, and K ions from the inlet during the HCl and the mud acid stages. On the other hand, the concentrations of those elements increased along the core depth. These results suggest that although the mud acid succeeded in dissolving Al, Fe, and K ions from the inlet, the secondary and tertiary reactions took place and they precipitated deeper in the core in the form of aluminum fluoride, iron compounds, and potassium hexafluorosilicates. This behavior can explain the increasing damage detected by the CT/NMR analysis along the core.

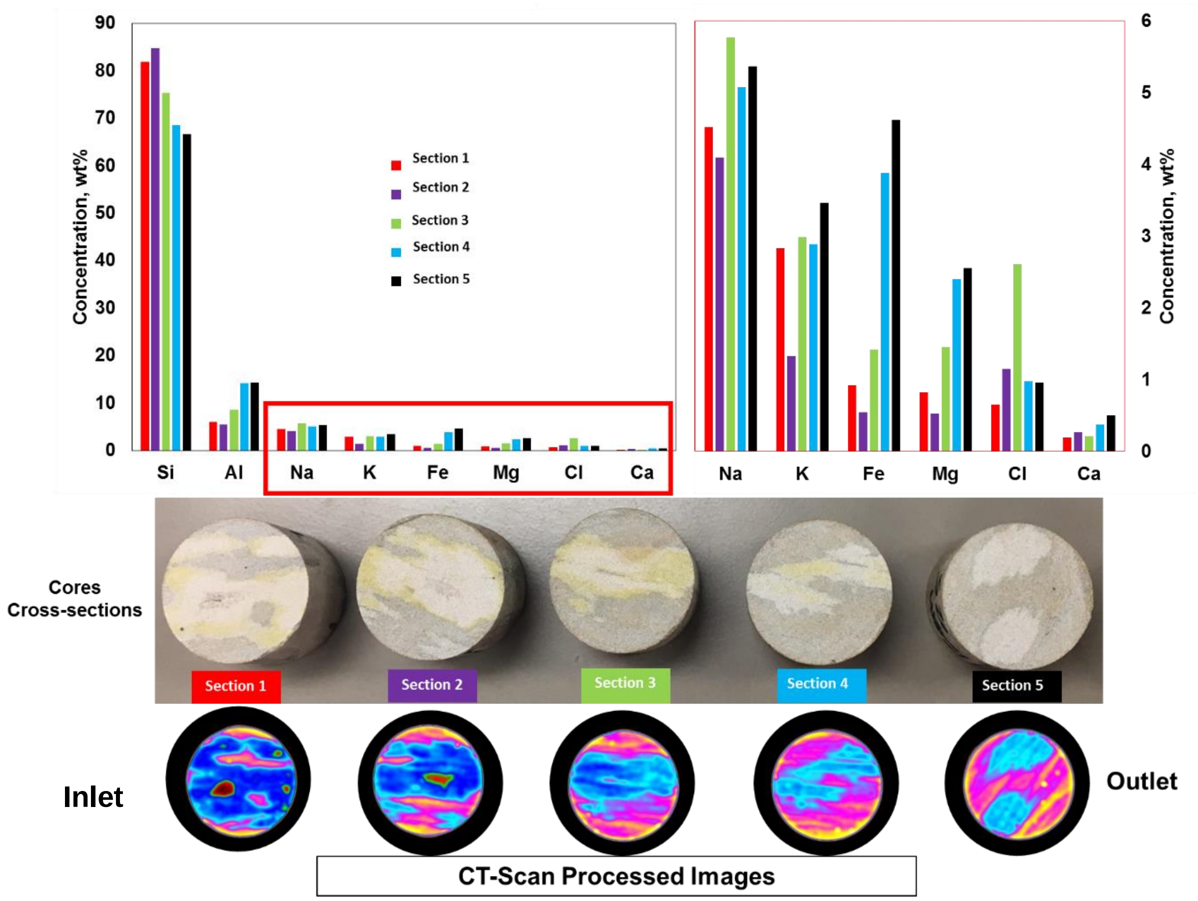

Fig. 54— XRF elemental analysis along a core stimulated as follows: saturated with 5 wt% NaCl brine, followed by deionized water, 5 wt% NaCl brine, 15 wt% HCl, 5 wt% NH_4Cl brine, and mud acid at 250˚F.

SEM Pore Structure Analysis

The interpretations from the CT histograms, the NMR pore size distribution, and the XRF analysis suggested the deposition of silica gel, aluminum fluoride, potassium hexafluorosilicates, and iron compounds in the dissolved dolomite pore space.

These changes in the pore structure was validated by slicing a cross section from one of the 15 wt% HCl stimulated cores and examining it under the SEM. The cross-section was determined based on the processed images from the CT analysis (**FIG. 55**). The right-hand side of the cross section represented the areas were formation damage was detected, while the left-hand side represented the section with successful dissolution and minimal damage. The SEM examination (Fig. 55) for the undamaged section showed quartz particles in granular form with large distinctive grain to grain spacing. Furthermore, the chemistry of the surface was studied using EDS and the silicon ion was mapped across the image field. The mapping showed that the silicon ion is scattered across the image field in moderate concentrations that comply with the mineralogical analysis of the Bandera sandstone. On the other hand, the damaged section showed an amorphous surface that resemble the silica gel morphology (Thomas et al. 2001). The surface exhibited high compaction with no distinctive grain to grain spacing. The silicon ion mapping also showed an intense presence across the image field showing the deposition of silica gel in between the dissolved pore structure. Other ions such as calcium and magnesium were below detection limit of the machine, which is interpreted by the dissolution of the dolomite minerals in both of the damaged and the stimulated sections.

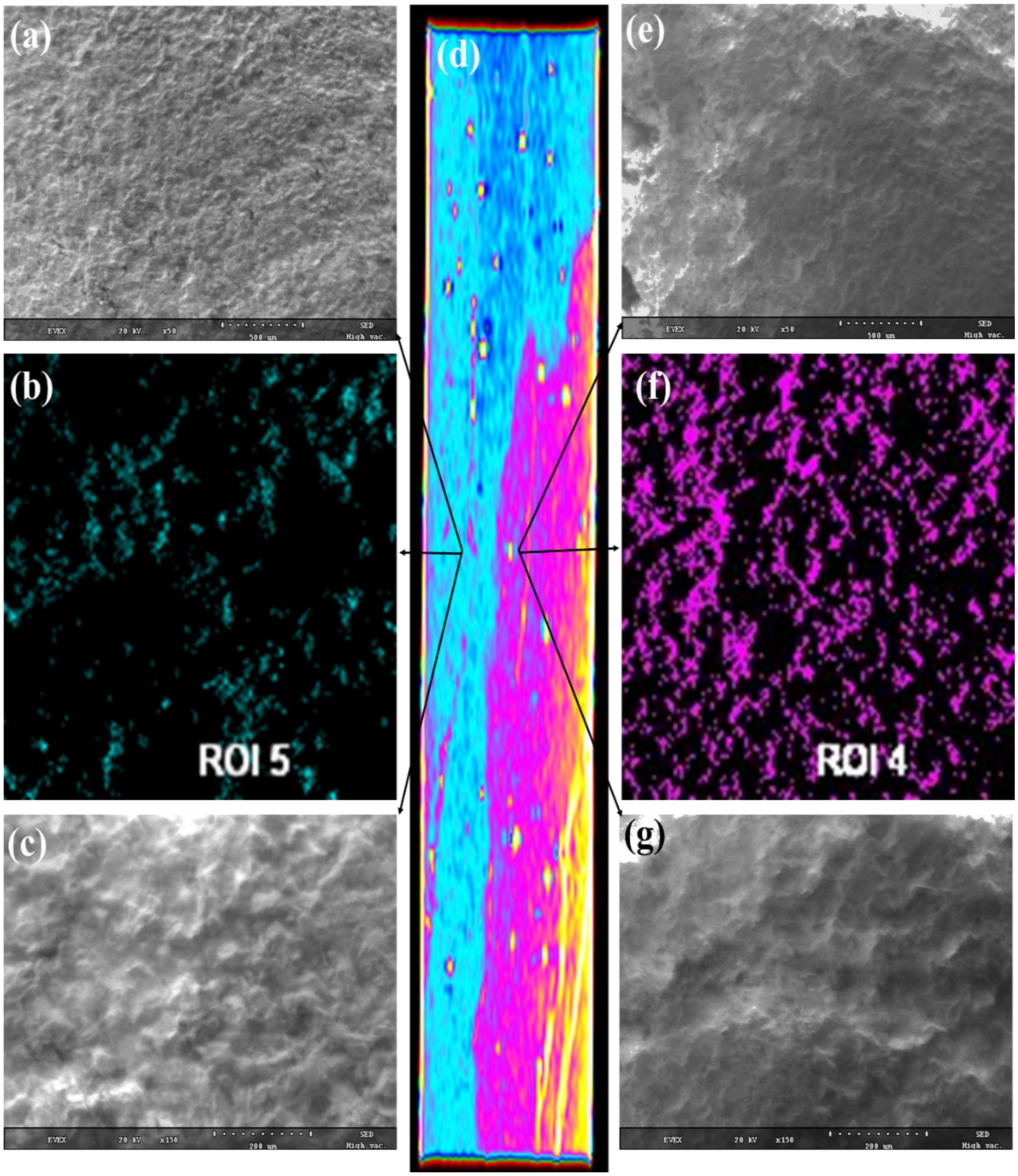

Fig. 55— SEM analysis for the stimulated and damaged sections for the 15 wt% HCl stimulated Bandera sandstone core at 150˚F, the core is flooded with 5 wt% NH$_4$Cl, deionized water, and 5 wt% NH4Cl brine before the acid stage. (a): An image field for the stimulated section showing the granular nature of the surface. (b): A representation of the silicon ion distribution on the stimulated surface. (c): A subfield of (a) showing the granular nature of the quartz particle. (d) A processed image for the Bandera sandstone core after stimulation showing stimulated and damaged sections. (e): An image field for the damaged section showing the amorphous nature of the silica compounds. (f): A representation of the Si ion distribution on the image field (e). (g): A subfield of (e) showing the absence of un-deformed quartz particles and absence of distinctive grain to grain spacing.

The second part of this analysis studied the mud acid stimulated core. The data shown in **Fig. 56** shows a cross-section from the outlet side of the core treated at 250˚F.

The initial optical examination of the section showed a light grey areas in between darker grey areas, which upon comparison to the CT scan processed image the light areas are defined as the low CT number areas, while the dark areas are the high CT number areas. The SEM analysis showed that the light areas are of distinctive wide pores and less deformed quartz particles. The darker areas showed amorphous surface that can be attributed to the precipitation of silica gel, aluminum fluoride, and/or potassium hexafluorosilicates. It also showed low number of tight pores on the surface.

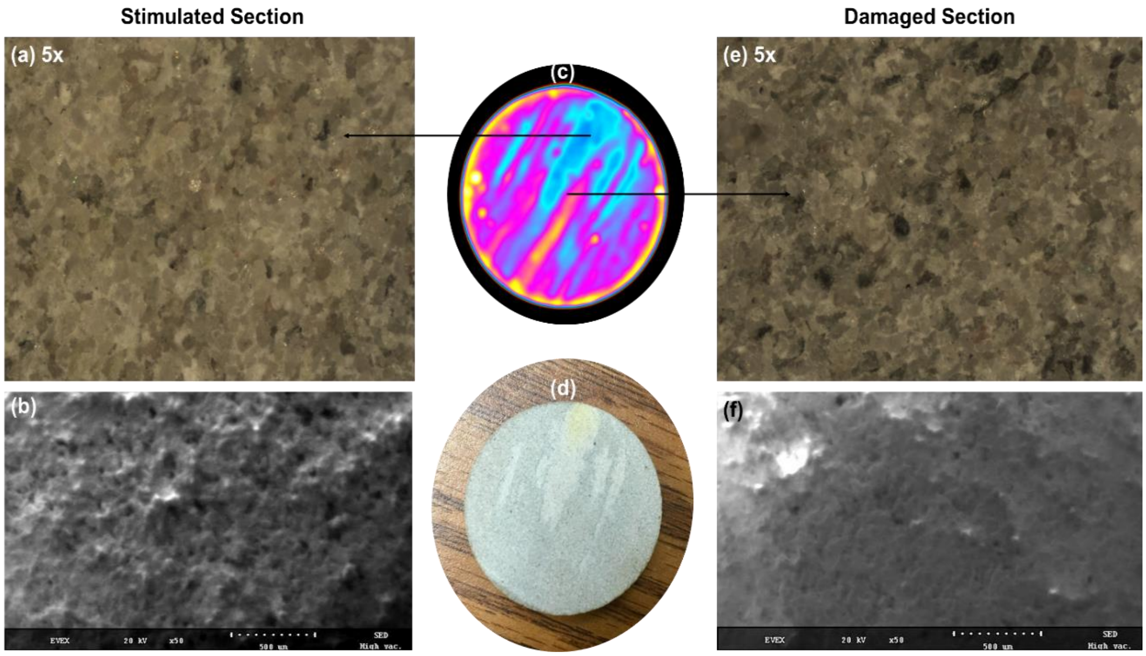

Fig. 56— SEM analysis for the stimulated and damaged sections for the 15 wt% HCl, 5 wt% NaCl brine, and Mud acid stimulated Bandera sandstone core at 250˚F. (a): An image field at 5x using optical microscope for the stimulated section (b): An image field for the stimulated section using SEM showing the granular nature of the surface and the abundance of pores. (c) A CT-processed image for the Bandera sandstone core after stimulation showing stimulated and damaged sections. (d) Optical Image for the core section. (e): An image field at 5x using optical microscope for the damaged section. (f): An image field for the damaged section using SEM showing the amorphous nature of the precipitating compounds and the scarcity of pores.

Conclusions

Key findings from this study leads to the following conclusions:

1. The smaller the cation and the higher its charge density the better and the prolonged the brine inhibition for incompatible fluids.

2. Fines migration induction using deionized water is detectable using CT scan average porosity technique.
3. The chemical mobilization of the clay minerals generated larger pore size in the core inlet, and plugged the core outlet.
4. The stimulation in presence of fines migration localizes the damage in the core outlet were the fines was present.
5. The stimulation process out comes in damaged and the undamaged cores are highly depending on temperature.
6. Stimulation at a temperature higher than 250˚F can lead to fines migration during the stimulation.
7. Pre-flush stage alone is capable of regaining the permeability of the Bandera sandstone formation.
8. The mud acid tends to precipitate secondary and tertiary reaction products by attacking all clay minerals present in the formation.
9. The novel processing technique for CT scan data proved to be able to detect and describe the formation damage process during stimulation.
10. The Bandera sandstone high dolomite content and high clay content result in dissolution along the core followed by restructuring the pore throats due to the precipitation of clay deformed alumino-silicates structures from both HCl, and HF interactions with clay minerals.

This work adds further insight on how HCl and HF interact with Bandera sandstone. The study shows the sensitivity of clay to pre-flush and mud acid stages. It accounts for the impact of the temperature on the way the acid reacts with the different minerals in sandstone. It confirms that fines migration affects sandstone porosity and is dependent on the mineralogical composition and the formation temperature. Finally, it introduces a new approach to study sandstone with better utilization of the CT scan data. This research helps layout and build a decision tree for the design of more successful acidizing treatments.

CHAPTER IV

NMR STUDY TO ASSESS FINES MIGRATION DAMAGE AND ITS REMOVAL USING REGULAR MUD ACID IN DIFFERENT SANDSTONE CORES[6]

Summary

The highly sensitive clay presence in both Berea and Kentucky sandstone during various stimulation operations makes them some critical formations when fines migration is addressed. Berea sandstone at 1% total clay content, although its low percentage it is proven to be determinate with double and quadruple permeability reduction upon fresh water exposure. Regular mud acid is known for its dissolving power of the alumino silicate minerals, yet the secondary and tertiary reaction still cast a damaging potential on the sandstone formation especially in presence of fines migration. This work aims to understand how those fines migration interacts with conventional HCl pre-flush and regular mud acid treatment in the Berea sandstone. Also, the impact of the hydrofluoric acid aided with formic acid preflush was examined to assess the clay content on the stimulation outcomes.

This work based on nuclear magnetic resonance (NMR) analysis; it was designed to understand experimentally the fundamentals of fines migration process and further investigate its behavior during acidizing process. Core flood test was conducted on 6 in. by 1.5 in. cores and fresh water was injected at 3 cm^3/min to induce fines migration. In

---

[6] Reprinted with permission from "NMR Study to Assess Fines Migration Damage and Its Removal Using Regular Mud Acid in Different Sandstone Cores" by Hanafy, A. M., Nasr-El-Din, H. A. 2016. Presented at the Abu Dhabi International Petroleum Exhibition & Conference, 7-10 November, Abu Dhabi, UAE, copyright 2016 by the Society of Petroleum Engineers. Reproduced with permission of SPE. Further reproduction prohibited without permission.

total three core flood tests were conducted after the cores were damaged by fines migration and at temperatures of 150 and 250°F. All cores were subjected to a 12 wt% HCl preflush followed by regular mud acid at a flow rate 3 cm^3/min. Each core was scanned using NMR, and computed tomography (CT-scan) to assess the fines migration quantity and distribution mechanism before and after their induction; and once more scanned after acidizing process. All of this work was repeated for cores from Kentucky sandstone to investigate the sensitivity to the clay content.

The acidizing process in presence of fines migration was proven to be temperature sensitive. The NMR analysis showed one order of magnitude reduction in the dominant pore size in the last two inches of the core at 150°F for Berea sandstone. At the higher temperature of 250°F the damage was clearer in the last four inches of the core. The CT-scan analysis followed the NMR analysis showing the same pattern in terms of porosity gain percentage that was higher at 150 compared to 250°F. The mud acid failed to dissolve the fines and the damage persist and resulted in a drop in permeability, total porosity, and tighter pore size distribution. On the other hand, although Kentucky formation exhibited high clay content the extent of damage was minor after acidizing in presence of fines migration.

In the end this work will add a further insight on the effect of clay content and nature on the acidizing process in both Berea and Kentucky sandstone. The NMR study showed how fines migration moves in the damaged cores. Furthermore, it will localize and quantify their damage and impact on stimulated formations. Finally, the work will add clearer understanding to how fines migration reacts with the pre-flush and regular mud acid.

Introduction

One important gap in the literature of formation damage evaluation is the application of field developed measurements to lab scale studies. Literature have proved the importance of total and effective porosity profiles derived from NMR tools rather than relying on Darcy's equation in terms of permeability changes. The mineralogical influence on porosity studies is another factor that should be eliminated when analysis is conducted with tools such as computed tomography analysis. Pore size distribution from NMR relaxation time was proved in the field to be more reliable when compared with gamma analysis (Coates et al. 1997).

The objective of this work is how the fines migration interact with acids, and where does the resulting damage is localized in the treated zone. The impact of the composition of the acid formula and how it interacts with the clay content impacting the resultant pore size distribution is assessed using NMR analysis. And finally the assessment of the temperature sensitivity and how it alters the outcomes of the process.

Experimental Studies

NMR Laboratory Measurements

NMR measurements were carried to assess the impact of inducing fines migration followed by acid stimulation on the treated core pore-size distribution in the Grey Berea and Kentucky sandstone. NMR measurements were performed using a 2 MHz NMR benchtop spectrometer, GeoSpec2 Core Analyzer (Mark of Oxford Instruments). Samples were saturated in two stages. First the cores were immersed in brine under vacuum in a vacuum saturation cell. This is followed by core flooding under 1000 psi overburden pressure and 500 psi back pressure to ensure full saturation. Car-Purcell-Meiboom-Gill (CPMG) pulse sequence was used to measure the T2 relaxation measurements. The work was conducted at echo spacing time of 200 µs and a target signal-to-noise ratio (SNR) of 200, while the number of scans was set to 48. The resulting data was corrected to produce the pore size distribution as a function of relaxation time based on correction factors of the core matrix and the brine properties according to Eq. 5.

$$\left(\frac{V}{S}\right) = \rho_2\left(\frac{1}{T_2} - \frac{1}{T_{2\,bulk}}\right) \quad . \quad \ldots\ldots\ldots\ldots\ldots\ldots\ldots\ldots\ldots\ldots\ldots\ldots \quad (5)$$

The $\frac{V}{S}$ is the fluid volume to the surface area of the grain representing the pore size in µm, ρ_2 is the relaxing strength of the grain surface, which is function of the rock minerology, T_2 is the total relaxation time in ms, and $T_{2\,bulk}$ is the function of the fluid filling the pores relaxation time (Kenyon et al. 1989).

Materials

The regular mud acid was clay stabilized by addition of ammonium chloride 5 wt%. Further on the HF was prepared from ammonium difluoride in HCl to produce a final acid concentration of 9 wt% HCl, and 3 wt% HF. Commercial corrosion inhibitor was added with loading 10 gpt in addition to 3 wt% formic acid as a corrosion inhibition intensifier. The fines migration was triggered by the injection of deionized water of resistivity of 18.2 MΩ.cm. All the treatments were conducted on 6 in. long by 1.5 in. diameter outcrop cores with initial properties shown in **Table 10**.

Core	Number of cores	Permeability, md	Porosity, vol%
GB1	2	80	19.7
GB2	2	110	17.5
Kentucky	3	0.3	15

Table 10— Permeability and porosity of the cores used in the study.

The mineral composition of each sandstone formation is listed in **Table 11**. All chemicals were American grade; the cores and the chemicals in this study was acquired from a local supplier.

Mineral, wt%	Berea	Kentucky
Quartz	87	66
Calcite	2	0
Dolomite	1	0
Illite	1	14
Chlorite	2	0
Kaolinite	4	Trace
Potassium feldspar	3	3
Plagioclase	0	12

Table 11— Mineralogical composition of Berea and Kentucky sandstone.

Methods

This work is mainly based on coreflooding followed by NMR analysis. First, all cores were saturated using 5 wt% ammonium chloride and permeability was determined by injecting the brine at different flow rates and applying Darcy’s equation. This was conducted at 1000 psi back pressure and 2000 psi overburden. All cores were scanned before and after saturation using computed tomography scanner (CT scanner) to produce porosity profile of the original cores; Toshiba Aquilion RXL scanner was used and the data was processed using Image-J software with a resolution of 0.5 mm. Then all cores were saturated by brine and scanned under NMR to determine the initial pore size distribution. This was followed by injecting deionized water using the coreflood setup at the same pressure conditions and at room temperature to induce fines migration at selected cores. The cores once again were examined under the NMR and the CT-scanner in order to measure the new pore size distribution and the porosity profile of the damaged cores. The effluent from the coreflood step was examined under the scan electron microscope to determine the nature of the produced fine particles.

In the second phase both Grey Berea and Kentucky cores were acidized at 150 and 250°F in order to assess the nature of the acidizing process in presence of fines migration and its temperature sensitivity. The acidizing process was designed of preflush using a 12 wt% HCl acid controlled by corrosion inhibitor, this stage to avoid secondary reaction with the calcite content in Grey Berea cores which is 3 wt% of the total mineralogy composition. This step was replaced by pumping 9 wt% formic acid in Kentucky cores due to the absence of calcite mineral and the sensitivity of the high clay content to HCl. Then both set of cores were acidized using regular mud acid formula. The Grey Berea cores was acidized at flow rate of 3 cm3/min while Kentucky cores were acidized at 1 cm3/min. This low flow rate was selected because of the low permeability of the Kentucky cores and the corresponding high pressure drop at higher flow rates.

After the acidizing process the cores were scanned one last time using the NMR and CT-scanner to identify the changes that happened to the pore size distribution and the porosity profile. This data was integrated in order to describe the nature of formation damage sustained during usage of regular mud acid in sandstone formations.

Results and Discussion

Grey Berea Acidizing

The first section of work was focused on Grey Berea. Cores GB1 were saturated using 5 wt% ammonium chloride using vacuum pump then flooded using the coreflood setup shown in **Fig. 57** for permeability assessment. After initial permeability and saturation cores were scanned using NMR to evaluate the original pore size distribution. The cores exhibited a porosity of 19.7 vol% and permeability of 80 md. Both cores were damaged by injection of deionized water at 3 cm3/min and the damage was tracked by the pressure drop across the core during the injection, later on the core was scanned again under the NMR for pore size distribution after damage.

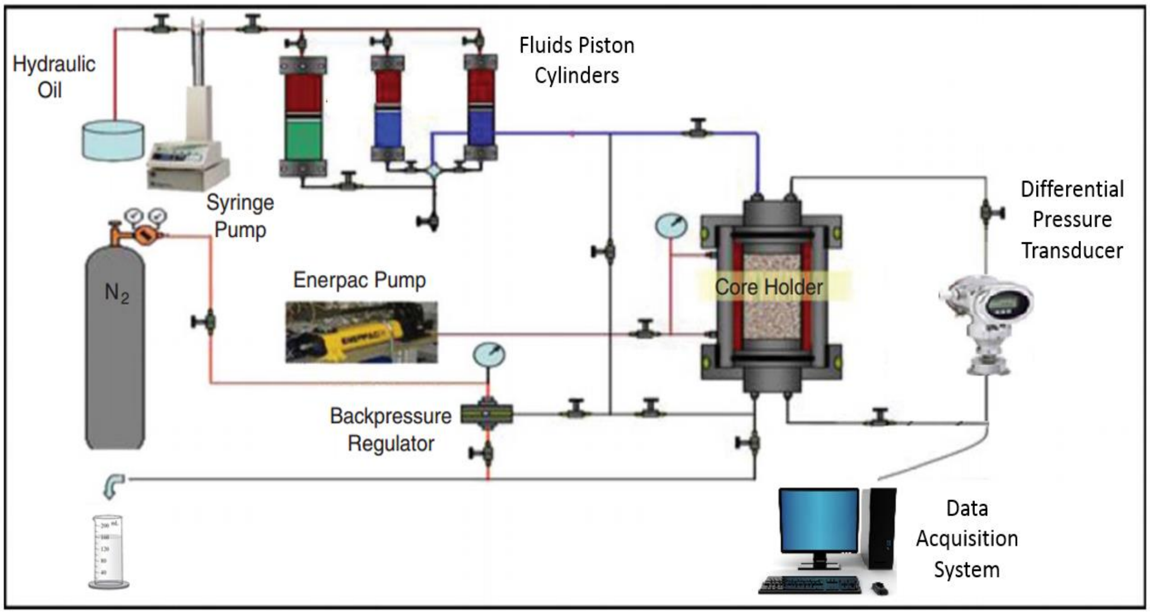

Fig. 57– Schematic of coreflood setup.

Saturation of the core was ensured by reaching pressure drop equilibrium across the core; upon injecting the deionized water the pressure drop started picking up gradually from 28 psi until it reached 50 psi at the end of the fines migration induction stage (**Fig. 58**). The presence of 1 wt% illite in the Berea cores could contribute to the pore throat blockage and fines migration due to its low concentration and its scattered distribution on the walls of the pore throats. Such nature will promote mobilization upon interacting with the deionized water due to the detachment of fine clay particles.

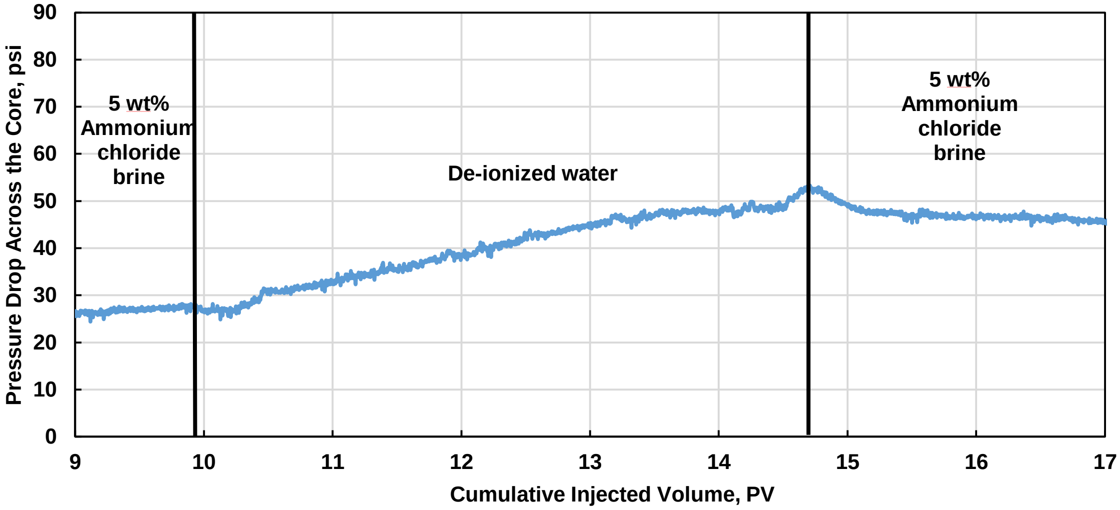

Fig. 58— Pressure drop across the Berea core during deionized water injection and damage due to fines migration.

Fig. 59, and **Fig. 60** show the pore size distribution of fresh grey Berea core versus the core damaged with deionized water inducing fines migration. The undamaged core exhibited a uniform pore size distribution of pore size in the range of 8 to 9 μm. The pore size distribution after induction of fines migration showed a new peak at pore size 1 μm while the intensity of the dominant pore size of the fresh core at 9 μm reduced and flattened down to the range of 10 μm. This could be attributed to the mobilization of the illite particles from the core inlet pore throats to the core outlet widening some of the original pores and plugging the rest. This is shown by the presence of a new narrower pore size, which elaborate the blockage of a high percentage of the homogenous natural pore size.

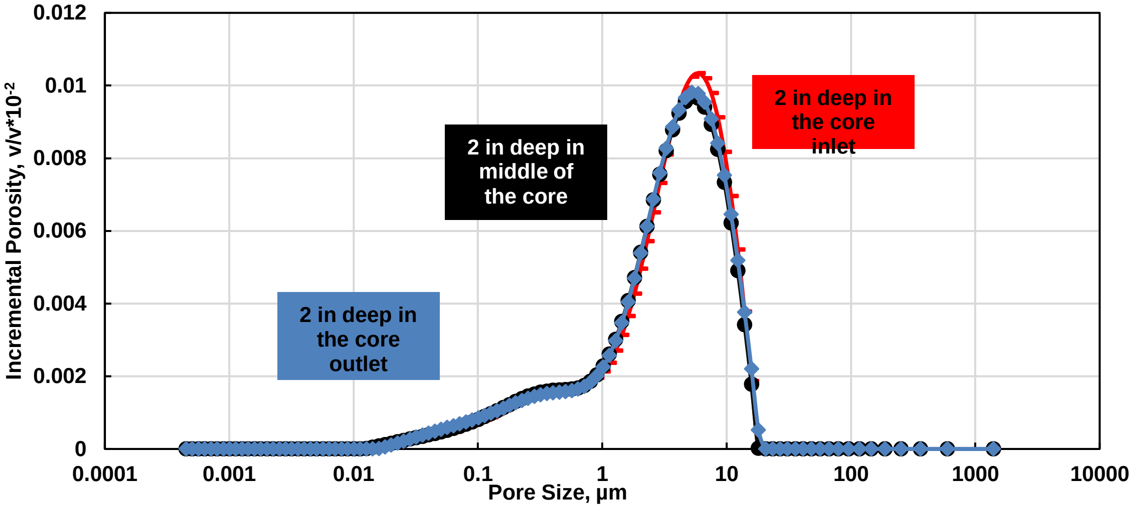

Fig. 59— NMR plot of incremental porosity versus pore size distribution of untreated Berea core.

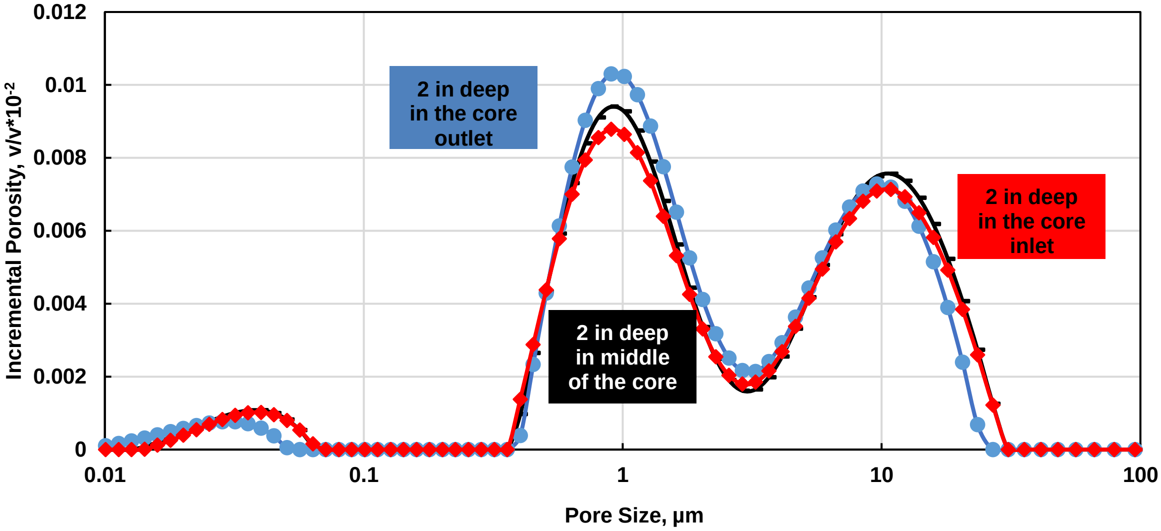

Fig. 60— NMR plot of incremental porosity versus pore size distribution of fines migration damaged Berea core.

The acidizing was conducted after heating the system for 4 hours while flowing brine to ensure equal heat distribution across the core; the homogeneity of heating was monitored in term of pressure drop stabilization. Preflush stage of 3 pore volumes of 12 wt% HCl was applied to flush away the calcite content and prevent its interaction with the mud acid and the precipitation of calcium fluoride was conducted at 150°F. During this stage as shown in **Fig. 61** there was a sudden increase in the pressure drop from 28 to 55 psi during the HCl preflush injection this could be attributed to the reaction between the HCl and the calcite minerals. Further on switching to regular mud acid the pressure drop decreased from 40 to 28 psi. At the end of the treatment there was no gain or lose in permeability overall. The continuum of pressure drop increase and decrease could be attributed to the damaging effect of the HCl to the clay content and the deposition of silica gel causing increase in pressure drop, while the drop is due to the dissolution of the calcite content. The pressure drop witnessed upon the injection of the regular mud acid containing HF can be justified since it is able to dissolve the silica gel.

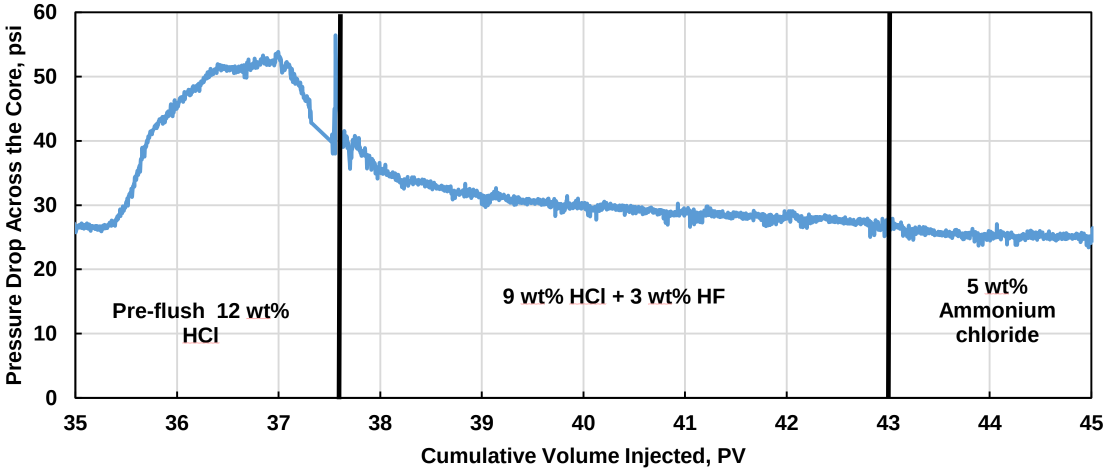

Fig. 61— Pressure drop across the Berea core during acidizing at 150°F in presence of fines migration damage induced using deionized water.

The comparison of the CT-scans before and after the acidizing after the cores were damaged by deionized water causing fines migration, showed clearly that the further the acid reach in the core the lower is the gain of the porosity (**Fig. 62**). This could be attributed to the accumulation of the fines migration toward the outlet of the core. Although the Grey Berea clay content is 8 %, the damage extend is obvious when compared to cores acidized in absence of fines migration. This results were confirmed by the NMR pore size distribution analysis. The presence of 2 wt% chlorite mineral seems to be of huge impact during acidizing due to its break down and blocking the pore structure by the amorphous silica structure and iron precipitation.

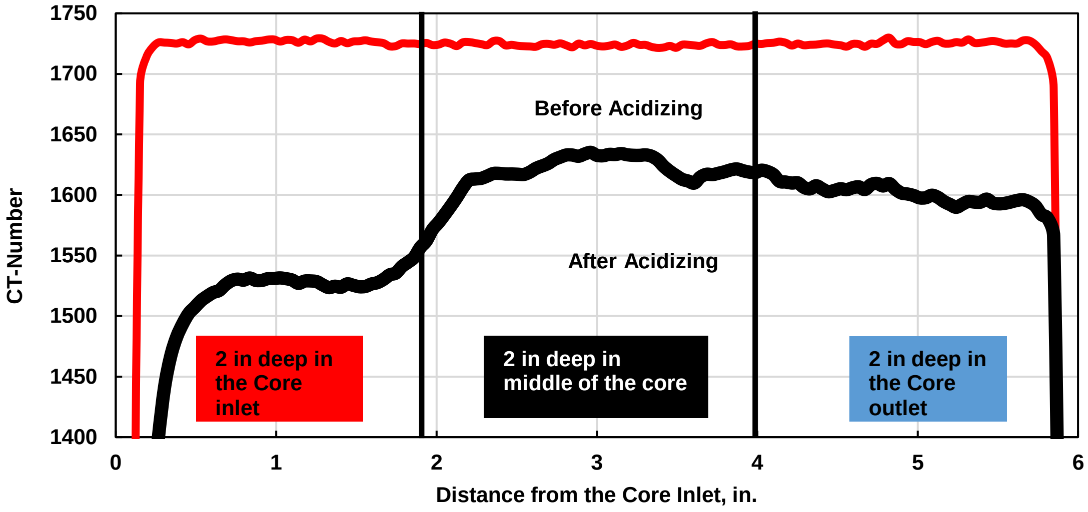

Fig. 62— CT-number variation after acidizing Berea core at 150°F in presence of fines migration damage induced using deionized water.

Fig. 63. shows the pore size distribution after acidizing in presence of fines migration. The pore size distribution of the first 2 in. from the inlet shows the natural pore size distribution at 10 µm. While the second 2 in. interval shows a decline in the pore size distribution to 8 µm. The last section showed a huge deterioration of the pore size distribution down from 10 to 1 µm. Such results are due to the localization and the swallowing of the clay particles in narrow pore throats toward the core outlet. The acid

damaging effect was intensified by the localized clay particles and blockage of the pore throats were magnified.

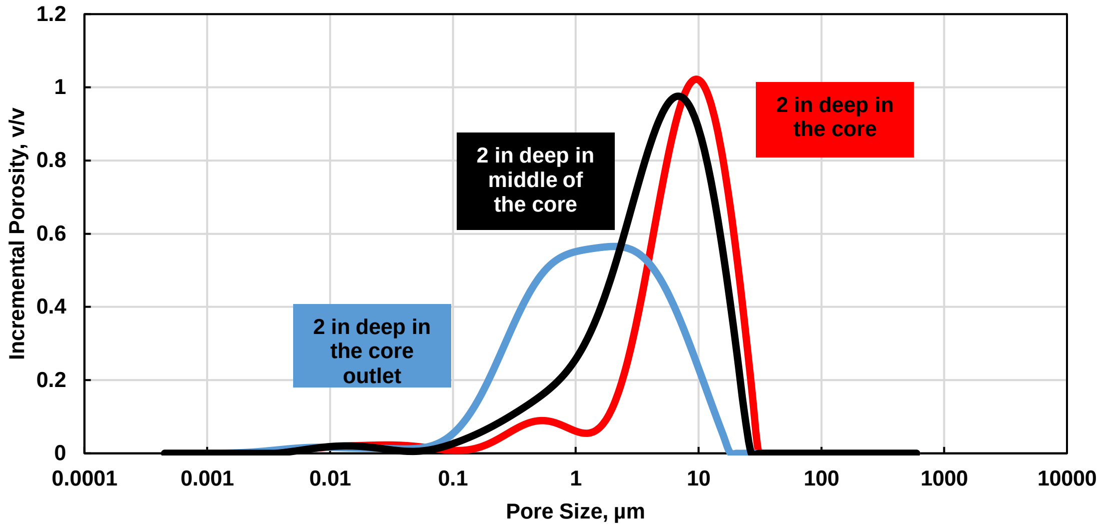

Fig. 63— NMR plot of incremental porosity versus pore size distribution of fines migration damaged Berea core after acidizing at 150°F.

The same procedure was repeated at 250°F in order to assess the impact of temperature on the redistribution of clay content. Their interaction in presence of preflush and regular mud acid stages at higher temperature was examined using core GB2 of porosity 17.5 vol% and permeability of 110 md. The pressure drop response (**Fig. 64**) was similar to the first case at 150°F yet the maximum pressure went up to a higher limit of 80 psi, this reflected the severity of the reaction due to the elevated temperature.

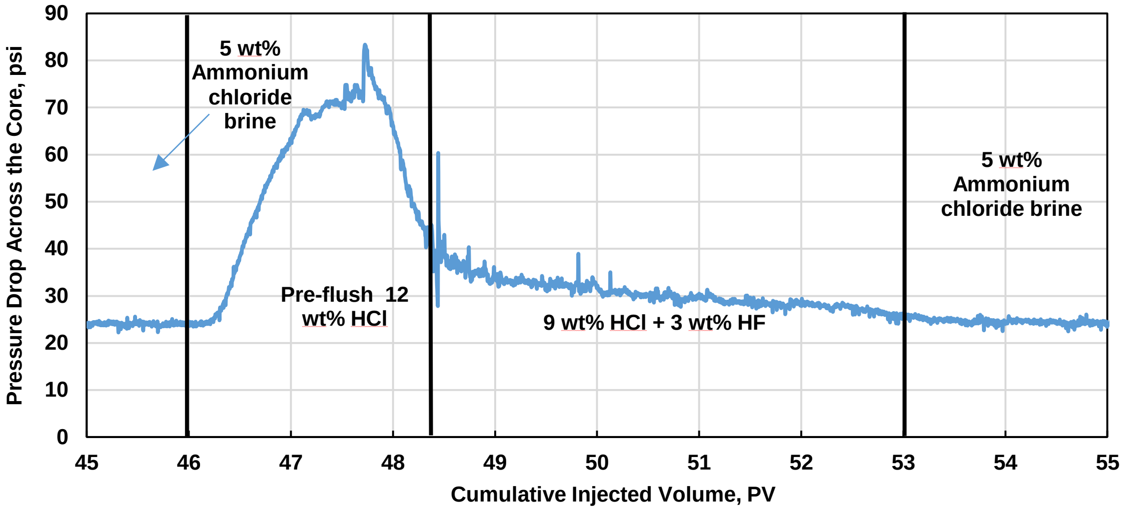

Fig. 64— Pressure drop across Berea core during acidizing at 250°F in presence of fines migration damage induced using deionized water.

The regular mud acid interval exhibited a steeper pressure decline down to the 28 psi; this steep decline is attributed to the higher efficiency of the HF to dissolve the silica gel that was precipitated at the preflush stage. Again the total permeability of the core wasn't changed. The CT-scan data (**Fig. 65**) showed an increase in the porosity gain at the inlet and a decline as deep further in the core toward the outlet.

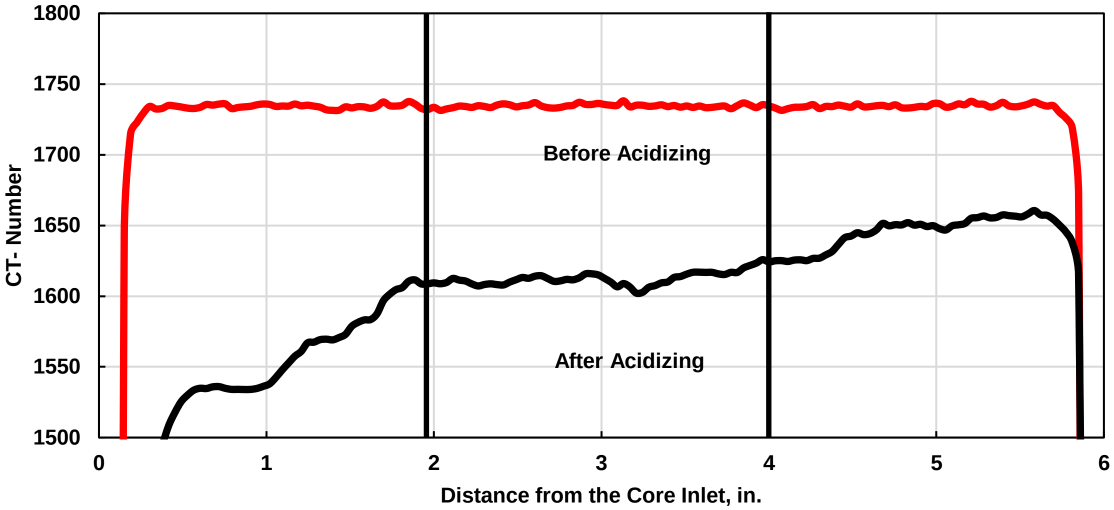

Fig. 65— CT-number variation after acidizing Berea core at 250°F in presence of fines migration damage induced using deionized water.

While the first 2 in. of the core showed similar pore size distribution to the 150°F case. The NMR data (**Fig. 66**) showed a decrease of the dominant pore size at the last 4 in. toward the outlet of the core to be in a pore size range going down from 10 µm before the acidizing to 0.1 µm after. This decrease in pore size explain the decrease in porosity gain toward the outlet noticed in CT-scan. The presence of 1 wt% total clay content, although it's lower than those of Bandera and Kentucky sandstone, it exhibits higher formation damage that increase with the increase of temperature.

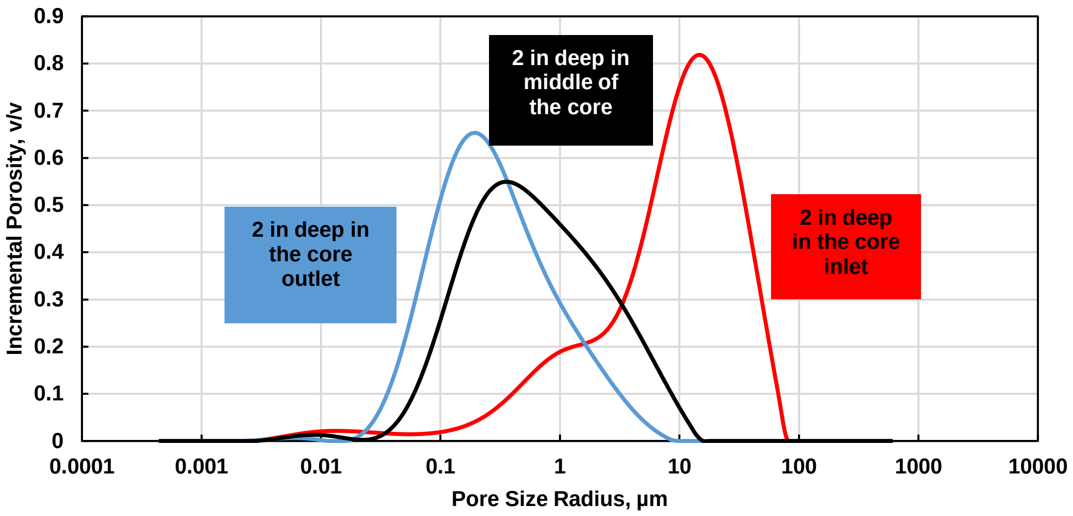

Fig. 66— NMR plot of incremental porosity versus pore size distribution of fines migration damaged Berea core after acidizing at 250°F.

Kentucky Sandstone Acidizing

The second part of the study focused on Kentucky sandstone of permeability 0.3 md and porosity of 15 vol%, such tight formation acidizing is one of the stimulation option to enhance its productivity. Also acid fracturing is one of the important stimulation options, this encouraged investigating how would such high clay content formation behave upon exposure to acid. This section of the work was conducted at lower flow rate of 1 cm^3/min to control the pressure drop.

The coreflood was conducted at 250°F after the core was saturated with 5 wt% ammonium chloride brine and then fines migration was induced by injecting deionized water at flow rate of 1 cm^3/min. During the deionized water injection, the pressure increased from 350 to 550 psi indicating damage and reduction of permeability **(Fig. 67)**. Due to the high clay content HCl based preflush was eliminated and replaced with a 9wt% formic acid preflush stage. The main acidizing stage was similar to the regular mud acid used for the Berea sandstone. During the preflush stage there was a step function increase of pressure indicating loss of permeability and describe the change in the viscosity.

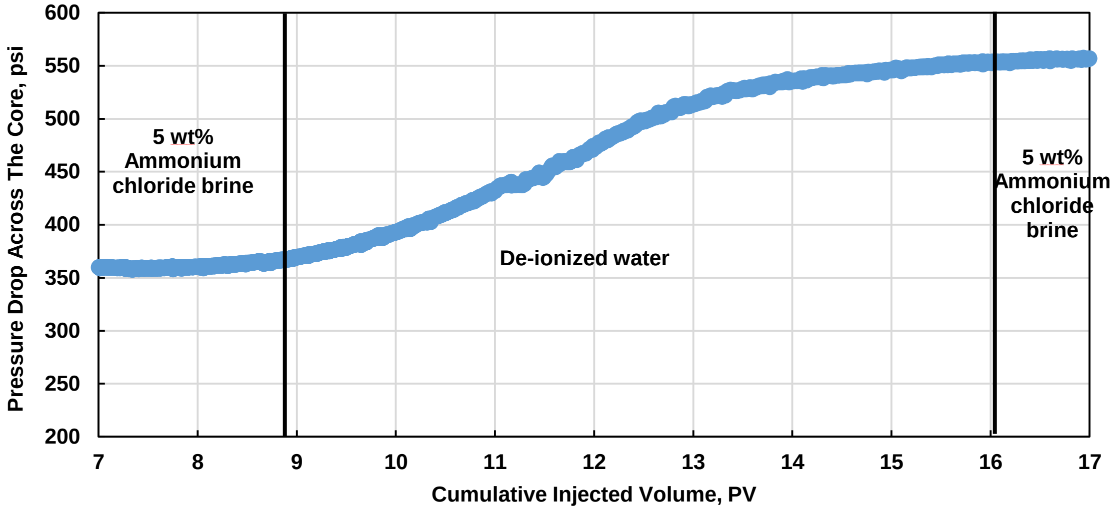

Fig. 67— Pressure drop across the Kentucky core during deionized water injection and fines migration damage induction.

Later on upon introduction of the regular mud acid pressure started building up (**Fig. 68**) from 280 to 420 psi. The pressure drop went back after reaching a peak until it reached 250 psi again. Due to the low permeability judging the permeability change is not valid based on the pressure drop.

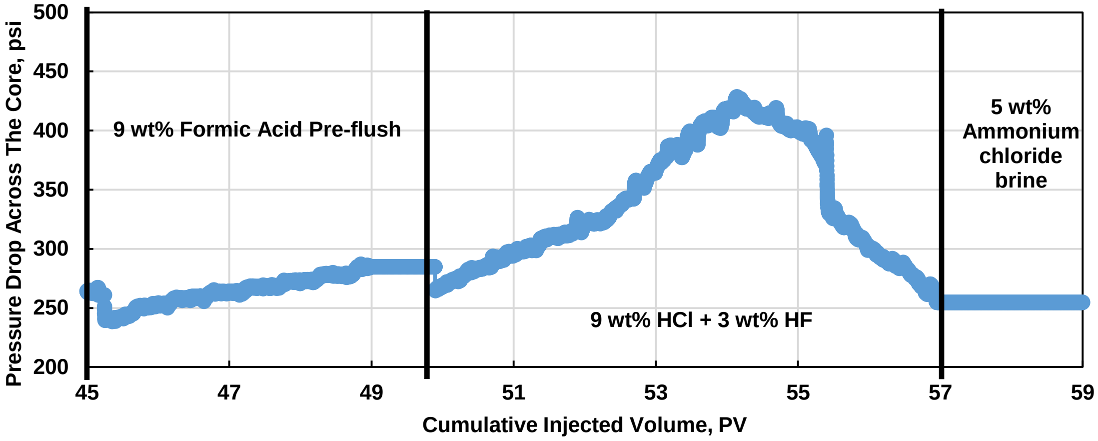

Fig. 68— Pressure drop across the Kentucky core during acidizing at 250°F in presence of fines migration damage induced using deionized water.

On the other hand, for the Grey Berea, the Kentucky core exhibited less damage induced by the triggering the fines migration. The pore size distribution after induction of fines migration showed a slight redistribution of the clay particles across the core, inlet pore size witnessed a lower incremental porosity and larger pore size when compared to the outlet higher incremental porosity and lower pore size as shown in **Fig. 69,** and **Fig. 70**.

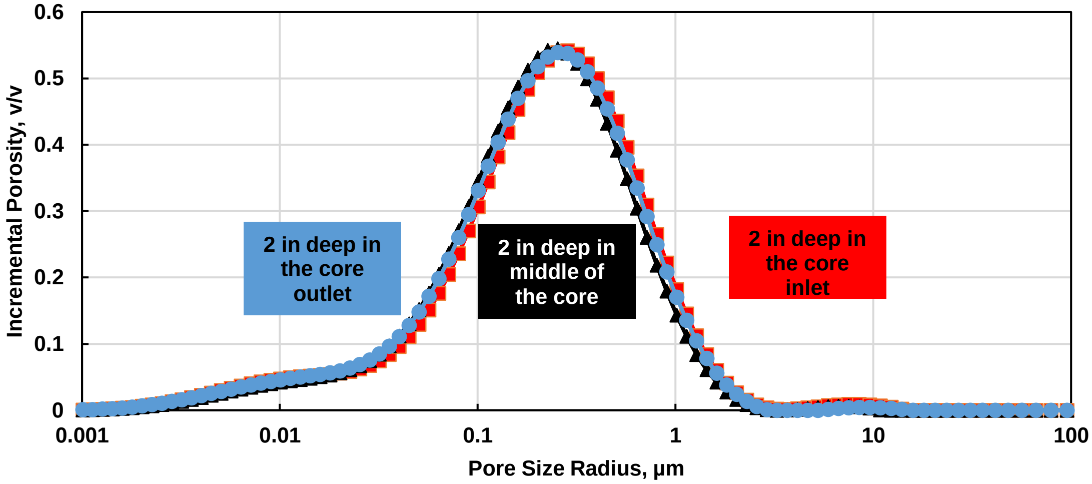

Fig. 69— NMR plot of incremental porosity versus pore size distribution of fines migration of untreated Kentucky sandstone core.

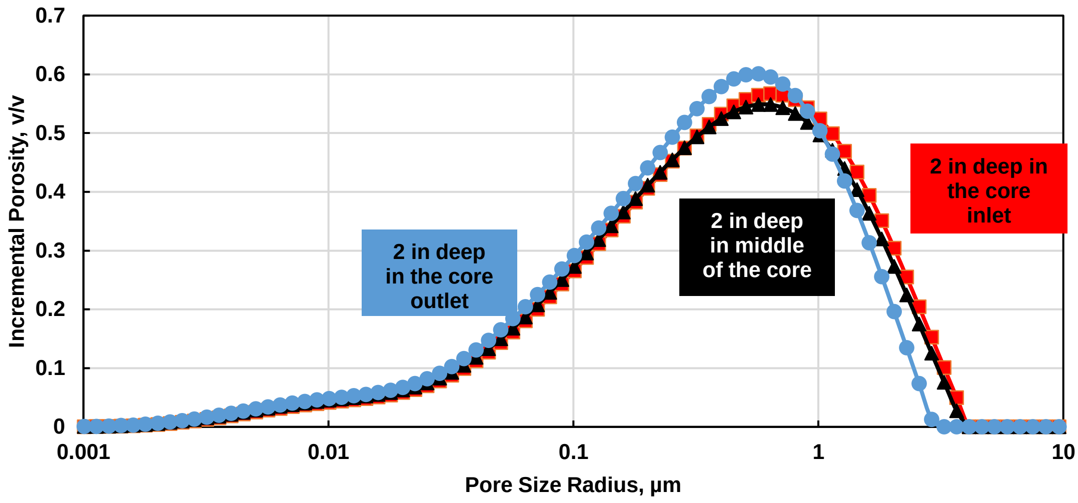

Fig. 70— NMR plot of incremental porosity versus pore size distribution of fines migration damaged Kentucky sandstone core.

The NMR scans after the acidizing (**Fig. 71**) showed a slight deviation of the pore size distribution, the last two inches of the core suffered a decrease in the dominant pore size of the outlet section when compared to the inlet of the core.

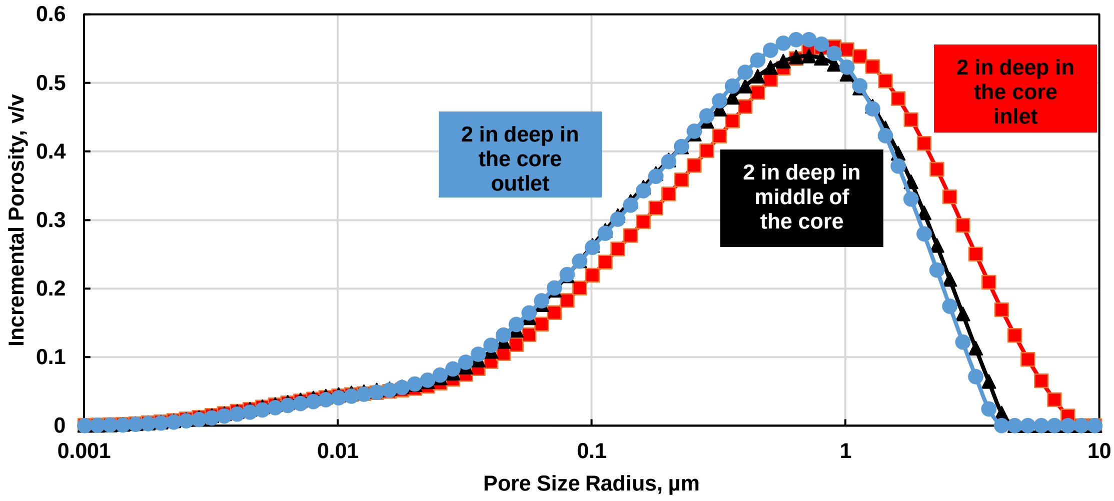

Fig. 71— NMR plot of incremental porosity versus pore size distribution of fines migration damage after acidizing at 250°F for Kentucky sandstone core.

The CT scans before and after the induction of fines migration (**Fig. 72**) came out with an increase in the CT number from 1800 to 1900 which shows a uniform porosity distribution before and after the damage.

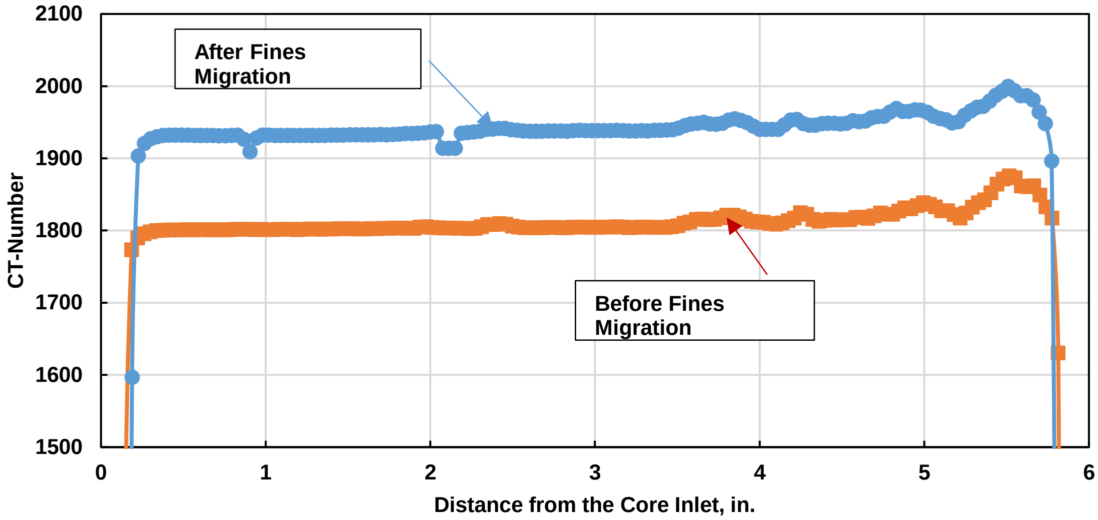

Fig. 72— CT-number variation after fines migration damage induced using deionized water for Kentucky sandstone core.

Furthermore, the after acidizing CT scans showed a uniform porosity gain along the core (**Fig. 73**), such result shows that fines migration didn't alter the pore structure of the core severely and kept it homogenous on the contrary of the Berea sandstone CT response. The acid also reacted uniformly along the core and the fines migration didn't alter the acidizing products more than slight gain in the inlet showing a higher pore size than the outlet. The high clay content resulted in uniformly distributed fines migration and a lower heterogeneity in the pore size distribution and nature which resulted in more uniform reaction along the core.

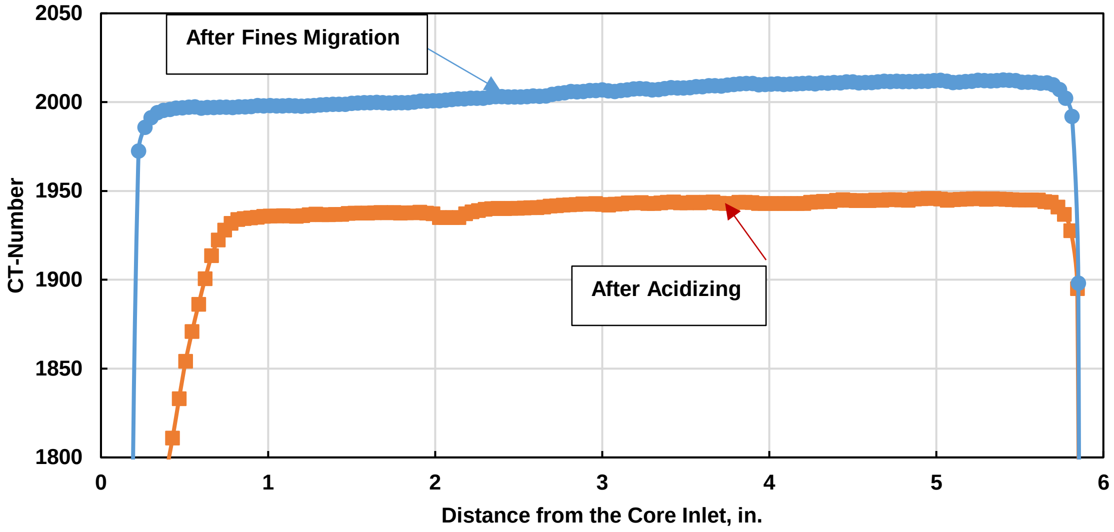

Fig. 73— CT-number variation after acidizing at 250°F in presence of fines migration damage induced using deionized water for Kentucky sandstone.

Although the total clay content of Kentucky sandstone is 17%, were 14 wt% of it is illite the magnitude of the damage due to deionized water injection didn't came equivalent to that high illitic content. This illitic nature shown in high concentration helped by making the illite consolidated with lower surface area exposure and less presence in the pore throats. This resulted in lower alteration of pore size distribution as shown in the NMR data. Further on the uniformity of the pore size and the less flow of fines in pore throats made the reaction outcome homogenous. The absence of chlorite minerals in Kentucky sandstone helped in lowering the impact of the acidizing damaging potential and the higher the stability of Kentucky sandstone.

Conclusions

Key findings from this study leads to the following conclusions:

1- The higher the illite content in the sandstone the lower the damaging impact of the fines migration.

2- The low concentration of chlorite and illite minerals is detrimental to the acidizing product than presence of big body of consolidate clay content.

3- The Berea sandstone suffers deep and strong damage upon acidizing at high temperature in terms of blockage of pore throats and lowering the average pore size of the last 2/3 of the treated formation.

4- The higher the temperature the more severe the damage even at lower extent of fines migration damage.

5- Kentucky sandstone although regular acidizing is not beneficial due to its low permeability showed a higher tolerance for acid species on fines migration in terms of the uniform pore size distribution before and after the treatment.

6- The high clay content formations are good candidate for acid fracture without the worry of blocking its fine pores due to the uniformity of the reaction and the higher the stability of the clay body.

Finally, the work will add a further depth on the location and the nature of the formation damage resulting from regular mud acid treatment in presence of fines migration. Hence, it assessed the impact of the clay content concentration and type on the severity of the formation damage and its contribution to loss of the formation productivity. This will give a better design criterion for matrix acidizing and acid fracturing in high clay content sandstone and shale formations.

CHAPTER V

A NEW METHOD TO ASSESS STIMULATION OF SANDSTONE CORES DAMAGED BY FINES MIGRATION[7]

Summary

Sandstone stimulation faces multiple challenges due to the heterogeneity of the formation and the sensitivity of its clay minerals. Fines migration results in lowering the formation productivity and complicates the stimulation process. Multiple field studies showed that treatment of fines migration is critical and can result in permanent damage of the wellbore. This study aims to locate, quantify, and describe the damage resulting of fines migration damage and its stimulation in sandstone formations and examine the impact of the clay content and its nature on the stimulation process.

This work is structured to evaluate the stimulation of fines migration damage in Bandera, Berea, and Kentucky sandstones. Fines migration was induced by injecting deionized water to trigger the mobilization of the clay minerals in the core. Both HCl or formic acid, and mud acid stages were injected following the fines migration induction. The new formation damage evaluation methodology utilizes computed tomography (CT) and nuclear magnetic resonance (NMR) scanning before and after the fines migration induction and its stimulation. The data from CT and NMR were combined and processed to generate a 3D representation of the cores pore structure, which gives an insight on how the clay nature impacts the stimulation process and the pore system.

---

[7] Reprinted with permission from “A New Method to Assess Stimulation of Sandstone Cores Damaged by Fines Migration” by Hanafy, A. M., Nasr-El-Din, H. A. 2018. Presented at the SPE Western Regional Meeting, 22-26 April, Garden Grove, California, USA, copyright 2018 by the Society of Petroleum Engineers. Reproduced with permission of SPE. Further reproduction prohibited without permission.

The developed technique exhibited an excellent ability to visualize the core porosity distribution and the changes in the pore structure following the fines migration damage and the acid treatment. The 3D representation succeeded to assess the magnitude and the location of the formation damage due to fines migration and its stimulation. The injection of deionized water in the studied formations resulted in a different petrophysical responses, which came matching the prediction built on the mineralogy and porosity mapping using computed tomography data. These changes in pore structure prevailed as a controlling variable of the acidizing process. The stimulation of the damaged cores at 150 and 250°F resulted in the deposition of the alumino silicates toward the core outlet. These deposits are attributed to the acid leaching of the aluminum and iron ions from the alumino silicate structures. The high temperatures resulted in the deposition of alumino silicates closer to the injection point. The enhancement in permeability noticed in all of the studied formations showed to be due to the induction of narrow channels in between heavily deformed pore structures.

This work added to the sandstone stimulation technology a new tool to assess the true impact of acid stimulation on fines migration damage. The high level of resolution of tracking the changes in the pore structure lay the road to optimize the treatments to enhance the productivity and lower the cost. This technique has a potential as a formation evaluation technique to evaluate other types of formation damage, such as fracturing fluids and water blockage.

Introduction

Sandstone stimulation using matrix acidizing is an experiment of guessing and practical experience. The heterogeneity of the sandstone reservoirs and the stratified nature of pay zones challenge the process of designing a successful treatment for every well. The nature of the reaction of HCl and HF with the different minerals determine the extent of success of the matrix acidizing. Petrophysical properties of the reservoir and the history leading to the formation damage are controlling variables to the success of the stimulation process. Multiple studies discussed the criteria upon which a reservoir would be a good candidate for matrix acidizing and how to select the appropriate acid system to enhance the efficiency of the stimulation process (Gatewood et al. 1970; McCune et al. 1975; Shuchart and Gdanski 1996; Al-Dahlan et al. 2001; Hartman et al. 2006).

This work aims to assess the impact of the differences in the petrophysical and mineralogical properties of Bandera, Berea, and Kentucky sandstones on fines migration damage and its stimulation. It assesses the impact of the clay minerals type, nature, and morphology on the stimulation outcomes. This study proposes an evaluation technique that works on describing the different formation damage mechanisms and its location while examining formation's acid and temperature sensitivities.

Experimental Studies

Materials

This study was designed to examine outcrops from Bandera, Berea, and Kentucky sandstone using 6 in. long by 1.5 in. core plugs. Sodium, and ammonium chlorides were used at 5 wt% concentration in 18.2 MΩ.cm deionized water solution and were supplied by a local supplier. HF was prepared by reacting HCl with ammonium bifluoride, which was supplied by a local supplier. The preflush stage for Bandera was 15 wt% HCl and for Berea sandstone it was 12 wt% HCl, both stages were prepared from a 36.5 wt% HCl stock purchased from VWR. Formic acid was used as a preflush for Kentucky sandstone at a concentration of 9 wt%, it was purchased from a local supplier. The mud acid used with the Bandera sandstone consisted of 12 wt% HCl and 3 wt% HF, while the mud acid for both Berea and Kentucky sandstones was 9 wt% HCl and 3 wt% HF. Both corrosion inhibitor and corrosion inhibitor intensifier were utilized to ensure the coreflood system integrity.

NMR

The transverse relaxation time of brine saturated cores was measured to describe their pore size distribution. A 2 MHZ Magritek bench-top spectrometer Core Analyzer was utilized to measure the T_2 relaxation time. The measurement utilized the Carr-Purcell-Meiboom-Gill (CPMG) pulse sequence (Carr and Purcell 1954). A 100 µs Echo Spacing Time (TE) was used and a target-to-noise ratio (SNR) of 200. Each core was scanned 16 times and the number of the echoes per experiment were 50,000. A 10,000 ms was allowed between each experiment to ensure a complete relaxation of the longitudinal magnetization. The T_2 relaxation time distribution is a function of the bulk relaxation time (T_{2bulk}), the surface relaxation time ($T_{2surface}$), and the diffusion-induced relaxation time ($T_{2diffusion}$). The T_2 is expressed by Eq. 4 (Coates et al. 1999):

$$\frac{1}{T_2} = \frac{1}{T_{2\,bulk}} + \frac{1}{T_{2\,surface}} + \frac{1}{T_{2\,diffusion}} \quad , \quad \ldots\ldots\ldots\ldots\ldots\ldots\ldots\ldots\ldots\ldots\ldots \quad (4)$$

The T_2 measurement were designed to eliminate the impact of the bulk and the diffusion terms, and the pore size distribution was calculated from the T_2 relaxation time, where $T_{2surface}$ is expressed by Eq. 5 (Zhi-Xiang et al. 2015):

$$\frac{1}{T_{2\,surface}} = \rho_2 \frac{s}{v} \quad , \quad \ldots\ldots\ldots\ldots\ldots\ldots\ldots\ldots \qquad (5)$$

Where $\frac{s}{v}$ is the surface-to-volume ratio of the pore space, and ρ_2 is the surface relaxivity.

CT-Scan

Conventional processing of CT-scan data in sandstone was limited to the calculation of the average porosity of each slice and tracking its changes along the core by tracking the CT-number changes with the alteration of the pore filling fluids (Vinegar 1986; Akin and Kovscek 2003). This work introduces the utilization of CT data segmenting and 3D plotting. This technique is used in tracking the hydraulic fracturing and enhanced oil recovery. This method divides each slice of the core into 0.3 by 0.3 mm pixel were each pixel have an attenuation number. The attenuation number is function of the pixel density, mineralogy, and fluid type. A histogram for the pixel attenuation number is plotted against its frequency of presence. Each data set of pixel density is broken down to four main group as follow: severe formation damage (tight pores), Moderate formation damage (low porosity), moderate dissolution (moderate porosity), strong dissolution (high porosity), and severe dissolution (washout). Each segment is described based on the change in the pixel's attenuation number after the treatment.

Novel Approach

The changes in the attenuation number can happen due to multiple variables other than the change in porosity. The production of amorphous by-product from the acid reaction with the rock mineral can result in lower or higher attenuation number. The proposed approach suggests the segmentation of the core pixels according to the assigned groups, and calibrate the assigned groups using the pore size distribution from the T_2 relaxation time. In order to track the changes in the pore size distribution, each core is sliced into 2 in. long core plugs. The graphs from pore size distribution are plotted and overlaid to monitor the changes in the pore size distribution along the core. The attenuation number histograms are compared to the pore size distribution to assure the resemblance in the distribution profiles. If a pixel reports a high attenuation number at the same zone the pore size distribution shows an enlargement in the pore size, the attenuation number is recognized to be due to rock transformation rather than porosity change. The segmentation process also aims to assess the continuity of the different assigned groups rather than scattered points, which is not explained by the fluid dynamics in porous media.

Experimental Methods

Initial Cores Evaluation

Detailed mineralogical and petrophysical assessments were conducted for the three sandstones tested in this study. Samples from each outcrop were evaluated using XRD, XRF, SEM, and EDS to describe the elemental and morphological presence of each mineral. The petrophysics of the cores was examined using coreflood, NMR, and CT-scan. Data from each analysis were cross-referenced and integrated with each other for a detailed description of the core properties.

Fines Migration Induction and Assessment

The impact of fines migration on the petrophysical properties was investigated using multiple core flooding studies were the cores were scanned using CT and NMR scanner before and after each coreflood. The initial core permeability and the fines migration damage induction were conducted using coreflood. The overburden pressure was maintained at 1,000 psi and the back pressure at 500 psi. The cores initial saturation and coreflooding were conducted using 5 wt% brine solution to prevent uncontrolled fines migration. Deionized water was injected in each of the Bandera and Berea cores at a flowrate of 3 cm^3/min, while in Kentucky sandstone the flow rate was maintained at 1 cm^3/min. The pressure drop across the core was monitored to track down the fines migration propagation in terms of permeability reduction.

Fines Migration Stimulation

The cores were subjected to a preflush stage of HCl or formic acid according to the mineralogical composition. Brine was injected after the preflush. Mud acid stage was pumped after brine and followed by post flush of brine. The stimulation was conducted at 150 and 250°F. The back pressure was raised above 1,000 psi to maintain the CO_2 dissolved in the acid. Overburden pressure was raised to 2,000 psi to ensure axial flow through the core.

Stimulation Tracking

The stimulation process was monitored using a combination between T_2 relaxation time and computed tomography. Each of the cores was divided into 3 sections each was 2 in. long. The smaller plugs were evaluated using NMR to track the changes in the pore size distribution along the core. The pore size distribution was calculated from the relaxation time and plotted versus its frequency (Coates et al. 1999; Zhi-Xiang et al. 2015). The number of pixels sharing the same attenuation number was plotted against each attenuation number. The CT data were processed and 3D models were built showing the stimulated sections, the damaged sections, and the rock matrix.

A segmented 3D model was built for each core before and after acid injection. The CT data was imported to Drishti CT processing software. A histogram was built including the pixels with attenuation number ranging from 400 to 2,000 HU, which shows the rock and pores system. The cores were segmented in 5 main sections: very low, low, moderate, high, and very high porosity zones. A 5 zones composited 3D model was generated and compared to a zone by zone segmented model to show the continuity of the studied pore structure features. Pre-treatment cores were scanned and processed in the same manner to investigate the homogeneity of the cores before stimulation.

Results and Discussion

Mineralogy Assessment

The three sandstones were examined using XRD to assess the crystallography and the concentration of the different minerals. **Table 12** shows the three sandstones to be of different mineralogical composition. The Bandera sandstone shows a quartz content of 59 wt% compared to 87 and 66 wt% in Grey Berea, and Kentucky sandstone, respectively. This quartz concentrations shows that the formations are low, moderate, and high quartz content examples. Both Grey Berea, and Kentucky carbonates content are low showing 3 and 0 wt% respectively, Bandera sandstone shows 15 wt% of dolomite mineral. The illite mineral, which is problematic to HCl preflush shows 10, 1, and 14 wt% in the Bandera, Berea, and Kentucky formations. Chlorite mineral is present at 1, 2, and 0 wt% in the same order. Both Berea and Kentucky contains potassium feldspar which is HF sensitive, while Bandera and Kentucky sandstones contain 12 wt% sodium feldspar. This mineralogical assessment shows that the three formations are composed of different mineralogical structures. The total clay content of the formations is 14, 7, and 14 wt% in Bandera, Berea, and Kentucky sandstone.

Mineral, wt%	Bandera	Grey Berea	Kentucky
Quartz	59	87	66
Calcite	0	2	0
Dolomite	15	1	0
Mica/Illite	10	1	14
Chlorite	1	2	0
Kaolinite	3	4	Trace
Plagioclase (Sodium Feldspar)	12	0	12
Orthoclase (Potassium Feldspar)	0	3	3

Table 12— Composition of Bandera, Grey Berea, and Kentucky sandstone formations, determined by XRD.

Initial Pore Size Distribution and Fines Migration Damage

The pore size distribution was measured for each of the cores using transverse relaxation time. The cores were measured while they were saturated with brine. Data shown in **Fig. 74** represents the pore size distribution for the Bandera sandstone core. The dominant pore size is 4 µm, yet the distribution is wide on the range between 0.01 and 10 µm.

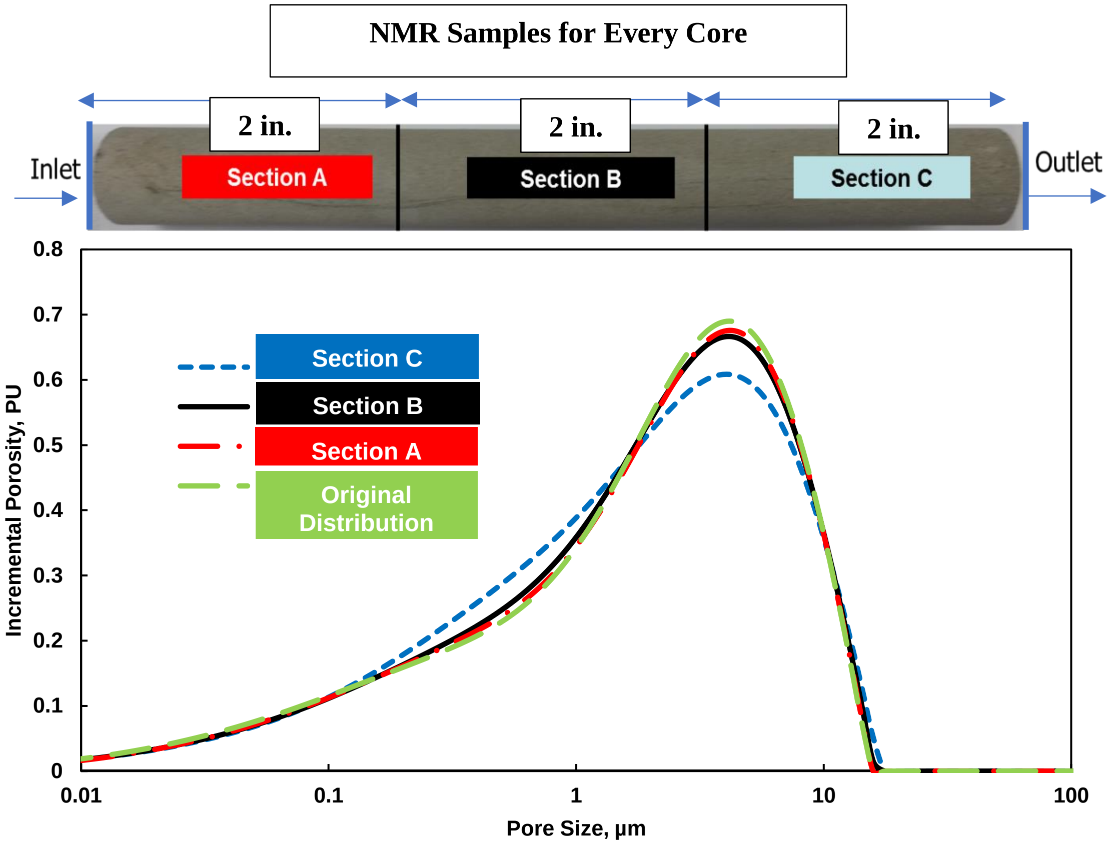

Fig. 74— Pore size distribution driven from T_2 relaxation time for Bandera sandstone before and after fines migration damage. Core was saturated with 5 wt% NaCl brine followed by deionized water flush then brine saturation.

The pore size distribution of the Berea sandstone (**Fig. 75**) came wider with dominant pore size of 8 µm with a wide distribution across the same range of the Bandera sandstone.

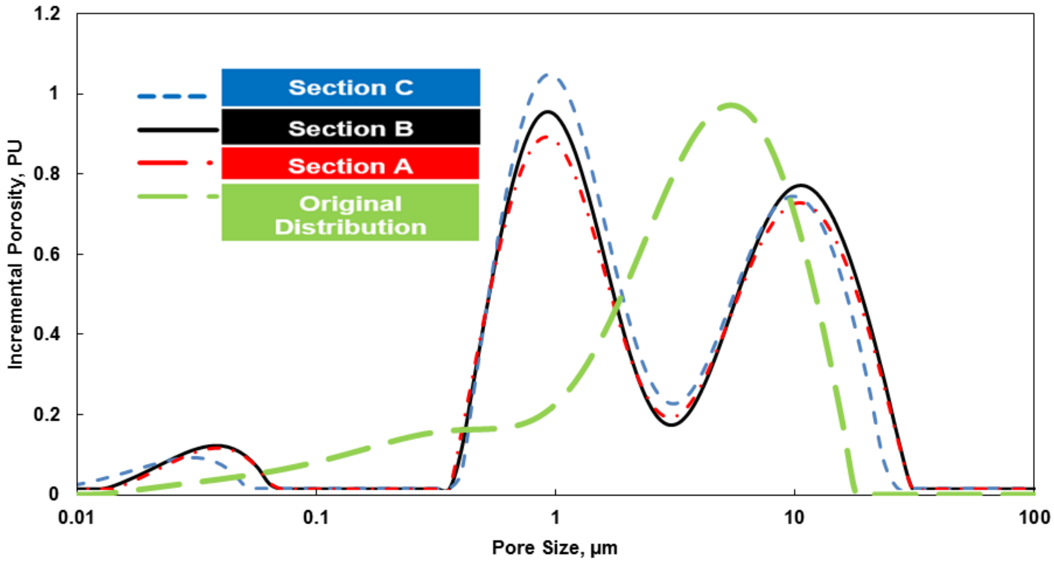

Fig. 75— Pore size distribution driven from T2 relaxation time for Berea sandstone before and after fines migration damage. Core was saturated with 5 wt% NH4Cl brine followed by deionized water flush then brine saturation.

The Kentucky sandstone (**Fig. 76**) dominant pore size is 0.5 µm with a tight distribution between 0.01 and 1 µm.

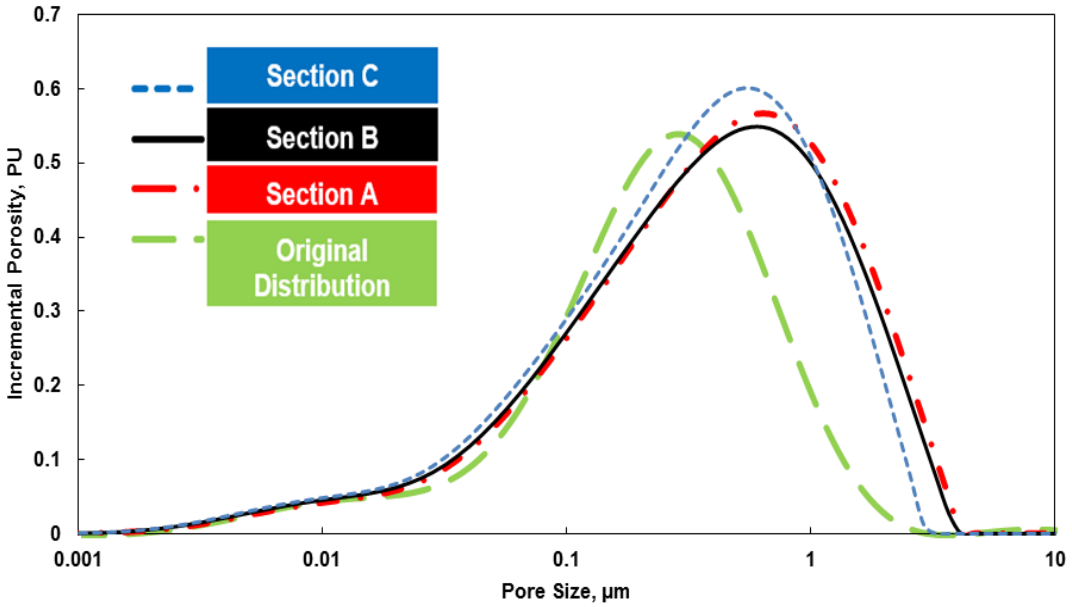

Fig. 76— Pore size distribution driven from T2 relaxation time for Kentucky sandstone before and after fines migration damage. Core was saturated with 5 wt% NH4Cl brine followed by deionized water flush then brine saturation.

Fines migration damage was induced in the three formations by injecting deionized water. The changes in the petrophysical properties of the cores due to fines migration came different from one core to the other. Berea sandstone exhibited the severest form of fines migration damage. The dominant peak at 8 µm was reduced to a lower incremental porosity and a new dominant peak showed up at 1 µm (Fig. 75). The Kentucky sandstone exhibited a widening in the large pores distribution from 1 to 3 µm (Fig. 77), yet no change on the smaller pores frequency was witnessed. The study of the variation of the pore size distribution in the core inlet, middle section, and outlet showed a similar trend with different magnitudes according to the formation. The changes in the three formations show widening in the pore size distribution of the inlet sections and tightening of the outlet sections. Although Berea sandstone is the formation with the lowest clay content, it is the formation with the highest severity of alteration in the pore size distribution upon deionized water injection. The pore size distribution of Bandera sandstone shows an increase in the frequency of the small pores in the outlet section with moderate increase in the pore size in the inlet section (Fig. 74). Kentucky sandstone with the highest illite mineral content shows a minimal variation in the pore size distribution. The NMR data combined with the XRD data showed that the two formations with illite content more than 10 wt% exhibited less fines migration damage than Berea sandstone, which contains 1 wt% illite and 7 wt% combined clay content. This suggests that the nature of the clay minerals in the pore throat is the controlling variable to its interaction with the chemical treatments designed for each formation.

Initial Cores Computed Tomography Segmentation

All of the cores in the study were scanned using CT-scanner at each stage of its damage and stimulation. The CT-scan data were processed according to the variation in the attenuation number at each stage. The data were segmented according to the analysis of the attenuation number histogram at each stage. In the untreated cores, each porosity range inside the core was determined to be in a range of attenuation number and colored in a designated color. The comparison of the three formations in **Fig. 77** showed that the clay content is present in different morphologies. The Bandera sandstone showed low porosity sections interbedded in the higher porosity section which can be assumed to be dolomite and quartz. Kentucky sandstone with 14 wt% clay content showed one solid connected body of low porosity extended across the core, which gets thicker toward the core outlet. The Berea sandstone showed scattered rings of low porosity in between the dominant moderate porosity body of the core. This analysis showed that although the Bandera and Kentucky sandstones are higher in clay content, the surface area of the clays that will be subjected to the chemicals are much less than the scattered clay in the pore throats of the Berea sandstone. This discussion can be supported by the NMR pore size distribution analysis after the fines migration damage resulting from deionized water injection.

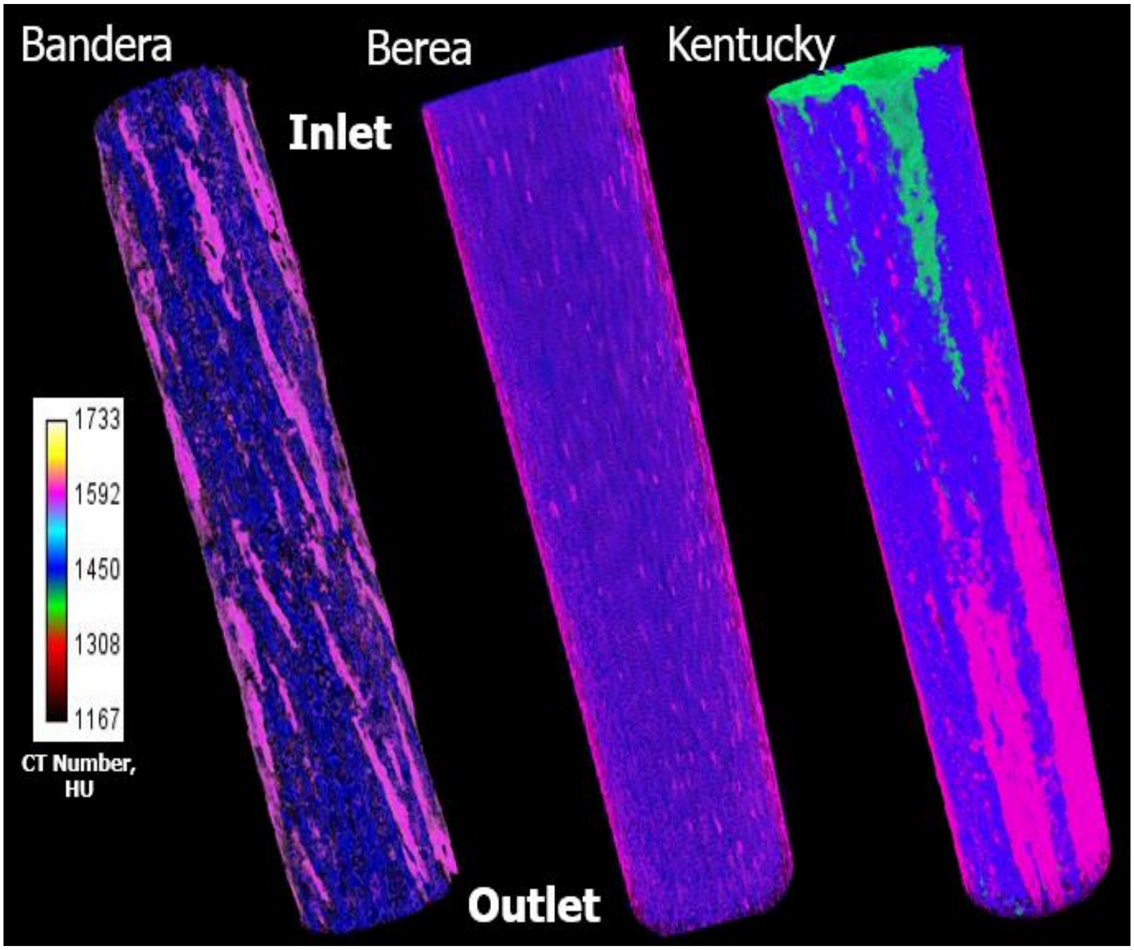

Fig. 77— Computed tomography 3D segmentation of the three formations in as received conditions. Purple zones are low porosity, blue zones are moderate porosity, and green zones are high porosity.

Impact of Acid Stimulation in Berea Sandstone

The first set of cores were the Berea sandstone. The stimulation was conducted at 150 and 250˚F using a preflush stage of 12 wt% HCl followed by brine post flush and a mud acid stage of 9 wt% HCl and 3 wt% HF followed by another brine post flush. The presented data in **Fig. 78** shows the acid pass across the core treated at 150˚F. The composited core representation showing all the porosity ranges in the core shows that a strong dissolution presented in green occurred in the core inlet. The segmented core showed that this dissolution extended for 2 in. in the core. The blue colored moderate porosity section shown to be around the dissolved areas and the damage areas. The segmented core shows that the damage is present at the last 4 in. of the core and its intensity increases in the center of the core. Although the green dissolution channels are getting thinner along the core, they are connected till the core outlet.

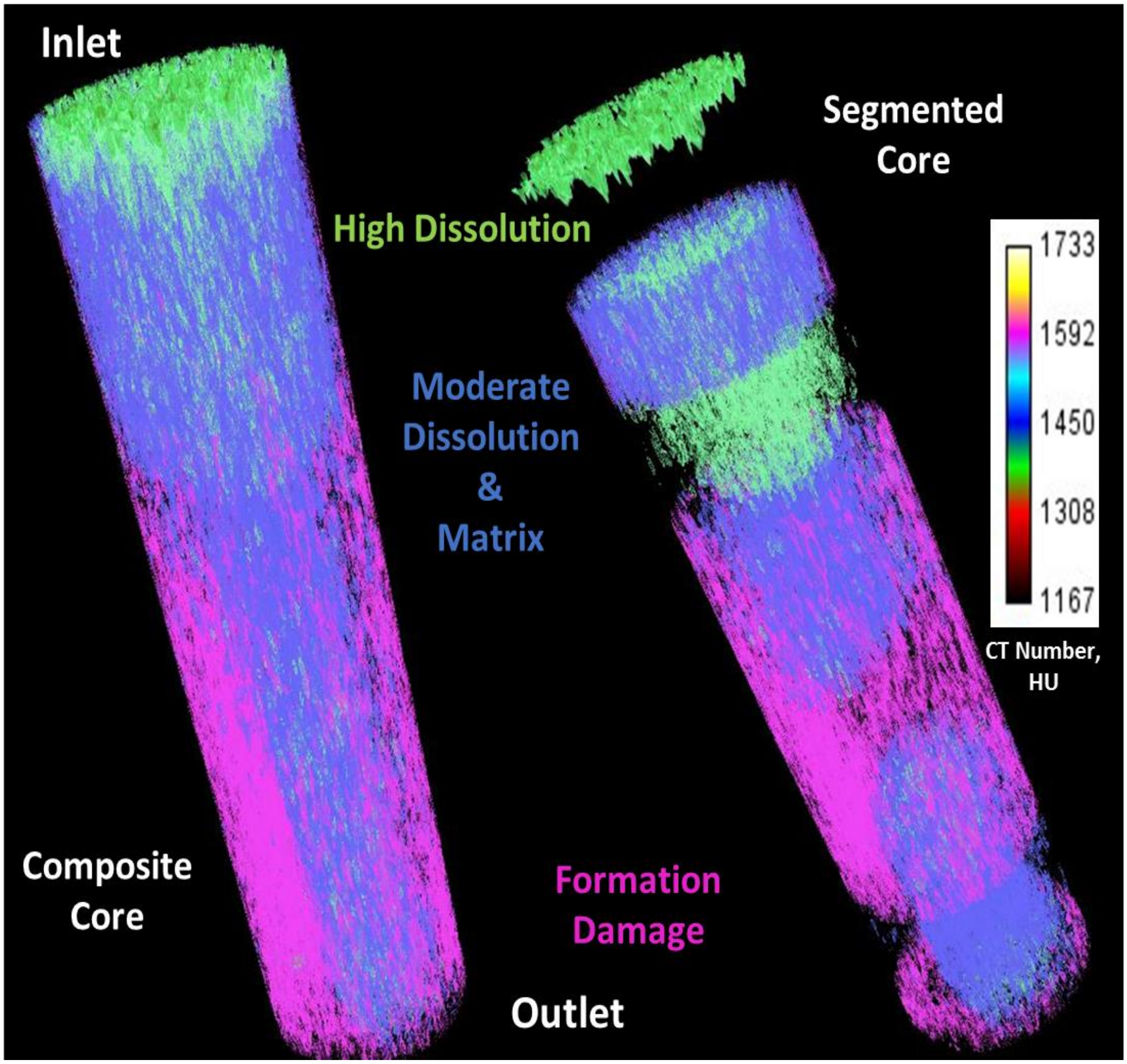

Fig. 78— Computed tomography 3D segmentation of the dissolved and deformed zones in Berea sandstone after HCl and mud acid stages at 150°F. Core was saturated as follow: 5 wt% NH4Cl brine, deionized water, brine saturated, 12 wt% HCl, brine postflush, 9 wt% HCl + 3 wt% HF, brine post flush. Purple zones are low porosity, blue zones are moderate porosity, and green zones are high porosity.

The NMR pore size distribution shown in **Fig. 79** supported the interpretation from the segmented CT-scan data. The pore size distribution of the core outlet exhibited a slight increase in the large pore size incremental porosity. The mid-section of the core showed an increase in the frequency of the smaller pore size. The pore size distribution of the core outlet was severely altered to a domination of smaller pores. In order to validate the data interpreted from the attenuation number variation with the pore size distribution, a histogram of the attenuation number of each pixel was plotted versus the frequency of its presence in the core. Upon the comparison of the generated histograms to the T_2 driven pore size distribution, it showed resemblance to the general patterns of the pore size distribution variation.

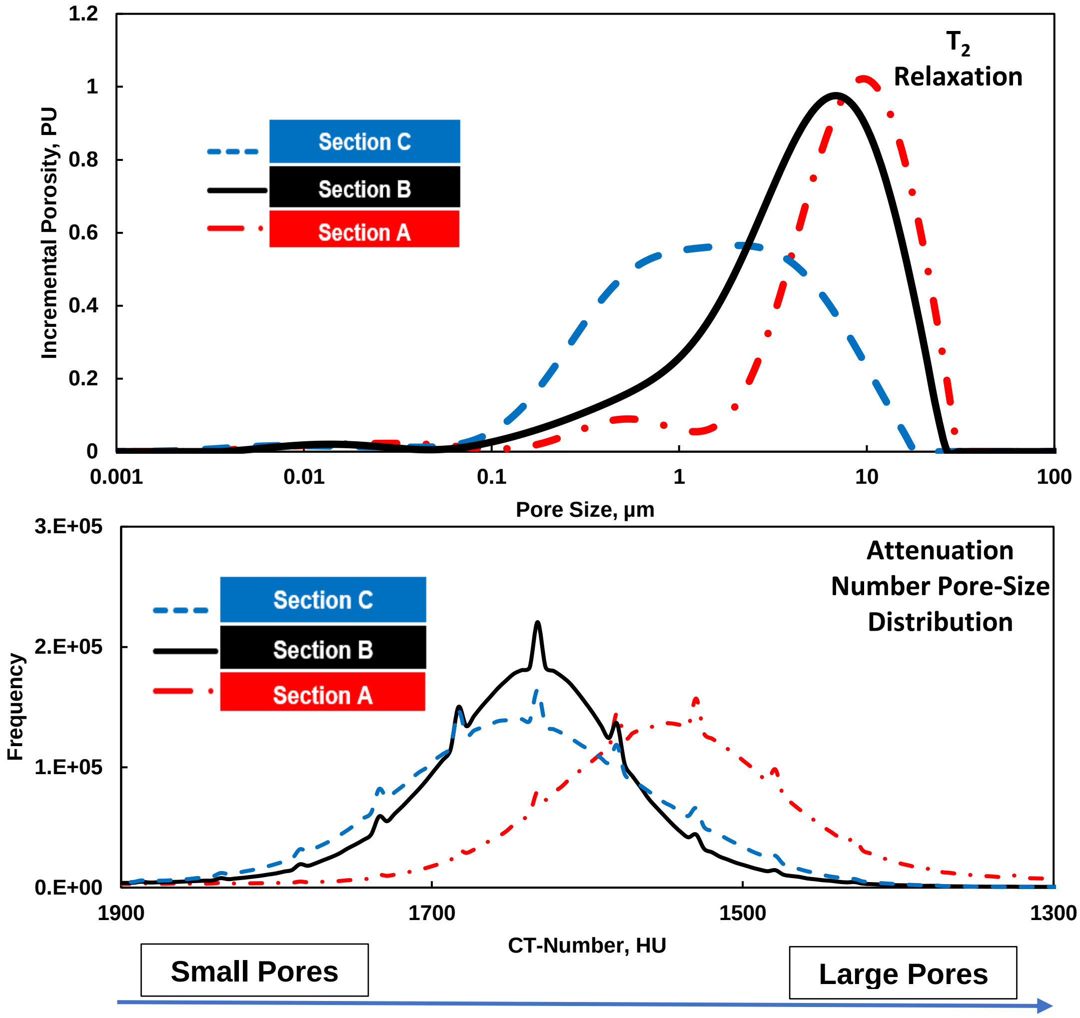

Fig. 79— Pore size distribution driven from T2 relaxation time versus pore size distribution driven from attenuation number for Berea sandstone after HCl and mud acid at 150°F. Core was saturated as follow: 5 wt% NH4Cl brine, deionized water, brine saturated, 12 wt% HCl, brine postflush, 9 wt% HCl + 3 wt% HF, brine post flush.

The treatment of the Grey Berea cores at 250˚F showed the sensitivity of the Berea formation for elevated temperature during matrix acidizing. The composited and segmented core presentations (**Fig. 80**) showed the increase in the dissolution in the core inlet. The damage also increased with the increase of the temperature. This came as a denser purple section in the mid and outlet sections of the core.

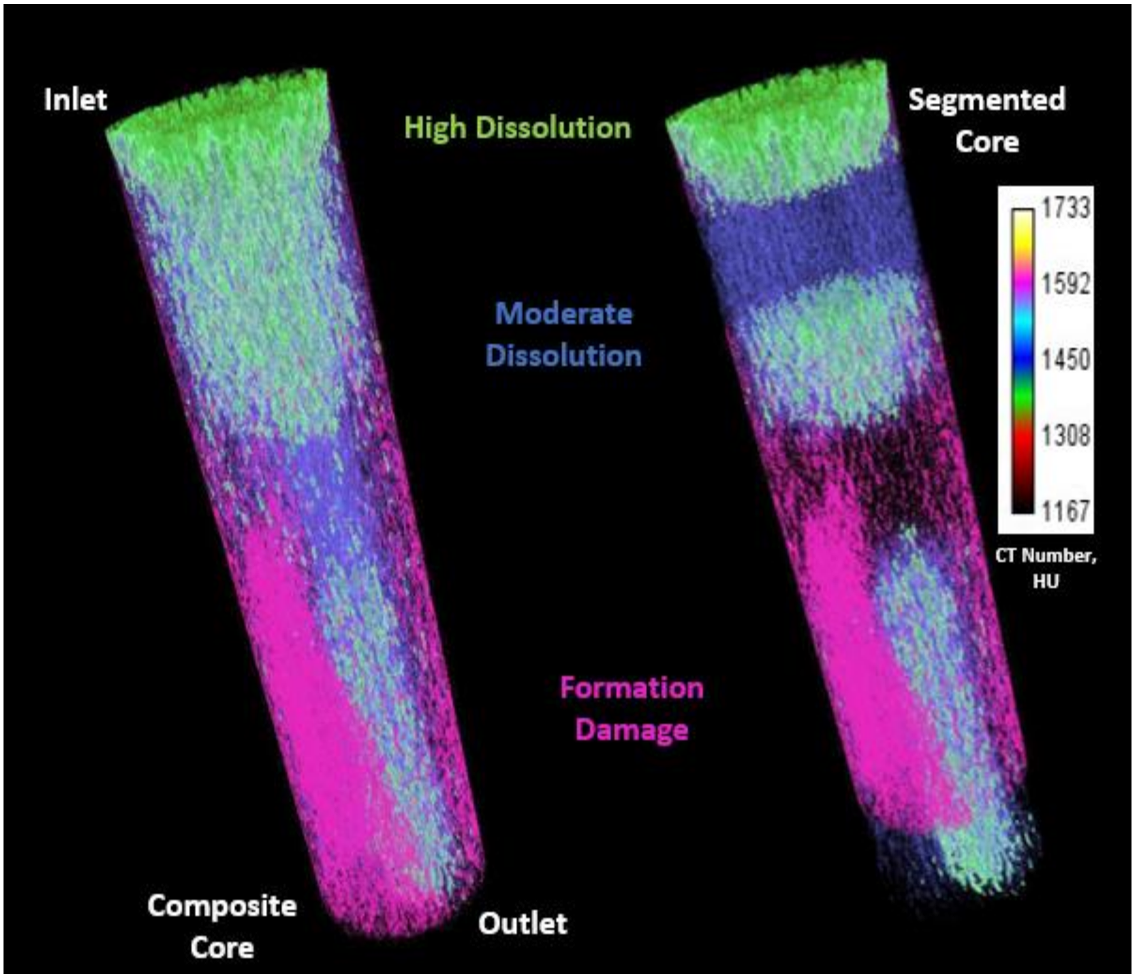

Fig. 80— Computed tomography 3D segmentation of the dissolved and deformed zones in Berea sandstone after HCl and mud acid stages at 250°F. Core was saturated as follow: 5 wt% NH_4Cl brine, deionized water, brine saturated, 12 wt% HCl, brine postflush, 9 wt% HCl + 3 wt% HF, brine post flush. Purple zones are low porosity, blue zones are moderate porosity, and green zones are high porosity.

The Pore size distribution (**Fig. 81**) came supporting this interpretation showing a domination of smaller pore sizes in the mid and the outlet sections. The attenuation number histogram followed the NMR distribution proving the validity of the interpretations of the 3D representation of the core after stimulation.

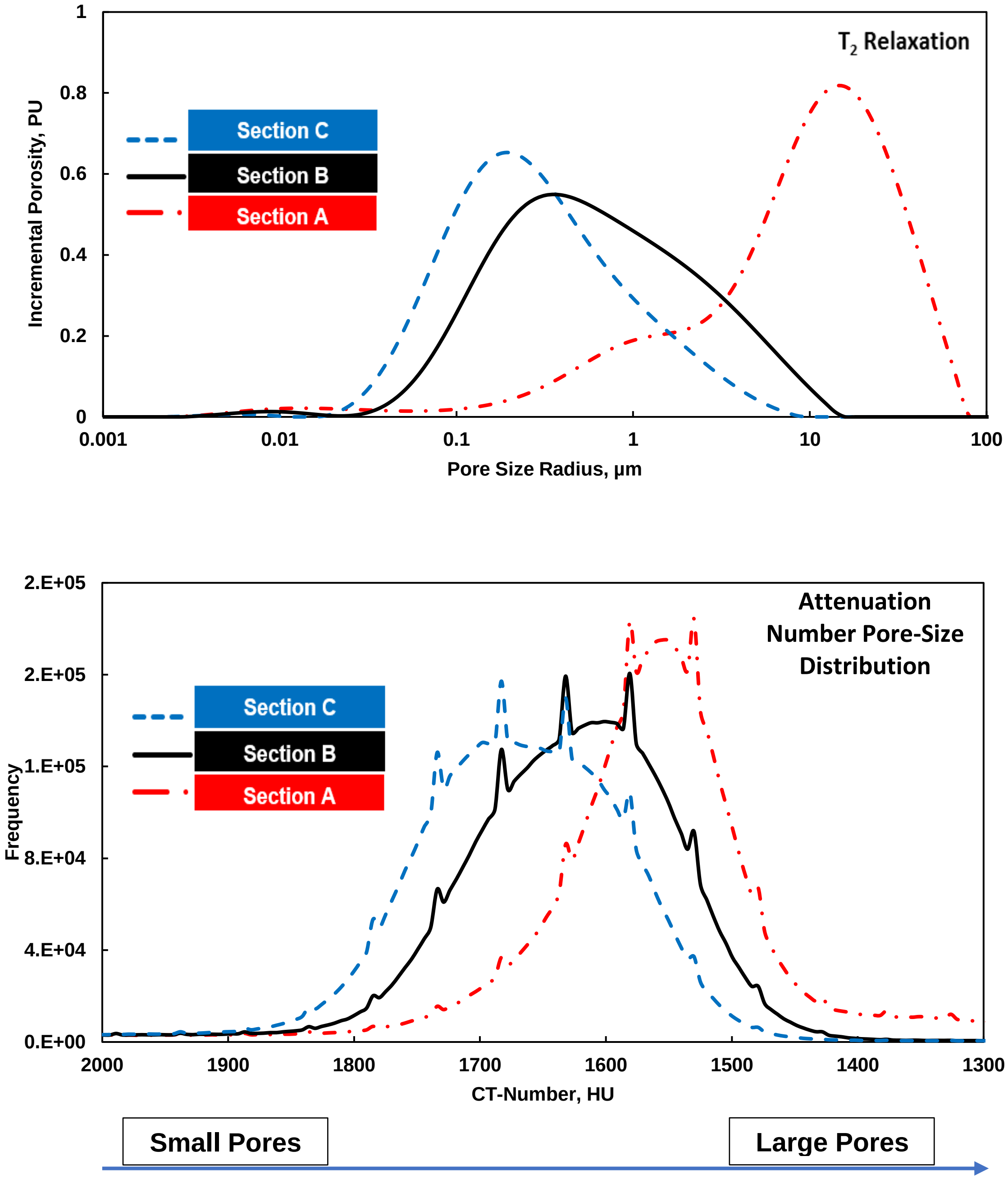

Fig. 81— Pore size distribution driven from T_2 relaxation time versus pore size distribution driven from attenuation number for Berea sandstone after HCl and mud acid at 250°F. Core was saturated as follow: 5 wt% NH_4Cl brine, deionized water, brine saturated, 12 wt% HCl, brine postflush, 9 wt% HCl + 3 wt% HF, brine post flush.

Although, the total clay content of the Berea sandstone is 7 wt% its impact on the core was severe. The scattered nature of the clay particles eased its mobilization to the core mid and outlet sections. The presence of illite and chlorite minerals in direct contact to the acid species during stimulation resulted in the production of silica gel among other forms of formation damage along the acid pass. The acid succeeded in opening a high dissolution channels at high temperature. Yet, the formation damage intensity around those channels came as strong as the dissolution. The low concentration of the carbonate minerals also reduced the ability of the acid to induce larger high dissolution channels at higher temperatures.

Impact of Acid Stimulation in Bandera Sandstone

As Bandera sandstone has a different clay nature and different response during the fines migration damage induction, the result upon stimulation was expected to be different. The injecting of a preflush stage of 15 wt% HCl and a mud acid stage of 12 wt% HCl and 3 wt% HF resulted in an enhancement in the core permeability. The closer examination of the core CT-scans using the new approach presented in this paper showed more information about the nature of the reaction pass during the stimulation. The data presented in **Fig. 82** shows the composited and segmented cores after stimulation at 150 and 250˚F. The first data set at 150˚F shows the dissolution channels getting thinner as it moves across the core toward the outlet. The interbedded low porosity sections shown earlier (Fig. 77) are witnessing re-arrangement. The segmented volume of the core is showing that the low porosity sections are getting thicker and connected as acid moves toward the core outlet. This data shows that the acid reacted with the clay minerals and resulted in redistribution of silica gel and other formation damage products from the clay reaction with HCl and HF. The last 2 in. of the core shows a heavily impacted area with a singular channel of moderate porosity gain, which is the only channel to explain the core permeability enhancement upon stimulation.

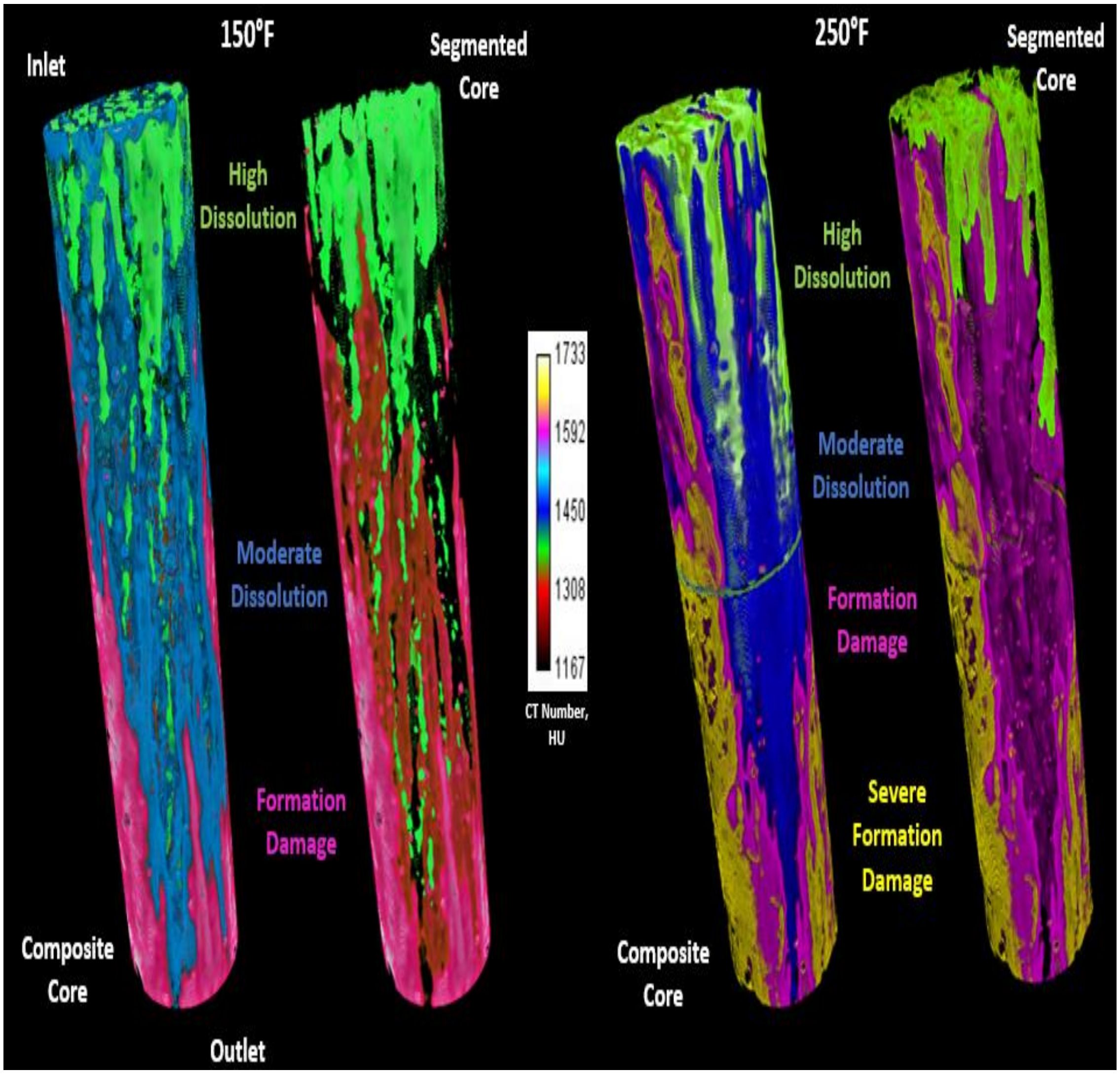

Fig. 82— Computed tomography 3D segmentation of the dissolved and deformed zones in Bandera sandstone before and after HCl and mud acid stages at 150 and 250°F. Cores were saturated as follow: 5 wt% NaCl brine, deionized water, brine saturated, 15 wt% HCl, brine postflush, 12 wt% HCl + 3 wt% HF, brine post flush. Yellow zones are very low porosity, purple zones are low porosity, blue zones are moderate porosity, and green zones are high porosity.

Again the NMR pore size distribution (**Fig. 83**) was compared to the pixel to pixel attenuation number histogram to validate the visualized data interpretation. Both data sets showed that the pores in the inlet section exhibited enlargement, which complies with the green section in the segmented core representation. The core outlet showed a reduction in the frequency of the large pores and an increase in the frequency of the smaller pores, which also complies with the density of the purple sections in the segmented core at 150˚F.

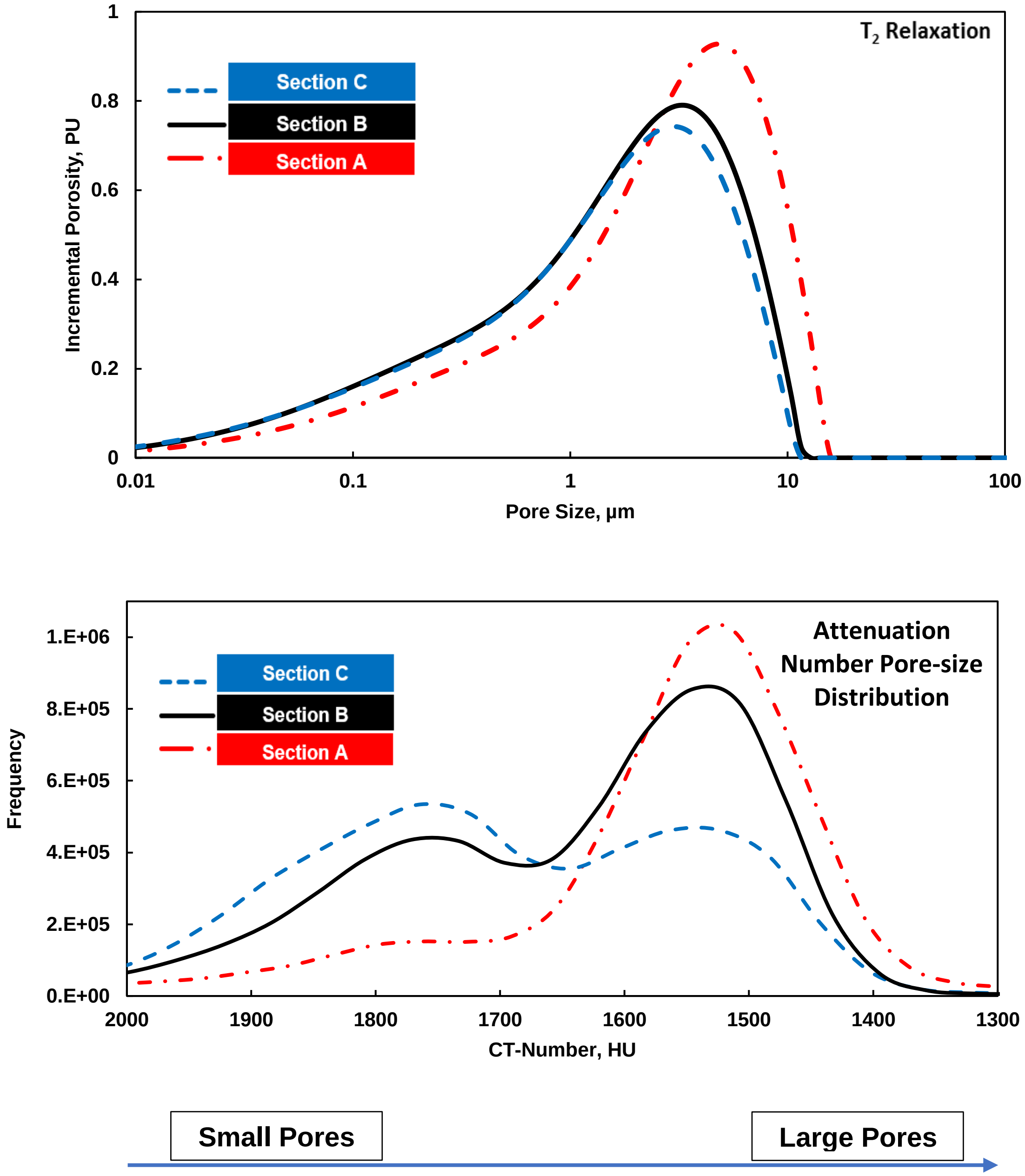

Fig. 83— Pore size distribution driven from T_2 relaxation time versus pore size distribution driven from attenuation number for Bandera sandstone after formic acid and mud acid at 150°F. Core was saturated as follow: 5 wt% NaCl brine, deionized water, brine saturated, 15 wt% HCl, brine postflush, 12 wt% HCl + 3 wt% HF, brine post flush.

The stimulation at 250˚F showed a determinate impact on the core. Although, the permeability was enhanced after the stimulation the composited and segmented core representation showed a severe pattern of formation damage. The segmented core in Fig. 82 shows that the low porosity formation damage purple sections is extending from the core inlet to the core outlet. Upon subtracting the moderate porosity region a connected packed body of low porosity was present and grows thicker toward the core outlet. The high temperature this time was not enough to force a continuous high dissolution channel from the core inlet to the outlet. The moderate porosity that continued and went thinner toward the core outlet is the only gain in porosity to explain the overall permeability enhancement. The stimulation at high temperature accelerated the clay reactions with the acid by attacking the clay bodies and precipitating different forms of formation damage such as silica gel and AlF_x compounds (Walsh et al. 1982; Simon and Anderson 1990; Gdanski 1994, 1998, and 1999).

The pore size distribution and the attenuation number histogram once again came supporting to the suggested interpretation from the CT-scan data. The distribution in **Fig. 84** shows an enlargement of the inlet section pore size and reduction in the middle and outlet sections of the cores. The core petrophysics and its relation with the clay content and its nature are shown to be controlling variables to the matrix stimulation process. The big bodies of clay minimized the surface area of reaction with acid at low temperatures, but resulted in a higher magnitude of damage at higher temperatures. The presence of high percentage of dolomite mineral helped to minimize the damaging impact of the clay mineral interaction with acid. The high-temperature stimulation accelerated the dissolution of the dolomite mineral and resulted in a singular channel to enhance the permeability.

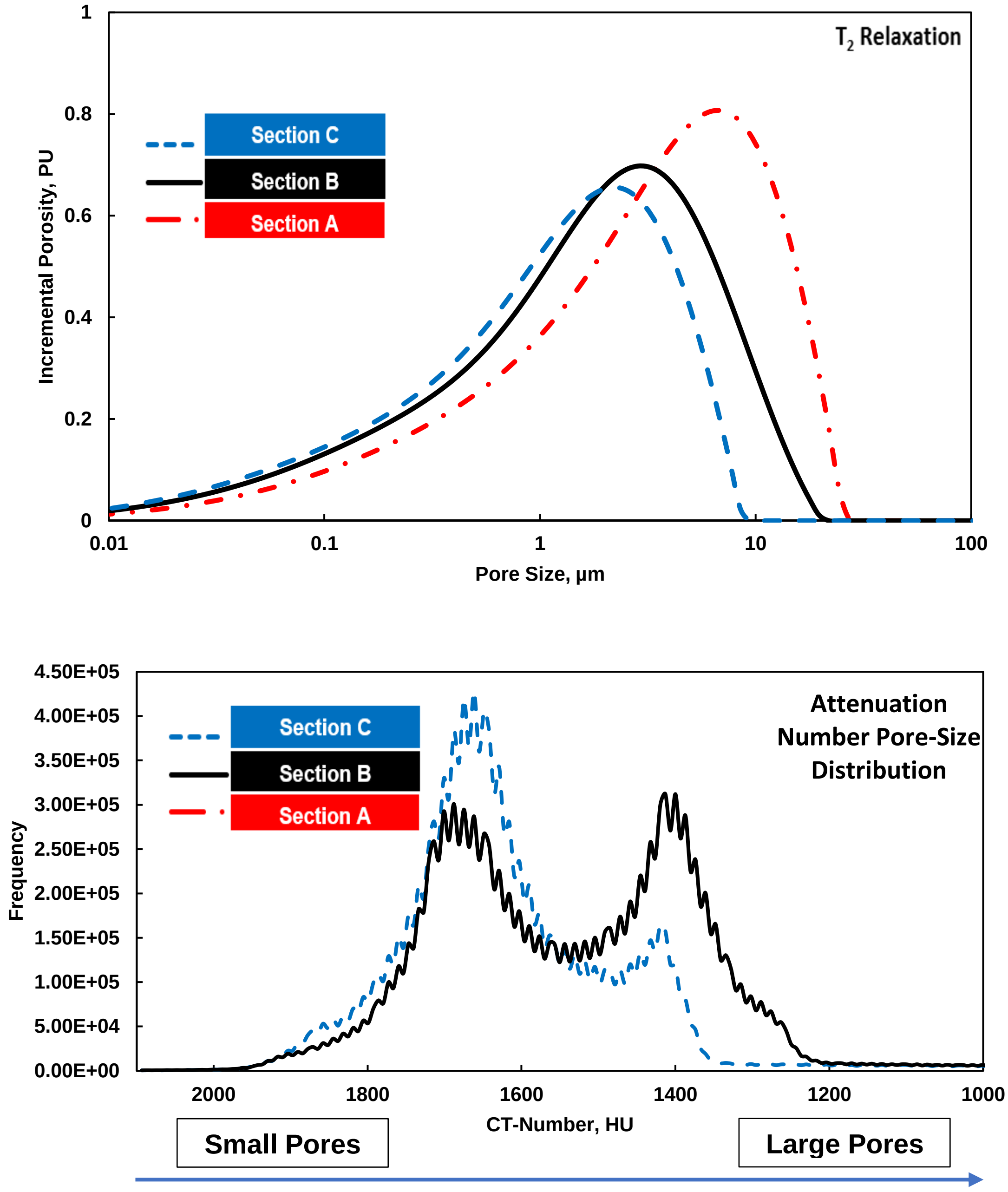

Fig. 84— Pore size distribution driven from T_2 relaxation time versus pore size distribution driven from attenuation number for Bandera sandstone after formic acid and mud acid at 250°F. Core was saturated as follow: 5 wt% NaCl brine, deionized water, brine saturated, 15 wt% HCl, brine postflush, 12 wt% HCl + 3 wt% HF, brine post flush.

Impact of Acid Stimulation in Kentucky Sandstone

The low permeability of Kentucky sandstone makes it unsuitable candidate for matrix acidizing. Since Kentucky sandstone contains 14 wt% clay content similar to the Bandera Sandstone, its clay nature and the absence of carbonate minerals are the reasons to include it in this study. The stimulation of this formation was conducted by injecting 9 wt% formic acid followed by mud acid of 9 wt% HCl and 3 wt% HF. The stimulation was only conducted at 250˚F. The close examination of the computed tomography data before and after stimulation shows that the low porosity purple bodies are slightly altered. The data in **Fig. 85** shows that the acid intensively dissolved the core face then proceeded in a channel of relatively high dissolution rate from the core inlet to the outlet as shown in the green body in the segmented core after stimulation. The low porosity bodies were shown wider and extended in the core inlet. Yet, their changes were minimal compared to the clays of the Bandera and Berea sandstone. The big continuous bodies of clays in the Kentucky sandstone minimized the acid interaction with the acid sensitive clays and minimized the corresponding formation damage.

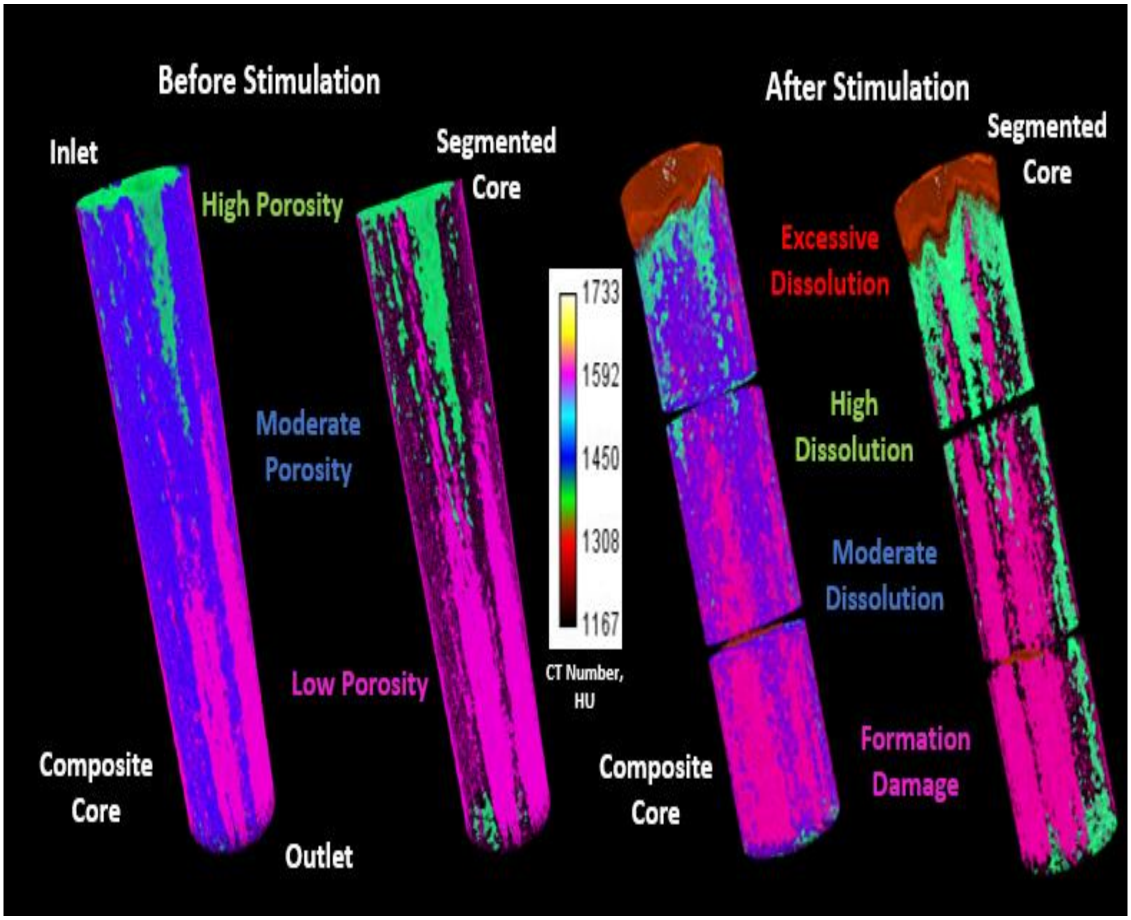

Fig. 85— Computed tomography 3D segmentation of the dissolved and deformed zones in Kentucky sandstone before and after formic acid and mud acid stages at 250°F. Core was saturated as follow: 5 wt% NH_4Cl brine, deionized water, brine saturated, 9 wt% formic acid, brine postflush, 9 wt% HCl + 3 wt% HF, brine post flush. Purple zones are low porosity, blue zones are moderate porosity, green zones are high porosity, and red zones are very high porosity.

The NMR pore size distribution (**Fig. 86**) shows that the distribution was impacted by the dissolution in the inlet section but other than that there was not much changes in the small pore sizes frequencies. The attenuation number histogram exhibited a similar pattern. The clay nature and the pore structure of the Kentucky sandstone forced the acid to open a singular channel on one side of the core with minimal impact on the rest of the core. This data show the suitability of this formation for acid fracturing without worrying about formation damage from the acid interaction with the 10 wt% of the illite mineral.

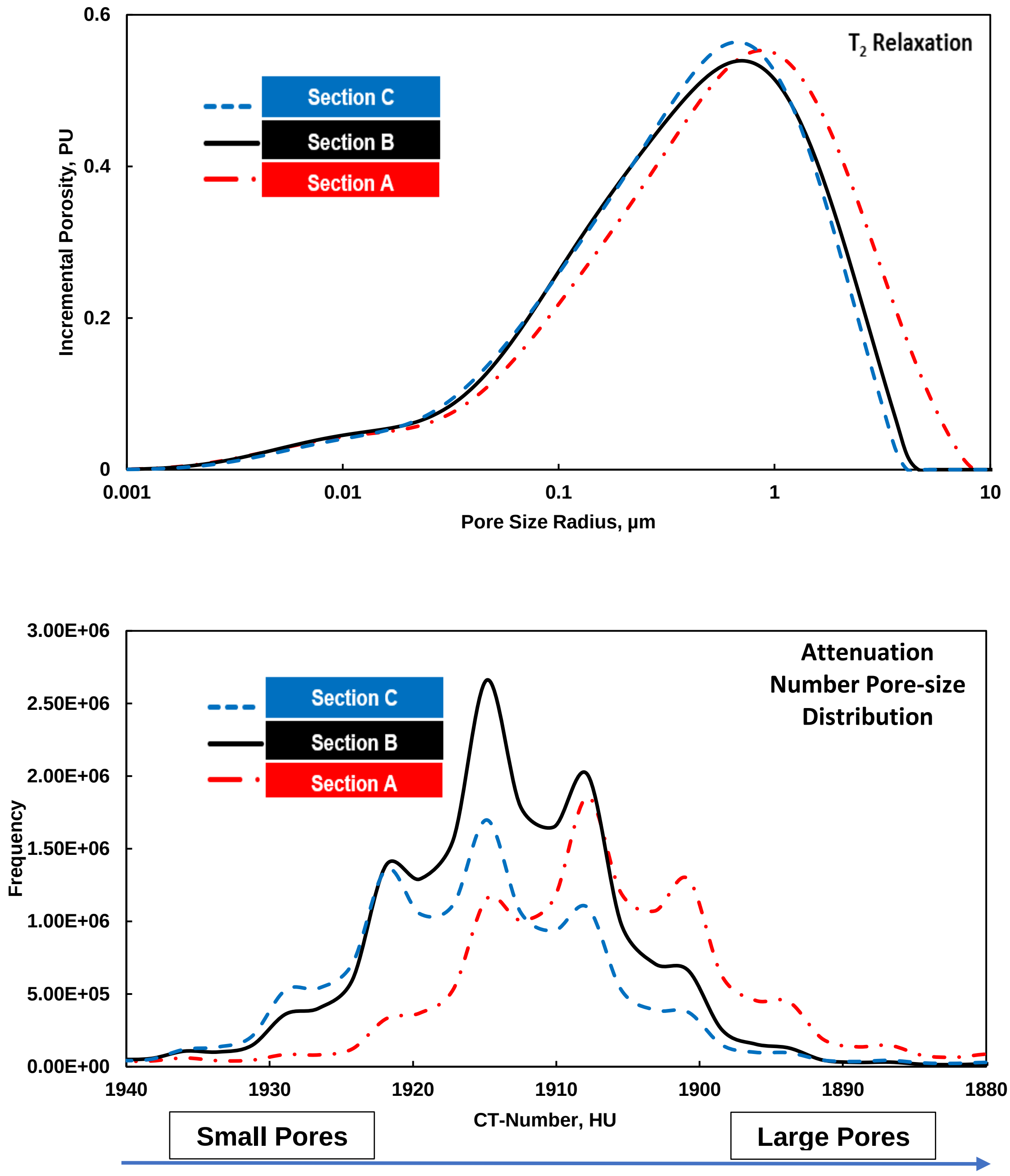

Fig. 86— Pore size distribution driven from T_2 relaxation time versus pore size distribution driven from attenuation number for Kentucky sandstone after formic acid and mud acid at 250°F. Core was saturated as follow: 5 wt% NH_4Cl brine, deionized water, brine saturated, 9 wt% formic acid, brine postflush, 9 wt% HCl + 3 wt% HF, brine post flush.

Conclusions

This study examined the impact of the clay content and its nature of presence in the pore structure on the outcome of the matrix acidizing process of different sandstone cores. The impact of temperature on Bandera and Grey Berea cores was investigated. Using the computed tomography segmentation combined with NMR pore size distribution the following conclusions were obtained:

1- Regardless of the total clay content, its presence in the sandstones pore throats as small and scattered particles makes it susceptible to mobilization and leads to an intensive fines migration damage.

2- The stimulation of sandstones with low but scattered clay content using HCl and HF results in severe deposition of silica gel and other forms of damage along the acid path at 150 and 250°F.

3- Sandstones with high clay content that is present as small interbedded bodies is less susceptible to fines migration damage and have a higher stability against HCl and HF acids up to 150°F.

4- The larger and the more connected the clay content in the treated sandstones the less vulnerable it becomes to fines migration or acid induced damages up to 250°F.

5- The enhancement of permeability after HCl and HF injection in sandstones damaged by fines migration is a result of narrow channels induced by acid between a heavily damaged matrix.

This work introduced a novel criterion and a new method to evaluate different sandstone formations to determine its suitability for matrix acidizing. It highlights the importance of describing the nature of the clay minerals in the formations and how it impact the stimulation process.

CHAPTER VI

NEW VISCOELASTIC SURFACTANT WITH IMPROVED DIVERSION CHARACTERISTICS FOR CARBONATE MATRIX ACIDIZING TREATMENTS[8]

Summary

Viscoelastic surfactants (VES) have been used to replace polymer-based fluids as effective, cleaner, and non-damaging viscofying carriers in frac-packing, acid fracturing, and matrix acidizing. However, several limitations challenge the use of VES-based fluids including: thermal instability, incompatibility with alcohol-based corrosion inhibitor, and intolerance to the presence of contaminating iron. This work introduces a new VES-based acid system for diversion in matrix acidizing that exhibits excellent thermal stability and diversion performance in both low-and high-temperature conditions.

Rheology measurements were conducted on spent VES-acid system as a function of temperature (77-300°F) at a pH of 4-5. The effect of acidizing additives on the VES viscosity was investigated. The additives included a corrosion inhibitor, non-emulsifier, iron-chelating agent, and iron-reducing agent. Single and dual coreflood experiments were performed using limestone core samples with an initial permeability range of 4-200 md and a permeability contrast of 1.5-55. Post CT-scan imaging was conducted to investigate the wormhole topography. The diversion characteristic of the new VES in the dual

---

[8] Reprinted with permission from “New Viscoelastic Surfactant with Improved Diversion Characteristics for Carbonate Matrix Acidizing Treatments” by Hanafy, A. M., Nasr-El-Din, H. A., Rabie, A. et al. 2016. Presented at the SPE Western Regional Meeting, 23-26 May, Anchorage, Alaska, USA, copyright 2016 by the Society of Petroleum Engineers. Reproduced with permission of SPE. Further reproduction prohibited without permission.

coreflood experiments was evaluated by the structure and the extent of wormhole propagation in the low-permeability core.

Rheological data for 15 wt% HCl spent VES-solutions showed a maximum viscosity of 200-800 cp over a temperature range of 150-170°F, depending on the VES concentration in the sample. Without acidizing additives, a minimum of 50 cp was obtained at 195, 230, 250, and 275°F at 4, 5, 6, and 8 vol% of the VES in solution, respectively. None of the tested acidizing additives had a negative impact on the VES viscosity. At 8% VES loading, the acidizing package was optimized such that a minimum of 75 cp was obtained at 300°F.

Dual coreflood experiments were conducted at 150 and 250°F, and the results proved the ability of the proposed VES to divert efficiently in limestone formations. Single coreflood experiments also confirmed these results. Coreflood data indicated that a range of permeability contrast of 4-10 is the optimum for diversion ability in terms of the final permeability enhancement of the low-permeability cores. The results revealed 18.6, 45.6, 82%, and infinity when the permeability contrast was 28.3, 14.4, 6.3, 1.63, respectively. A dual coreflood experiment was conducted for two cores with a permeability contrast of 1.6 at 150°F. The VES-acid system in the presence of all acidizing additives exhibited divergent performance that exceeded the performance of the VES in the absence of additives. These results prove the stable performance of the VES and the enhancement in viscosity response after addition of both the iron-control agent and the non-emulsifier, which resulted in less acid leak off and better wormhole structure.

Introduction

The aims of this work are to investigate the VES-based acid's ability for diversion at elevated temperatures and multiple permeability contrast ratios, and to evaluate the impact of iron contamination on the VES rheology and, by extension on its diversion ability. Moreover study the impact of acid additives on its diversion abilities.

Experimental Studies

Materials

Acid solutions used in this work were prepared by dilution from a concentrated HCl ACS-grade stock, obtained from Sigma Aldrich. Triplicate manual titration using a 1 N NaOH solution showed a concentration of 35.84±0.12 wt% of the concentrated stock. The viscoelastic surfactant was a cationic surfactant. Calcium chloride was an ACS grade obtained from Sigma Aldrich. Derivative of alkynyl alcohol was used as a corrosion inhibitor. An iron-controlling agent (33 wt% solution of ammonium Nitrilotri-acetate), cationic non-emulsifier, and mercaptan-based iron reducing agent were used as additives to the acid package.

Rheology Measurements

VES samples were prepared to simulate spent conditions of 15 wt% HCl. Therefore, for each 100 ml of spent acid sample, 93 ml of 30 wt% $CaCl_2$, 1 ml of a corrosion inhibitor (CI), 6 ml of the viscoelastic surfactant (VES), 0.1 ml of iron controlling agent, and 0.1 ml of a non-emulsifier were mixed using a high-shear-rate blender. The trapped air bubbles were removed using a centrifuge at 4000 rpm for 20 minutes. A Grace 5600 rheometer was used to conduct all viscosity measurements as a function of temperature

(75-300°F) at 400 psi. All parts in contact with the sample were manufactured from Hastelloy C-276 to resist acids.

Coreflood Setup

A coreflood setup, illustrated in **Fig. 87**, was used to simulate the matrix stimulation treatment. The figure shows a dual (parallel) coreflood experiment. In the case of single coreflood experiments, the same setup was used with only one core holder. A pressure regulator was used to apply a back pressure of 1,100 psi on the outlet of both cores. This pressure is enough to maintain the CO_2 dissolved in the spent fluid (Fredd and Fogler 1998b). A pressure transducer was connected to each of the core holders to measure the pressure drop and transfer the data to a connected computer. A hand pump was used to provide an overburden pressure of 1,600 psi for both cores. A new core was used in each experiment, and the cores were imaged using a CT scan technique after each run. All experiments were conducted in a closed oven to provide a constant uniform temperature. Samples from the core effluent were collected throughout the experiment, diluted, and subjected to Ca and Fe concentration measurements using an Inductively Coupled Plasma spectrometer (or ICP).

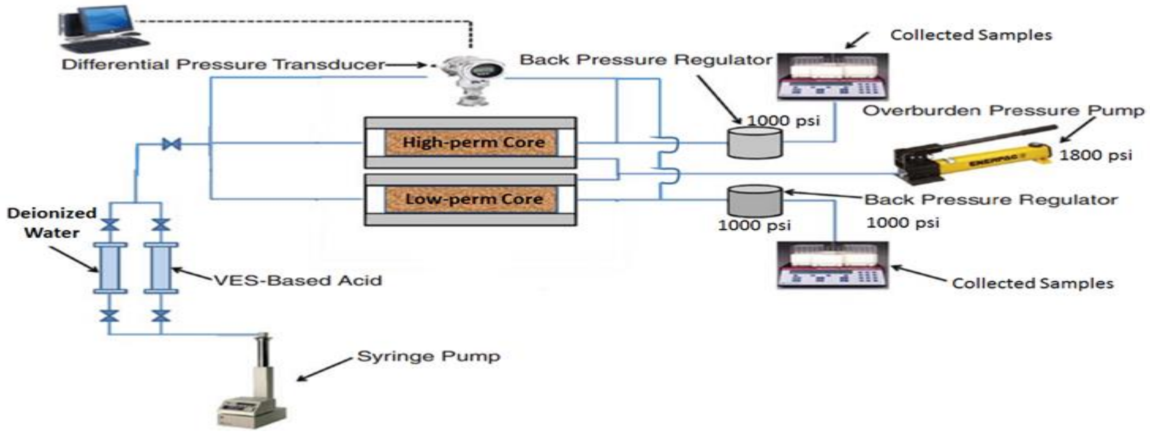

Fig. 87— Dual coreflood setup.

Coreflood Procedure

The procedure outlined below was followed for all coreflood experiments:

1. Through the valves on the inlet line of each core holder, deionized water was injected in one core at a time at room temperature using several injection rates until the pressure drop stabilized, and the initial permeability, pore volume, and porosity were determined.
2. The injection rate was then adjusted to 1 cm^3/min, and the flow was allowed to enter both cores. The core holder, inlet, and outlet lines were all kept in an oven, in which temperature was then adjusted to the desired temperature (150 or 250°F).
3. After pressure stabilization at the new temperature, the flow switched from deionized water to the VES-based acid solution. The pressure drop was then recorded until breakthrough was observed.
4. A post-coreflood CT scan was then conducted on both cores, and the corresponding 3D images were generated.

Results and Discussion

Rheology Measurements

Viscosity of VES spent solutions was quantified as a function of temperature at a shear rate of 100 s^{-1}. After preparation, the pH of the solution was adjusted to be between 4-5 using potassium hydroxide. Viscosity of the VES solutions was measured in the presence and the absence of most of the common acidizing additives such as corrosion inhibitor, iron-chelating agent, iron-reducing agent, and non-emulsifier. **Fig. 88** illustrates the viscosity measurements of the new VES in the absence of acidizing additives at concentrations of 4-8 vol% as a function of temperature. For all data sets, a maximum viscosity was observed over a range of temperature between 150-170°F. The magnitude of the viscosity at these peaks varied from 200-800 cp, showing that the VES can perform efficiently for low-temperature acidizing. Increasing the VES concentration significantly increased the viscosity and extended the temperature range in which the VES can be applied. With a minimum of 50 cp, the VES can be used at 195, 230, 250, and 275°F at 4, 5, 6, and 8 vol%, respectively.

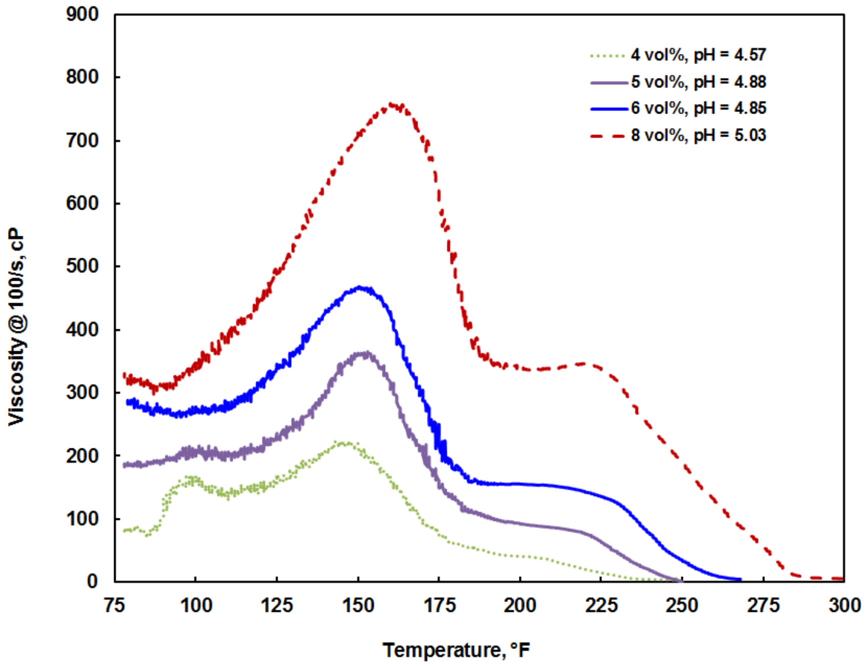

Fig. 88— Viscosity of the VES solutions in spent conditions at 4-8 vol% in the absence of acidizing additives as a function of temperature.

The viscosity of the VES solutions was then measured at different VES concentrations in the presence of several types of acidizing additives, such as a corrosion inhibitor (5 gpt), non-emulsifier (1 gpt), iron controlling agent (1 gpt), iron reducing agent (3 gpt). None of these measurements showed a significant reduction in viscosity (**Fig. 89**). The viscosity of the VES solutions was also measured with different loads of a corrosion inhibitor in the presence of the other acidizing additives. The data, shown in **Fig. 90,** indicates a very good level of compatibility, which did not affect the VES viscosity as reported for other VES systems (Nasr El-Din et al. 2008).

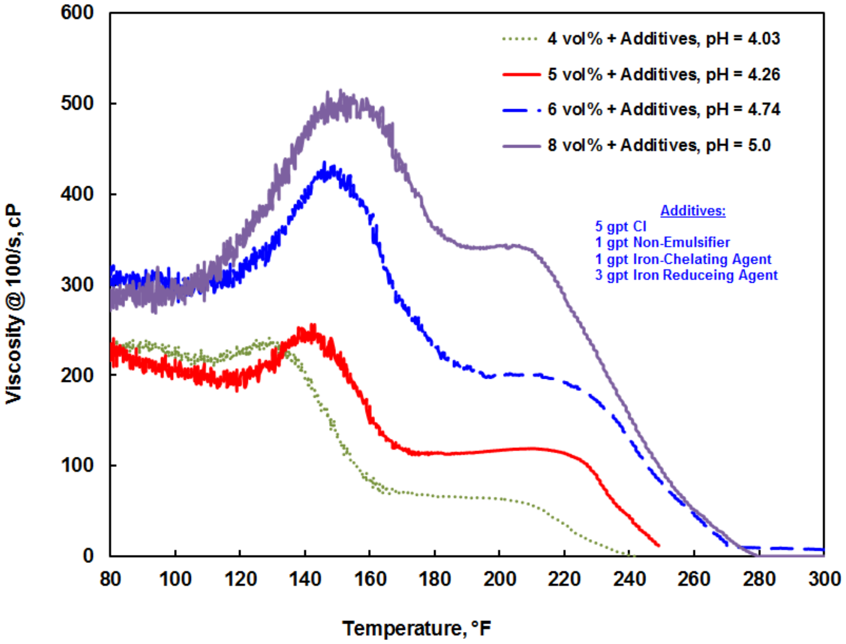

Fig. 89— Viscosity of the VES solutions in spent conditions at 4-8 vol% in the presence of acidizing additives as a function of temperature.

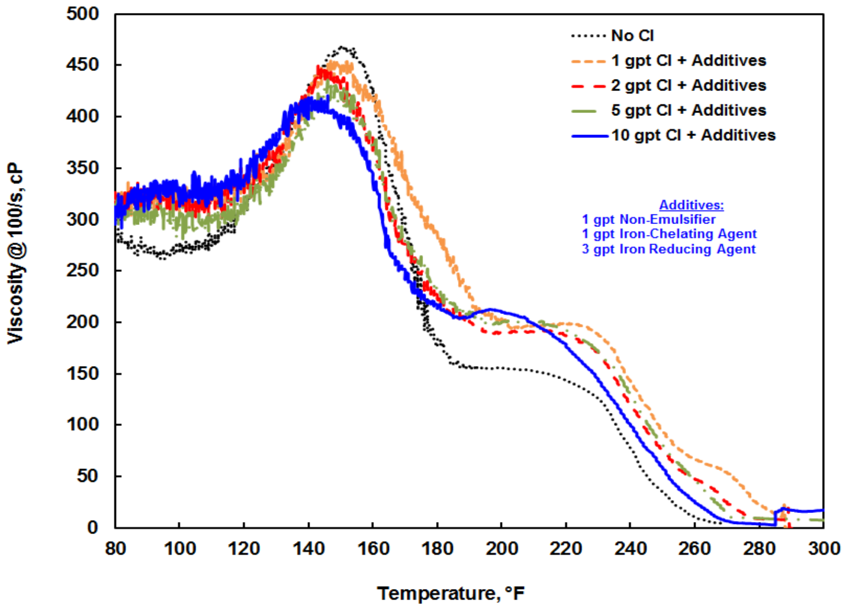

Fig. 90— Viscosity of 6 vol% of VES solutions in spent conditions at different loads of a compatible corrosion inhibitor in the presence of acidizing additives as a function of temperature.

Fig. 91 shows the viscosity of the new VES at 8 vol% without additives, in the presence of additives, and in the presence of additives with 50 pptg of potassium iodide as a corrosion intensifier. At this particular concentration of VES, the presence of additives was found to enhance the viscosity such that at 300°F a 75 cp can be reached with the presence of the whole package of additives, and a 50 cp can be achieved with additives and the intensifier. This data shows that optimizing the package in terms of the concentration of each component can be targeted to meet both viscosity and corrosion requirements.

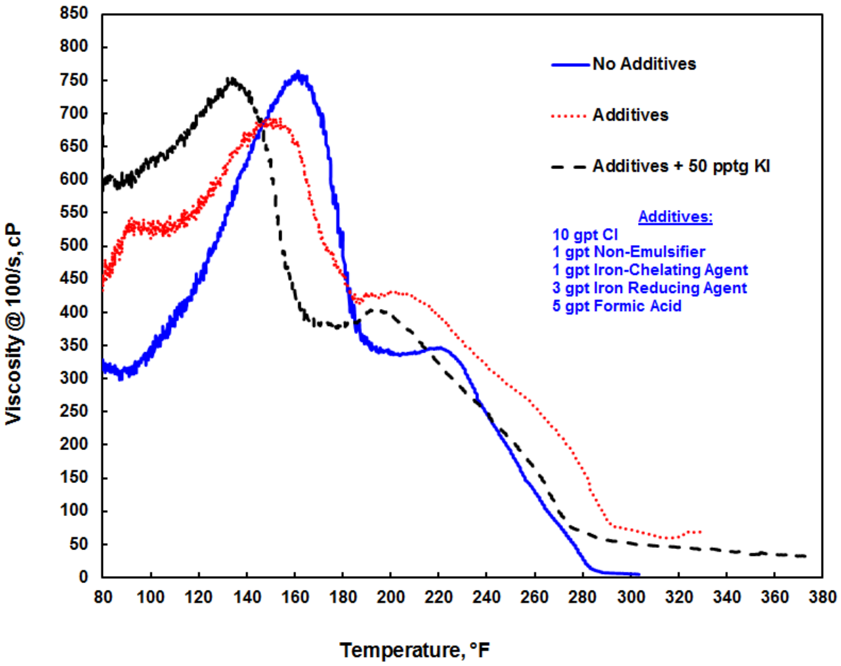

Fig. 91— Viscosity of 8 vol% of VES solutions in spent conditions with additives in the presence and absence of a corrosion intensifier.

Dual Coreflood for Diversion Evaluation

Using low- and high-permeability cores with initial porosity and permeability (**Table 13)**, the first dual coreflood (DC-01) test was conducted at 150°F. This run was performed using two cores with permeability of 119.6 and 4.23 md, respectively. This is equivalent to an initial permeability contrast of 28.3.

Table 14 gives other relevant test conditions. The results (**Fig. 92)** shows the pressure drop across the two cores against the cumulative injected volume. The data clearly show a proper degree of diversion supported by the cyclic profile in the pressure drop. A maximum increase in pressure drop rose from the base line (3.15 psi) to 34.8 psi, i.e. 11 fold. A breakthrough was observed in the high-permeability core after the injection of 0.72

PV, which was calculated based on the pore volume of both cores. **Table 15**, gives other related data.

Core	**Core Pore Volume, cm^3**	**Porosity, Vol%**	**Initial Permeability, md**
Low-Perm, LP-70	26.17	15.06	4.23
High -Perm, HP-03	26.78	15.41	119.6

Table 13— Comparison of the two cores used in dual coreflood DC-01.

HCl Concentration, wt%	15
VES Concentration, Vol%	4
CI Concentration, Vol%	1
Temperature, °F	150
Injection Rate, cm^3/min	1

Table 14— Test conditions for dual coreflood DC-01.

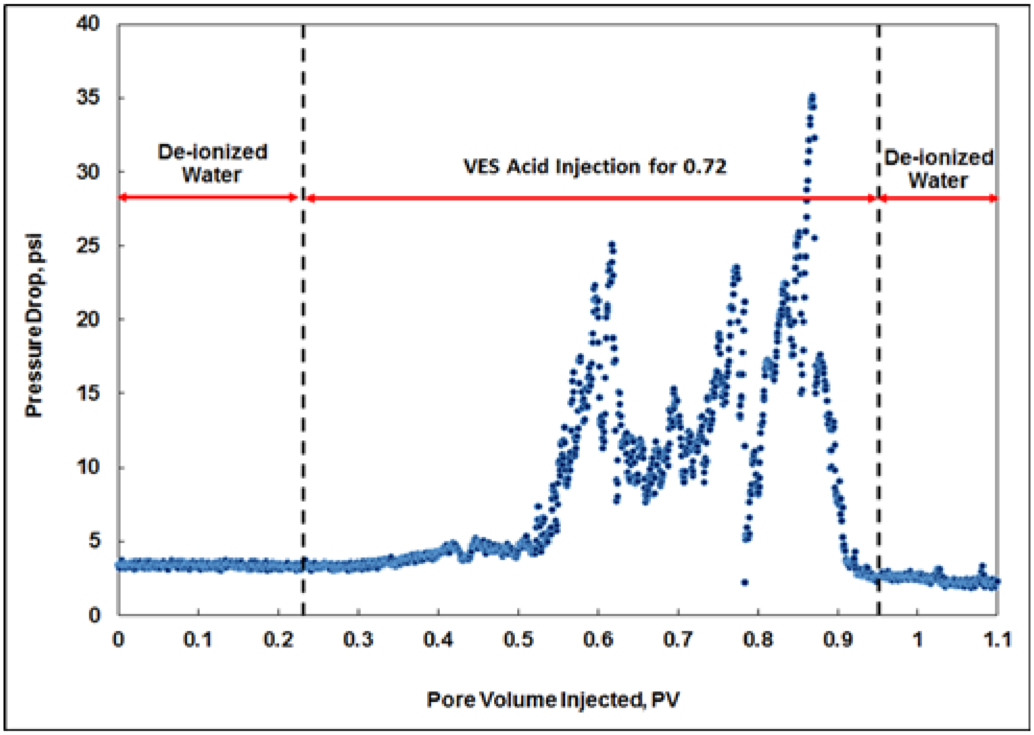

Fig. 92— Pressure drop across the cores during the injection of the VES-based acid solution in coreflood DC-01.

	Coreflood DC-01	**Coreflood DC-02**	**Coreflood DC-03**	**Coreflood DC-04**
Injection Flow Rate, cm3/min	1	1	1	1
Pore Volume of both Cores, cm3	52.95	52.95	47.6	45.83
Total Acid Injected, PV	0.72	0.5	0.987	0.611

Table 15— Result data related to coreflood experiments: DC-01, DC-02, DC-03 and DC-04.

A post CT scan, illustrated in **Fig. 93**, showed the structure and determined the length of the wormhole created in each core. In the high-permeability core (HP-03), a deviated, branched wormhole was formed and reached the breakthrough. A shorter wormhole was also observed in the low-permeability core (LP-70). The acid was able to create a wormhole with a length of 1.12 in. in the low-permeability core, which is 18.6% of the total core length. The low diversion performance is anticipated to the high difference in permeability, which is believed to limit the flow in the low-permeability core, and, hence, shorten the wormhole propagation. The pressure drop profile and the CT-scan images after coreflood DC-01 showed a high degree of diversion in the high-permeability core (HP-03). Although a breakthrough was observed in the high-permeability core, the CT-scan image confirms that the acid was also able to stimulate part of the low-permeability core, and that a degree of diversion was obtained.

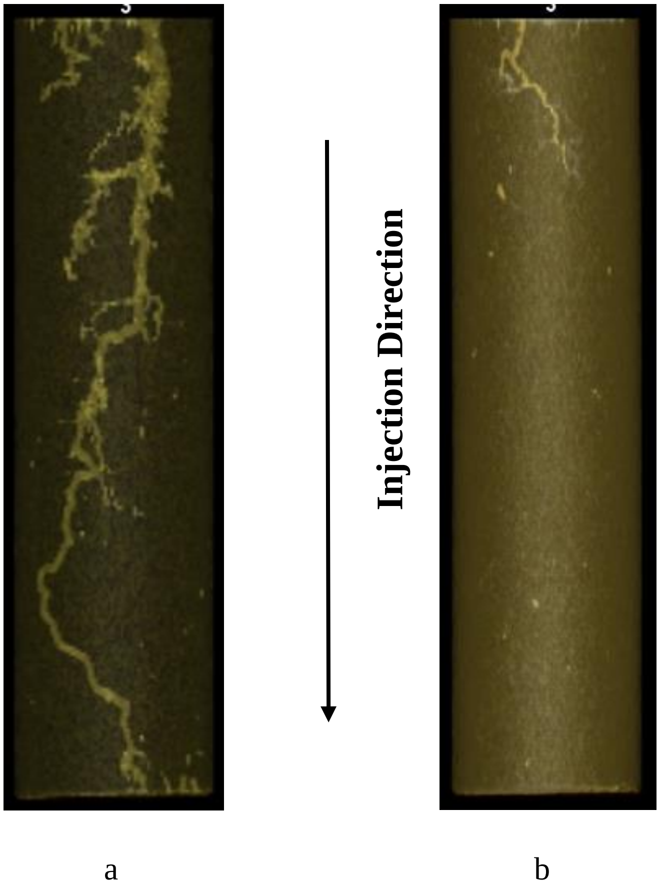

Fig. 93— 3D images of the wormholes created in the two cores used in core-flood DC-01: (a) HP-03, and (b) LP-70.

Fig. 94 shows the pressure drop across the core versus the cumulative injected pore volume for DC-02 at 150°F. In this test, the permeability contrast was reduced to 14.4. The results show a repeated cyclic profile in the pressure drop, indicating a good degree of diversion. The pressure drop increased from 1 to 7 psi after switching to the acid from a previous stabilized stage using DI-water.

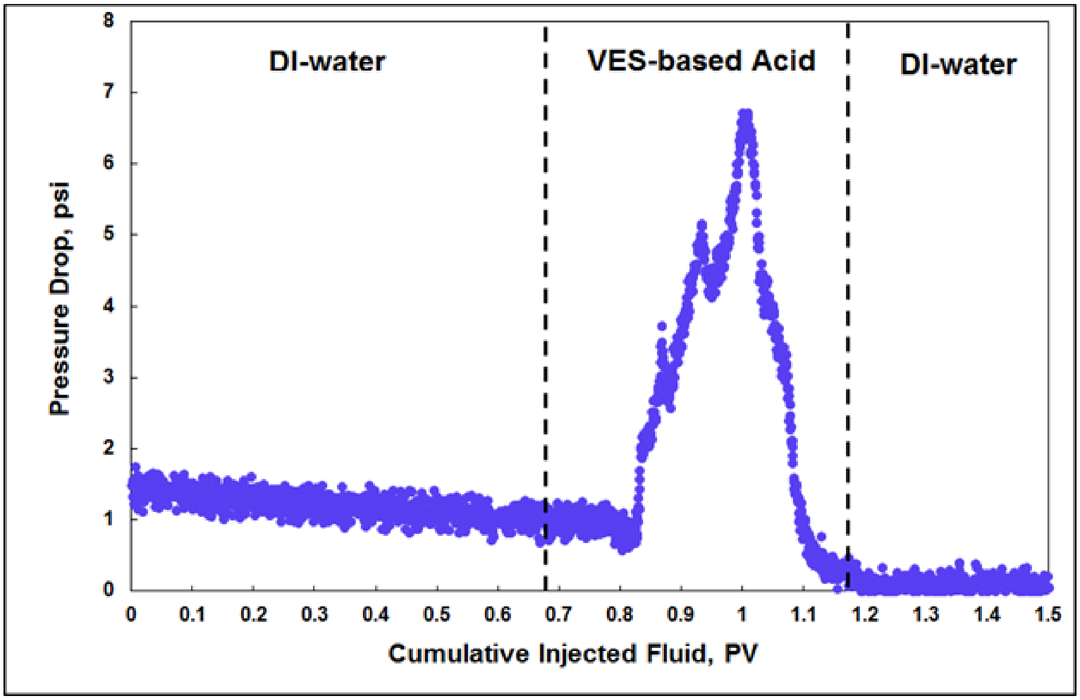

Fig. 94— Pressure drop across the core coreflood DC-02 at 150°F.

Fig. 95 shows the CT-image of the two cores after the test, and illustrates a complete wormhole (breakthrough) in the high-permeability core and a 2.74 inch wormhole in the low-permeability core. The latter represents a stimulation of 45.6% of the total length of the core (6 in.).Table 15**,** summarizes the main results of this test and shows that a total of 0.5 PV of the acid was consumed for the breakthrough in the high permeability core and the stimulated wormhole in the low-permeability core.

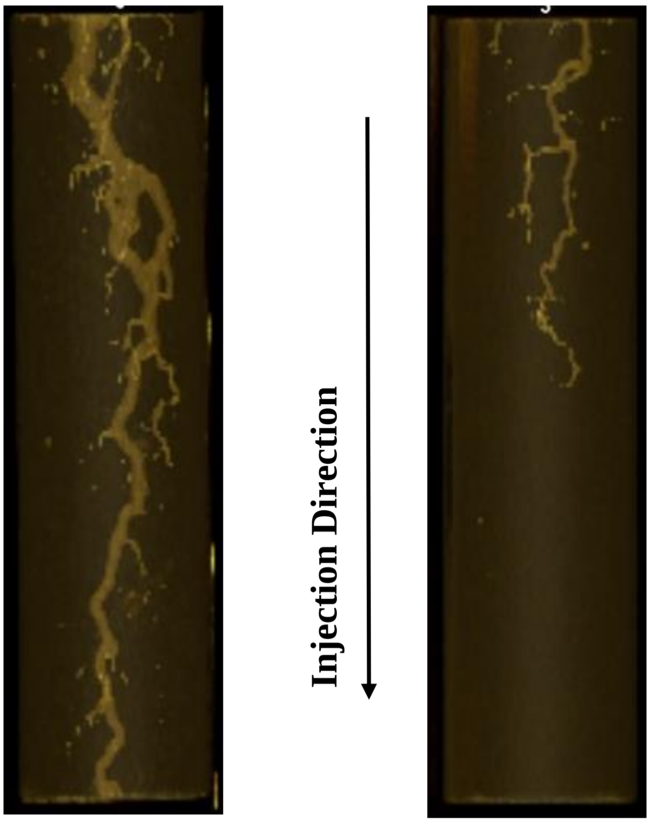

a b

Fig. 95— CT-image of the cores after the dual coreflood DC-02 at 150°F.

Fig. 96 shows a significant sign of the acid reaction on the core inlet for the high-permeability core (HP-04), as well as a sign for the breakthrough at the core outlet, while **Fig. 97** illustrates only a sign for the entering acid at the core inlet in the low-permeability core (LP-10) and no breakthrough.

a b

Fig. 96— Core inlet and outlet of the high-permeability core (HP-04) used in DC-02: (a) core inlet, and (b) core outlet.

a b

Fig. 97— Core inlet and outlet of the low-permeability core LP-10 used in DC-02: (a) core inlet, and (b) core outlet.

The permeability contrast was then reduced to 1.63 as in DC-03. The pressure drop profile is shown in **Fig. 98**. The pressure drop increased from 10 to 115 psi. The injection flow data appear in **Table 16**. The CT-images of the two wormholes formed in this test are shown in **Fig. 99** and interestingly demonstrate a reverse effect in which the complete worm holing (breakthrough) was observed in the low-permeability core, and a 3.6 in. wormhole was created in the high-permeability core. This change reflects the highest level of diversion in which the build-up viscosity in the high-permeability core forced the flow to stimulate the low-permeability core completely until the breakthrough. **Fig. 100** shows a comparison of the change in the length of the wormhole created in the low-permeability cores over the three experiments.

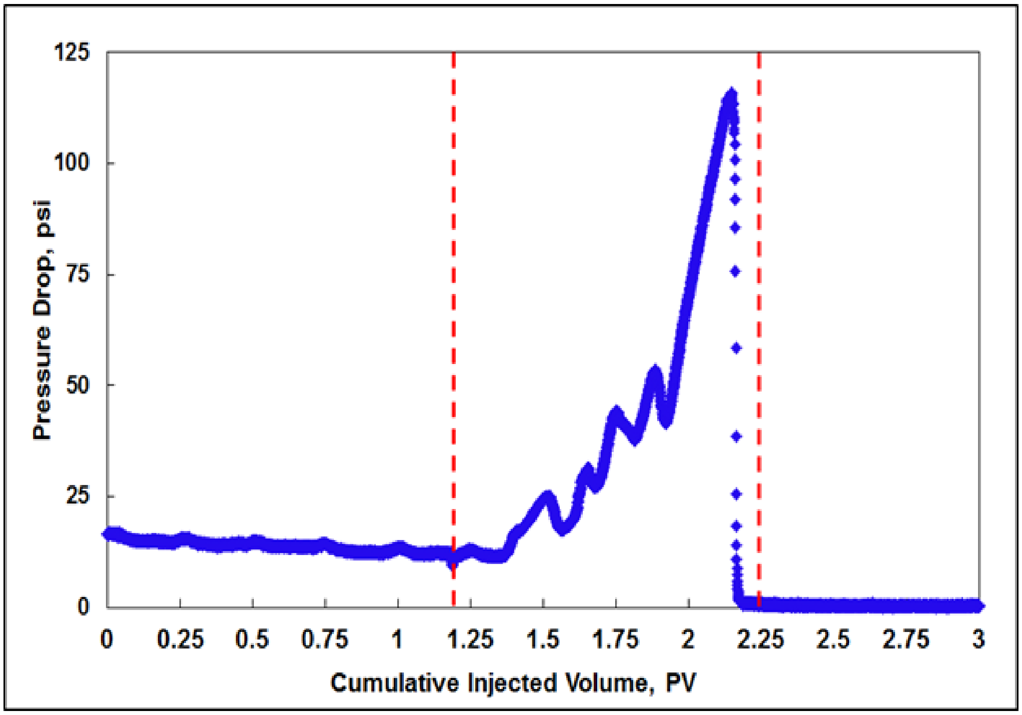

Fig. 98— Pressure drop across the core coreflood DC-03 at 150°F.

Core	Core Pore Volume, cm^3	Porosity, Vol%	Initial Permeability, md
MP-05	24.07	13.85	10
MP-01	21.78	12.35	8.6

Table 16— Core data for SC-01 and SC-02.

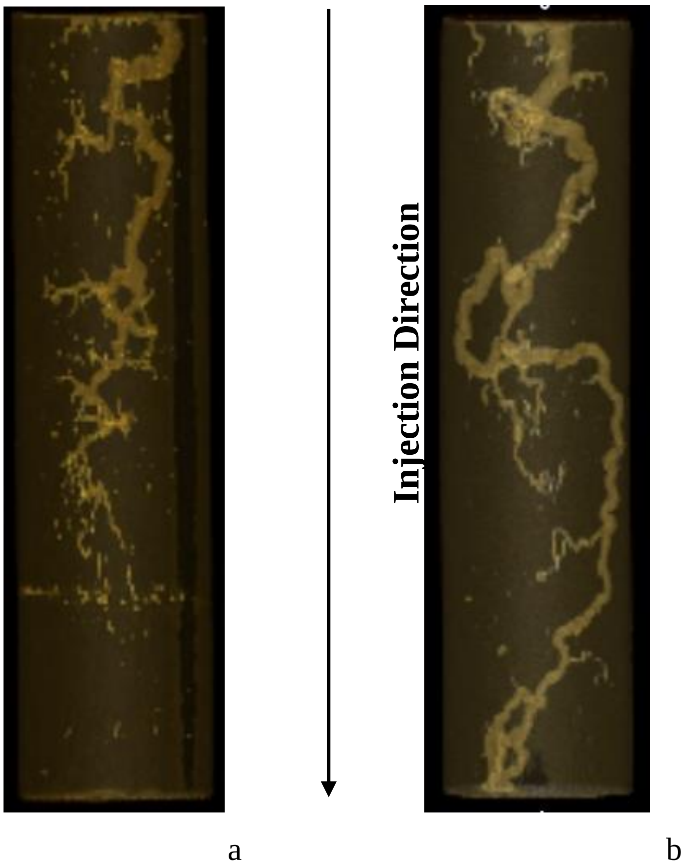

Fig. 99— CT-image of the cores after the dual coreflood DC-03 at 150°F: (a) high-permeability core (MP-06), and (b) low-permeability core (LP-04).

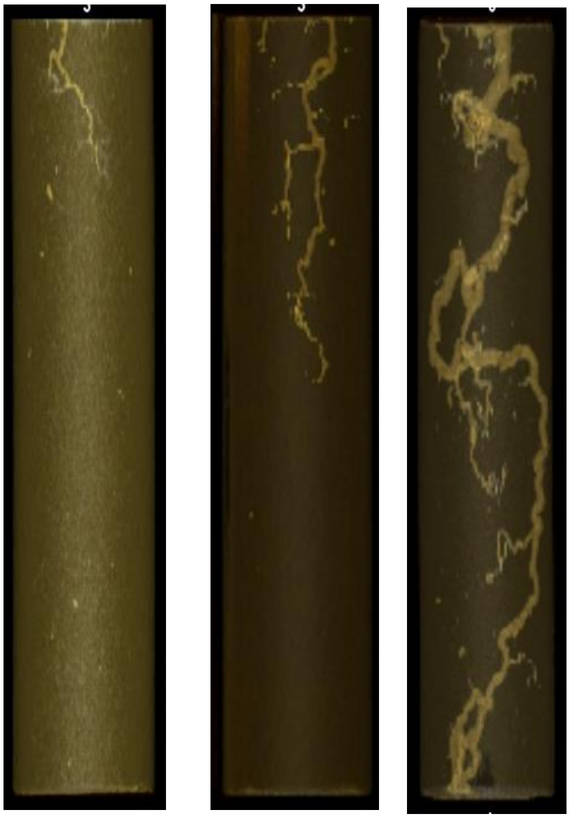

Experiment	DC-01	DC-02	DC-03
Low-perm Core	LP-07	LP-10	LP-07
K-ratio	28.3	14.4	1.63
Wormhole Length, inch	1.12	2.74	6
% Stimulation in the low-perm core	18.6	45.6	100

Fig. 100— A comparison of the change in the length of the wormhole created in the low-permeability cores.

Effect of Acid Additives on the VES-Acid Performance

To understand the performance of the proposed VES-acid system in field application, the impact of additives was examined through one more dual coreflood run to validate the results from the rheological study. This part of the work was conducted with all acid additives (**Table 17**) included at 150°F and was compared to the dual core-flood DC-03 in order to determine and quantify the additives impact on the acidizing process.

HCl Concentration, wt%	15
VES Concentration, Vol%	4
CI Concentration, Vol%	1
Non-emulsifier, gpt	1
Iron Control Agent, gpt	1
Temperature, °F	150

Table 17— Test Conditions for coreflood experiments DC-04.

The results from pressure drop tracking versus the cumulative injected pore volumes (**Fig. 101)** showed a sudden increase in pressure drop from 10 to 20 upon injection of the acid system into the cores, and this was attributed to the change of the viscosity from deionized water to VES-acid. This was followed by successive intervals of pressure drop increase and decrease with a fluctuation magnitude of 10 to 20 psi. This fluctuation is a typical response for in-situ gelled acids that describes the dissolution of the calcite minerals and then the gel formation to divert the acid. The pressure drop kept rising in absolute value up to 60 psi before it went down to zero to show breakthrough. At the beginning of the experiment, the outlet effluent was fractionated according to the permeability contrast to be 1.6 ml of the high permeability core Lp-09 to each one ml coming out of the low permeability core LP-06. This ratio remained constant for 0.25 PV injected; then this ratio changed to be 1.4 ml of effluent from the low-permeability core to each 1 ml of the effluent from the high-permeability core. This could be attributed to the viscosity build up in the high-permeability core and the divergent of the flow to the low-permeability core. After breakthrough, it was clear that only the low-permeability core was producing, while the high permeability core stopped production. This was an indication that the breakthrough happened in the low-permeability core at the time the high-permeability core was totally blocked by the gel.

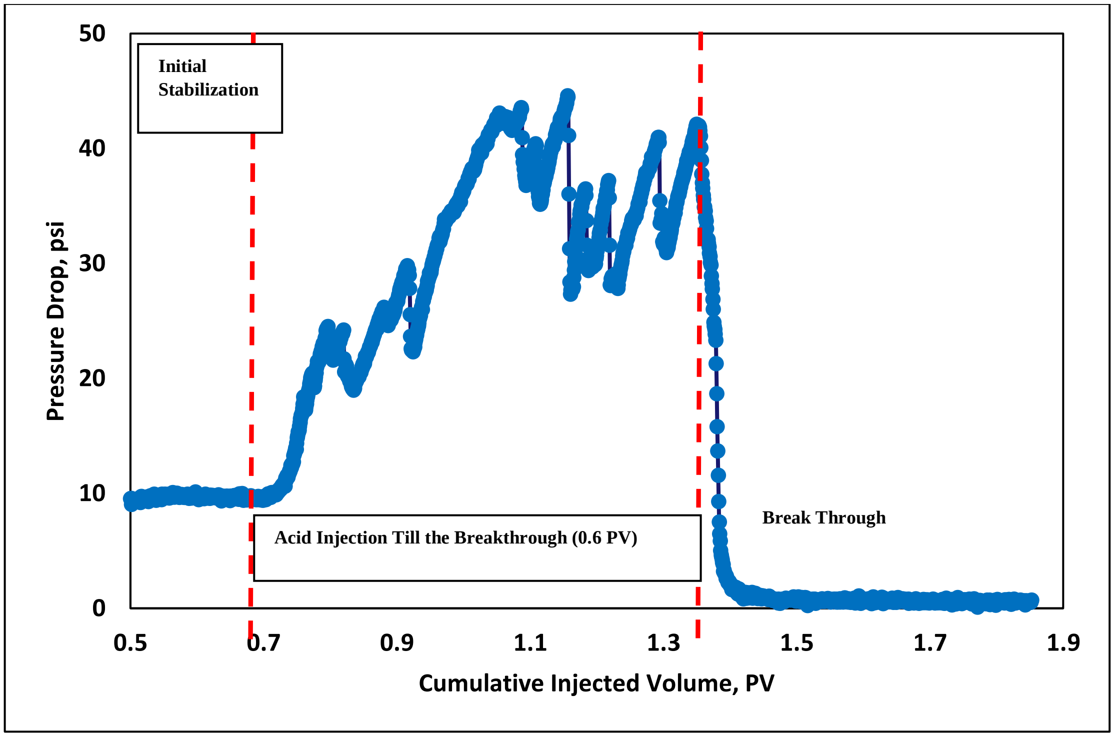

Fig. 101— Pressure drop across the core coreflood DC-04 at 150°F.

The CT scan analysis shown in **Fig. 102** demonstrates a proof to the coreflood observation showing a complex curvilinear wormhole in core number Lp-06 that is continuous from the inlet to the outlet of the core. The core LP-09 showed a discontinued but still complex wormhole extending to 80% of the core that could not reach the outlet. The CT images showed that VES succeeded in diverting the flow from the high-permeability core to the other core. Furthermore, the acidizing process achieved a high extent of wormhole complexity in each of the treated cores to expose higher surface area of the core for better productivity enhancement.

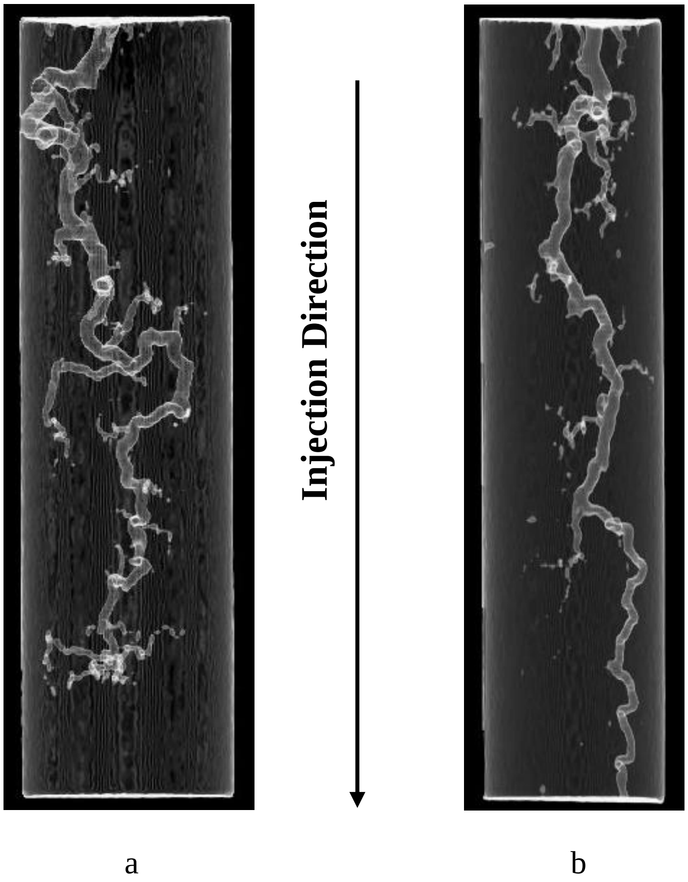

Fig. 102— CT-image of the cores after the dual coreflood DC-04 at 150°F: (a) high-permeability core (LP-09), and (b) low-permeability core (LP-06).

During this procedure, a total of 0.7 PV was injected to achieve the same results from the no-additive DC-03 experiment which consumed 0.9 PV. This reduction in the pore volume shows lower acid leak off and higher efficiency for the wormholing since the wormholes from both treatments at the low-permeability cores are identical. Moreover, the extent of the wormhole in the high-permeability core in experiment DC-04 is deeper if compared to the high-permeability core from experiment DC-03. This could be attributed to the contribution of the acid additives to increase the viscosity of the pumpable system, as shown in the comparison of Fig. 88, and Fig. 89. This higher viscosity contributed to lower leak off and supported a better wormhole progress.

Effect of Temperature on the VES-Acid Performance

To investigate the effect of temperature on the performance of VES-based acid, two coreflood experiments (SC-01 and SC-02) were conducted at 150 and 250°F, respectively. Data on each core and the condition of the tests are listed in Table 16 and **Table 18**. The pressure profile of both experiments is shown in **Fig. 103**, and **Fig. 104,** which illustrate a very good diversion effect of the VES tested in both cases. **Fig. 105** compares the two wormholes created after experiment and demonstrates curvilinear structures confirming the diversion effect.

HCl Concentration, wt%		15
VES Concentration, Vol%		4
CI Concentration, Vol%		1
Temperature, °F	**SC-01**	150
	SC-02	250

Table 18— Test Conditions for coreflood experiments SC-01 and SC-03.

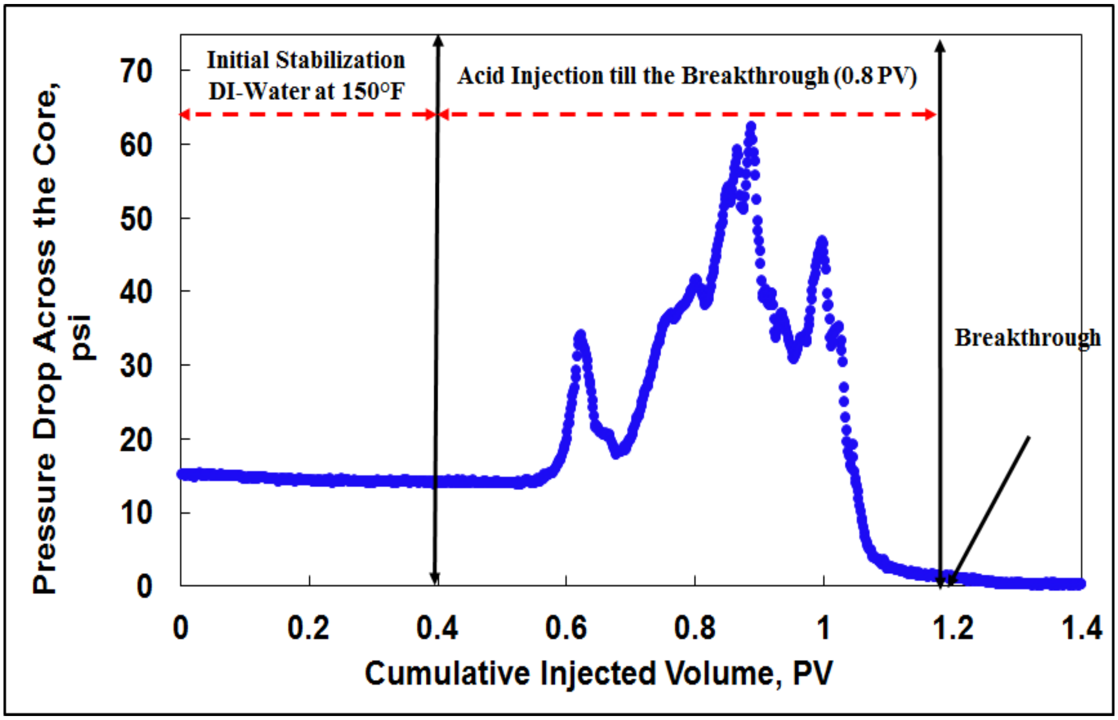

Fig. 103— Pressure drop across the core, coreflood SC-01 at 150°F.

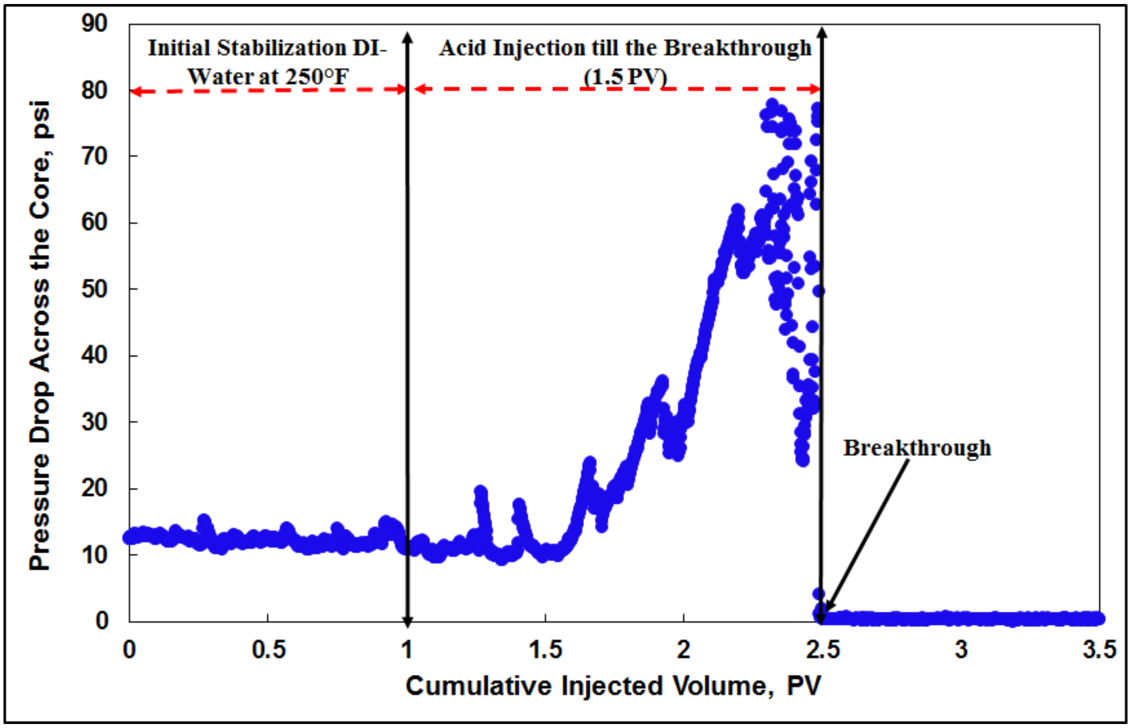

Fig. 104— Pressure drop across the core, coreflood SC-02 at 250°F.

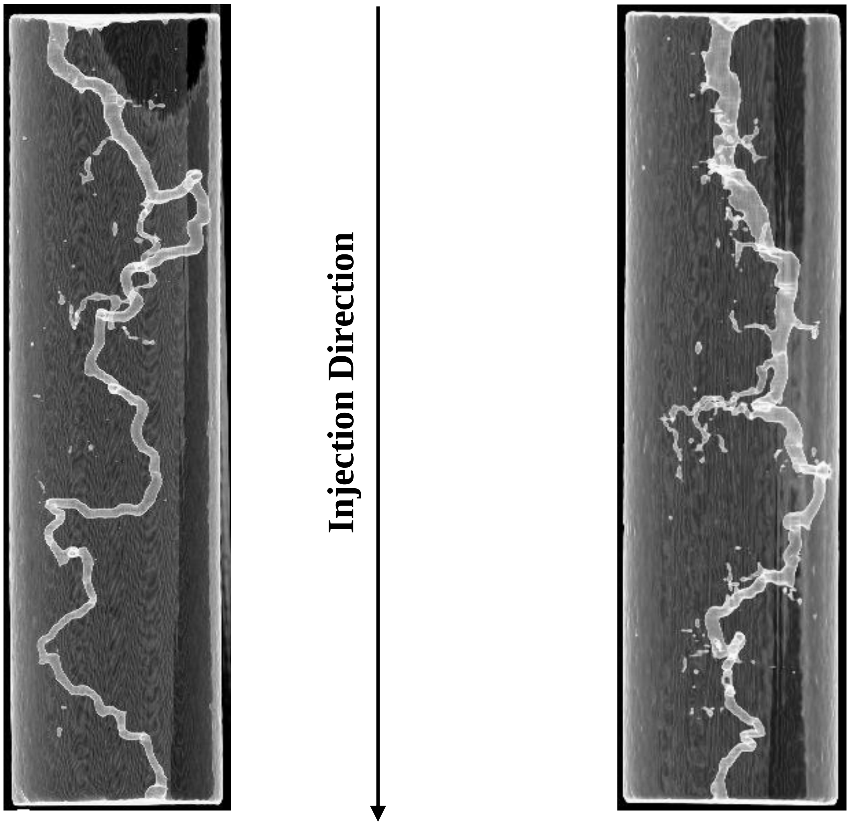

a b

Fig. 105— CT-image of the cores after the coreflood experiments: (a) SC-01 at 150°F, and (b) SC-02 at 250°F.

Conclusions

Key findings from this study leads to the following conclusions:

1. Viscosity of 15 wt% HCl spent VES-solutions showed a maximum viscosity of 200-800 cp over a temperature range of 150-170°F, depending on the VES concentration in the sample.
2. Increasing the VES concentration significantly increased the viscosity and extended the temperature range in which the VES can be applied.
3. In the absence of additives, a minimum of 50 cp was obtained at 195, 230, 250, and 275°F at 4, 5, 6, and 8 vol%, respectively.

4. None of the tested acidizing additives had a negative impact on the VES viscosity. At 8% VES loading, the acidizing package was optimized such that a minimum of 75 cp was obtained at 300°F.
5. Dual coreflood experiments conducted at 150 and 250°F proved the ability of the proposed VES to divert efficiently in limestone formations, as evaluated by the structure and the extent of wormhole propagation in the low-permeability core
6. A permeability contrast of 4-10 is the optimum for diversion ability in terms of the final enhancement in permeability of the low-permeability cores. The results revealed 18.6, 45.6, and 100% stimulation in the low-permeability core when the permeability contrast was 28.3, 14.4, and 1.63, respectively.
7. The pressure drop profiles and the CT-scanned wormhole structures of two single coreflood experiments at both 150 and 250°F indicated a very good diversion effect of the tested VES.
8. A dual coreflood experiment conducted in the presence of all acidizing additives showed that the wormhole breakthrough happened in the low-permeability core, which proves the diverging ability of the proposed VES at 150°F and stresses its superiority in building more efficient wormholes compared to the same experiment in the absence of additives.
9. The presence of acid additives at 4% VES loading enhanced the viscosity and decreased the acid leak off, resulting in better wormhole structure.

This work introduces a new VES system with high efficiency and compatibility to regular acid additives. The dual core flood analysis showed real time tracking for the wormholing process and showed the effect of permeability contrast on the divergent system efficiency.

CHAPTER VII

CORROSION INHIBITORS CHEMISTRIES AND THEIR IMPACT ON THE VES BASED ACID SYSTEMS RHEOLOGICAL AND INHIBITION PROPERTIES

Summary

Viscoelastic surfactants (VES) are essential components in one of the established self-diverting acid systems. Yet, their thermal stability limits their application in elevated temperatures. Recently, the industry has been working on introducing new VES chemistries by modifying the hydrophilic functional groups to enhance thermal characteristics. However, those new chemistries are challenged by their compatibility to acid-additives such as corrosion inhibitors, emulsifiers, and iron control agents. This work aims to study the nature and the mechanism of the interaction between the VES and the corrosion inhibitor chemistry. Also, it generates a decision tree that can modify the corrosion inhibitors selection and formulation to be compatible with the newly introduced VES systems.

This study is based on the rheology and the corrosion inhibition tests, complimented by detailed chemical analysis and microscopic study. Thiourea and quaternary ammonium compound corrosion inhibition families are selected to investigate their interaction with the cationic and zwitterionic surfactants. Each mixture of the corrosion inhibitor and the VES is blended in a 15 and 20 wt% HCl acid mixture, then assessed for its rheology at different shear rates, different CI concentrations, and at various temperatures up to 280˚F in live and spent conditions. Each component of the acid mixture

was examined using (FTIR) for their initial fingerprint. Then, each acid mixture was assessed before and after each rheology and corrosion test to track the changes of the mixture functional groups. Each mixture was examined under a polarizing microscope to assess its colloidal nature and its overall stability. Selected acid mixtures were evaluated for their corrosion inhibition ability. N-80 steel coupons were immersed staticly in the acid mixture for 6 hours at 150 and 250˚F, then the corrosion rate was calculated based on the weight loss. The coupons from the corrosion test were examined using an optical microscope.

The present study showed that the surface charge of the corrosion inhibitor and the surfactant controls the rheological and the inhibition properties of the mixture. The thiourea mixtures formed fine, monodispersed particles in the cationic VES which enhanced the rheological performance in live and spent conditions. The mixing of thiourea with a zwitterionic surfactant produced a coarse polydespersed particles that agglomerated and reduced the rheological properties of the VES acid mixture. The quaternized corrosion inhibitor exhibited an opposite property in every aspect. It enhanced the rheology of the zwitterionic surfactant while reducing the cationic surfactant. Particles with similar charge repulsed each other, lowering the rheology and the metal coupons surface coverage. The corrosion rate using opposite charge inhibitor and surfactant is lower than the similar charge chemicals corrosion rate. The FTIR analysis showed that there is no detected reaction between the corrosion inhibitor and the surfactants.

This work gives an insight into the complex nature of the interactions between corrosion inhibitors and visco elastic surfactants. It explains the positive and negative impact of the different corrosion inhibitors on the rheological properties of the VES acid system. Also, it explains the poor inhibition characteristics of such CI in the presence of VES, although it performs excellently in straight HCl acid system.

Introduction

The stimulation process is essentially an iron reactive fluid pumped down the tubing to react with the formation. This trip in the tubing will result in corrosion of the tubing that will result in dual damage to the process. First, it will carry the tubing leached iron particles to the formation causing formation damage, and secondly, it weakens the tubing shortening its lifetime. That is why the corrosion is an issue to be addressed when any stimulation fluid is pumped downhole for stimulation. Although inhibitors are essential for corrosion protection, their chemistries are of a devastating impact on other additives such as VES in a self-diverting acid system.

This work aims to investigate the nature and the mechanism of the interaction between the corrosion inhibitors and the VES families. This will be through the assessment of the corrosion inhibitor surface charge, geometry, and concentration impact on the VES self-diverting acid system rheological and corrosion inhibition properties.

Experimental Studies

Materials

Both cationic and zwitterionic surfactants are represent in this study. Thiourea is used in methanol and aided with tall oil acid. Quaternary ammonium compound is used in iso-propyl alcohol aided with fatty acids. All VES and CI are used as received. Hydrochloric acid is a 36.6 wt% ACS reagent grade provided by a local supplier. Acid solvent is an 18.2 MΩ.cm deionized water.

Chemicals Interaction and Surface Charge Assessment

Each acid mixture was monitored by FTIR before and after exposure to high temperatures. This was to track down the change in the integrity and the ratio of the essential functional groups of both the VES and corrosion inhibitor after mixing at 150˚F. Samples from the rheology assessment were examined at life acid conditions. In order to assure that HCl has no impact on the FTIR spectrum, another portion of VES was mixed with the corresponding corrosion inhibitor and examined by FTIR at the same temperature, then both results were compared.

The surface charge of each molecule was calculated and a 3-d molecular structure with Van der Waals surface was constructed. This was to predict the colloidal interactions between the surfactants and the corrosion inhibitors. The molecular geometries were optimized to reveal the complexity of the structure. That was to predict the physical ability of the molecules to come near each other, and to predict how they will pack in the corrosion inhibition layer on the metal surface during the corrosion test.

Effect of Corrosion Inhibitor on the VES Rheology

The impact of the corrosion inhibitor active ingredient on the VES micelles entanglement and integrity was examined through the apparent viscosity measurements. Each corrosion inhibitor and VES combination was mixed in 15 and 20 wt% HCl while the concentration of the VES was kept at 6 wt%, and the corrosion inhibitors were examined at 10 and 20 gpt. The mixing was at high shear rate followed by centrifugation at 4000 rpm for 10 minutes to eliminate the air bubble in the acid body. All samples were assessed using a high pressure, high temperature rheometer (GRACE 5600). Each sample was evaluated at 100 and 150˚F for their rheology performance at variable shear rates between 1 and 100 s^{-1}. Samples were assessed at a constant shear rate of 100 s^{-1} at 150˚F. Each of the prepared acid mixtures was spent by reacting with $CaCO_3$ powder until the pH reaches 4.5. Then the spent acid was assessed for its rheological performance and thermal stability at 280˚F for three hours at a shear rate of $100s^{-1}$.

Acid Solution Microscopic Properties

To understand the impact of the surface potential and the geometry of the surfactants and the CIs on the solution rheology, all acid mixtures were examined under polarizing optical microscope. Samples were mounted on a glass slit and imaged using incident and transmitted lights. Every corrosion inhibitor was examined in HCl in the absence and the presence of the VES. Each solution was imaged at different magnifications between 5 and 100x. The detected features were digitized using the Image-J software to count and measure each of the noticed features.

Corrosion Inhibition Assessment

The corrosion inhibition performance of the different corrosion inhibitors with the cationic VES in the 15 wt% HCl acid mixtures was evaluated using N-80 low carbon steel coupons. A static test was conducted at 150˚F and 1000 psi in a hast-alloy container. Each coupon was immersed in 800 cm^3 of acid mixture to ensure the minimal acid to surface area ratio of 22 cm^3/in^2 is achieved. The coupons were sanded and washed with deionized water then weighted before mounting on hast-alloy coupon holder. The test was conducted for six hours.

Upon the test completion, the coupons were retrieved and the corrosion inhibitor deposited layer were examined using optical microscope. This was to determine the coverage, the integrity, and the thickness of the deposited corrosion inhibition layer. The surface of the coupon was examined for pitting and excessive corrosion spots. Finally, the coupon was again washed with iso propyl alcohol and deionized water before final weight measurement. The corrosion rate is calculated using Eq.8 as follow:

$$C_r = \frac{W_i - W_f}{A_o} \quad . \quad \ldots\ldots\ldots\ldots\ldots\ldots\ldots\ldots \quad (8)$$

Where W_i is the initial weight before the test, W_f is the final weight after the test, A_0 is the initial surface area of the coupon. The final corrosion rate is reported in lb/ft^2 after six hours**.**

Results and Discussion

Chemistry and Surface Charge Assessment

The mixing of the thiourea or the quaternized corrosion inhibitor with the cationic surfactant for two hours at 150°F exhibited an identical FTIR spectrum. Both corrosion inhibitors concentrations were below the FTIR detection limits. However, the functional groups from the cationic surfactant were clearly intact after mixing with the different inhibitors. This data shows that the nature of the interaction is not chemically.

The molecular structure simulation, optimization, and surface charge representation of the surfactants and the corrosion inhibitors exhibited a complex molecules with both physical and surface charge limitations that complicates their interactions (**Fig. 106**). The thiourea molecule is a simple molecule in a single plane with negative electrostatic charge around the nitrogen atoms. The quaternized inhibitor shows a complex structure in two plans with positive charge around the nitrogen molecules. The cationic surfactant molecular optimization showed that the nitrogen atom is holding a positive charge, but it is not easily accessible at certain planes. The zwitterionic surfactant came simpler and the negative charge is accessible from all directions equally.

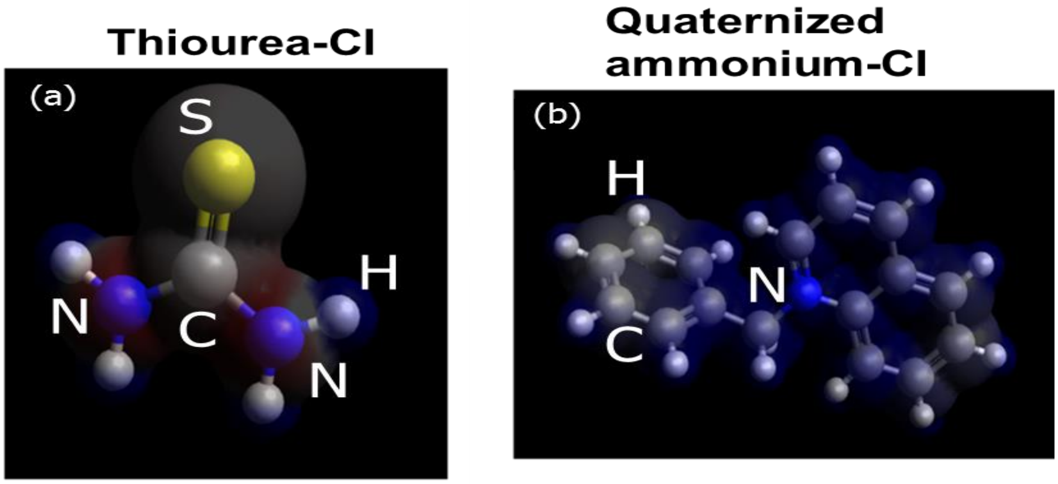

Fig. 106— Electrostatic potential Van der Waals surface for (a) thiourea CI, and (b) quaternized ammonium CI molecules.

Rheology Assessment

The change of the corrosion inhibitor type in the acid mixture with 6 wt% cationic VES resulted in different response in terms of apparent viscosity versus shear rate. The thiourea exhibited a positive synergetic impact on the life acid rheology, producing a shear thinning rheological performance. The apparent viscosity (**Fig. 107**) at 10 gpt CI was 170 cp at 1 s^{-1} shear rate and 100˚F. Upon increasing the shear rate to 100 s^{-1}, it went down to 100 cp. The second round of measurement was conducted at 150˚F. This time the apparent viscosity went down from 150 to 100 cp. This minimal variation at those two temperatures shows that the system is thermally stable at this temperature range. This shows that there is positive interaction between the cationic surfactants and thiourea fatty acid mixture. This behavior can be attributed to the opposite surface charge, and the small molecular size of the thiourea that conform to the cationic surfactant geometry. The quaternary ammonium based corrosion inhibitor showed a shear thickening rheological performance. The addition of 10 gpt of the corrosion inhibitor resulted in a 50 cp apparent viscosity (Fig. 107) at 100˚F. Upon the increase of the shear rate from 1 to 100 s^{-1} the viscosity didn’t respond and it was 50 cp along the shear ramp. At 150˚F, the viscosity of the mixture went down to 6 cp and was slightly increasing with the increase of the shear rate. This performance was reported in some cationic surfactant systems and was attributed due to phase separation in the VES mixture (Truong and Walker 2000). The formation of two phases is attributed to incompatibility between the surfactant and the acid mixture. This result in the formation of the shear induced structures (SIS) that breaks down the VES rheology (Wunderlich et al. 1987).

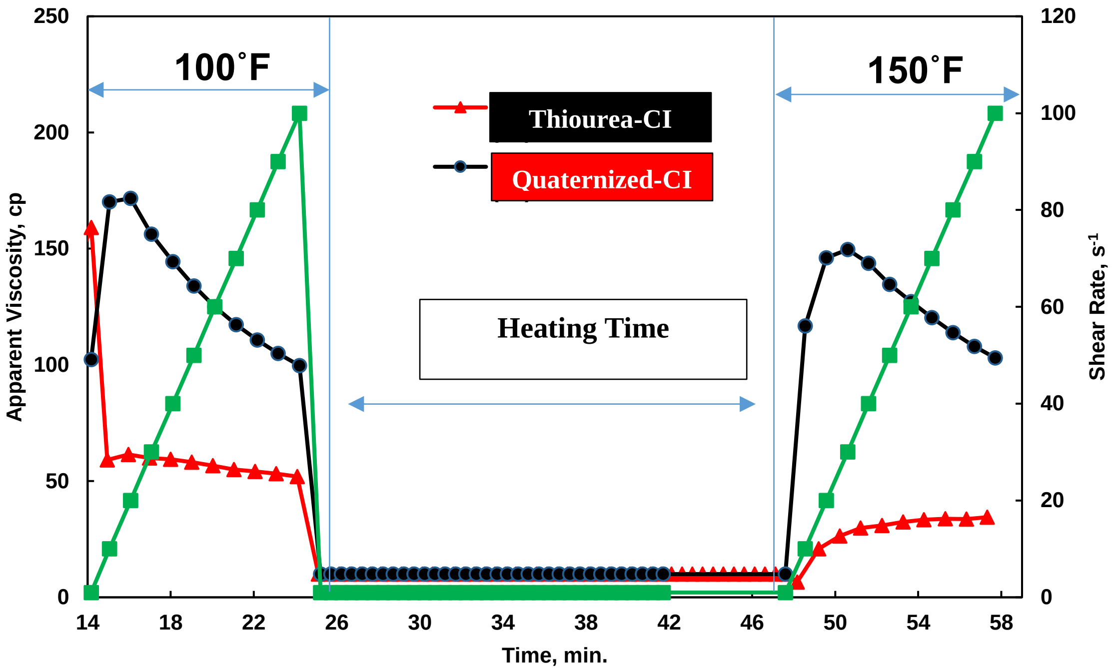

Fig. 107— Apparent viscosity versus shear rate for 6 wt% cationic surfactant in 15 wt% HCl and different corrosion inhibitors.

The apparent viscosity of the acid mixtures was evaluated at constant shear rate of 100 s^{-1} and 150˚F. This time, the concentration of the corrosion inhibitors was altered between 10 and 20 gpt to examine its impact on rheology. The data shown in **Fig. 108** complies with Fig. 107 showing the positive impact of thiourea on the cationic VES. The viscosity climbed up from 30 cp at room temperature to 78 cp at 150˚F. This final temperature was held for 20 minutes to examine the system stability. The mixture performed consistent at 75 cp. Upon raising the concentration of thiourea to 20 gpt the room temperature viscosity went up to 87 cp. This performance can be attributed to the increase of the fatty acid chains that was reported in the literature to be of positive impact on the VES rheology until a threshold concentration. This concentration depends on the fatty acid length and the VES degree of hydrolysis (Yu et al. 2012). At higher temperatures, the viscosity of the mixture (Fig. 108) kept rising until it reached a maximum of 135 cp at 150˚F, then the viscosity started to decrease.

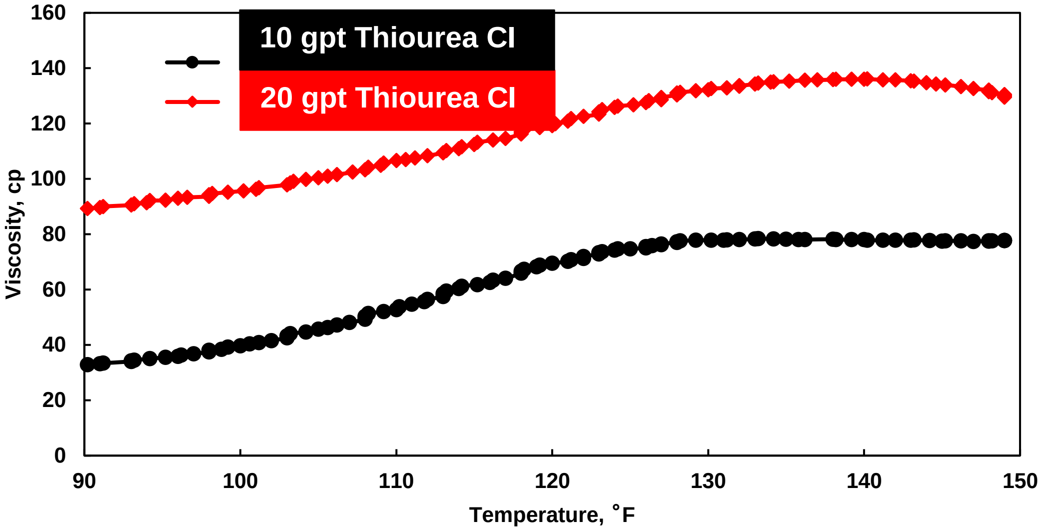

Fig. 108— Apparent viscosity at constant shear rate of 100 s-1 for thiourea corrosion inhibitor in 15 wt% HCl and 6 wt% cationic surfactant.

The quaternized corrosion inhibitor showed an intensive reduction in the apparent viscosity of the life acid as shown in **Fig. 109**. The first mixture with 10 gpt of the corrosion inhibitor exhibited an apparent viscosity of 65 cp at room temperature. Upon heating, the viscosity declined with the temperature increase until it reached 18 cp at 150˚F. The addition of 20 gpt of the corrosion inhibitor resulted in a similar pattern of viscosity decline with temperature increase that reached 20 cp at the end of the heating ramp at 150˚F. This result shows that the destructive impact of the quaternized compound on the cationic surfactant is instantaneous and happens at any concentration.

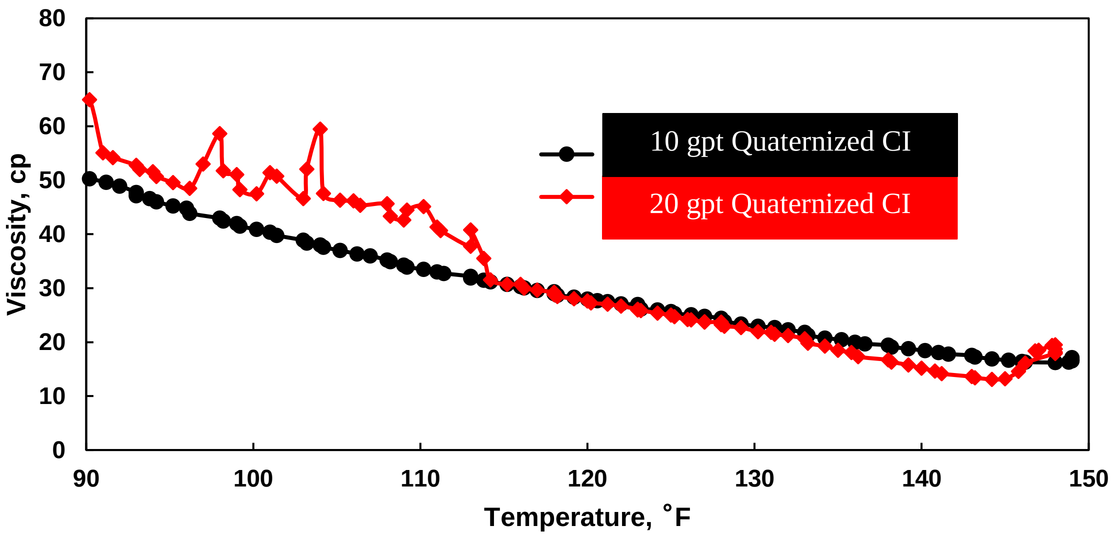

Fig. 109— Apparent viscosity at constant shear rate of 100 s-1 for quaternized corrosion inhibitor in 15 wt% HCl and 6 wt% cationic surfactant.

Impact of CI Surface Charge on Cationic and Zwitterionic Surfactants at Spent Conditions

The third part for the rheological study was to assess the CI charge impact on the rheology of the VES acid mixture at spent conditions. This part of the work was assessed at shear rates between 1 and 100 s^{-1} and temperatures between 100 and 280˚F. Four acid mixtures were formulated. Both corrosion inhibitors were evaluated in the presence of the cationic and zwitterionic surfactants.

The first formula combined the thiourea corrosion inhibitor with the cationic VES, which exhibited a positive synergetic performance as predicted from live acid study. As shown in **Fig. 110** the apparent viscosity was 130 cp at 100˚F and 100 s^{-1} shear rate. At 150˚F, the apparent viscosity climbed up to 210 cp at the same shear rate. The spent condition mixture exhibited shear thinning behavior at both 100 and 150˚F, which proves that the mixture is compatible with no phase separation along both the heating and shear ramps. Upon switching from cationic surfactant to zwitterionic surfactant the apparent viscosity trends were inverted. The mixing of the thiourea corrosion inhibitor with the zwitterionic surfactant showed a negative impact on the apparent viscosity at 100 s^{-1} shear rate. The change of the VES charge resulted in an incompatible mixture. The viscosity went to a maximum of 140 cp at 110˚F, then it declined to 0.1 cp at 280˚F.

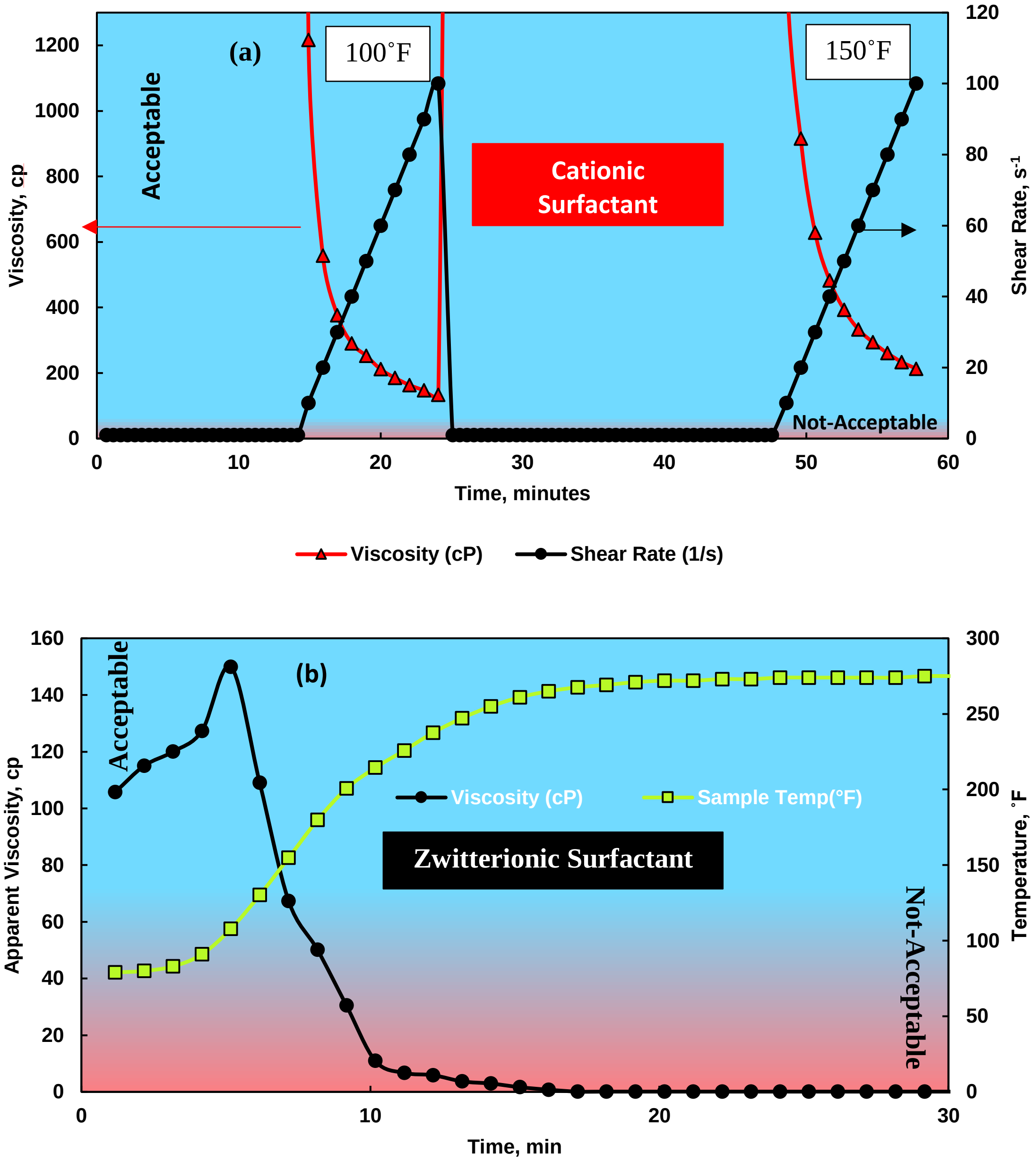

Fig. 110— Apparent viscosity at 10 gpt thiourea corrosion inhibitor in spent condition with 6 wt% (a) cationic and (b) zwitterionic surfactants.

The mixing of quaternized corrosion inhibitor with the cationic VES exhibited a negative impact on the mixtures apparent viscosity (**Fig. 111**). The mixture reached 600 cp at 110°F, then declined fast to 300 cp at 150˚F, then to 0.1 cp at 280˚F. The last formula of quaternized inhibitor with the zwitterionic VES also exhibited inversion in the rheological properties (Fig. 111). The viscosity reached a maximum of 300 cp at 200˚F, then declined slowly from 250 cp at 280˚F to reach 180 cp maintain a viscosity above 75 cp for one hour. This rheological behavior showed that the inversion of the surfactant charge has inverted all the rheological properties, which suggest an investigation in the surface charge and how it impacts the corrosion inhibitor and surfactant interaction.

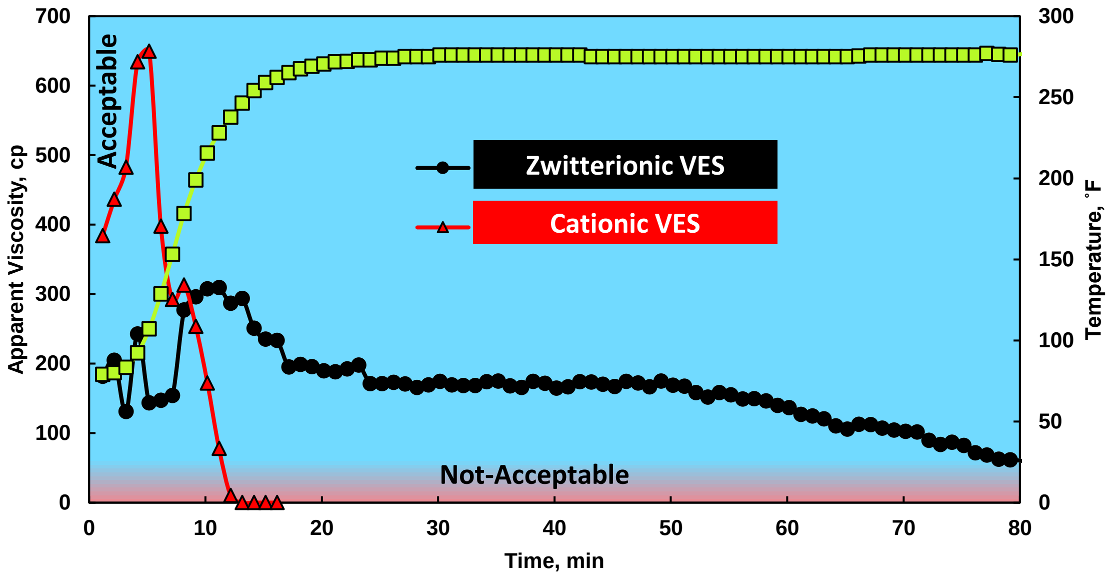

Fig. 111— Apparent viscosity at constant shear rate of 100 s^{-1} for a 10 gpt quaternized corrosion inhibitor in spent condition with 6 wt% cationic or zwitterionic surfactant.

Live and Spent Acid Micro-Properties

Live Acid Characterization. To explain the rheological performance, the colloidal properties of the different corrosion inhibitors dispersed in 15 wt% HCl was investigated using an optical microscope at magnifications up to 100x. The thiourea addition to the acid with no surfactant formed a dispersion of thiourea particles across the live acid (**Fig. 112**). The addition of 10 gpt thiourea showed an intense dispersion of a particle size between 1 and 5 µm. The addition of 20 gpt thiourea showed an intense increase in the average number of the dispersed particles from 400 to 1,200 particles in the same size range. Some dispersed particles were found at larger particle size ranging between 7 to 18 µm. The addition of the VES changed the nature of the acid mixture drastically. At both concentrations, the average number of the detected particles went down to 70 particles per size bin. This enhancment in the dispersion intensity can be attributed to the compatibility between the corrosion inhibitor and the cationic surfactant. This compatibility was suggested before, due to the enhancement in the rheological properties of the acid mixture. This monodisperse, fine distribution of dispersed particles in the acid mixture enhanced the hydrodynamic interaction between the thiourea and the cationic surfactant. Also, the charge difference enhanced the electrostatic attraction force between the surfactant and the dispersed phase which raised the mixture viscosity (Parkinson et al. 1970; Al-mutairi et al. 2007). The increase in the apparent viscosity of the mixture at 20 gpt thiourea comes from the increase in the dispersed particle, which reduce the particle to particle spacing and increases the hydrodynamic interaction and the viscosity. However, the increase in the dispersed particles number was the reason of the reduction in the viscosity at higher temperature due to the agglomeration of the particles forming a polydispersed coarse particles (Barnes 1994; Pal 1996).

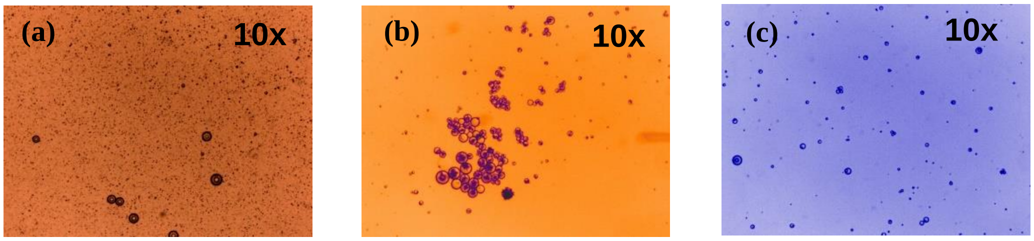

Fig. 112— 10 gpt thiourea corrosion inhibitor in 15 wt% HCl mixed with (a): no VES, (b): 6 wt% zwitterionic VES, (c): 6 wt% cationic VES. Live acid conditions.

The quaternized ammonium compound behaved on the contrary to the thiourea based corrosion inhibitor. Upon mixing 10 gpt CI with the 15 wt% HCl, dispersed particles were heavily observed with 1,200 particles in the size range between 1 and 2 μm (**Fig. 113**). Larger particles were observed at lower frequency of 20 particles. The increase in the concentration of the corrosion inhibitor exhibited an agglomeration of the CI particles to be a connected network in the live acid. The addition of the VES resulted in further reduction in the number of the particles in size range of 1 μm and the increase in the larger particles size frequency at both 10 and 20 gpt CI concentrations. The count in the size range of 4 to 18 μm raised up from 1 to 10 particles per size to be 5 to 60 per size. This increase in the larger particle size frequency and the corresponding decrease in the smaller particles suggests an agglomeration of the inhibitor particles and incompatibility with the cationic VES. This incompatibility showed a polydispersity coarse particle size which impacted the ability of the fluid to disperse energy, which explains the reduction in the rheology.

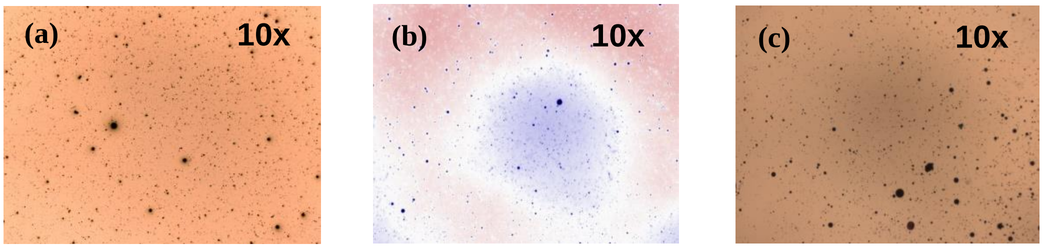

Fig. 113— 10 gpt quaternized corrosion inhibitor in 15 wt% HCl mixed with (a): no VES, (b): 6 wt% zwitterionic VES, (c): 6 wt% cationic VES.

The repulsion between the similar charge particles of the VES and the corrosion inhibitor eased the VES flow lowering its viscosity. Once more the samples were examined under the microscope after the rheology test at 150˚F. The thiourea based corrosion inhibitor was finely dispersed in the cationic VES mixture (**Fig. 114**). The quaternized corrosion inhibitor aggregated particles extended and connected to each other's, forming a network of particles all across the cationic VES body (**Fig. 115**).

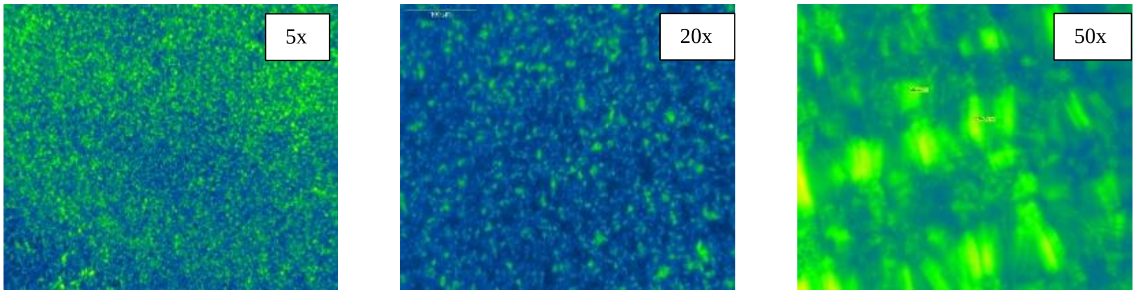

Fig. 114— 10 gpt Thiourea in 15 wt% HCl and 6 wt% cationic VES at 150°F.

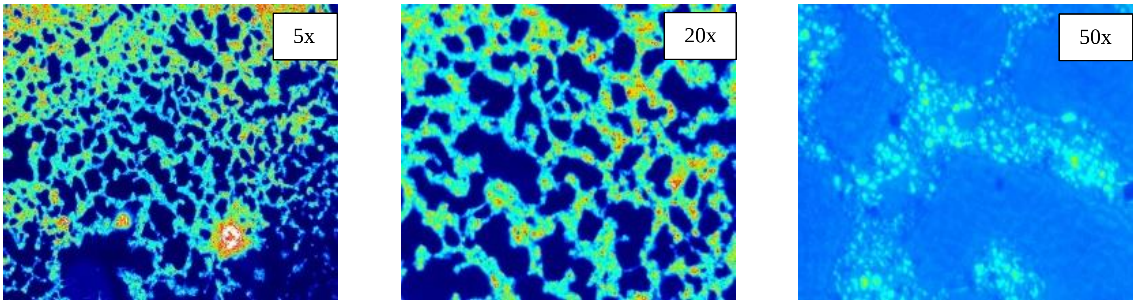

Fig. 115— 10 gpt quaternized inhibitor in 15 wt% HCl and 6 wt% cationic VES at 150°F.

This data shows the nature of the interaction between the VES and CI is based on the formed CI particle size distribution, which is determined by the surface charge density of the CI and its structural compatibility with the surface charge density of the VES. The data explains the shear thinning nature of the thiourea system with the cationic surfactant. Pal (1996) showed that the smaller the particle size of the dispersed CI, the better the shear thinning behavior. The coarser the dispersed CI particles the lower the shear thinning impact. This colloidal study explains the failure of the quaternized ammonium compound to behave as shear thinning upon mixing with the cationic surfactant as shown in Fig. 107

due to the phase separation and the formation of shear induced structures (Wunderlich et al. 1987).

The same work conducted on the cationic surfactant was repeated on the zwitterionic surfactant to validate our interpretations. An inversion in both the rheological and the colloidal properties was expected. The addition of 10 gpt thiourea in a 15 wt% HCl mixture with a 6 wt% zwitterionic VES resulted in a clear inversion in the CI particles dispersion nature. The particle size of the dispersed CI went up from 1 to 17 μm. The thiourea particles exhibited agglomeration forming larger bodies. Further magnification showed disordered inclusions in the CI emulsions ring. This inclusion behaved like an agglomeration of the VES strings. Upon constructing a particle size distribution for the thiourea emulsions in both cationic and the zwitterionic surfactants, a clear inversion in the particle size distribution was noticed (**Fig. 116**). This inversion in the colloidal nature of the acid mixture explains the inversion in the rheological properties of the same corrosion inhibitor with an opposite charge surfactant.

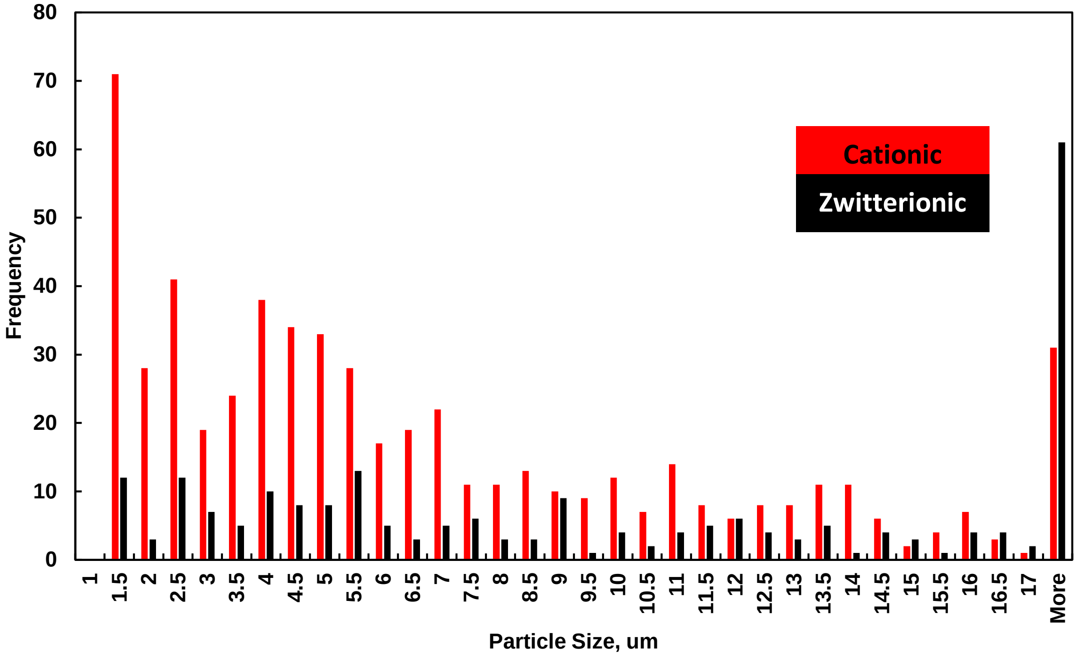

Fig. 116— 10 gpt Thiourea inhibitor dispersion properties in 15 wt% HCl and 6 wt% cationic versus zwitterionic surfactants in live conditions.

The quaternized inhibitor also inverted its dispersed particles properties upon mixing with the zwitterionic VES. The formed particle size decreased from 17 µm to the 1 to 5 µm particle size range. At higher magnification, a clear segregation between the CI particles was noticed. The particle size distribution histograms in both cationic and the zwitterionic surfactants exhibited severe inversion in the particle size distribution (**Fig. 117**).

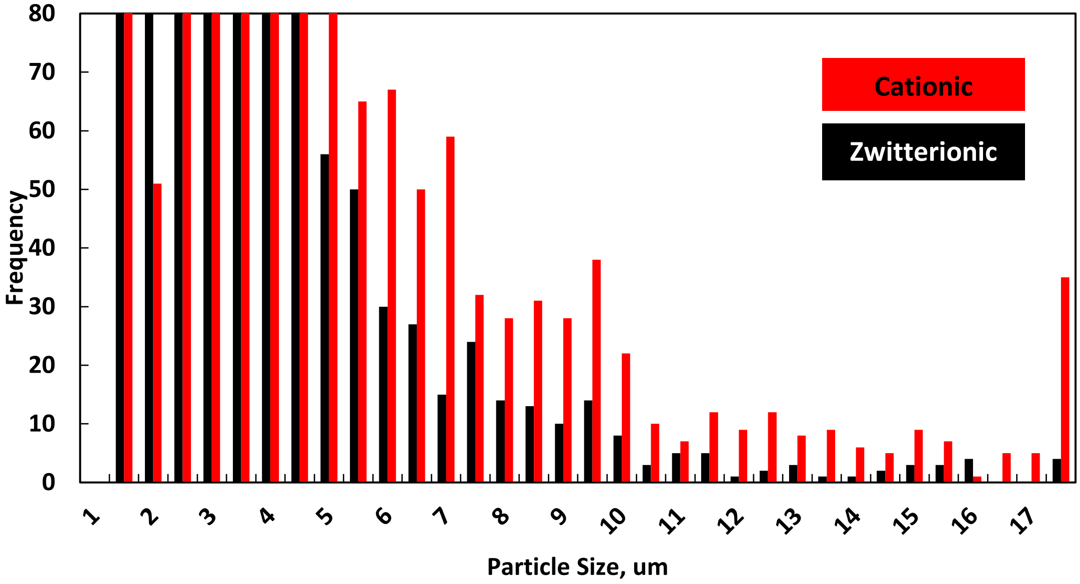

Fig. 117— 10 gpt quaternized inhibitor dispersion properties in 15 wt% HCl and 6 wt% cationic versus zwitterionic surfactants in live conditions.

Corrosion Test

Two N-80 coupons were exposed to acid mixture composed of 15 wt% HCl and 6 wt% cationic VES. The first coupon tested the inhibition ability of 10 gpt thiourea inhibitor. The test was conducted for 6 hours at 150°F. The coupon was 2.27 in^2 in surface area and its initial weight was 7.54 gm. After the test the final weight was 7.52 gm (**Table 19**). This loss was converted to corrosion rate of 0.0029 lb/ft^2. Such a low weight loss and the corresponding low corrosion rate shows a successful inhibition. The thiourea inhibitor succeeded to co-exist with the VES for 6 hours at 150°F. This could be attributed to the compatibility between the two components witnessed during the rheology assessment.

The coupon was further investigated under an optical microscope using incident light technique and magnification powers up to 100 times the original sample. Upon comparison of the optical images collected after the test to those before the test, it was clearly obvious that there is a consistent layer of polymer like deposit on the coupon surface (**Fig. 118**). After the coupons were flushed using deionized water, this polymer layer was still attached to the surface. Upon soaking the coupon in chloroform, the membrane degraded and was absorbed by the chloroform. The surface was examined under the optical microscope once more. The layer this time disappeared and the surface of the metal started to oxidize to both ferrous and ferric zones.

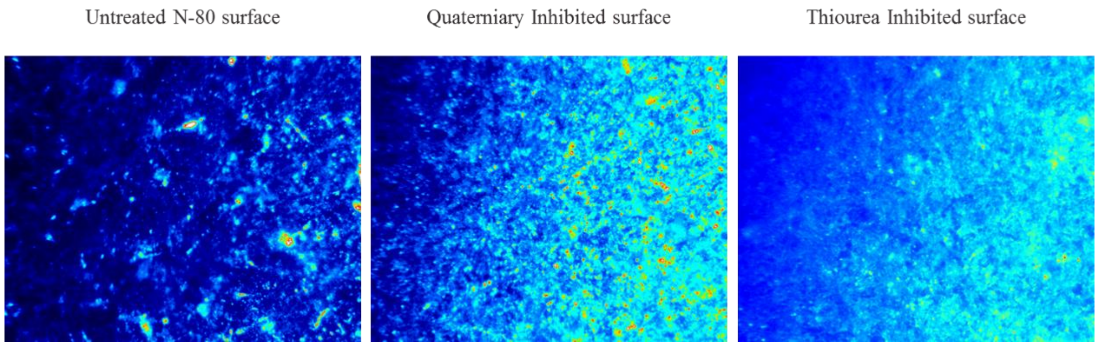

Untreated N-80 surface

Quaterniary Inhibited surface

Thiourea Inhibited surface

Fig. 118— N-80 metal surface before and after corrosion test in presence of different corrosion inhibitors with cationic surfactants.

The second coupon was exposed to the same acid mixture, this time 10 gpt of the quaternized inhibitor was used. The coupon lost 0.5 gm in 6 hours (Table 19). This corresponds to a corrosion rate of 0.0586 lb/ft^2. This corrosion rate is slightly higher than the acceptable range at this temperature. This type of performance can be attributed to the similar surface charge that resulted in less packing interaction between the cationic surfactant and the quaternized inhibitor. This type of interaction lowered the metal coverage area and resulted in more corrosion.

Sample	**W_i**	**W_f**	**$W_{difference}$, lb**	**L**	**W**	**D**	**A, in^2**	**Corrosion Rate, lb/ft^2**	**Concentration**	**Type**	**VES, wt%**	**Acid, wt%**
C-1	7.54	7.52	4.7E-05	2.0	0.5	0.06	2.3	0.0029	10 gpt	Thiourea	6	15
C-2	7.44	7.02	0.00092	1.99	0.49	0.05	2.27	0.058	10 gpt	Quaternized	6	15

Table 19— Corrosion rate for different corrosion inhibitors and cationic surfactant in 15 wt% HCl.

The optical microscopy came as predicted with lower coverage than the thiourea layer. The images showed a polymer like coverage with disturbed areas (Fig. 114). This time the oxidization process and the surface staining happened before the chloroform stage. Upon testing the stained surface under the microscope, zones of covered and oxidized zones coexisted next to each other.

All the images from the optical microscope were processed using Image-J®. This additional step created a method to quantify the coverage in a digital form and avoid human error quantifying the coverage. The coverage on each pixel of the surface was accounted toward the total degree of coverage on the metal surface. The polymer layer exhibited a higher reflectance compared to the uncovered surface. Each sample was examined digitally, and a histogram showing the reflectance versus its frequency was constructed. This analysis (**Fig. 119**) showed digitally that the thiourea had a better coverage compared to quaternized inhibitor when they are mixed in 15 wt% HCl with 6 wt% cationic VES.

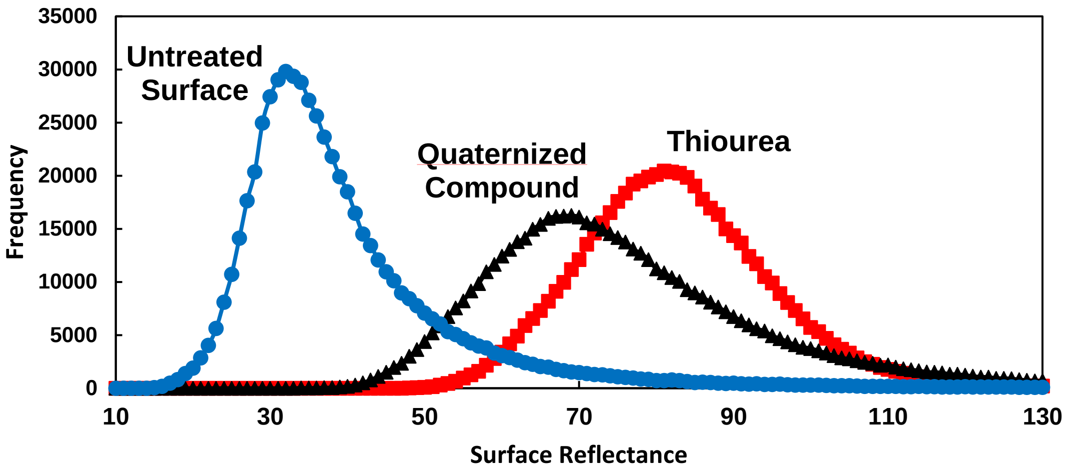

Fig. 119— Inhibitor surface coverage on N-80 coupons before and after corrosion test with 15 wt% HCl and 6 wt% cationic surfactant.

Conclusions

The present study examined the interaction between two main corrosion inhibitors in the oil field industry with a cationic and a zwitterionic surfactant. This study came out with multiple conclusions as follow:

1- The corrosion inhibitors are major contributor to the reduction of the VES acid system rheological performance.

2- There is no chemical reaction between the examined corrosion inhibitors and the surfactants.

3- The synergetic or the reducing impact of the corrosion inhibitors comes from the surface charge of the molecules and how they interact with the surfactant molecules.

4- The enhancement in the rheological properties comes from the formation of small and monodispersed CI particles with opposite charge to the VES medium.

5- The opposite charge between the corrosion inhibitor and the surfactant increase the attraction forces and reduce the mobility of the surfactant causing an increase in the apparent viscosity.

6- The phase segregation between the surfactant and the corrosion inhibitor lowers the system viscosity and exhibit a shear thickening behavior.

7- At high corrosion inhibitor concentrations, the high-volume ratio of the corrosion inhibitor reduces the compatibility of the surfactant and the corrosion inhibitor at higher temperatures due to their agglomeration to larger particles.

8- The geometrical and the surface charge compatibility between the surfactants and the corrosion inhibitors determine the system corrosion inhibition capabilities.

9- Opposite charge inhibitors and surfactants result in higher corrosion resisting film packing and lower corrosion rate.

This work described the nature of the interaction between the corrosion inhibitors and viscoelastic surfactants. It introduces solid criteria for corrosion inhibitor selection in VES based self-diverting acid system. The produced data and the introduced evaluation mechanism can be implemented to refine the chemistries of both the VES and the corrosion inhibitors for higher temperatures self-diverting acid systems.

CHAPTER VIII

CONCLUSIONS

The mineralogical study presented in chapter two showed that Bandera sandstone is a more complicated formation than the data in the literature reported. The formation is mainly composed of quartz, dolomite kaolinite, illite, and albite. Those minerals are size distributed as 65 wt% sand, 17.45 wt% silt, and 9.17 wt% clay. The separation of the different mineral sizes and their analysis separately enhanced the ability to determine and quantify the composing minerals. The size based analysis showed detailed and more clear mineralogical analysis. Minerals such as feldspars, chlorite, titanium oxide, zirconium silicates, muscovite, phosphate calcium apatite, and amphiboles was detected using SEM and TEM analysis. In addition, the analysis succeeded in describing the morphology of the clay minerals and their average surface area. The cation exchange capacity showed the chemical stability of the clay minerals. The 5 cmol/kg CEC came from the kaolinite and chlorite minerals in the formation. The absence of minerals such as the smectite and mica helped to lower down the CEC which stabilized the chemistry of the clay cut of the formation.

The work in chapter three investigated the fines migration driving mechanism, and their impact on stimulation process, and tracked with high resolution the formation damage. The inhibition cation size and its charge controlled the magnitude of the fines migration. The stimulation in the presence of fines migration behaves differently and with more localized damage compared to the stimulation of the undamaged cores. The extent and the magnitude of the damage are highly sensitive to the increase in the temperature. CT scan coupled by NMR showed the ability to track down damage in treated cores with a high level of resolution. The mud acid stage showed a detrimental impact on the pore size distribution and the pore structure in all of the cores and under all of the different treatment conditions. The formation damage was mainly due to the silica gel and the products of the secondary and tertiary reactions with the clay minerals. The enhancement of the permeability of the cores are resulting from dissolution of the dolomite minerals forcing limited channels along the core. On the other hand, the mud acid clay interaction type of damage plugged the rest of the core and altered its pore structure. The slicing of the cores according to the computed tomography representation and its examination under SEM showed visually the changes in the pore structure. The XRF analysis for the core slices showed the changes in the pore structure chemistries upon stimulation.

The work in chapter four studied the acidizing of different sandstone formations using regular mud acid after custom pre flush treatments. This study showed the intense impact of the clay nature and composition on the fines migration magnitude. Moreover, it showed different responses with mud acid stimulation. The mineralogical differences between the Bandera, Berea, and Kentucky sandstone controlled the stimulation out comes in terms of permeability and pore structure alteration. The pore size distribution showed a high damaging potential of fines migration when the clay concentration is low and scattered in the pore throats. Stimulation of Berea sandstone using mud acid resulted in severe damaging impact. This damage came clear in terms of losing permeability, and tighter pore size distribution. On the other hand, the high clay content in the Kentucky sandstone exhibited a higher stability. The nature of the clay content being impeded in the formation matrix not scattered in the pore throat made it stable to deionized water and resulted in less fines migration damage. Additionally, the mud acid showed minimal formation damage compared to the stimulation of the Berea or the Bandera sandstone.

The work in chapter five aimed to use the computed tomography combined with the NMR analysis to investigate the impact of the clay minerals nature of presence in the different sandstones on fines migration damage and its stimulation. The study of Bandera, Grey Berea, and Kentucky sandstone showed that the total clay content is not a criteria to predict the extent of fines migration damage or the result of sandstone stimulation. The 3D segmentation of the data showed that Berea sandstone with the lowest total clay content is the formation with the most scattered clay content in the pore structure. This nature made it the formation with highest magnitude of fines migration damage and the highest formation damage extent upon stimulation. The Bandera sandstone with higher clay content showed more stability against fines migration damage and matrix acidizing up till 150°F. The stimulation of Bandera sandstone at 250°F, showed higher extent of damage. Kentucky sandstone, showed higher stability than both Grey Berea and Bandera sandstone against both fines migration damage and its stimulation. The degree of the clay content scattering in the pore structure is the controlling variable for both fines migration damage and its stimulation.

The work in chapter six investigated a new viscoelastic surfactant for acid diversion in carbonate matrix acidizing at 250˚F. The compatibility of the VES with several acidizing additives including a corrosion inhibitor, a non-emulsifier, an iron-chelating agent, and an iron reducing agent was investigated by rheological analysis. The cationic VES showed a higher thermal stability reaching 250˚F. The higher the concentration of the VES the higher the thermal stability. The additives contribute to lowering down the rheological performance at spent acid condition. Optimum package of acid additives was delivered to attain 50 cp at 300˚F. The new VES showed the ability to divert in permeability contrast ranging between 4 to 10 between the high and the low permeability cores. Dual core flood studies aided with CT scan wormhole tracking showed the ability of the VES acid system to divert in temperature up to 250˚F.

The work in chapter seven examined the interaction between two main corrosion inhibitors in the oil field industry with a cationic and an zwitterionic viscoelastic surfactants. This study came out with multiple conclusions as follows: The corrosion inhibitors are major contributor to the reduction of the VES acid system rheological performance. There is no chemical reaction between the examined corrosion inhibitors and the surfactants. The synergetic or the reducing impact of the corrosion inhibitors comes from the surface charge of the molecules and how they interact with the surfactant molecules. The enhancement in the rheological properties comes from the formation of small and monodispersed emulsions with opposite charge to the VES medium. The opposite charge between the corrosion inhibitor and the surfactant increase the attraction forces and reduce the mobility of the surfactant causing an increase in the apparent viscosity. The phase segregation between the surfactant and the corrosion inhibitor lowers the system viscosity and exhibit a shear thickening behavior. At high corrosion inhibitor concentrations, the high-volume ratio of the corrosion inhibitor reduces the compatibility of the surfactant and the corrosion inhibitor at higher temperatures due to their agglomeration to larger particles. The geometrical and the surface charge compatibility between the surfactants and the corrosion inhibitors determine the system corrosion inhibition capabilities. Opposite charge inhibitors and surfactants result in higher corrosion resisting film packing and lower corrosion rate. This work described the nature of the interaction between the corrosion inhibitors and viscoelastic surfactants. It introduces solid criteria for corrosion inhibitor selection in VES based self-diverting acid system. The produced data and the introduced evaluation mechanism can be implemented to refine the chemistries of both the VES and the corrosion inhibitors for higher temperatures self-diverting acid systems.

This research adds new tool to better design the matrix acidizing treatments for both sandstone and limestone formations. The CT/NMR tool add a deeper level of resolution to enhance the ability assess the selected acid impact on the sandstone pore structure especially during fines migration treatment. The deeper understanding in VES acid based systems and how does corrosion inhibitors influence these systems gives a guide line to formulate a better acid diversion systems for high permeability contrast limestone reservoirs.

REFERENCES

Akin, S. and Kovscek, A. R. 2003. Computed Tomography in Petroleum Engineering Research. *Geological Society, London, Special Publications* **215** (1): 23-38.

Al-Dahlan, M. N., Nasr-El-Din, H. A., and Al-Qahtani, A. A. 2001. Evaluation of Retarded HF Acid Systems. Presented at the SPE International Symposium on Oilfield Chemistry, Houston, Texas, 13-16 February. SPE-65032-MS. https://doi.org/10.2118/65032-MS.

Al-Ghamdi, A. H., Mahmoud, M. A., Wang, G. et al. 2014. Acid Diversion by Use of Viscoelastic Surfactants: The Effects of Flow Rate and Initial Permeability Contrast. *SPE J.* **19** (06): 1-203. SPE-142564-PA. http://dx.doi.org/10.2118/142564-PA.

Al-Mubarak, T., AlKhaldi, M., AlMubarak, M. et al. 2015. Investigation of Acid-Induced Emulsion and Asphaltene Precipitation in Low Permeability Carbonate Reservoirs. Presented at the SPE Saudi Arabia Section Annual Technical Symposium and Exhibition, Al-Khobar, 21-23 April. SPE-178034-MS. http://dx.doi.org/10.2118/178034-MS.

Al-Mutairi, S. H., Hill, A. D., and Nasr-El-Din, H. A. 2007. Effect of Droplet Size, Emulsifier Concentration and Acid Volume Fraction on the Rheological Properties and Stability of Emulsified Acids. Presented at the European Formation Damage Conference, Scheveningen, The Netherlands, 30 May-1 June. SPE-107741-MS. https://doi.org/10.2118/107741-MS.

Al-Mutawa, M., Al-Anzi, E. H. D., Jemmali, M. et al. 2005. Zero Damaging Stimulation and Diversion Fluid: Field Cases from the Carbonate Formations in North Kuwait. *SPE Pro & Fac* **20** (2):94-105. SPE-80225-PA. https://doi.org/10.2118/80225-PA.

Barnes, H. A., 1994. Rheology of Emulsions—a Review. *Colloids and Surfaces A: Physicochemical and Engineering Aspects* **91** (1994): 89-95.

Carr, H. Y. and Purcell, E. M. 1954. Effects of Diffusion on Free Precession in Nuclear Magnetic Resonance Experiments. *Physical Review* **94** (3): 630.

Chang, F. F., Qu, Q., and Frenier, W. 2001. A Novel Self-Diverting-Acid Developed for Matrix Stimulation of Carbonate Reservoirs. Presented at the SPE International Symposium on Oil Field Chemistry, Houston, Texas, 13-16 February. SPE-65033-MS. https://doi.org/10.2118/65033-MS.

Chang, F. F., Qu, Q., and Miller, M. J. 2002. Fluid System Having Controllable Reversible Viscosity. U.S. Patent No. 6,399,546.

Clubley, B. G. 1990. Chemical Inhibitors for Corrosion Control. Boca Raton, Florida: CRC Press INC.

Coates, G. R., Menger, S., Prammer, M., et al. 1997. Applying NMR Total and Effective Porosity to Formation Evaluation. Presented at SPE Annual Technical Conference and Exhibition, San Antonio, Texas, 5-8 October. SPE-38736-MS. http://dx.doi.org.ezproxy.library.tamu.edu/10.2118/38736-MS.

Coates, G. R., Xiao, L., and Prammer, M. G. 1999. NMR Logging Principles and Applications: Halliburton Energy Services.

Crews, J. B. and Huang, T. 2007. Internal Breakers for Viscoelastic-Surfactant Fracturing Fluids. Presented at the SPE International Symposium on Oilfield Chemistry Conference, Houston, Texas, 28 February-2 March. SPE-106216-MS. http://dx.doi.org.ezproxy.library.tamu.edu/10.2118/106216-MS.

Deng, Y., G. N. White, and J. B. Dixon. 2009. Soil Mineralogy Laboratory Manual. 11th edition. Published by the authors, Department of Soil and Crop Sciences, Texas A&M University, College Station, Texas 77843-2474.

Dill, R. W., and Keeney, B. R. 1978. Optimizing HCl-Formic Acid Mixtures for High Temperature Stimulation. Presented at the SPE Annual Fall Technical Conference and Exhibition. Houston, Texas, 1-3 October. SPE-7567-MS. http://dx.doi.org.ezproxy.library.tamu.edu/10.2118/7567-MS.

Dreiss, C. A. 2007. Wormlike Micelles: Where do We Stand? Recent Developments, Linear Rheology and Scattering Techniques. *Soft Matter* **3** (8): 956-970.

Fredd, C. N. and Fogler, F. H. 1998a. Alternative Stimulation Fluids And Their Impact On Carbonate Acidizing. *SPEJ* **3** (1): 34-41. SPE-31074-PA. http://dx.doi.org/10.2118/31074-PA.

Fredd, C. N. and Fogler, F. H. 1998b. Influence of Transport and Reaction on Wormhole Formation in Porous Media. *AIChE* **44** (9): 1933-1949.

Fu, D. and Chang, F. 2005. Composition and Methods for Treating a Subterranean Formation. U.S. Patent No. 6,929,070.

Gatewood, J. R., Hall, B. E., Roberts, L. D. et al. 1970. Predicting Results of Sandstone Acidizing. *J Pet Technol* **22** (6): 693-700. SPE-2622-PA. https://doi.org/10.2118/2622-PA.

Gdanski, R. 1998. Kinetics of Tertiary Reactions of Hydrofluoric Acid on Aluminosilicates. *SPE Prod & Oper* **13** (2): 75–80. SPE-31076-PA. http://dx.doi.org.ezproxy.library.tamu.edu/10.2118/31076-PA.

Gdanski, R. 1999. Kinetics of the Secondary Reaction of HF on Alumino-Silicates. *SPE Prod & Fac* **14** (4): 260-268. SPE-59094-PA. https://doi.org/10.2118/59094-PA.

Gdanski, R. D. 1994. Fluosilicate Solubilities Affect HF Acid Compositions. *SPE Prod & Fac* **9** (4): 225-229. SPE-27404-PA. https://doi.org/10.2118/27404-PA.

Gdanski, R. D. 2000. Kinetics of the Primary Reaction of HF on Alumino-Silicates. *SPE Prod & Oper* **15** (4): 279–287. SPE-37459-MS. http://dx.doi.org.ezproxy.library.tamu.edu/10.2118/37459-MS.

Guichard, J. A., Allison, D., Gdanski, R. D. et al. 1996. An Overview of HF Acid as Applied to the Wilcox Sand in Reddell Field, Southwest Louisiana. Presented at the SPE Formation Damage Control Symposium, Lafayette, Louisiana, 14-15 February. SPE-31139-MS. https://doi.org/10.2118/31139-MS.

Hartman, R. L., Lecerf, B., Frenier, W. W. et al. 2006. Acid-Sensitive Aluminosilicates: Dissolution Kinetics and Fluid Selection for Matrix-Stimulation Treatments. *SPE Prod & Oper* **21** (2): 194-204. SPE-82267-PA. https://doi.org/10.2118/82267-PA.

Hill, D. G. 2005. Gelled Acid. United States Patent Application Publication, US2005/0065041 A1.

Hull, K. L., Sayed, M., and Al-Muntasheri, G. A. 2016. Recent Advances in Viscoelastic Surfactants for Improved Production From Hydrocarbon Reservoirs. *SPE J.* **21** (4): 1,340-1,357. SPE-173776-PA. https://doi.org/10.2118/173776-PA.

Ji, Q., Zhou, L., & Nasr-El-Din, H. A. 2016. Acidizing Sandstone Reservoirs With Aluminum-Based Retarded Mud Acid. *SPE j.* **21** (3): 1050-1060. SPE-169395-PA. http://dx.doi.org/10.2118/169395-PA.

Kalfayan, L. I., and Martin, A. N. 2009. The Art and Practice of Acid Placement and Diversion: History, Present State and Future. Presented at the SPE Annual Technical Conference and Exhibition, New Orleans, Louisiana, 4-7 October. SPE-124141-MS. http://dx.doi.org.ezproxy.library.tamu.edu/10.2118/124141-MS.

Kenyon, W.E., Ehrlich, R., Horkowitz, K. et al. 1989. Pore-Size Distribution and NMR in Microporous Cherty Sandstones. Presented at the SPWLA 30th Annual Logging Symposium, Denver, Colorado, 11–14 June. SPWLA-1989-LL.

Khilar, K. C. and Fogler, H. S. 1983. Water Sensitivity of Sandstones. *SPE J.* **23** (1): 55-64. SPE-10103-PA. http://dx.doi.org.ezproxy.library.tamu.edu/10.2118/10103-PA.

Lewis, R., Singer, P., Jiang, T. et al. 2013. NMR T_2 Distributions in the Eagle Ford Shale: Reflections on Pore Size. Presented at the SPE Unconventional Resources Conference-USA, The Woodlands, Texas, 10-12 April. SPE-164554-MS. http://dx.doi.org/10.2118/164554-MS.

Li, L., Nasr-El-Din, H. A., and Cawiezel, K. E. 2010. Rheological Properties of a New Class of Viscoelastic Surfactant. *SPE Prod & Oper* **25** (3): 355–366. SPE-121716-PA. http://dx.doi.org/10.2118/121716-PA.

Lungwitz, B., Fredd, C., Brady, M., Miller, et al. 2007. Diversion and Cleanup Studies of Viscoelastic Surfactant-Based Self-Diverting Acid. *SPE Prod & Oper* **22** (1): 121-127.SPE-86504-PA. http://dx.doi.org.ezproxy.library.tamu.edu/10.2118/86504-PA.

MaGee, J., Buijse, M. A., and Pongratz, R. 1997. Method for Effective Fluid Diversion when Performing a Matrix Acid Stimulation in Carbonate Formations. Presented at the SPE Middle East Oil Show, Bahrain, 15-18 March. SPE-37736-MS. http://dx.doi.org.ezproxy.library.tamu.edu/10.2118/37736-MS.

Mahmoud, M. A., Nasr-El-Din, H. A., & De Wolf, C. A. 2015. High-Temperature Laboratory Testing of Illitic Sandstone Outcrop Cores With HCl-Alternative Fluids. *SPE Pro & Oper* **30** (1): 43–51. SPE-147395-PA. http://dx.doi.org/10.2118/147395-PA.

McCune, C. C., Ault, J. W., and Dunlap, R. G. 1975. Reservoir Properties Affecting Matrix Acid Stimulation of Sandstones. *J Pet Technol* **27** (5): 633-640. SPE-4552-PA. https://doi.org/10.2118/4552-PA.

Muecke, T. W. 1979. Formation Fines and Factors Controlling Their Movement in Porous Media. *J Pet Technol.* **31** (2): 144-50. SPE-7007-PA. http://dx.doi.org/10.2118/7007-PA.

Mungan, N. 1965. Permeability Reduction Through Changes in pH and Salinity. *J Pet Technol.* **17** (12): 1449-53. SPE-1283-PA. http://dx.doi.org/10.2118/1283-PA.

Musharova, D., Mohamed, I. M., and Nasr-El-Din, H. A. 2012. Detrimental Effect of Temperature on Fines Migration in Sandstone Formations. Presented at the SPE International Symposium and Exhibition on Formation Damage Control, Lafayette, Louisiana, USA, 15-17 February. SPE-150953-MS. http://dx.doi.org/10.2118/150953-MS.

Nasr-El-Din, H. A. and Samuel, M. M. 2007. Lessons Learned from Using Viscoelastic Surfactants in Well Stimulation. *SPE Prod & Oper* **22** (1): 112-120. SPE-90383 PA. http://dx.doi.org.ezproxy.library.tamu.edu/10.2118/90383-MS.

Nasr-El-Din, H. A., Al-Ghamdi, A. H., Al-Qahtani, A. A. et al. 2008. Impact of Acid Additives on the Rheological Properties of a Viscoelastic Surfactant and Their Influence on Field Application. *SPE J.* **13** (1): 35-47. SPE-89418-PA. https://doi.org/10.2118/89418-PA.

Nasr-El-Din, H. A., Chesson, J. B., and Cawiezel, K. E. 2006. Lessons Learned and Guidelines for Matrix Acidizing With Viscoelastic Surfactant Diversion in Carbonate Formations. Presented at the SPE Annual Technical Conference and Exhibition, San Antonio, Texas, 24-27 September. SPE-102468-MS. http://dx.doi.org.ezproxy.library.tamu.edu/10.2118/102468-MS.

Nasr-El-Din, H. A., Erbil, M., and El-Gamal, S. 2005. Successful Application of Foamed Viscoelastic Surfactant-Based Acid. Presented at the SPE European Formation Damage Conference, Sheveningen, The Netherlands, 25-27 May. SPE-95006-MS. http://dx.doi.org.ezproxy.library.tamu.edu/10.2118/95006-MS.

Nasr-El-Din, H. A., Samuel, E., and Samuel, M. 2003. Application of New Class of Surfactants in Stimulation Treatments. Presented at the SPE International Improved Oil Recovery Conference in the Asia Pacific, Kuala Lumpur, 20-21 October.SPE-84898-MS. http://dx.doi.org.ezproxy.library.tamu.edu/10.2118/84898-MS.

Nasr-El-Din, H. A., Taylor, K. C., and Al-Hajji, H. H. 2002. Propagation of Cross-Linkers Used in In-Situ Gelled Acids in Carbonate Reservoirs. Presented at the SPE/DOE Improved Oil Recovery Symposium, Tulsa, Oklahoma, 13-17 April. SPE-75257-MS. http://dx.doi.org.ezproxy.library.tamu.edu/10.2118/75257-MS.

Nelson, E. B. et al. 2005. Viscosity Reduction of Viscoelastic-Based Fluids. U.S. Patent No. 6,881,709.

Pal, R. 1996. Effect of Droplet Size on the Rheology of Emulsions. *AIChE Journal* **42** **(**11): 3,181-3,190.

Parkinson, C., Matsumoto, S., and Sherman, P. 1970. The Influence of Particle-Size Distribution on The Apparent Viscosity of Non-Newtonian Dispersed Systems. *Journal of colloid and interface science* **33** (1): 150-160.

Qu, Q. et al. 2002. Compositions Containing Aqueous Viscosifying Surfactants and Methods for Applying Such Compositions in Subterranean Formations. U.S. Patent No. 6,435,277.

Rabie, A. I. and Nasr-El-Din, H. A. 2015. Effect of Acid Additives on the Reaction of Stimulating Fluids During Acidizing Treatments. Presented at the SPE North Africa Technical Conference and Exhibition, Cairo, Egypt, 14-16 September. SPE-175827-MS. http://dx.doi.org.ezproxy.library.tamu.edu/10.2118/175827-MS.

Rostami, A. and Nasr-El-Din, A. H. 2009. Review and Evaluation of Corrosion Inhibitors Used in Well Stimulation. SPE International Symposium on Oilfield Chemistry, The Woodlands. Texas, 20-22 April. SPE-121726-MS. https://doi.org/10.2118/121726-MS.

Samuel, M., Card, R. J., Nelson, E. B. et al. 1997. Polymer-Free Fluid for Hydraulic Fracturing. Presented at the SPE Annual Technical Conference and Exhibition, San Antonio, Texas, 5-8 October. SPE-38622-MS. https://doi.org/10.2118/38622-MS.

Samuel, M., Marcinew, R., Al-Harbi, et al. 2003. A New Solids-Free Non-Damaging High-Temperature Lost-Circulation Pill: Development and First Field Applications. Presented at the SPE Middle East Oil Show, Bahrain, 9-12 June. SPE-81494-MS. http://dx.doi.org.ezproxy.library.tamu.edu/10.2118/81494-MS.

Schembre, J. M., Tang, G. Q. and Kovscek, A. R., 2006. Interrelationship of Temperature and Wettability on the Relative Permeability of Heavy Oil in Diatomaceous Rocks. *SPE Res Eval & Eng* **9** (3): 239-250. SPE-93831-PA. http://dx.doi.org.ezproxy.library.tamu.edu/10.2118/93831-PA.

Shu, Y., Wang, G., Nasr-El-Din, H. A., and Zhou, J. 2015. Interactions of Fe (III) and Viscoelastic-Surfactant-Based Acids. *SPE Prod & Oper*. **31** (1): 29-46. SPE-165149-PA. http://dx.doi.org/10.2118/165149-PA.

Shuchart, C. E. and Buster, D. C. 1995. Determination of the Chemistry of HF Acidizing with the Use of 19_F NMR Spectroscopy. Presented at the SPE International Symposium on Oilfield Chemistry, San Antonio, Texas, 14-17 February. SPE-28975-MS. http://dx.doi.org.ezproxy.library.tamu.edu/10.2118/28975-MS.

Shuchart, C. E. and Gdanski, R. D. 1996. Improved Success in Acid Stimulations with a New Organic-HF System. Presented at the European Petroleum Conference, Milan, Italy, 22-24 October. SPE-36907-MS. https://doi.org/10.2118/36907-MS.

Simon, D. E. and Anderson, M. S. 1990. Stability of Clay Minerals in Acid. Presented at the SPE Formation Damage Control Symposium, Lafayette, Louisiana, 22-23 February. SPE-19422-MS. https://doi.org/10.2118/19422-MS.

Smith, C. F. and Hendrickson, A. R. 1965. Hydrofluoric Acid Stimulation of Sandstone Reservoirs. *J Pet Technol* **17** (2): 215-222. SPE-980-PA. https://doi.org/10.2118/980-PA.

Smith, C. L., Anderson, J. L., and Roberts, P. G. 1969. New Diverting Techniques for Acidizing and Fracturing. Presented at the SPE California Regional Meeting, San Francisco, California, 6-7 November. SPE-2751-MS. http://dx.doi.org.ezproxy.library.tamu.edu/10.2118/2751-MS.

Taylor, K. C. and Nasr-El-Din, H. A. 2002. Coreflood Evaluation of In-Situ Gelled Acids. Presented at the SPE International Symposium and Exhibition on Formation Damage Control, Lafayette, Louisiana, 20-21 February. SPE-73707-MS. http://dx.doi.org.ezproxy.library.tamu.edu/10.2118/73707-MS.

Taylor, K. C. and Nasr-El-Din, H. A. 2003. Laboratory Evaluation of In-Situ Gelled Acids for Carbonate Reservoirs. *SPE J.* **8** (4): 426-434. SPE-87331-PA. http://dx.doi.org.ezproxy.library.tamu.edu/10.2118/87331-PA.

Thomas, R. L., Nasr-El-Din, H. A., Lynn, J. D. et al. 2001. Precipitation During the Acidizing of a HT/HP Illitic Sandstone Reservoir in Eastern Saudi Arabia: A Laboratory Study. Presented at the SPE Annual Technical Conference and Exhibition, New Orleans, Louisiana, 30 September-3 October. SPE-71690-MS. https://doi.org/10.2118/71690-MS.

Truong, M. T. and Walker, L. M. 2000. Controlling the Shear-Induced Structural Transition of Rodlike Micelles using Nonionic Polymer. *Langmuir* **16** (21): 7,991-7,998.

Vinegar, H. J. 1986. X-Ray CT and NMR Imaging of Rocks. *J Pet Technol* **38** (3): 257-259. SPE-15277-PA. https://doi.org/10.2118/15277-PA.

Walsh, M. P., Lake, L. W., and Schechter, R. S. 1982. A Description of Chemical Precipitation Mechanisms and Their Role in Formation Damage During Stimulation by Hydrofluoric Acid. *J Pet Technol* **34** (9): 2,097-2,112. SPE-10625-PA. https://doi.org/10.2118/10625-PA.

Wehunt, C. D., Van Arsdale, H., Warner, J. L. et al. 1993. Laboratory Acidization of an Eolian Sandstone at 380°F. Presented at the SPE International Symposium on Oilfield Chemistry, New Orleans, Louisiana, 2-5 March. SPE-25211-MS. https://doi.org/10.2118/25211-MS.

Woo, G. T., Lopez, H., Metcalf, A. S., et al. 1999. A New Gelling System for Acid Fracturing. Presented at the Mid-Continent Operations Symposium, Oklahoma City, Oklahoma, 28-31 March. SPE-52169-MS. http://dx.doi.org.ezproxy.library.tamu.edu/10.2118/52169-MS.

Wunderlich, I., Hoffmann, H., and Rehage, H. 1987. Flow Birefringence and Rheological Measurements on Shear Induced Micellar Structures. *Rheologica Acta* **26** (6): 532-542.

Yang, F., Nasr-El-Din, H. A., and Al-Harbi, B. M. 2012. Acidizing Sandstone Reservoirs Using HF and Formic Acids. Presented at the SPE International Symposium and Exhibition on Formation Damage Control, Lafayette, Louisiana, 5-17 February. SPE-150899-MS. http://dx.doi.org.ezproxy.library.tamu.edu/10.2118/150899-MS.

Yeager, V. and Shuchart, C. 1997. In Situ Gels Improve Formation Acidizing. *Oil & Gas J.* **95** (3): 70-72.

Yu, M., Mu, Y., Wang, G. et al. 2012. Impact of Hydrolysis at High Temperatures on the Apparent Viscosity of Carboxy Betaine Viscoelastic Surfactant-Based Acid: Experimental and Molecular Dynamics Simulation Studies. *SPE J.* **17** (4): 1,119-1,130. SPE-142264-PA. https://doi.org/10.2118/142264-PA.

Zhi-Xiang, L., Jeffrey, P., and Yi-Qiao, S. 2015. Robust Determination of Surface Relaxivity from Nuclear Magnetic Resonance DT 2 Measurements. *Magnetic Resonance* **259** (2015): 146-152.